Advances in Civil Engineering

Artificial Intelligence Applications in Sustainable Material Analysis and Design

Lead Guest Editor: Ravindran Gobinath
Guest Editors: Isaac Ibukun Akinwumi and Hamid Reza Pourghasemi

Artificial Intelligence Applications in Sustainable Material Analysis and Design

Advances in Civil Engineering

Artificial Intelligence Applications in Sustainable Material Analysis and Design

Lead Guest Editor: Ravindran Gobinath
Guest Editors: Isaac Ibukun Akinwumi and Hamid Reza Pourghasemi

Contents

Hindawi
Advances in Civil Engineering
Volume 2022, Article ID 9343330, 15 pages
https://doi.org/10.1155/2022/9343330

Research Article

An Artificial Neural Network Based Prediction of Mechanical and Durability Characteristics of Sustainable Geopolymer Composite

P. Manikandan,[1] **K. Selija**,[2] **V. Vasugi**,[1] **V. Prem Kumar**,[3] **L. Natrayan**,[4] **M. Helen Santhi**,[1] **and G. Senthil Kumaran**[5]

[1]*School of Civil Engineering, Vellore Institute of Technology, Chennai Campus, Tamil Nadu, India*
[2]*Department of Civil Engineering, Indian Institute of Technology, Guwahati, Assam, India*
[3]*Department of Civil Engineering, Sree Vidyanikethan Engineering College, Tirupati, Andhra Pradesh, India*
[4]*Department of Mechanical Engineering, Saveetha School of Engineering, SIMATS, Chennai, Tamil Nadu, India*
[5]*Department of Civil Engineering, Copper Belt University, Kitwe, Zambia*

Correspondence should be addressed to P. Manikandan; manikandan.p2016@vitstudent.ac.in, V. Vasugi; vasugi.v@vit.ac.in, and G. Senthil Kumaran; kumaran.gs@cbu.ac.zm

Received 28 April 2022; Revised 20 July 2022; Accepted 12 August 2022; Published 20 September 2022

Academic Editor: Ravindran Gobinath

Despite the growing environmental consequences of cement production, geopolymer concrete now has gradually evolved as an ecologically sustainable product. This study experimentally investigates the effect of addition of different proportions (0%, 10%, and 20%) of rice husk ash (RHA) and polypropylene (PP) fibers (0%, 0.1%, and 0.3%) on the mechanical and durability characteristics of fly ash (FA)-based geopolymer mortars. The strength property is assessed by testing the mortar specimen by uniaxial compressive strength and flexural strength while the durability properties were tested with water absorption, water sorptivity, and acid (10% concentration of H_2SO_4) resistance tests. The experimental findings revealed that the PP fiber addition is not significant in improving the compressive strength, while the addition up to 0.3% by volume had shown good improvement in flexural behavior. Water absorption increases with an increment in the replacement proportion of RHA. Water sorptivity also increases with an increase in RHA substitution levels. Furthermore, an artificial neural network prototype was proposed in this work to forecast the mechanical and durability properties of fiber reinforced FA-RHA blended geopolymer mortar. The ANN architecture was constructed utilizing the mechanical and durability characteristics of FA-RHA blended geopolymer mortar procured through experimental investigation. The RHA substitution proportion, sodium hydroxide (NaOH) liquid concentration, and polypropylene fiber content have been employed as input parameters in the construction of ANN framework. The predicted strength values of mechanical and durability tests achieved from the ANN framework agree well with experiment results. Use of geopolymer mortar has a high potential in repairing the structural elements, and further studies can be done on applying this mortar for the repairs.

1. Introduction

Ordinary Portland Cement (OPC) is commonly used as a traditional binding material in all concreting projects. The manufacturing of OPC consumes a tremendous amount of energy and disperses a huge proportion of carbon dioxide into the Earth's atmosphere. To mitigate carbon dioxide emissions, a new promising binder known as geopolymer was introduced [1]. Numerous researches have been carried out on the effective and comprehensive utilization of different industrial waste materials in the manufacturing process of geopolymer concrete [2]. Its manufacturing process includes the formulation of binders from the alumina and silica rich sources acquired from the industrial byproducts or low-cost materials such as fly ash (FA), ground granulated blast furnace slag (GGBS), metakaolin (MK), rice husk ash (RHA), high magnesium nickel slag (HMNS), palm oil fuel ash (POFA), waste glass powder (WGP), red mud, etc. using an alkali activator solution [3–5]. The presence of binding material in geopolymer

binder is supplemented by industrial/agricultural wastes that comprises pozzolanic characteristics comparable to OPC and abundant in alumina and silica proportions [6–8]. In order to extract the silica and alumina sourced from the raw materials, the alkali-activated solution is employed as a catalyst which contains a mixture of sodium hydroxide (NaOH) and sodium silicate (Na_2SiO_3) solutions [9, 10].

FA and RHA are industrial byproducts of thermal power stations and rice husk burning, respectively. The principal objective of producing a geopolymer composite from an industrial byproduct is to promote a sustainable alternative for conventional Portland cement concrete by significantly lowering greenhouse gas emissions and industrial waste disposal concerns [11–13]. Earlier studies showed that the effectiveness and usage of higher molarity of alkaline solution significantly influence the early strength of the geopolymer concrete [3, 14, 15]. Literature reported that the required mechanical properties of the geopolymer concrete specimens could be achieved in the ambient curing conditions [16, 17]. On the other hand, FA-GGBS based geopolymer binders produced excellent mechanical and microstructural characterizations even after the exposure to elevated temperatures [18, 19]. The addition of copper slag in the FA type geopolymer concrete resulted in higher compressive strength results [20, 21]. Partial incorporation of RHA with FA in geopolymer concrete resulted in an increase in durability and mechanical strength properties [22, 23]. Incorporation of RHA as a source material in the slag-based geopolymer concrete resulted in greater compressive and split-tensile strength results [24].

ANN is based on machine learning framework that simulates a network of biological neural networks. It can be used extensively in the domain of science and engineering to overcome extremely complex problems [25, 26]. The ANN framework outperforms other techniques in aspects of nonlinear connection among input parameters [27]. According to recent findings, the ANN structure can be used successfully in the construction and building materials stream to estimate their strength properties with precision [28–30]. Khademi et al. employed multiple linear regression (MLR), artificial neural network, and adaptive neurofuzzy inference system (ANFIS) techniques to estimate the 28-day compressive strength of concrete [31]. Apart from mechanical strength, other important parameters like mix design [32], cement content [33], replacement level of recycled coarse aggregates [34], drying shrinkage of concrete [35], slump values [36], etc. can also be predicted with the help of neural networks along with experimental results. Several studies described that the compressive, split-tensile, and flexural (mechanical) properties of FA-based geopolymer matrix are predicted with the application of the ANN framework [37, 38].

Although the usage of FA in geopolymer production is significantly reported in the kinds of literature, the use of RHA and fibers is scanty. This experimental investigation is aimed at exploring the influence of fiber and RHA in the fly ash based geopolymer mortar, since the potential use of geopolymer mortar as a repair material for the strengthening of structures. In addition to this ANN framework was developed using Levenberg-Marquardt (LM) Algorithm in MATLAB-2018a to estimate the mechanical and durability strength results of fiber incorporated RHA-FA-based geopolymer mortar.

Table 1: Chemical constituents of geopolymer precursors.

Chemical components (%)	Fly ash	Rice husk ash
SiO_2	63.39	87.42
Al_2O_3	26.85	2.85
CaO	2.54	0.71
Fe_2O_3	5.57	0.56
MgO	0.42	0.37
ZnO	—	0.02
MnO	0.02	—
LOI	0.30	0.88

2. Materials and Experimental Program

2.1. Materials and Sample Preparation. In this study, the materials procured for the geopolymer mortar preparation were FA and RHA. The FA and RHA obtained from Kolkata were used as the source materials. Table 1 presents the chemical compositions of the geopolymeric precursor products acquired from X-ray fluorescence (XRF) analysis. Locally resourced river sand with specific gravity 2.5 was used as fine aggregate. The mixture of commercially available sodium hydroxide (flakes type) and sodium silicate (liquid gel type) sourced and supplied by Sharma brothers, India, was employed as an alkaline activator solution. The alkali activator solution was produced by blending sodium silicate solution with a molar ratio (SiO_2/Na_2O) of 2.65 and sodium hydroxide. The specific gravity and molar mass of the sodium silicate solution and sodium hydroxide pellets employed were 1.52 and 2.14 and 123 g/mol and 38.8 g/mol, respectively. The source materials present in the FA and RHA geopolymer mortars were enhanced by the alkali activator solution. Commercially available PP fibers and sulfuric acid were used. Figure 1 illustrates the visual appearances of the geopolymeric source materials (RHA and FA) and PP fibers used in this investigation.

A partial replacement of FA was carried out using RHA (0%, 10%, and 20%) with the addition of polypropylene fiber of 0.0%, 0.1%, and 0.3% by volume and mixed thoroughly with alkaline activator solution to obtain uniform slurry. Fine aggregate was then introduced to the slurry in the ratio of 1 to FA to obtain geopolymer mortars. Geopolymer specimens were prepared in two layers using $70 \times 70 \times 70$ mm cubes and vibrated for about two minutes in table vibrator to remove the entrapped air present in mortars. The geopolymer mortar specimens thus prepared were cured in the hot air oven for about 24 hours at the temperature of 110°C and then kept in the ambient conditions until further testing.

2.2. Experimental Approach. The various mix proportions considered for the experimental investigations on FA-RHA geopolymer mortar influenced with polypropylene fibers are listed below. The mixes with varying % of RHA and the

(a) (b) (c)

Figure 1: Visual appearance of materials used in the study: (a) RHA, (b) FA, and (c) PP fibers.

Table 2: Details of the geopolymer mortar mixes.

Mix ID	FA (Kg/m^3)	RHA (Kg/m^3)	Fiber (%)	FA (%)	RHA (%)	Molarity of NaOH
$G_{1\text{-}3}$	600	0	0	100	0	5 M, 10 M, 15 M
$G_{4\text{-}6}$	600	0	0.1	100	0	5 M, 10 M, 15 M
$G_{7\text{-}9}$	600	0	0.3	100	0	5 M, 10 M, 15 M
$G_{10\text{-}12}$	540	60	0	90	10	5 M, 10 M, 15 M
$G_{13\text{-}15}$	540	60	0.1	90	10	5 M, 10 M, 15 M
$G_{16\text{-}18}$	540	60	0.3	90	10	5 M, 10 M, 15 M
$G_{19\text{-}21}$	480	120	0	80	20	5 M, 10 M, 15 M
$G_{22\text{-}24}$	480	120	0.1	80	20	5 M, 10 M, 15 M
$G_{25\text{-}27}$	480	120	0.3	80	20	5 M, 10 M, 15 M

polypropylene fibers resulted in 27 mixes, as reported in Table 2. The strength reported was the average of three identical specimens. To achieve the preferred workability in all mixture proportions, the alkaline to binder ratio and sodium silicate to sodium hydroxide fraction were selected to 0.5 and 2.5, respectively. For all of the mix composition, the quantities of fine aggregates, binder content, sodium silicate solution, and sodium hydroxide flakes selected were 600 kg/m^3, 600 kg/m^3, 257.15 kg/m^3, and 102.85 kg/m^3, respectively.

Universal Testing Machine (UTM) was used for calculating the uniaxial compressive strength of geopolymer mortars at 28 days as per IS 516 (1959) provisions. The flexural strength characteristics of fiber reinforced FA-RHA based geopolymer mortar specimens were ascertained in accordance with IS 516 (1959) standards using a Universal Testing Machine of 1000 kN capacity [39]. Prism samples of size 40 × 40 × 160 mm were casted and examined for flexural performance after 28 days. The method monitored for the determination of water absorption of geopolymer samples was in accordance with ASTM C 642 standards [40]. After measuring the weights of 28-day-old geopolymer mortar samples, they were dried at 110°C for 24 hours before being immersed in water. The specimens were then removed from the water and wiped clean and directly weighed in saturated surface dry conditions to find an increase in weight.

Existing literature reports proved that geopolymer binders were acid resistant, providing them a promising and alternative construction material for the sewer environment. This study examines the durability of FA-RHA based geopolymer mortars subjected to 10% sulfuric acid concentration for 56 days and tested for its strength according to ASTM C 643 standards [41]. The rate of capillary rise absorption by mortar cube is ascertained by the sorptivity test. The samples are initially coated with waterproof enamel paint on all sides except the bottom and top surfaces, so as to allow capillary uptake of water only from the bottom. The specimens are then conditioned at 110°C for 24 hours to obtain constant mass. Test samples are made to rest on supports (a supporting wire mesh in the present case) in a manner such that only the lowest 2 to 5 mm of the cube is underwater. The rise in the mass of the sample with time is noted. Then water uptake per unit area of concrete surface I (g/mm^2) is plotted with the square root of time for the suction periods (t). Hence $I = C + \mathrm{St}^{1/2}$ where I = increase in mass per unit area (g/mm^2); t = time, measured in minutes at which the mass is determined; S = sorptivity in g/mm^2/min$^{0.5}$; $C = a$ constant.

3. Prediction of Strength and Durability Characteristics Using ANN

ANN is indeed a massively simultaneous computing intelligence processing architecture which operates equivalent to biological neural systems [42]. It also has the ability to comprehend and extrapolate mostly from provided

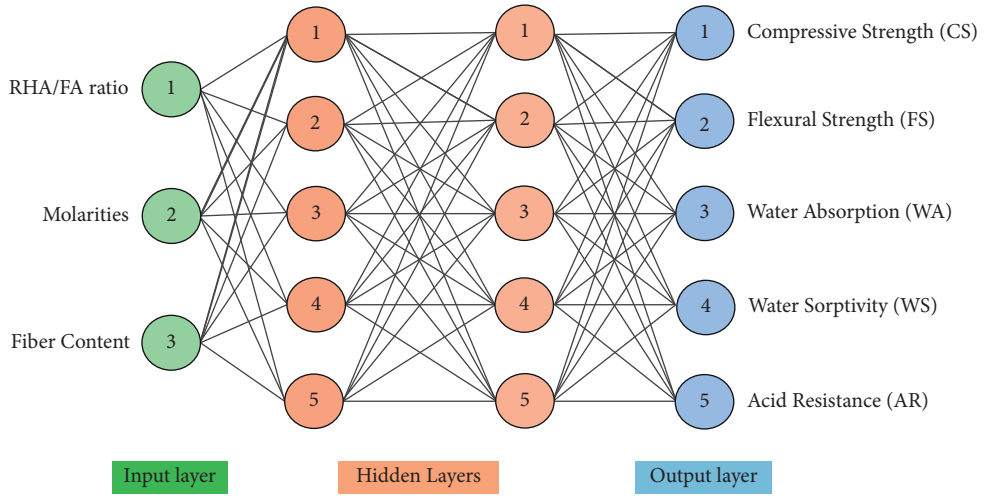

Figure 2: ANN (3-5-5-5) architecture selected for the preset study.

Table 3: The ranges of input and output parameters selected in ANN framework.

Si. No.	Variables	Units	Limits	Remarks
1.	RHA/FA ratio	—	0 to 0.25	
2.	NaOH concentration	M	5 to15	Inputs
3.	Fiber content	%	0 to 0.3	
4.	Compressive strength	MPa	40 to 62	
5.	Flexural strength	MPa	7.5 to 12.4	
6.	Water absorption	%	0.759 to 4.0	Outputs
7.	Water sorptivity	$mm/min^{0.5}$	0.208 to 1.10	
8.	Acid resistance	MPa	20 to 44	

information and intended to deliver appropriate responses even though the group of input variables comprises an inconsistency or is ambiguous [37, 43]. It comprises several interlinked engineered neuron-like structures, each of which delivers a distinct response (Y) from most of the inputs (X_j) across equation (1) [44]. The activation function (f) is associated with the sum of input parameters procured from the sum function and determines the neuron's output. Phrase (H) illustrates the amount of the input parameters that can be anticipated using equation (2), and "b" is the bias coefficient, which is applied to influence the activation function.

$$Y = f(H) = \frac{1}{1 + e^{-H}}, \tag{1}$$

$$S = \sum_{j=1}^{n} X_j W_j + b. \tag{2}$$

Since the ANN framework constitutes three components, it can be regarded as a Multilayer Perception (MLP) structure, as illustrated in Figure 2. The first layer (input layer) contains three independent variables (RHA/FA ratio, different molarities, and percent of fibers) that are used for entering data. The second layer is regarded as the hidden layer or computational layer, whereas the third layer is recognized as the output layer, from which ANN model estimates compressive, flexural, water absorption, acid resistance, and water sorptivity values.

Different variables such as RHA/FA ratio, varying concentrations of NaOH solution, and percentages of polypropylene fibers have a significant impact on the strength and durability characteristics of geopolymer mortar mixes [45, 46]. Hence, the RHA/FA ratio, different molarities, and percentages of polypropylene fibers were preferred as input parameters for the geopolymer mortar mixes, and the target variables were compressive strength (CS), flexural strength (FS), water absorption (WA), water sorptivity (WS), and acid resistance (AR) of geopolymer mortar specimens.

The overall amount of hidden compartments and the number of neurons in every hidden compartment in the ANN structure could be ascertained through implementing the handful of assessments throughout the training and testing period until the desired outcomes are achieved with negligible error values. The LM algorithm was implemented in ANN model with feedforward backpropagation technique to estimate the durability and mechanical properties of geopolymer mortar using an ANN model with two hidden layers and five neurons in each layer. Out of 27 experimental test results, 19 were selected for training, 4 for testing, and 4 for validation phase. The limits for input and output responses considered for this study are listed in Table 3. The accuracy of the output responses recorded from the

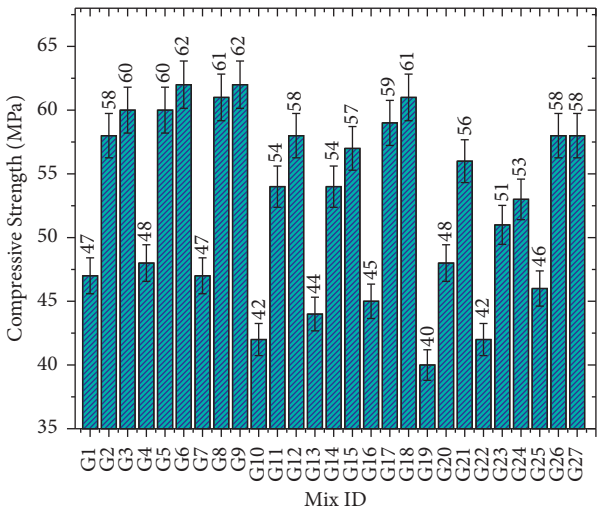

Figure 3: Compressive strength development of FA-RHA based geopolymer mortars.

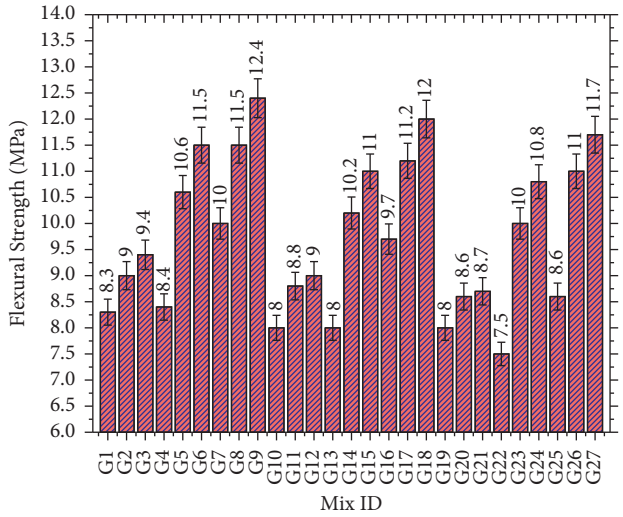

Figure 4: Flexural strength development of FA-RHA based geopolymer mortars.

developed ANN framework were ascertained in terms of error percentages using the following equation [44]:

$$\text{error prediction (\%)} = \frac{\text{experimental results} - \text{predicted results}}{\text{experimental results}} \times 100. \quad (3)$$

4. Results and Discussion

4.1. Compressive Strength. The compressive strength development of ambient cured (110°C for 24 hours) FA-based geopolymer mortar samples containing varying proportions of RHA (0%, 10%, and 20%), polypropylene fibers (0%, 0.1%, and 0.3%), and NaOH solution concentrations (5 M, 10 M, and 15 M) was represented in Figure 3. According to Figure 3, the highest compressive strength value of 62 MPa was

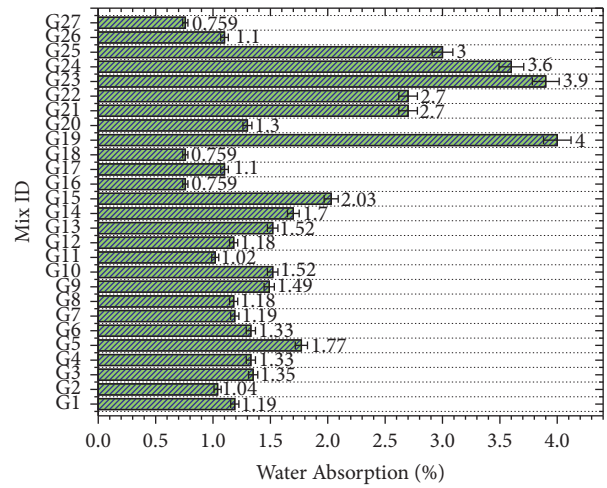

Figure 5: Water absorption results of geopolymer mortar specimens.

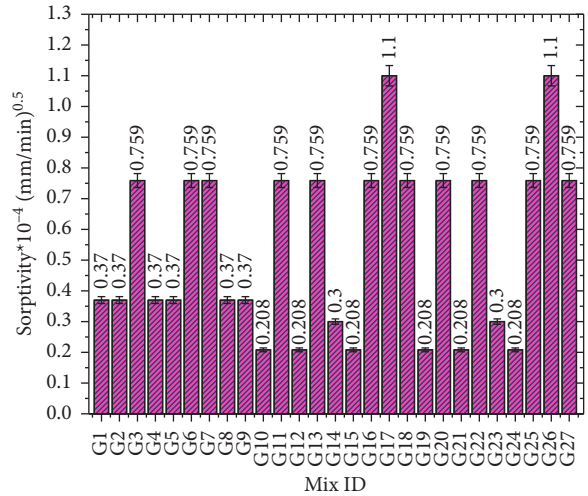

Figure 6: Water sorptivity test results for geopolymer mortar samples.

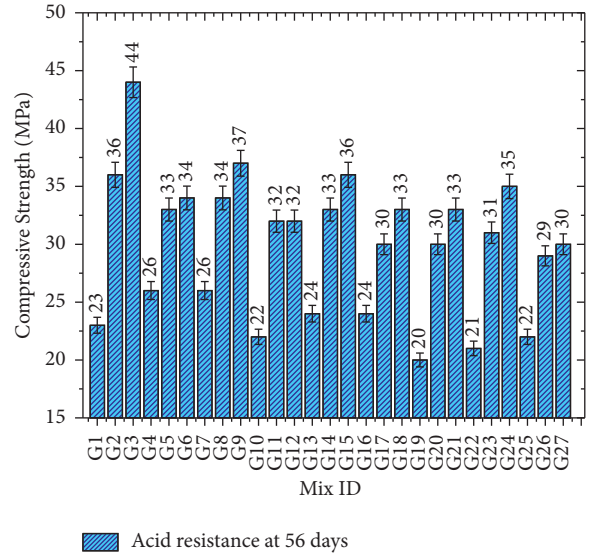

Figure 7: Compressive strength at 56 days of 10% of H_2SO_4 solution exposure.

Table 4: Percentage of error values obtained from the ANN framework.

Mix ID	Predicted error in percentage (%)				
	Compressive strength	Flexural strength	Water absorption	Sorptivity	Acid resistance
G1	1.91	3.61	−3.36	2.16	2.17
G2	−0.17	−1.11	−2.88	−3.78	−3.89
G3	−2.97	−1.06	−1.48	−3.95	−1.59
G4	1.46	−1.19	−3.76	3.24	2.69
G5	0.17	3.77	−3.39	−2.70	1.82
G6	−0.32	1.74	−4.51	−2.24	0.65
G7	0.19	3.50	−2.52	2.11	−3.27
G8	0.66	2.61	−2.54	−2.70	−3.88
G9	−1.13	−1.61	−2.01	2.97	1.54
G10	−3.21	1.25	−1.97	−0.96	−4.77
G11	0.19	3.41	4.90	−1.84	−2.97
G12	0.69	−3.33	−2.54	−5.77	1.78
G13	1.36	−2.50	−4.61	−0.66	2.63
G14	2.22	−1.96	−4.12	6.33	−0.64
G15	0.35	0.91	−3.94	−2.40	0.69
G16	−0.89	3.09	−5.40	−2.77	−0.21
G17	1.86	−1.79	−1.82	−6.36	−1.00
G18	−0.66	1.67	−5.40	1.98	3.52
G19	−1.50	2.13	−2.75	1.92	−6.15
G20	−1.04	−1.16	−3.08	−0.79	4.17
G21	1.25	−1.15	−4.81	−1.44	1.39
G22	0.95	−4.00	−2.96	2.37	3.24
G23	2.94	2.00	3.33	1.33	−1.03
G24	−1.13	−0.93	1.94	−3.37	0.74
G25	0.43	3.49	−4.00	2.24	−0.23
G26	−0.55	−1.82	−4.55	−1.82	−3.00
G27	0.69	0.85	−2.77	−1.45	2.33

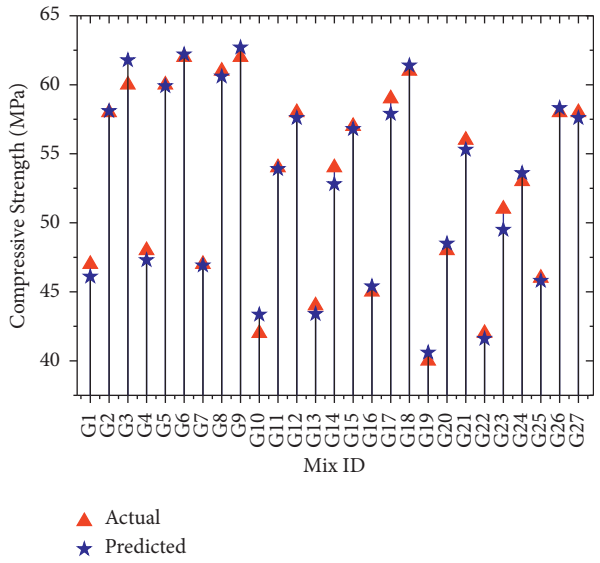

Figure 8: Comparison of experimental and predictive compressive strength results.

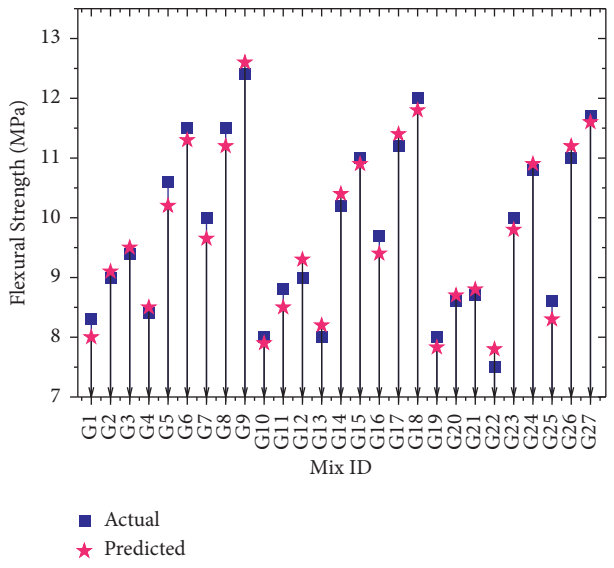

Figure 9: Comparison of experimental and predictive flexural strength results.

ascertained for G6 and G9 mortar mixes featuring 100 percent FA. Due to the higher geopolymerization reaction, equivalent higher compressive strength results were observed for mortar mixes containing 10% and 20% substitution levels of RHA with a 15 M concentration of NaOH solution [47, 48]. In addition, the compressive strength properties of geopolymer specimens consisting of 10 M and 15 M concentration of NaOH solution were comparable. Furthermore, it can be stated that inclusion of different proportion of PP fibers did not produce significant change in the compressive strength of FA-RHA based geopolymer mortars.

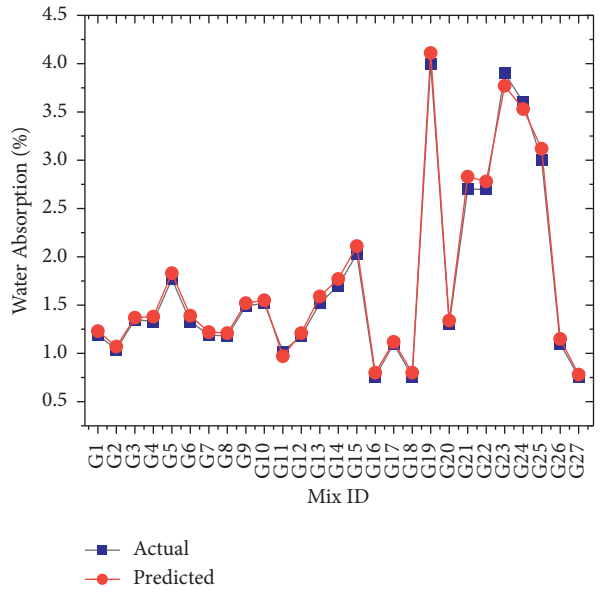

Figure 10: Comparison of experimental and predictive water absorption values.

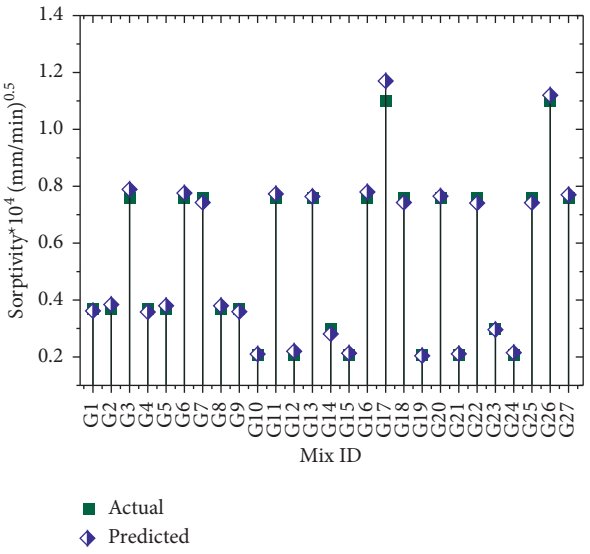

Figure 11: Comparison of experimental and predictive sorptivity results.

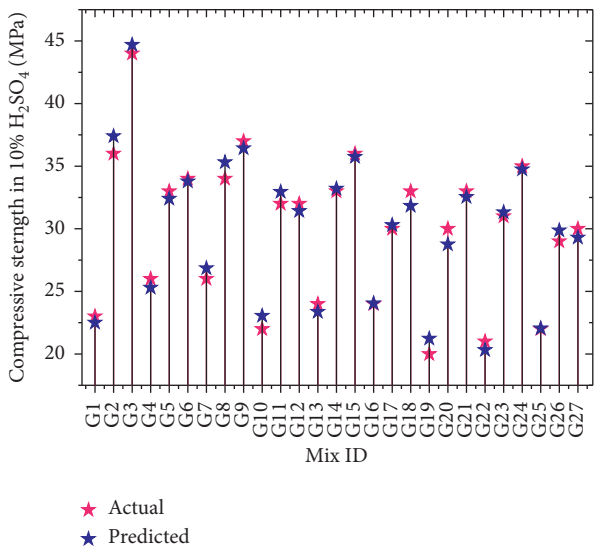

Figure 12: Comparison of experimental and predictive acid resistance results.

4.2. Flexural Strength. Figure 4 depicts the flexural strength characteristics of various geopolymer mortar mixes evaluated in this experimental investigation. From Figure 4, it can be observed that the incorporation of 0.3 percent polypropylene fibers in FA-RHA blended geopolymer mortars resulted in a marginal increase in flexural strength characteristics for G7, G8, G9, G16, G17, G18, G25, G26, and G27 mixes when compared to the other mortar mix proportions. The maximum flexural strength of 12.4 MPa was recorded for the geopolymer mix G9 comprising 100% FA and 0.3% polypropylene fiber. Furthermore, the experimental results of flexural tests revealed that a higher concentration (15 M) of NaOH solution resulted in a significant increase in flexural strength of geopolymer specimens [15, 49]. A higher concentration of NaOH solution enhances the solubility of Al and Si ions from the precursor materials, resulting in the generation of relatively strong Si–O–Al, C-A-S-H, and N-A-S-H gels which resulted in the increase in strength properties. However, the different RHA substitution levels have no effect on the development of flexural strength in FA-based geopolymer mortars. The increased proportion of RHA results in a significant concentration of unreacted RHA granules in the geopolymer mixture, resulting in a relatively weak and less ductile geopolymer matrix. The enhanced quantity of SiO_2 disruptions the interaction of Si and Al particles ultimately results in a lesser density geopolymer binder with lower flexural strength [50].

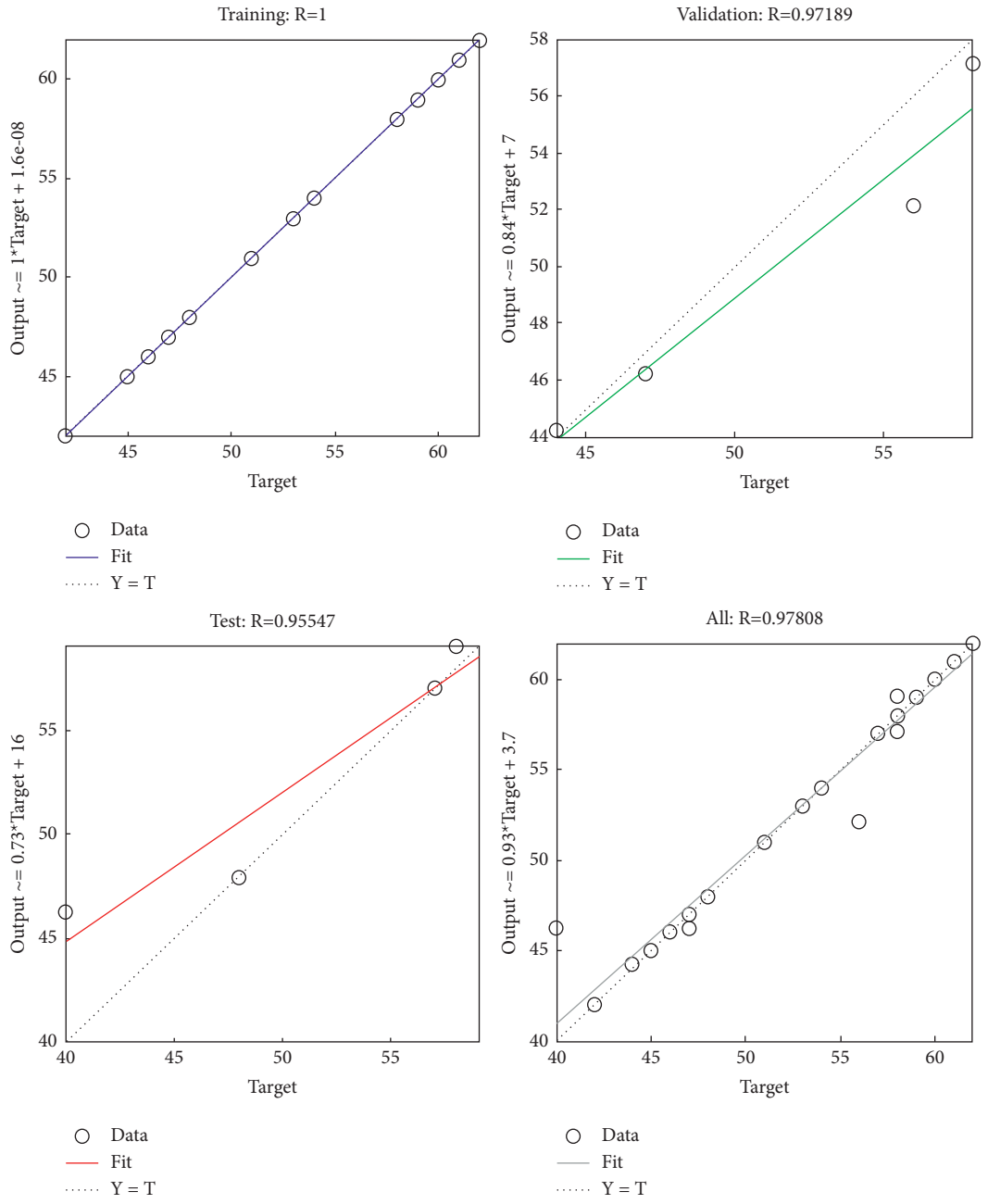

Figure 13: Assessment of predicted compressive strength results.

4.3. Water Absorption. Figure 5 demonstrates the water absorption test results after 240 mins for oven cured FA-based geopolymer mortar specimens with varying levels of RHA (0%, 10%, and 20%), polypropylene fibers (0%, 0.1%, and 0.3%), and NaOH (5 M, 10 M, and 15 M). From Figure 5, it can be observed that G7, G8, G9, G16, G17, G18, G25, G26, and G27 geopolymer mixes with 0.3 percent PP fiber incorporation had lower water absorption than the other mixes.

The behavior of the PP fibers restricts the formation of microcracks, which reduces the water absorption capacity of the mortar mixes. Furthermore, the PP fiber's non-absorbability (hydrophobicity) nature contributed to a decrease in waster absorption capacity [51]. Moreover, introducing 20% RHA replacement levels to FA-based geopolymer mortar resulted in increased water absorption test result compared to other combinations.

4.4. Water Sorptivity. Water sorptivity test results for the series of the FA-based geopolymer mortars substituted with varying proportions of RHA (0%, 10%, and 20%) and polypropylene fibers (0%, 0.1%, and 0.3%) under the influence of different NaOH solution (5 M, 10 M, and 15 M) were represented in Figure 6. From the test results it can be observed that the rate of water absorption for geopolymer mortars containing (100% FA) and (90% FA: 10% RHA) produced less sorptivity values. On the other hand,

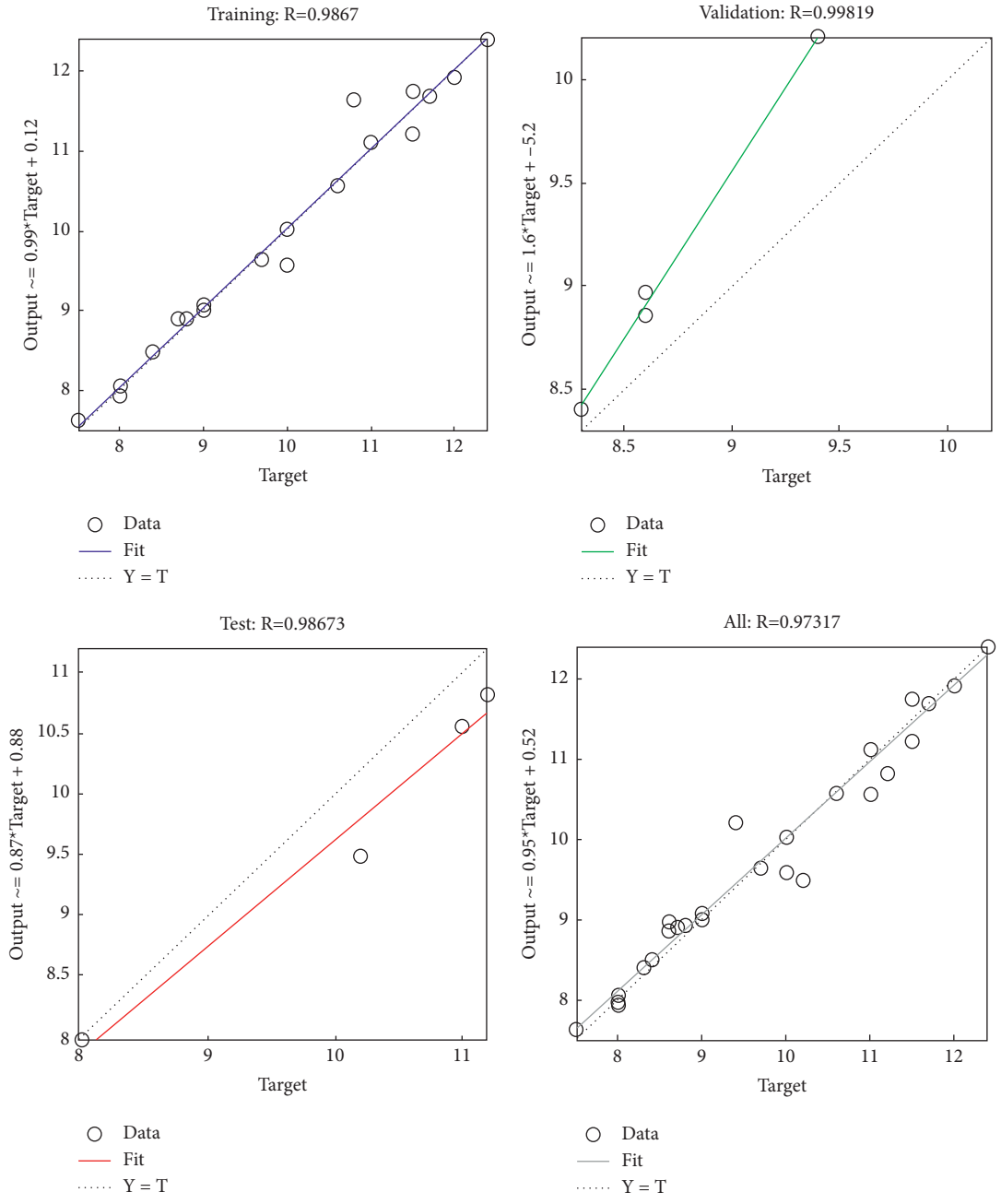

Figure 14: Assessment of predicted flexural strength values.

geopolymer mortar mixes constituting 80% FA and 20% RHA showed higher rate of water absorption due to the inferior properties of RHA particles such as higher water absorption capacity than FA [50].

4.5. Acid Resistance. Figure 7 demonstrates the compressive strength progression of polypropylene fiber (0%, 0.1%, and 0.3%) reinforced geopolymer mortar samples immersed in 10% H_2SO_4 solution for 56 days with different levels of RHA (0%, 10%, and 20%) under varying concentrations of NaOH solution. According to Figure 7, geopolymer mixtures with higher molar concentrations of NaOH solution (10 M and 15 M) demonstrate a similar phenomenon in compressive strength results; meanwhile combinations with a 5 M concentration of NaOH produced relatively low strength values. Consequently, geopolymer mixes featuring 100 FA achieved superior compressive strength performance in an acid (10% H_2SO_4) environment, whereas mortar samples enclosing 10% and 20% RHA percentages developed comparatively lower strength results. From the experimental outcomes, it can be inferred that increase in

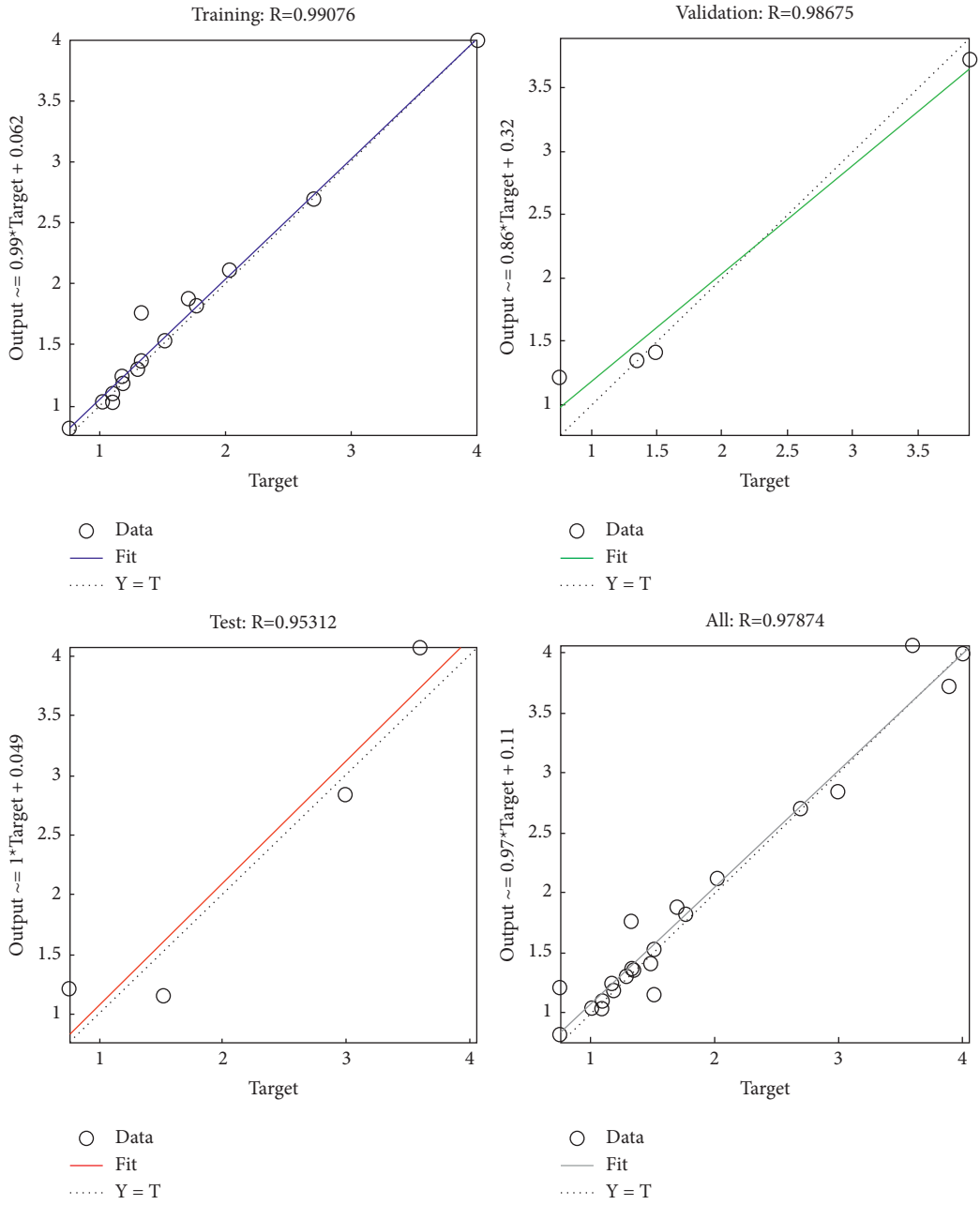

Figure 15: Prediction evaluation of water absorption results.

RHA substitution levels in FA-based geopolymer mortar resulted in the gradual decrease in compressive strength under acid environment.

5. Prediction of Strength and Durability Properties Using ANN

The percentages of error values for the strength and durability characteristics of geopolymer mortars obtained from ANN model were listed in Table 4. As seen in Table 4, it can be stated that the maximum percentages of error observed for the geopolymer mortar mixes under compressive, flexural, water absorption, sorptivity, and acid resistance test results were found to be 2.94%, 4.0%, 5.40%, 6.36%, and 6.15%, respectively. The error values obtained from (3) are negligible as the error percentage for all the predicted values is less than 10 percentage. According to the preceding sentence, the ANN framework could be utilized to estimate the mechanical and durability characteristics of fiber influenced FA-RHA-based geopolymer mortars. The comparison between the experimental and the predicted values of compressive strength results for fiber influenced FA-RHA based geopolymer mortars is expressed in Figure 8. Figure 9 depicts the correlation among the predicted and experimental flexural strength results. In case of water absorption test results, the variation between experimental and predicted values is illustrated in Figure 10. Consequently, Figures 11 and 12 represent the variation of predicted and

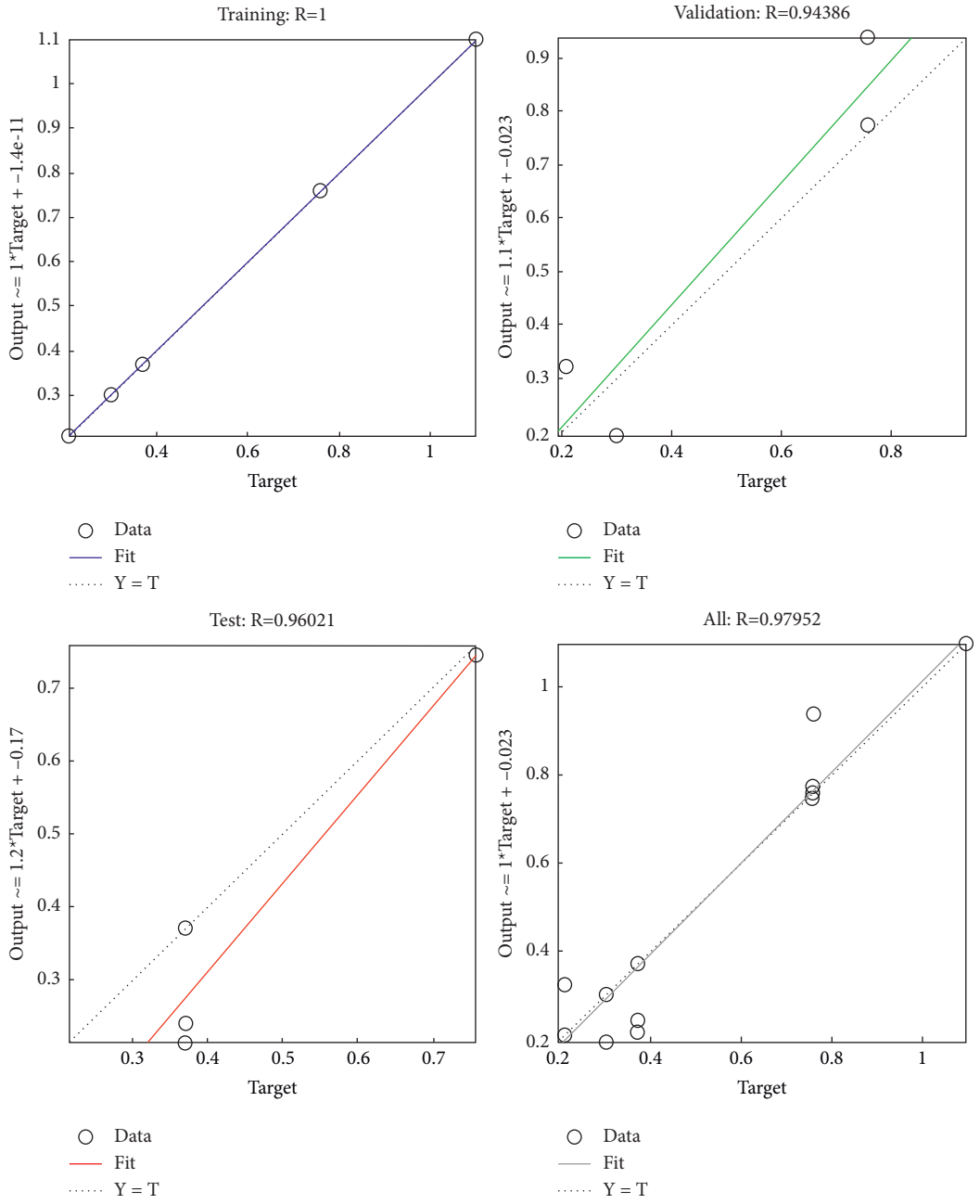

Figure 16: Prediction evaluation of sorptivity outcomes.

experimental results for sorptivity and acid resistance test of fiber reinforced FA-RHA blended geopolymer mortars, respectively. Figures 8–12 demonstrate that the outcomes for strength and durability evaluated through experimental and ANN methods were closely similar. According to the preceding statements, the established ANN (3-5-5-5) structure can be used to estimate the strength and durability features of FA-RHA-based geopolymer mortars comprising PF fibers with a low error percentage. Moreover, the strength values determined from experimental and predicted studies were limited by the ratios of RHA/FA, different molarities of NaOH solution, and percentage of polypropylene fibers added.

The cumulative coefficient of correlation (R) for compressive strength results at the stage of training, validation, testing, and the association of three levels in the ANN framework was measured as 1, 0.97189, 0.95547, and 0.97808, as seen in Figure 13. For flexural outcomes, the calculated R values throughout training, validation, testing, and the combination of three-phased convergence were computed from Figure 14 as 0.98670, 0.99819, 0.98673, and 0.97317, respectively. Figure 15 illustrates the R values for water absorption results at the time of training, testing, and association of three stages as 0.99076, 0.98675, 0.95312, and 0.97874, respectively. Consequently, Figures 16 and 17 demonstrate the regression evaluation and efficiency of

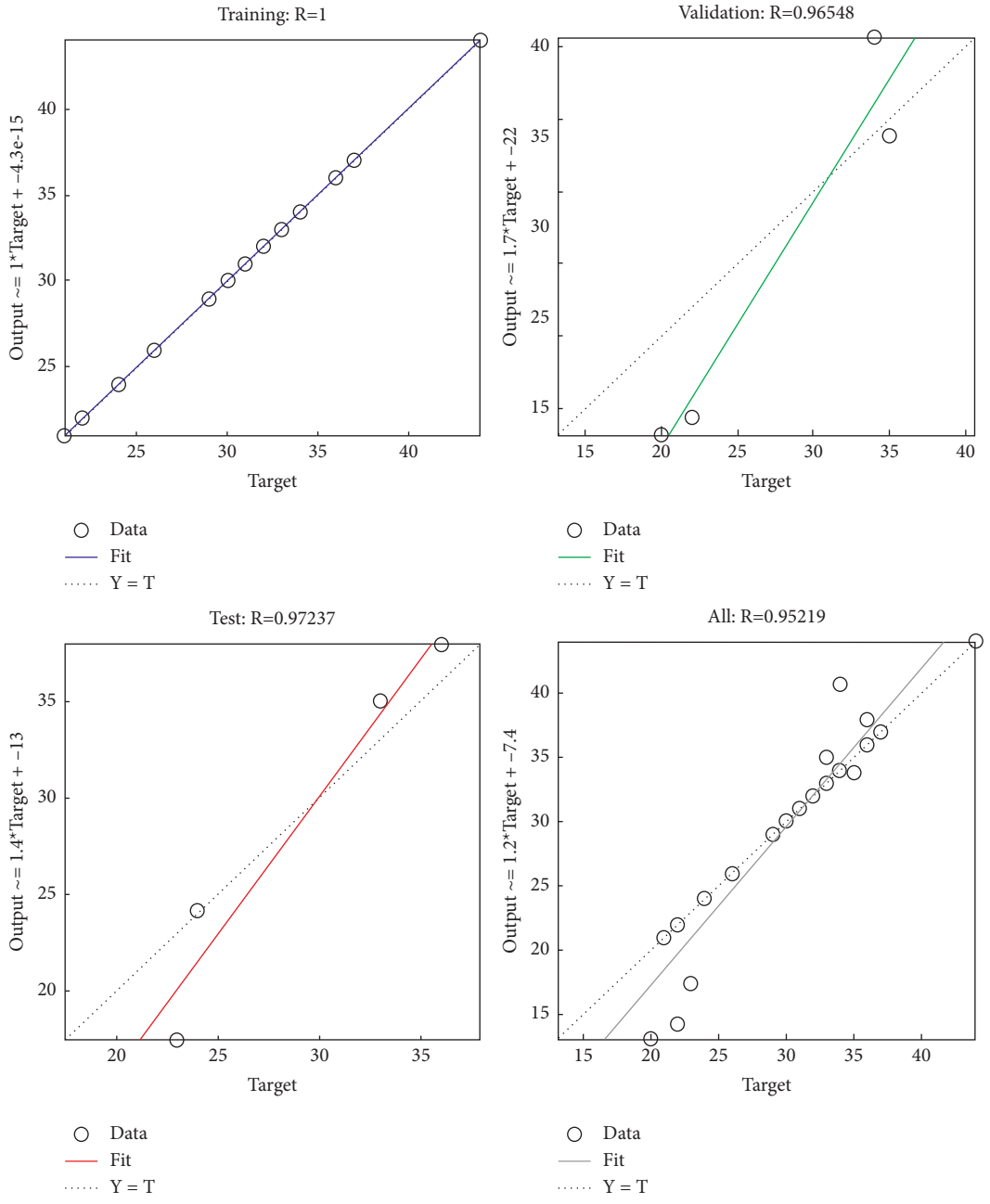

Figure 17: Assessment of predicted acid resistance results.

the water sorptivity and acid resistance results in the form of R values.

R values larger than 0.9 explicitly indicate a strong association among the observed and simulation outcomes across all instances [37, 38]; the developed ANN structure, which has been performed using measured data, precisely anticipated the intended outputs.

6. Conclusions

The following are the conclusions compiled from the experimental and predicted test results based on the influence of RHA substitution levels, concentration of NaOH solution, and fiber content in FA-based geopolymer mortars:

(i) The geopolymer mortars (G5 and G8) containing 10 M concentration of sodium hydroxide solution produced the maximum compressive strength results of 62 MPa.

(ii) Geopolymer mortar strength decreases with rice husk ash addition (20%). However, the replacement of fly ash by rice husk ash geopolymer mortar strength is higher than the control mortar.

(iii) Geopolymer mortar with and without fiber does not vary much in compressive strength, whereas

higher residual compressive strengths were obtained after the exposure of 10% of sulfuric acid.

(iv) The flexural strength characteristics of the FA-RHA based geopolymer mortar increase with higher PP fiber (0.3%) proportions.

(v) Water absorption and water sorptivity increase with an increment in rice husk ash substitution levels.

(vi) Sustainable geopolymer mortar can be developed from source materials like FA and RHA, which are obtained as industrial byproducts.

(vii) Mechanical and durability strength properties of RHA-FA-based geopolymer mortar could be predicted with the application of ANN framework using experimental results.

(viii) The ANN structure constructed in this investigation for assessing the mechanical and durability characteristics of fiber influenced FA-RHA blended geopolymer mortar was proved to be efficient as the predicted results are in comparison with the actual results.

Data Availability

The data used to support the findings of this study are included within the article. Should further data or information be required, these are available from the corresponding author upon request.

Conflicts of Interest

The authors declare that there are no conflicts of interest.

Acknowledgments

The authors express their gratefulness to the Manipur Public Works Department and Superintending Engineer Er. N. Subhas for their guidance and the amenities offered to complete the experimental work. The researchers would also like to credit Vellore Institute of Technology, Chennai campus, India, for their assistance in completing this work. The authors are grateful for the assistance provided by Copper Belt University, Zambia.

References

[1] J. Davidovits, "Geopolymers - inorganic polymeric new materials," *Journal of Thermal Analysis*, vol. 37, no. 8, pp. 1633–1656, 1991.

[2] C. K. Ma, A. Z. Awang, and W. Omar, "Structural and material performance of geopolymer concrete: a review," *Construction and Building Materials*, vol. 186, pp. 90–102, 2018.

[3] S. Detphan and P. Chindaprasirt, "Preparation of fly ash and rice husk ash geopolymer," *Int. J. Miner. Metall. Mater.*vol. 16, no. 6, pp. 720–726, 2009.

[4] P. Manikandan and V. Vasugi, "A critical review of waste glass powder as an aluminosilicate source material for sustainable geopolymer concrete production, " *silicon*," *Silicon*, vol. 13, no. 10, pp. 3649–3663, 2021.

[5] A. Jan, Z. Pu, K. A. Khan et al., "A review on the effect of silica to alumina ratio, alkaline solution to binder ratio, calcium oxide + ferric oxide, molar concentration of sodium hydroxide and sodium silicate to sodium hydroxide ratio on the compressive strength of geopolymer concrete," *Silicon*, vol. 14, no. 7, pp. 3147–3162, 2021.

[6] M. Mustafa, A. Bakri, H. Mohammed, H. Kamarudin, I. K. Niza, and Y. Zarina, "Review on fly ash-based geopolymer concrete without Portland Cement," *Journal of Engineering and Technology Research*, vol. 3, no. 1, pp. 1–4, 2011.

[7] Y. M. Liew, C. Y. Heah, A. B. Mohd Mustafa, and H. Kamarudin, "Structure and properties of clay-based geopolymer cements: a review," *Progress in Materials Science*, vol. 83, pp. 595–629, 2016.

[8] A. M. Mustafa Al Bakri, H. Kamarudin, M. Bnhussain, K. Nizar, A. R. Rafiza, and Y. Zarina, "The processing, characterization, and properties of fly ash based geopolymer concrete," *Reviews on Advanced Materials Science*, vol. 30, no. 1, pp. 90–97, 2012.

[9] P. Manikandan, L. Natrayan, S. Duraimurugan, and V. Vasugi, "Influence of waste glass powder as an aluminosilicate precursor in synthesizing ternary blended alkali-activated binder," *Silicon*, vol. 14, Article ID 0123456789, 2022.

[10] A. Hassan, M. Arif, and M. Shariq, "Use of geopolymer concrete for a cleaner and sustainable environment – a review of mechanical properties and microstructure," *Journal of Cleaner Production*, vol. 223, pp. 704–728, 2019.

[11] N. A. Eren, R. Alzeebaree, A. Çevik, A. Niş, A. Mohammedameen, and M. E. Gülşan, "The the effects of recycled tire rubbers and steel fibers on the performance of self-compacting alkali activated concrete," *Periodica Polytechnica: Civil Engineering*, vol. 65, no. 3, pp. 890–900, 2021.

[12] A. Niş, N. A. Eren, and A. Çevik, "Effects of nanosilica and steel fibers on the impact resistance of slag based self-compacting alkali-activated concrete," *Ceramics International*, vol. 47, no. 17, pp. 23905–23918, 2021.

[13] M. E. Gülşan, R. Alzeebaree, A. A. Rasheed, A. Niş, and A. E. Kurtoğlu, "Development of fly ash/slag based self-compacting geopolymer concrete using nano-silica and steel fiber," *Construction and Building Materials*, vol. 211, pp. 271–283, 2019.

[14] G. S. Ryu, Y. B. Lee, K. T. Koh, and Y. S. Chung, "The mechanical properties of fly ash-based geopolymer concrete with alkaline activators," *Construction and Building Materials*, vol. 47, pp. 409–418, 2013.

[15] L. Krishnaraj, P. T. Ravichandran, P. R. Kannan Rajkumar, and P. Keerthy Govind, "Effectiveness of alkali activators on nano structured flyashin geopolymer mortar," *Indian Journal of Science and Technology*, vol. 933 pages, 2016.

[16] J. Temuujin, A. Van Riessen, and K. J. D. MacKenzie, "Preparation and characterisation of fly ash based geopolymer mortars," *Construction and Building Materials*, vol. 24, no. 10, pp. 1906–1910, 2010.

[17] K. Kaur, J. Singh, and M. Kaur, "Compressive strength of rice husk ash based geopolymer: the effect of alkaline activator," *Construction and Building Materials*, vol. 169, pp. 188–192, 2018.

[18] K. K. Ramagiri and A. Kar, "Effect of high-temperature on the microstructure of alkali-activated binder," *Materials Today Proceedings*, vol. 28, pp. 1123–1129, 2020.

[19] K. K. Ramagiri, D. R. Chauhan, S. Gupta, A. Kar, D. Adak, and A. Mukherjee, "High-temperature performance of ambient-

cured alkali-activated binder concrete," *Innov. Infrastruct. Solut.*vol. 6, no. 2, pp. 71–11, 2021.

[20] K. Mahendran and N. Arunachelam, "Performance of fly ash and copper slag based geopolymer concrete," *Indian Journal of Science and Technology*, vol. 9, no. 2, 2016.

[21] A. Niş and İ. Altındal, "Compressive strength performance of alkali activated concretes under different curing conditions," *Periodica Polytechnica: Civil Engineering*, vol. 65, no. 2, pp. 556–565, 2021.

[22] A. L. Freire, C. D. Moura-Nickel, G. Scaratti et al., "Geopolymers produced with fly ash and rice husk ash applied to CO2 capture," *Journal of Cleaner Production*, vol. 273, Article ID 122917, 2020.

[23] N. Shyamananda Singh, S. Thokchom, and R. Debbarma, "Properties of fly ash and rice husk ash blended geopolymer with sodium aluminate as activator solution," *Eng. Appl. Sci. Res.*vol. 48, no. 1, pp. 92–101, 2021.

[24] A. Mehta and R. Siddique, "Sustainable geopolymer concrete using ground granulated blast furnace slag and rice husk ash: strength and permeability properties," *Journal of Cleaner Production*, vol. 205, pp. 49–57, 2018.

[25] T. Ji, T. Lin, and X. Lin, "A concrete mix proportion design algorithm based on artificial neural networks," *Cement and Concrete Research*, vol. 36, no. 7, pp. 1399–1408, 2006.

[26] V. Vasugi and P. Manikandan, "The potential use of waste glass powder in slag based geopolymer concrete-An environmental friendly material," *International Journal of Environment and Waste Management*, vol. 1, no. 1, p. 1, 2022.

[27] F. Khademi, M. Akbari, S. M. Jamal, and M. Nikoo, "Multiple linear regression, artificial neural network, and fuzzy logic prediction of 28 days compressive strength of concrete," *Frontiers of Structural and Civil Engineering*, vol. 11, no. 1, pp. 90–99, 2017.

[28] A. K. M. Monjurul hasan, "Artificial neural network for concrete mix design," *UKIERI Concr. Congr. - Innov. Concr. Constr*, vol. 4, 2013.

[29] C. Manikanta, P. Manikandan, S. Duraimurugan, S. Elavenil, and V. Vasugi, "Pozzolanic properties of agro waste ashes for potential cement replacement predicted using ANN," *Journal of Physics: Conference Series*, vol. 1716, no. 1, Article ID 012018, 2020.

[30] M. Ahmadi, H. Naderpour, and A. Kheyroddin, "ANN model for predicting the compressive strength of circular steel-confined concrete," *International Journal of Civil Engineering*, vol. 15, no. 2, pp. 213–221, 2017.

[31] F. Khademi, S. M. Jamal, N. Deshpande, and S. Londhe, "Predicting strength of recycled aggregate concrete using artificial neural network, adaptive neuro-fuzzy inference system and multiple linear regression," *International Journal of Sustainable Built Environment*, vol. 5, no. 2, pp. 355–369, 2016.

[32] J. W. Oh, I. W. Lee, J. T. Kim, and G. W. Lee, "Application of neural networks for proportioning of concrete mixes," *ACI Materials Journal*, vol. 96, no. 1, pp. 61–67, 1999.

[33] J. Noorzaei, S. Hakim, and M. Jaafar, "Development of artificial neural networks for predicting concrete compressive strength," *International Journal of Engineering & Technology*, vol. 4, no. 2, pp. 141–153, 2007.

[34] A. Hammoudi, K. Moussaceb, C. Belebchouche, and F. Dahmoune, "Comparison of artificial neural network (ANN) and response surface methodology (RSM) prediction in compressive strength of recycled concrete aggregates," *Construction and Building Materials*, vol. 209, pp. 425–436, 2019.

[35] L. Bal and F. Buyle-Bodin, "Artificial neural network for predicting drying shrinkage of concrete," *Construction and Building Materials*, vol. 38, pp. 248–254, 2013.

[36] M. Barbuta, R.-M. Diaconescu, and M. Harja, "Using neural networks for prediction of properties of polymer concrete with fly ash," *Journal of Materials in Civil Engineering*, vol. 24, no. 5, pp. 523–528, 2012.

[37] A. A. Shahmansouri, M. Yazdani, S. Ghanbari, H. Akbarzadeh Bengar, A. Jafari, and H. Farrokh Ghatte, "Artificial neural network model to predict the compressive strength of eco-friendly geopolymer concrete incorporating silica fume and natural zeolite," *Journal of Cleaner Production*, vol. 279, Article ID 123697, 2021.

[38] D. Dao, H. B. Ly, S. H. Trinh, T. T. Le, and B. T. Pham, "Artificial intelligence approaches for prediction of compressive strength of geopolymer concrete," *Materials*, vol. 12, pp. 983–6, 2019.

[39] Is 516-1959, "Indian standard methods of tests for strength of concrete," *IS 516(Reaffirmed 2004)*, vol. 59, pp. 1–30, 1959.

[40] Astm C642, "Standard test method for density, absorption, and voids in hardened concrete," *Annu. B. ASTM Stand*, ASTM International, PA, USA, pp. 1–3, 2013.

[41] Astm C 642-06, "Standard test method for density, absorption, and voids in hardened concrete," *Annu. B. ASTM Stand*, pp. 1–3, ASTM International, PA, USA, 1997.

[42] P. Manikandan and V. Vasugi, "Potential utilization of waste glass powder as a precursor material in synthesizing eco-friendly ternary blended geopolymer matrix," *Journal of Cleaner Production*, vol. 355, Article ID 131860, 2022.

[43] Y. Kellouche, B. Boukhatem, M. Ghrici, R. Rebouh, and A. Zidol, "Neural network model for predicting the carbonation depth of slag concrete," *Asian J. Civ. Eng.*vol. 22, no. 7, pp. 1401–1414, 2021.

[44] L. Natrayan and M. Senthil Kumar, "An integrated artificial neural network and Taguchi approach to optimize the squeeze cast process parameters of AA6061/Al2O3/SiC/Gr hybrid composites prepared by novel encapsulation feeding technique," *Materials Today Communications*, vol. 25, Article ID 101586, 2020.

[45] R. Alzeebaree, A. Çevik, A. Mohammedameen, A. Niş, and M. E. Gülşan, "Mechanical performance of FRP-confined geopolymer concrete under seawater attack," *Advances in Structural Engineering*, vol. 23, no. 6, pp. 1055–1073, 2020.

[46] R. Alzeebaree, A. O. Mawlod, A. Mohammedameen, and A. Niş, "Using of recycled clay brick/fine soil to produce sodium hydroxide alkali activated mortars," *Advances in Structural Engineering*, vol. 24, no. 13, pp. 2996–3009, 2021.

[47] K. Nagendra Reddy, K. Surya Narayana, J. Damodhar Reddy, B. Sarath Chandra, and Y. Himath Kumar, "Effect of sodium hydroxide and sodium silicate solution on compressive strength of metakaolin and GGBS geopolymer," *International Journal of Civil Engineering & Technology*, vol. 8, no. 4, pp. 1905–1917, 2017.

[48] S. Thokchom, P. Ghosh, and S. Ghosh, "Durability of fly ash geopolymer mortars in nitric acid–effect of alkali (Na2o) content/geopolimerinio skiedinio, pagaminto naudojant lakiuosius pelenus, ilgaamžiškumas azoto rūgštyje: šarmų (Na2o) kiekio poveikis," *Journal of Civil Engineering and Management*, vol. 17, no. 3, pp. 393–399, 2011.

[49] C. Shijagurumayum, N. S. Singh, and S. Thokchom, "Fibre reinforced alkali activated composites exposed to elevated

temperature," *Eng. Appl. Sci. Res.*vol. 49, no. 4, pp. 593–602, 2022.

[50] F. U. A. Shaikh, "Mechanical and durability properties of fly ash geopolymer concrete containing recycled coarse aggregates," *International Journal of Sustainable Built Environment*, vol. 5, no. 2, pp. 277–287, 2016.

[51] J. Blazy and R. Blazy, "Polypropylene fiber reinforced concrete and its application in creating architectural forms of public spaces," *Case Studies in Construction Materials*, vol. 14, Article ID e00549, 2021.

Hindawi
Advances in Civil Engineering
Volume 2022, Article ID 8214859, 24 pages
https://doi.org/10.1155/2022/8214859

Research Article

Compressive Strength Prediction of Alkali-Activated Slag Concretes by Using Artificial Neural Network (ANN) and Alternating Conditional Expectation (ACE)

Xiaoyu Qin, Qianmin Ma, Rongxin Guo, Zhigang Song, Zhiwei Lin, and Haoxue Zhou

Yunnan Key Laboratory of Disaster Reduction in Civil Engineering, Faculty of Civil Engineering and Mechanics, Kunming University of Science and Technology, Kunming 650500, China

Correspondence should be addressed to Qianmin Ma; maqianmin666@163.com

Received 5 May 2022; Revised 25 June 2022; Accepted 9 July 2022; Published 2 August 2022

Academic Editor: Ravindran Gobinath

Compressive strength of alkali-activated slag (AAS) concrete is influenced by multi-factors in a nonlinear way. Both artificial neural network (ANN) and alternating conditional expectation (ACE) models of 3-day (3 d) and 28-day (28 d) compressive strength of AAS were established in this study by using the data reported in related literature, where alkali concentration of activator ($Na_2O\%$), modulus of activator (Ms), water/binder ratio (W/B), surface area of slag (SA), and basicity index of slag (K_b) were taken as input parameters. The models were employed later to predict 3 d and 28 d compressive strength of AAS concretes, respectively, and the results were validated by experimental work. The results show that both the ANN and the ACE models had adequate accuracy, no matter 3 d or 28 d compressive strength was considered. Compared to the 3 d compressive strength, due to data scattering that increased with the increase of data size, both the models did not yield a higher accuracy in the case of 28 d strength. However, also due to the increase in data size, both the models were more feasible to implement 28 d strength prediction as a result of sufficient learning and training during modeling. In addition, based on ACE analysis, the weight-influencing compressive strength of AAS decreased in a sequence of $Na_2O\% > Ms > W/B > K_b > SA$. If data size was sufficiently large, it was more suitable to establish an ANN model for compressive strength prediction of AAS concretes. Otherwise, ACE could be considered as an alternative to yield an acceptable result.

1. Introduction

Alkali-activated slag (AAS), in which alkali activator (such as sodium silicate solution, known as water glass, WG) blends with ground granulated blast-furnace slag, has received widespread attention due to its extremely low CO_2 emission and superior performance [1]. Concrete manufactured by using AAS instead of Portland cement (PC) is potentially employed in structural construction. On the other hand, performance testing of concrete is usually time-consuming via experimental work. In this context, prediction based on mathematic models has shown its practical significance. As one of the most basic and the most important performances of concrete, compressive strength is largely dependent on material components and their characteristics. Different from PC, whose compressive strength mainly depends on water-binder ratio, compressive strength dependence of AAS comes from both alkali activator and slag, as well as water-binder ratio. Such multi-factor conditions will certainly bring much more challenges for compressive strength prediction of AAS.

Bagheri et al. [2] established an artificial neural network (ANN) by using the data obtained from the authors' experimental work, followed by using genetic programming (GP) to conduct a prediction for compressive strength of boron-based alkali-activated fly ash-slag system. To develop the ANN model, percentages of fly ash and slag, as well as ratios of B, Si, and Na in the alkali activator were taken as input variables. Totally 114 series of data were collected and 70%, 15%, and 15% of the data were used for training, testing, and validation, respectively. A very low error value of less than 0.1 confirmed the high accuracy of the model. After a GP

based on 20 series of experiments, R^2 of 0.95 and root mean square error (RMSE) of 0.07 were obtained, respectively, implying a good feasibility of the model for such a prediction. Also, an ANN model was developed for compressive strength of alkali-activated fly ash-slag concretes in the study carried out by Nagajothi and Elavenil [3]. Twenty groups of data obtained from their own experiment were used for establishment of the model, where slag-fly ash ratio and river sand–manufactured sand ratio were used as input parameters. Finally, mean absolute error (MAE), RMSE, and mean absolute percentage error (MAPE) of 0.042, 0.094, and 0.001 were obtained, respectively, exhibiting that the model had high accuracy. Faridmehr et al. [4] also developed an ANN model for compressive strength of alkali-activated fly ash-slag self-compacting concretes, where contents of fly ash and slag, as well as curing age were taken as input parameters. Within the total 6 groups of data based on their own experiment, 70% and 30% of the data were used for training and testing, respectively. Reliability of the model was evaluated by comparing its error to the ones obtained from multiple linear regression (MLR) model and genetic algorithm combined with ANN (GA-ANN) model. Finally, relatively lower MAE of 1.78, mean squared error (MSE) of 5.98, RMSE of 2.45, and average absolute error (AAE) of 0.04 were obtained, respectively. Shariatmadari et al. [5] used alkali-activated volcanic ash-slag-PC to stabilize sandy soil, and developed ANN and evolutionary polynomial regression (EPR) models based on their own experimental results. Replacements of volcanic ash and slag in PC, concentration of alkali activator, alkali to binder ratio, Na/Al, Si/Al, curing time, and curing temperature were employed as input parameters. Training, testing, and validation used 75%, 10%, and 15% of data, respectively. After several trials, based on RMSE and MAE of 0.0439 and 0.0336, respectively, the ANN model with architecture of 8-5-10-1 was proved as the most accurate one. Zhang et al. [6] proposed a chemical-informed machine learning model for compressive strength of alkali-activated fly ash-slag system. To build the model, relatively comprehensive features were considered as input parameters, including contents of fly ash, slag, NaOH, WG, water, fine aggregates and coarse aggregates, reactivity modulus, hydraulic modulus, silica modulus, alumina modulus, lime modulus, Na_2O in WG, SiO_2 in WG, water in WG, relative humidity, as well as age. Training and testing used 70% and 30% of data (676 groups in total from literature), respectively. Eventually, high accuracy was achieved with a low MAE of 3.228 MPa.

From the above, it can be seen that ANN has been successfully used to estimate compressive strength of alkali-activated materials. Most studies have been carried out on alkali-activated fly ash-slag and other alkali-activated systems rather than AAS, which, however, has more important significance in engineering practice currently. Furthermore, the data used in most studies were from their own experimental work. This could have resulted in a relatively small data size and then followed by a decrease in accuracy and feasibility when using the local optimum model to solve a global issue.

In this context, this study will focus on compressive strength of AAS concretes by using the ANN approach. In the development of the ANN model, data will be collected as fully as possible from literature. After the model with sufficient accuracy has been established, its feasibility will be evaluated by using own experimental work. For comparison, alternating conditional expectation (ACE) analysis will also be conducted and the weight of the influencing factors on the compressive strength of AAS concretes will be determined elementarily by using such method.

2. Data Collection and Modeling

2.1. Data Collection. ANN and ACE models were established in this study to predict compressive strength of AAS concretes with WG as alkali activator. Data used for the model establishment was collected from related literature published publicly. The influence on strength of AAS should be from both alkali activator and slag, as well as their proportion. Considering the importance of the influencing parameters, alkali concentration of WG (Na_2O%), modulus of WG (Ms), water/binder ratio (W/B), surface area of slag (SA), and basicity index of slag (K_b) were taken as the input parameters of the models [7–13]. Other parameters, such as binder content, which are less important and then not typically considered in the literature, are not adopted in this study for model establishment. Na_2O%, Ms, W/B, and Kb should be calculated according to formulae (1)–(4) [14–17]. If NaOH was used in the alkali activator as well together with WG, NaOH should be treated as a part of WG. Therefore, "WG" in the formulae means the WG after NaOH adjustment. Compressive strengths of AAS at curing ages of 3 d and 28 d were considered as output parameters. Finally, 171 and 309 sets of data were successfully selected for 3 d and 28 d compressive strength prediction, respectively. Literature used and input/output parameter values listed in Tables 1 and 2 gives the number of tests, range of variation, and average and standard deviation values for each of the references presented in Table 1. Parts of the data in the Table 1 have same inputs but different output values. This is because other influencing factors rather than the five mentioned above were also considered in the literature, but here only the five factors were concerned.

$$Na_2O\% = \frac{Na_2O\,in\,WG}{slag} * 100\%, \tag{1}$$

$$Ms = \frac{SiO_2\,in\,WG}{Na_2O\,in\,WG}, \tag{2}$$

$$\frac{W}{B} = \frac{\text{additional water} + \text{water in WG}}{\text{slag} + SiO_2\text{ in WG} + Na_2O\text{ in WG}}, \tag{3}$$

$$K_b = \frac{CaO + MgO}{SiO_2 + Al_2O_3}. \tag{4}$$

2.2. ANN Modeling. ANN is a kind of general mathematical model to solve nonlinear system problems. It processes information by imitating human neural network [67]. Due to its strong generalization ability, it has been applied

Table 1: Literatures and input/output parameters.

Ref.	Input parameters					Output parameters	
	Na_2O%	Ms	W/B	SA (m^2/kg)	K_b	Compressive strength (MPa)	
						3 d	28 d
[18]	4.0	0.75	0.47	527	0.96	25.16	43.80
	4.0	1.00	0.47	527	0.96	16.44	48.96
	4.0	1.50	0.47	527	0.96	—	48.05
	4.0	2.00	0.47	527	0.96	—	33.44
	6.0	0.75	0.47	527	0.96	31.15	46.71
	6.0	1.00	0.47	527	0.96	35.60	53.94
	6.0	1.50	0.47	527	0.96	32.29	60.72
	6.0	2.00	0.47	527	0.96	12.31	59.82
	8.0	0.75	0.47	527	0.96	34.62	51.69
	8.0	1.00	0.47	527	0.96	32.60	54.98
	8.0	1.50	0.47	527	0.96	23.66	58.44
	8.0	2.00	0.47	527	0.96	—	54.83
[19]	4.0	1.50	0.28	485	0.99	—	81.20
	4.0	1.50	0.32	485	0.99	50.10	79.10
	4.0	1.50	0.37	485	0.99	29.10	74.10
	4.0	1.50	0.41	485	0.99	—	62.20
	4.0	1.50	0.32	485	0.99	40.30	79.50
	4.0	1.50	0.32	485	0.99	46.00	78.10
	4.0	1.50	0.32	485	0.99	51.40	82.40
	4.0	1.50	0.32	485	0.99	52.10	80.50
	4.0	1.50	0.32	485	0.99	48.60	77.10
	4.0	1.50	0.32	485	0.99	52.30	77.90
	3.0	1.50	0.33	485	0.99	—	55.10
	5.0	1.50	0.29	485	0.99	54.30	97.60
	6.0	1.50	0.27	485	0.99	46.20	102.60
	4.0	1.00	0.33	485	0.99	38.20	73.20
	4.0	2.00	0.33	485	0.99	46.10	86.50
	4.0	1.50	0.32	313	0.99	41.30	75.80
	4.0	1.50	0.32	679	0.99	55.10	85.20
[20]	5.0	1.50	0.46	523	1.14	10.72	20.74
	7.0	1.50	0.46	523	1.14	—	27.57
	9.0	1.50	0.46	523	1.14	14.73	25.11
	5.0	1.80	0.46	523	1.14	—	27.29
	7.0	1.80	0.46	523	1.14	19.09	40.19
	9.0	1.80	0.46	523	1.14	28.78	57.73
	5.0	2.00	0.46	523	1.14	—	28.49
	7.0	2.00	0.46	523	1.14	24.57	46.03
	9.0	2.00	0.46	523	1.14	50.68	58.92
[21]	5.0	1.50	0.35	462	1.00	—	79.60
	5.0	1.50	0.40	462	1.00	—	69.40
	5.0	1.50	0.45	462	1.00	—	61.30
	5.0	1.50	0.50	462	1.00	—	47.20
	5.0	1.50	0.55	462	1.00	—	31.60
	5.0	1.50	0.35	462	1.00	—	82.20
	5.0	1.50	0.40	462	1.00	—	72.50
	5.0	1.50	0.45	462	1.00	—	63.50
	5.0	1.50	0.50	462	1.00	—	52.70
	5.0	1.50	0.55	462	1.00	—	42.10
	5.0	1.50	0.35	462	1.00	—	84.00
	5.0	1.50	0.40	462	1.00	—	59.20
	5.0	1.50	0.45	462	1.00	—	57.10
	5.0	1.50	0.50	462	1.00	—	45.90
	5.0	1.50	0.55	462	1.00	—	36.30
[22]	7.0	1.80	0.46	523	0.94	—	40.50
	9.0	1.80	0.46	523	0.94	—	60.10
	9.0	2.00	0.46	523	0.94	—	62.70

Table 1: Continued.

Ref.	Input parameters					Output parameters	
	Na_2O%	Ms	W/B	SA (m^2/kg)	K_b	Compressive strength (MPa)	
						3 d	28 d
[23]	10.0	1.50	0.33	450	1.28	18.70	25.00
	12.0	1.50	0.33	450	1.28	19.60	27.20
	14.0	1.50	0.33	450	1.28	22.50	29.60
	10.0	1.20	0.33	450	1.28	30.20	40.40
	12.0	1.20	0.33	450	1.28	36.00	46.80
	14.0	1.20	0.33	450	1.28	42.80	50.40
	10.0	1.00	0.33	450	1.28	35.60	50.40
	12.0	1.00	0.33	450	1.28	49.10	61.00
	14.0	1.00	0.33	450	1.28	50.40	64.40
	10.0	0.80	0.33	450	1.28	40.10	55.70
	12.0	0.80	0.33	450	1.28	44.60	64.60
	14.0	0.80	0.33	450	1.28	49.10	65.40
[24]	8.0	1.40	0.28	455	1.04	28.60	57.60
[25]	4.0	0.40	0.51	525	1.10	—	33.27
	4.0	0.80	0.51	525	1.10	—	38.95
	4.0	1.20	0.50	525	1.10	—	46,77
	6.0	0.40	0.50	525	1.10	—	44.07
	6.0	0.80	0.49	525	1.10	—	52.36
	6.0	1.20	0.48	525	1.10	—	79.70
	8.0	0.40	0.48	525	1.10	—	36.76
	8.0	0.80	0.47	525	1.10	—	82.68
	8.0	1.20	0.46	525	1.10	—	75.26
[26]	4.0	1.00	0.44	515	1.08	31.49	56.56
	6.0	1.00	0.36	515	1.08	44.30	73.00
	8.0	1.00	0.33	515	1.08	54.33	76.90
	4.0	1.25	0.30	515	1.08	24.24	59.91
	6.0	1.25	0.35	515	1.08	42.63	76.07
	8.0	1.25	0.31	515	1.08	50.43	77.46
	4.0	1.50	0.25	515	1.08	17.83	62.41
	6.0	1.50	0.34	515	1.08	39.29	78.02
	8.0	1.50	0.29	515	1.08	41.24	79.41
[27]	4.0	1.00	0.35	435	0.99	—	24.44
	4.0	1.00	0.50	435	0.99	—	20.19
	4.0	1.00	0.65	435	0.99	—	18.32
[28]	4.0	2.06	0.44	300	0.84	—	14.40
	6.0	2.06	0.47	300	0.84	—	20.30
	8.0	2.06	0.45	300	0.84	10.50	24.00
	4.0	2.06	0.44	300	0.84	10.90	38.00
	6.0	2.06	0.36	300	0.84	28.50	53.90
	8.0	2.06	0.31	300	0.84	29.50	52.50
	4.0	2.06	0.27	350	0.84	—	15.90
	6.0	2.06	0.47	350	0.84	—	22.20
	8.0	2.06	0.45	350	0.84	10.80	25.00
	4.0	2.06	0.44	350	0.84	—	51.70
	6.0	2.06	0.36	350	0.84	27.60	67.10
	8.0	2.06	0.31	350	0.84	29.20	68.20
	4.0	2.06	0.27	400	0.84	—	16.70
	6.0	2.06	0.47	400	0.84	10.30	23.90
	8.0	2.06	0.45	400	0.84	11.00	27.30
	4.0	2.06	0.44	400	0.84	11.40	54.40
	6.0	2.06	0.37	400	0.84	26.80	70.10
	8.0	2.06	0.31	400	0.84	33.80	72.40
[29]	2.0	1.25	0.40	400	0.99	65.52	67.63
	2.0	0.75	0.40	400	0.99	44.03	51.08
	1.5	1.67	0.40	400	0.99	51.43	73.09
	1.5	1.00	0.40	400	0.99	36.46	58.83

Table 1: Continued.

Ref.	Input parameters					Output parameters	
	Na_2O%	Ms	W/B	SA (m^2/kg)	K_b	Compressive strength (MPa)	
						3 d	28 d
[30]	5.0	2.40	0.23	399	1.01	44.30	59.45
	5.0	2.00	0.23	399	1.01	54.35	68.64
	5.0	2.00	0.47	399	1.01	54.39	68.44
	5.0	2.40	0.47	399	1.01	44.37	59.26
[31]	5.0	2.40	0.53	300	1.01	—	49.75
	5.0	2.40	0.53	400	1.01	—	67.64
	5.0	2.40	0.53	500	1.01	—	73.09
[32]	6.0	0.50	0.47	446	1.05	56.25	42.03
	6.0	1.00	0.47	446	1.05	68.01	54.06
	6.0	1.50	0.47	446	1.05	84.14	58.98
	6.0	2.00	0.47	446	1.05	87.97	68.55
	8.0	0.50	0.47	446	1.05	74.66	55.75
	8.0	1.00	0.47	446	1.05	82.05	63.15
	8.0	1.50	0.47	446	1.05	92.47	70.55
	8.0	2.00	0.47	446	1.05	100.40	78.49
[33]	6.0	1.00	0.47	485	0.93	—	87.30
	4.9	1.50	0.47	485	0.93	—	81.11
	4.1	2.00	0.47	485	0.93	—	85.31
[34]	4.3	2.00	0.44	385	1.24	—	39.50
[35]	5.0	1.20	0.44	325	0.92	—	83.13
[36]	10.8	3.20	0.45	400	0.99	40.11	59.35
	9.6	3.20	0.50	400	0.99	39.25	51.62
	10.0	3.20	0.55	400	0.99	28.51	45.65
	10.5	3.20	0.60	400	0.99	25.86	36.13
[37]	6.0	1.20	0.35	424	0.90	97.66	118.00
	8.0	1.20	0.35	424	0.90	101.30	123.20
	10.0	1.20	0.35	424	0.90	84.41	108.70
	6.0	1.40	0.35	424	0.90	90.68	111.50
	8.0	1.40	0.35	424	0.90	91.30	113.10
	10.0	1.40	0.35	424	0.90	89.96	110.10
	6.0	1.60	0.35	424	0.90	89.34	114.40
	8.00	1.60	0.35	424	0.90	95.40	118.20
	10.0	1.60	0.35	424	0.90	87.29	109.00
[38]	4.0	1.25	0.40	370	0.88	—	60.10
[39]	4.0	0.80	0.50	435	0.99	29.80	42.07
	5.0	0.80	0.50	435	0.99	32.43	48.10
	6.0	0.80	0.50	435	0.99	37.68	51.05
[40]	10.0	1.00	0.45	498	0.91	—	54.82
	10.0	1.00	0.45	435	0.93	—	29.66
	10.0	1.00	0.45	450	0.94	—	34.55
[41]	9.2	1.25	0.55	385	0.80	32.92	39.55
[42]	4.0	1.50	0.50	450	1.08	—	48.02
	6.0	1.50	0.50	450	1.08	—	68.89
	10.0	1.50	0.50	450	1.08	—	78.71
[43]	4.0	0.50	0.40	515	1.06	—	45.09
	4.0	1.00	0.40	515	1.06	—	50.41
	4.0	1.50	0.40	515	1.06	—	56.45
	6.0	0.50	0.40	515	1.06	—	55.38
	6.0	1.00	0.40	515	1.06	—	55.74
	6.0	1.50	0.40	515	1.06	—	63.20
	8.0	0.50	0.40	515	1.06	—	47.99
	8.0	1.00	0.40	515	1.06	—	56.05
	8.0	1.50	0.40	515	1.06	—	61.31

Table 1: Continued.

Ref.	Input parameters					Output parameters	
	Na_2O%	Ms	W/B	SA (m^2/kg)	K_b	Compressive strength (MPa)	
						3 d	28 d
[44]	8.0	0.48	0.55	345	1.22	—	18.10
	12.0	0.48	0.55	345	1.22	—	34.00
	16.0	0.48	0.55	345	1.22	—	39.10
[45]	0.4	0.50	0.33	430	0.99	38.99	41.11
	0.4	0.80	0.33	430	0.99	41.78	48.86
	0.4	1.20	0.33	430	0.99	27.91	30.02
	0.4	1.50	0.33	430	0.99	48.78	55.86
	0.4	1.80	0.33	430	0.99	43.77	53.33
	0.4	2.10	0.33	430	0.99	42.31	51.87
	0.4	2.30	0.33	430	0.99	27.72	41.54
	0.4	1.50	0.33	430	0.99	26.42	50.53
	0.6	1.50	0.33	430	0.99	45.58	78.29
	0.8	1.50	0.33	430	0.99	35.50	60.90
	1.0	1.50	0.33	430	0.99	49.36	81.97
[46]	4.3	0.41	0.44	501	1.14	—	28.00
	3.9	1.22	0.44	501	1.14	—	46.40
[47]	4.0	0.75	0.28	527	0.66	—	26.08
	4.0	1.00	0.28	527	0.66	—	36.32
	4.0	1.50	0.28	527	0.66	—	36.80
	4.0	2.00	0.28	527	0.66	—	25.65
	6.0	0.75	0.28	527	0.66	—	15.57
	6.0	1.00	0.28	527	0.66	—	8.91
	6.0	1.50	0.28	527	0.66	—	60.00
	6.0	2.00	0.28	527	0.66	—	41.20
	8.0	0.75	0.28	527	0.66	—	1.28
	8.0	1.00	0.28	527	0.66	—	6.24
	8.0	1.50	0.28	527	0.66	—	39.68
	8.0	2.00	0.28	527	0.66	—	23.73
[48]	3.0	1.00	0.41	405	0.55	38.39	—
	4.0	1.00	0.40	405	0.55	53.05	—
[49]	3.7	1.40	0.30	338	1.16	67.10	99.40
	3.0	1.70	0.30	338	1.16	52.50	86.50
	2.6	1.99	0.30	338	1.16	32.60	77.00
	2.3	2.29	0.30	338	1.16	—	65.20
	2.0	2.39	0.30	338	1.16	—	44.20
	1.8	2.94	0.30	338	1.16	—	53.80
	1.6	3.27	0.30	338	1.16	—	55.50
	1.4	3.60	0.30	338	1.16	—	52.20
[50]	4.0	0.50	0.45	453	1.07	43.47	84.00
	4.0	0.80	0.45	453	1.07	51.58	107.60
	4.0	1.00	0.45	453	1.07	53.05	123.80
	4.0	1.20	0.45	453	1.07	56.00	126.00
	4.0	1.50	0.45	453	1.07	57.47	128.20
	4.0	1.80	0.45	453	1.07	47.16	127.50
	4.0	2.00	0.45	453	1.07	46.42	126.70
	4.0	2.20	0.45	453	1.07	36.84	76.63
	4.0	2.50	0.45	453	1.07	—	34.63
	2.0	1.50	0.45	453	1.07	—	30.92
	3.0	1.50	0.45	453	1.07	27.83	105.90
	4.0	1.50	0.45	453	1.07	58.74	128.30
	5.0	1.50	0.45	453	1.07	72.66	140.70
	6.0	1.50	0.45	453	1.07	81.16	151.50
	7.0	1.50	0.45	453	1.07	64.15	116.70

Table 1: Continued.

Ref.	Input parameters					Output parameters	
	Na_2O%	Ms	W/B	SA (m^2/kg)	K_b	Compressive strength (MPa)	
						3 d	28 d
[51]	4.0	2.50	0.29	458	0.97	30.88	63.95
	4.0	2.00	0.29	458	0.97	49.23	83.25
	4.0	1.50	0.29	458	0.97	61.58	102.90
	4.0	0.50	0.29	458	0.97	70.88	90.25
	4.0	1.00	0.29	458	0.97	68.53	99.10
[52]	2.4	0.50	0.28	461	1.01	—	33.38
	2.4	1.00	0.29	461	1.01	—	48.48
	2.4	2.00	0.32	461	1.01	—	70.13
	2.4	0.50	0.28	420	1.03	—	51.26
	2.4	1.00	0.29	420	1.03	—	69.14
	2.4	2.00	0.32	420	1.03	—	87.02
[53]	5.0	1.00	0.40	487	1.03	30.94	54.54
	5.0	1.50	0.40	487	1.03	38.35	61.76
	5.0	2.00	0.40	487	1.03	41.26	70.99
[54]	4.0	0.75	0.50	520	1.10	—	44.97
	6.0	0.75	0.50	520	1.10	—	84.09
	4.0	1.00	0.50	520	1.10	—	41.72
	6.0	1.00	0.50	520	1.10	—	79.69
[55]	2.3	0.55	0.49	420	1.01	—	16.00
	2.7	0.75	0.50	420	1.01	11.90	18.30
	2.7	0.75	0.50	615	1.08	15.30	23.60
	2.7	0.75	0.50	817	1.07	17.30	25.90
	3.1	0.85	0.51	420	1.01	12.90	20.40
	5.4	0.55	0.50	420	1.01	22.30	35.20
	6.6	0.75	0.50	420	1.01	26.70	41.90
	6.6	0.75	0.50	615	1.08	28.70	44.60
	6.6	0.75	0.50	817	1.07	31.40	48.60
	7.9	0.85	0.51	420	1.01	33.50	49.60
[8]	8.0	0.75	0.50	425	0.84	—	81.10
	8.0	1.00	0.50	425	0.84	—	80.90
	8.0	1.25	0.50	425	0.84	—	58.90
	8.0	1.50	0.50	425	0.84	—	57.50
[56]	4.0	0.60	0.43	428	1.03	34.65	62.46
	4.0	0.90	0.43	428	1.03	40.15	69.88
	4.0	1.20	0.43	428	1.03	33.68	76.98
	4.0	1.50	0.43	428	1.03	45.33	81.81
	3.0	0.60	0.43	428	1.03	28.70	49.01
	3.0	0.90	0.43	428	1.03	27.28	62.35
	3.0	1.20	0.43	428	1.03	23.02	68.03
	3.0	1.50	0.43	428	1.03	—	68.32
[57]	4.0	0.75	0.50	460	0.93	11.55	24.23
	4.0	1.00	0.50	460	0.93	11.70	33.84
	4.0	1.25	0.50	460	0.93	11.99	34.51
	4.0	1.50	0.50	460	0.93	11.88	28.84
	6.0	0.75	0.50	460	0.93	14.36	24.95
	6.0	1.00	0.50	460	0.93	12.96	25.51
	6.0	1.25	0.50	460	0.93	—	27.46
	6.0	1.50	0.50	460	0.93	—	22.16
	8.0	0.75	0.50	460	0.93	14.25	36.02
	8.0	1.00	0.50	460	0.93	14.25	36.78
	8.0	1.25	0.50	460	0.93	11.80	39.08
	8.0	1.50	0.50	460	0.93	10.57	32.64
[58]	5.8	1.00	0.47	410	1.02	42.30	67.80
	5.8	1.00	0.47	410	1.02	45.30	85.00
	5.8	1.50	0.47	410	1.02	55.00	98.00

Table 1: Continued.

Ref.	Input parameters					Output parameters	
	Na_2O%	Ms	W/B	SA (m^2/kg)	K_b	Compressive strength (MPa)	
						3 d	28 d
[59]	5.0	1.00	0.28	465	1.04	—	82.75
	10.0	1.00	0.28	465	1.04	—	71.23
	15.0	1.00	0.28	465	1.04	—	48.12
	5.0	1.50	0.28	465	1.04	—	85.04
	10.0	1.50	0.28	465	1.04	—	65.85
	5.0	2.00	0.39	465	1.04	—	86.83
	10.0	2.00	0.39	465	1.04	—	48.84
[60]	3.0	1.00	0.25	600	1.14	52.07	67.08
	3.0	1.00	0.25	800	1.14	62.21	91.39
	3.0	1.00	0.25	1000	1.14	57.62	77.08
[61]	6.0	0.80	0.38	413	0.91	—	86.00
	6.0	1.20	0.38	413	0.91	—	80.80
[62]	2.9	1.00	0.42	502	0.90	—	45.00
	2.9	1.00	0.42	503	0.97	—	36.92
	2.9	1.00	0.40	499	0.87	—	44.62
	2.9	1.00	0.40	507	0.93	—	71.15
	2.9	1.00	0.40	501	0.98	—	78.85
	2.9	1.00	0.40	502	0.95	—	39.62
	2.9	1.00	0.40	496	0.81	—	38.08
	2.9	1.00	0.40	499	0.77	—	37.69
[63]	4.0	0.75	0.50	460	0.93	35.07	39.89
[64]	5.1	1.50	0.51	460	1.05	64.25	100.00
[65]	4.0	0.40	0.44	410	0.81	—	54.70
	4.0	0.80	0.44	410	0.81	—	59.70
	4.0	1.20	0.44	410	0.81	—	58.50
	4.0	1.60	0.44	410	0.81	—	52.30
	6.0	0.40	0.44	410	0.81	—	62.40
	6.0	0.80	0.44	410	0.81	—	78.40
	6.0	1.20	0.44	410	0.81	—	74.10
	6.0	1.60	0.44	410	0.81	—	71.00
	8.0	0.40	0.44	410	0.81	—	75.20
	8.0	0.80	0.44	410	0.81	—	76.10
	8.0	1.20	0.44	410	0.81	—	87.20
	8.0	1.60	0.44	410	0.81	—	88.30
[66]	4.0	1.65	0.48	401	0.98	31.38	57.48
	6.0	1.65	0.48	401	0.98	49.27	78.89
	4.0	1.00	0.48	401	0.98	29.03	47.80
	6.0	1.00	0.48	401	0.98	44.28	60.70

Table 2: Analysis of input/output parameters.

Ref.		Input parameters					Output parameters	
		Na_2O%	Ms	W/B	SA (m^2/kg)	K_b	Compressive strength (MPa)	
							3 d	28 d
[18]	Number of tests						9	12
	Range	[4.00–8.00]	[0.75–2.00]	0.47	527.00	0.96	[12.31–35.60]	[33.44–60.72]
	Average	6.00	1.31	0.47	527.00	0.96	27.09	51.28
	Standard deviation	1.71	0.50	0.00	0.00	0.00	8.29	7.73
[19]	Number						14	17
	Range	[3.00–6.00]	[1.00–2.00]	[0.27–0.41]	[313–679]	0.99	[29.10–55.10]	[55.10–102.60]
	Average	4.12	1.50	0.32	487.00	0.99	46.51	79.30
	Standard deviation	0.60	0.18	0.03	64.80	0.00	7.23	11.02

Table 2: Continued.

Ref.		Input parameters					Output parameters	
		Na_2O%	Ms	W/B	SA (m^2/kg)	K_b	Compressive strength (MPa)	
							3 d	28 d
[20]	Number						6	9
	Range	[5.00–9.00]	[1.50–2.00]	0.46	523.00	1.14	[10.72–50.68]	[20.74–58.92]
	Average	7.00	1.77	0.46	523.00	1.14	24.76	36.90
	Standard deviation	1.73	0.22	0.00	0.00	0.00	14.27	14.42
[21]	Number						—	15
	Range	5.00	1.50	[0.35–0.55]	462.00	1.00	—	[31.60–84.00]
	Average	5.00	1.50	0.45	462.00	1.00	—	58.97
	Standard deviation	0.00	0.00	0.07	0.00	0.00	—	16.50
[22]	Number						—	3
	Range	[7.00–9.00]	[1.80–2.00]	0.46	523.00	0.94	—	[40.50–62.70]
	Average	8.33	1.87	0.46	523.00	0.94	—	54.43
	Standard deviation	1.15	0.12	0.00	0.00	0.00	—	12.14
[23]	Number						12	12
	Range	[10.00–14.00]	[0.80–1.50]	0.33	450.00	1.28	[18.70–50.40]	[25.00–65.40]
	Average	12.00	1.13	0.33	450.00	1.28	36.56	48.41
	Standard deviation	1.71	0.27	0.00	0.00	0.00	11.55	14.91
[24]	Number						1	1
	Range	8.00	1.40	0.28	455.00	1.04	28.60	57.60
	Average	8.00	1.40	0.28	455.00	1.04	28.60	57.60
	Standard deviation	0.00	0.00	0.00	0.00	0.00	0.00	0.00
[25]	Number						—	9
	Range	[4.00–8.00]	[0.40–1.20]	[0.46–0.51]	525.00	1.10	—	[33.27–82.68]
	Average	6.00	0.80	0.49	525.00	1.10	—	52.42
	Standard deviation	1.73	0.35	0.02	0.00	0.00	—	19.49
[26]	Number						9	9
	Range	[4.00–8.00]	[1.00–1.50]	[0.25–0.44]	515.00	1.08	[17.83–54.33]	[56.56–79.41]
	Average	6.00	1.25	0.33	515.00	1.08	38.42	71.08
	Standard deviation	1.73	0.22	0.05	0.00	0.00	11.89	8.88
[27]	Number						—	3
	Range	4.00	1.00	[0.35–0.65]	455.00	1.04	—	[18.32–24.44]
	Average	4.00	1.00	0.50	455.00	1.04	—	20.98
	Standard deviation	0.00	0.00	0.15	0.00	0.00	—	3.14
[28]	Number						12	
	Range	[4.00–8.00]	2.06	[0.27–0.47]	[300–400]	0.84	[10.30–33.80]	[14.40–72.40]
	Average	6.00	2.06	0.39	350.00	0.84	20.02	39.89
	Standard deviation	1.68	0.00	0.07	42.00	0.00	9.76	21.10
[29]	Number						4	4
	Range	[1.50–2.00]	[0.75–1.67]	0.40	400.00	0.99	[36.46–65.52]	[51.08–73.09]
	Average	1.75	1.17	0.40	400.00	0.99	49.36	62.66
	Standard deviation	0.29	0.39	0.00	0.00	0.00	12.39	9.70
[30]	Number						2	2
	Range	5.00	[2.00–2.40]	0.23	399.00	1.01	[44.30–54.35]	[59.45–68.64]
	Average	5.00	2.20	0.23	399.00	1.01	49.33	64.05
	Standard deviation	0.00	0.28	0.00	0.00	0.00	7.11	6.50
[31]	Number						—	3
	Range	5.00	2.40	0.53	[300–500]	1.01	—	[49.75–73.09]
	Average	5.00	2.40	0.53	400.00	1.01	—	63.49
	Standard deviation	0.00	0.00	0.00	100.00	0.00	—	12.21
[32]	Number						8	8
	Range	[6.00–8.00]	[0.50–2.00]	0.47	446.00	1.05	[56.25–100.40]	[42.03–78.49]
	Average	7.00	1.25	0.47	446.00	1.05	80.74	61.45
	Standard deviation	1.07	0.60	0.00	0.00	0.00	14.08	11.32

Table 2: Continued.

Ref.		Input parameters					Output parameters	
		Na_2O%	Ms	W/B	SA (m^2/kg)	K_b	Compressive strength (MPa)	
							3 d	28 d
[33]	Number						—	3
	Range	[4.10–6.00]	[1.00–2.00]	0.47	485.00	0.93	—	[81.11–87.30]
	Average	5.00	1.50	0.47	485.00	0.93	—	84.57
	Standard deviation	0.95	0.50	0.00	0.00	0.00	—	3.16
[34]	Number						—	1
	Range	4.30	2.00	0.44	385.00	1.24	—	39.50
	Average	4.30	2.00	0.44	385.00	1.24	—	39.50
	Standard deviation	0.00	0.00	0.00	0.00	0.00	—	0.00
[35]	Number						—	1
	Range	5.00	1.20	0.44	325.00	0.92	—	83.13
	Average	5.00	1.20	0.44	325.00	0.92	—	83.13
	Standard deviation	0.00	0.00	0.00	0.00	0.00	—	0.00
[36]	Number						4	4
	Range	[9.60–10.80]	3.20	[0.45–0.60]	400.00	0.99	[25.86–40.11]	[36.13–59.35]
	Average	10.23	3.20	0.53	400.00	0.99	33.43	48.19
	Standard deviation	0.53	0.00	0.06	0.00	0.00	7.30	9.80
[37]	Number						9	9
	Range	[6.00–10.00]	[1.20–1.60]	0.35	424.00	0.90	[84.41–101.30]	[108.70–123.20]
	Average	8.00	1.40	0.35	424.00	0.90	91.93	114.02
	Standard deviation	1.73	0.17	0.00	0.00	0.00	5.28	4.92
[38]	Number						—	1
	Range	4.00	1.25	0.40	370.00	0.88	—	60.10
	Average	4.00	1.25	0.40	370.00	0.88	—	60.10
	Standard deviation	0.00	0.00	0.00	0.00	0.00	—	0.00
[39]	Number						3	3
	Range	[4.00–6.00]	0.80	0.50	435.00	0.99	[29.80–37.68]	[42.07–51.05]
	Average	5.00	0.80	0.50	435.00	0.99	33.30	47.07
	Standard deviation	1.00	0.00	0.00	0.00	0.00	4.01	4.58
[40]	Number						—	3
	Range	10.00	1.00	0.45	[435–498]	[0.91–0.94]	—	[29.66–54.82]
	Average	4.00	1.00	0.45	461.00	0.93	—	39.68
	Standard deviation	0.00	0.00	0.00	32.91	0.02	—	13.34
[41]	Number						1	1
	Range	9.20	1.25	0.55	385.00	0.80	32.92	39.55
	Average	9.20	1.25	0.55	385.00	0.80	32.92	39.55
	Standard deviation	0.00	0.00	0.00	0.00	0.00	0.00	0.00
[42]	Number						—	3
	Range	[4.00–10.00]	1.50	0.50	450.00	1.08	—	[48.02–78.71]
	Average	6.67	1.50	0.50	450.00	1.08	—	65.21
	Standard deviation	3.06	0.00	0.00	0.00	0.00	—	15.67
[43]	Number						—	9
	Range	[4.00–8.00]	[0.50–1.50]	0.40	515.00	1.06	—	[45.09–61.31]
	Average	6.00	1.00	0.40	515.00	1.06	—	54.62
	Standard deviation	1.73	0.43	0.00	0.00	0.00	—	5.90
[44]	Number						—	3
	Range	[8.00–16.00]	0.48	0.55	345.00	1.22	—	[18.10–39.10]
	Average	12.00	0.48	0.55	345.00	1.22	—	30.40
	Standard deviation	4.00	0.00	0.00	0.00	0.00	—	10.95
[45]	Number						11	11
	Range	[0.40–1.00]	[0.50–2.30]	0.33	430.00	0.99	[26.42–49.36]	[30.02–81.97]
	Average	0.51	1.47	0.33	430.00	0.99	38.92	54.03
	Standard deviation	0.21	0.52	0.00	0.00	0.00	8.42	15.37

Table 2: Continued.

Ref.		Input parameters					Output parameters	
		Na_2O%	Ms	W/B	SA (m^2/kg)	K_b	Compressive strength (MPa)	
							3 d	28 d
[46]	Number						—	2
	Range	[3.90–4.30]	[0.41–1.22]	0.44	501.00	1.14	—	[28.00–46.40]
	Average	4.10	0.82	0.44	501.00	1.14	—	37.20
	Standard deviation	0.28	0.57	0.00	0.00	0.00	—	13.01
[30]	Number						—	2
	Range	5.00	[2.00–2.40]	0.47	399.00	1.01	—	[59.26–68.44]
	Average	5.00	2.20	0.47	399.00	1.01	—	63.85
	Standard deviation	0.00	0.28	0.00	0.00	0.00	—	6.49
[47]	Number						—	12
	Range	[4.00–8.00]	[0.75–2.00]	0.28	527.00	0.66	—	[1.28–60.00]
	Average	6.00	1.31	0.28	527.00	0.66	—	26.79
	Standard deviation	1.71	0.50	0.00	0.00	0.00	—	17.05
[48]	Number						2	—
	Range	[3.00–4.00]	1.00	[0.40–0.41]	405.00	0.55	[38.39–53.05]	—
	Average	3.50	1.00	0.41	405.00	0.55	45.72	—
	Standard deviation	0.71	0.00	0.01	0.00	0.00	10.37S	—
[49]	Number						3	8
	Range	[1.40–3.70]	[1.40–3.60]	0.30	338.00	1.16	[32.60–67.10]	[44.20–99.40]
	Average	2.30	2.45	0.30	338.00	1.16	50.73	66.73
	Standard deviation	0.77	0.77	0.00	0.00	0.00	17.32	19.19
[50]	Number						13	15
	Range	[2.00–7.00]	[0.50–2.50]	0.45	453.00	1.07	[27.83–81.16]	[30.92–151.50]
	Average	4.20	1.50	0.45	453.00	1.07	53.58	107.27
	Standard deviation	1.15	0.51	0.00	0.00	0.00	14.22	35.90
[51]	Number						5	5
	Range	4.00	[0.50–2.50]	0.29	458.00	0.97	[30.88–70.88]	[63.95–102.90]
	Average	4.00	1.50	0.29	458.00	0.97	56.22	87.89
	Standard deviation	0.00	0.79	0.00	0.00	0.00	16.48	15.42
[52]	Number						—	6
	Range	2.40	[0.50–2.00]	[0.28–0.32]	[420–461]	[1.01–1.03]	—	[33.38–87.02]
	Average	2.40	1.17	0.30	440.50	1.02	—	59.91
	Standard deviation	0.00	0.68	0.02	22.46	0.01	—	19.15
[53]	Number						3	3
	Range	5.00	[1.00–2.00]	0.40	487.00	1.03	[30.94–41.26]	[54.54–70.99]
	Average	5.00	1.50	0.40	487.00	1.03	36.85	62.43
	Standard deviation	0.00	0.50	0.00	0.00	0.00	5.32	8.25
[54]	Number						—	4
	Range	[4.00–6.00]	[0.75–1.00]	0.50	520.00	1.10	—	[41.72–84.09]
	Average	5.00	0.88	0.50	520.00	1.10	—	62.62
	Standard deviation	1.15	0.14	0.00	0.00	0.00	—	22.37
[55]	Number						9	10
	Range	[2.30–7.90]	[0.55–0.85]	[0.49–0.51]	[420–817]	[1.01–1.08]	[11.90–33.50]	[16.00–49.60]
	Average	4.66	0.73	0.50	538.40	1.04	22.22	32.41
	Standard deviation	2.16	0.10	0.01	167.03	0.03	8.21	13.07
[8]	Number						—	4
	Range	8.00	[0.75–1.50]	0.50	425.00	0.84	—	[57.50–81.10]
	Average	8.00	1.13	0.50	425.00	0.84	—	69.60
	Standard deviation	0.00	0.32	0.00	0.00	0.00	—	13.18
[56]	Number						7	8
	Range	[3.00–4.00]	[0.60–1.50]	0.43	428.00	1.03	[23.02–45.33]	[62.35–81.81]
	Average	3.50	1.05	0.43	428.00	1.03	33.26	67.36
	Standard deviation	0.53	0.36	0.00	0.00	0.00	7.71	9.96

Table 2: Continued.

Ref.		Input parameters					Output parameters	
		Na_2O%	Ms	W/B	SA (m^2/kg)	K_b	Compressive strength (MPa)	
							3 d	28 d
[57]	Number						10	12
	Range	[4.00–8.00]	[0.75–1.50]	0.50	460.00	0.93	[11.55–14.36]	[22.16–39.08]
	Average	6.00	1.13	0.50	460.00	0.93	12.53	30.50
	Standard deviation	1.71	0.29	0.00	0.00	0.00	1.34	5.66
[58]	Number						3	3
	Range	5.80	[1.00–1.50]	0.47	410.00	1.02	[42.30–55.00]	[67.80–98.00]
	Average	5.80	1.17	0.47	410.00	1.02	47.53	83.60
	Standard deviation	0.00	0.29	0.00	0.00	0.00	6.64	15.15
[59]	Number						—	7
	Range	[5.00–10.00]	[1.00–2.00]	[0.28–0.39]	465.00	1.04	—	[48.12–86.83]
	Average	8.57	1.43	0.31	465.00	1.04	—	69.81
	Standard deviation	3.78	0.45	0.05	0.00	0.00	—	16.42
[60]	Number						3	3
	Range	3.00	1.00	0.25	[600–1000]	1.14	[52.07–62.21]	[67.08–91.39]
	Average	3.00	1.00	0.25	800.00	1.14	57.30	78.52
	Standard deviation	0.00	0.00	0.00	200.00	0.00	5.08	12.22
[61]	Number						—	2
	Range	6.00	[0.80–1.20]	0.38	413.00	0.91	—	[80.80–86.00]
	Average	6.00	1.00	0.38	413.00	0.91	—	83.40
	Standard deviation	0.00	0.28	0.00	0.00	0.00	—	3.68
[62]	Number						—	8
	Range	2.90	1.00	[0.40–0.42]	[496–503]	[0.77–0.98]	—	[36.92–78.85]
	Average	2.90	1.00	0.41	501.13	0.90	—	48.99
	Standard deviation	0.00	0.00	0.01	3.27	0.08	—	16.47
[63]	Number						1	1
	Range	4.00	0.75	0.50	460.00	0.93	35.07	39.89
	Average	4.00	0.75	0.50	460.00	0.93	35.07	39.89
	Standard deviation	0.00	0.00	0.00	0.00	0.00	0.00	0.00
[64]	Number						1	1
	Range	5.10	1.50	0.51	460.00	1.05	64.25	100.00
	Average	5.10	1.50	0.51	460.00	1.05	64.25	100.00
	Standard deviation	0.00	0.00	0.00	0.00	0.00	0.00	0.00
[65]	Number						—	12
	Range	[4.00–8.00]	[0.40–1.60]	0.44	410.00	0.81	—	[52.30–88.30]
	Average	6.00	1.00	0.44	410.00	0.81	—	69.83
	Standard deviation	1.71	0.47	0.00	0.00	0.00	—	12.16
[66]	Number						4	4
	Range	[4.00–6.00]	[1.00–1.65]	0.48	401.00	0.98	[29.03–49.27]	[47.80–78.89]
	Average	5.00	1.33	0.48	401.00	0.98	38.49	61.22
	Standard deviation	1.15	0.38	0.00	0.00	0.00	9.83	12.99
3 d total	Number						171	—
	Range	[0.40–14.00]	[0.50–3.20]	[0.23–0.60]	[300–1000]	[0.55–1.28]	[10.30–101.30]	—
	Average	5.65	1.39	0.40	457.37	1.01	41.62	—
	Standard deviation	2.91	0.54	0.08	84.70	0.12	21.40	—
28 d total	Number						—	309
	Range	[0.40–16.00]	[0.40–3.60]	[0.23–0.65]	[300–1000]	[0.66–1.28]	—	[1.28–151.50]
	Average	5.59	1.37	0.41	459.05	0.99	—	59.70
	Standard deviation	2.72	0.57	0.08	74.84	0.12	—	25.96

successfully in the field of civil engineering in recent years [68–72]. ANN models consist of three layers: input layer, hidden layer(s), and output layer. The number of neurons in both the input and the output layers is just the number of parameters in the corresponding layers. Determination of the number of layers and number of neurons in each layer is relatively complex for the hidden layer(s), which is generally done by trial-and-error. Connection between neurons should be implemented by using a linear/nonlinear transfer function. Input parameters in the input layer are fed to the output layer through the hidden layer(s). If outputs were not desired, they would bring error signals to back-propagate

Table 3: Performance comparison between different network structures (MPa).

		5-10-1		5-13-1		5-(6, 6)-1	
		Training	Testing	Training	Testing	Training	Testing
3 d compressive strength	MAE	7.47	6.78	11.28	9.89	8.01	7.23
	RMSE	14.89	18.21	16.34	17.11	16.41	19.62
28 d compressive strength	MAE	19.73	7.98	15.64	5.79	16.26	10.15
	RMSE	17.25	13.99	14.89	10.95	15.03	11.76

into the input layer to minimize the error by modifying the weight of each neuron there. In this context, training is very important in ANN modeling, and sufficient data size is needed to guarantee its accuracy.

In this study, the five parameters, Na_2O%, Ms, W/B, SA, and K_b, were treated as the neutrons in the input layer, and compressive strength of AAS was the neutron in the output layer. The determination of the hidden layer was made by trial and error. Both single-layer and double-layer were tried in this study. For both cases, number of the neutrons in the hidden layer was equal to root of the sum of input and output node numbers, plus a constant value less than 10 in general [73]. After several trials (a sample of performance comparison is given in Table 3), one hidden layer was determined to be used, and the number of the neutrons in the hidden layer was 10 and 13 for 3 d and 28 d compressive strength, respectively, according to the MAE and the RMSE error evaluations (to be described in section 2.4). Therefore, ANN model structures of 5-10-1 and 5-13-1 were used eventually in this study for compressive strength prediction of AAS at curing ages of 3 d and 28 d, respectively, as shown in Figure 1. For both the networks, 70%, 15%, and 15% of the data collected from literature were randomly selected for training, testing, and validation, respectively. Number of training period, learning rate, and minimum error of the training were set as 1000, 0.01, and 0.00001, respectively. After a comparison between Gradient Descent method and Levenberg-Marquardt algorithm, the latter was used for training due to its higher accuracy. The results to be reported were the optimum solution after 50 times of training.

2.3. ACE Modeling. ACE nonparametric regression technique, which has strong feasibility and high accuracy, is essentially a kind of response surface function. It is usually used to establish a mapping relationship between inputs and outputs which are already known by the approach of data fitting, as given in Ref. [74].

$$\theta(Y) = \varphi(X_1) + \varphi(X_2) + \cdots\cdots + \varphi(X_n) + \varepsilon_1, \quad (5)$$

$$Y = \theta_{-1}(\varphi(X_1) + \varphi(X_2) + \cdots\cdots + \varphi(X_n)) + \varepsilon_2, \quad (6)$$

where X_1, $X_2 \cdots\cdots X_n$ are input parameters; $\varphi(X_1), \varphi(X_2) \cdots\cdots \varphi(X_n)$ are response surface functions of X_1, $X_2 \cdots\cdots X_n$; Y is output parameter; $\theta(Y)$ is response surface function of Y; θ_{-1} is inverse function of θ; ε_1 and ε_2 are accuracy errors.

As the accuracy error ε is difficult to be determined, correction coefficient λ is usually introduced to modify formula (6), and finally, formula (7) is obtained as given below.

$$Y = \lambda\theta_{-1}(\varphi(X_1) + \varphi(X_2) + \cdots\cdots + \varphi(X_n)). \quad (7)$$

Furthermore, influencing weight of each input parameter on the output parameter could be analyzed elementarily by using ACE approach as well during the calculation.

In this study, X_1, $X_2 \cdots\cdots X_5$ were nominated as Na_2O%, Ms, W/B, SA, and K_b, respectively, as input parameters. Their values were collected from literature as detailed in Section 2.1. Input parameters were imported in ACE calculation software S-PLUS to calculate their corresponding response surface function $\varphi(X_1)$, $\varphi(X_2) \cdots\cdots \varphi(X_5)$. After that, a mapping relationship was established between the response surface functions and output parameters, namely, compressive strength of AAS at curing ages of 3 d and 28 d, respectively, by data fitting regression. The values of the strength were also collected from literature as detailed in Section 2.1.

2.4. Error Evaluation. Both mean absolute error (MAE) and root mean square error (RMSE) were used in this study to evaluate accuracy of both the ANN and the ACE models. MAE and RMSE values are to be zero when the values predicted and tested are exactly the same. Error increases with the increase of MAE and RMSE values. Calculations of MAE and RMSE are given in formulae (8) and (9) according to the literature [2–6]. Furthermore, agreement between predicted and measured values together with coefficient of determination was also applied to better assess the applicability of the proposed networks.

$$\text{MAE} = \sum_{i=1}^{n} \frac{|y_i - z_i|}{n} \quad (8)$$

$$RMSE = \left(\sum_{i=1}^{n} \frac{(y_i - y_i)^2}{n} \right)^{1/2} \quad (9)$$

where y_i (y_1, y_2, ...y_n) are the values tested; z_i (z_1, z_2, ...z_n) are the values predicted; n is the number of data.

2.5. Experimental Validation. Eleven AAS concrete mixes were prepared in this study, their compressive strength was tested at curing ages of 3 d and 28 d, respectively, to validate the results predicted by using both the ANN and the ACE models.

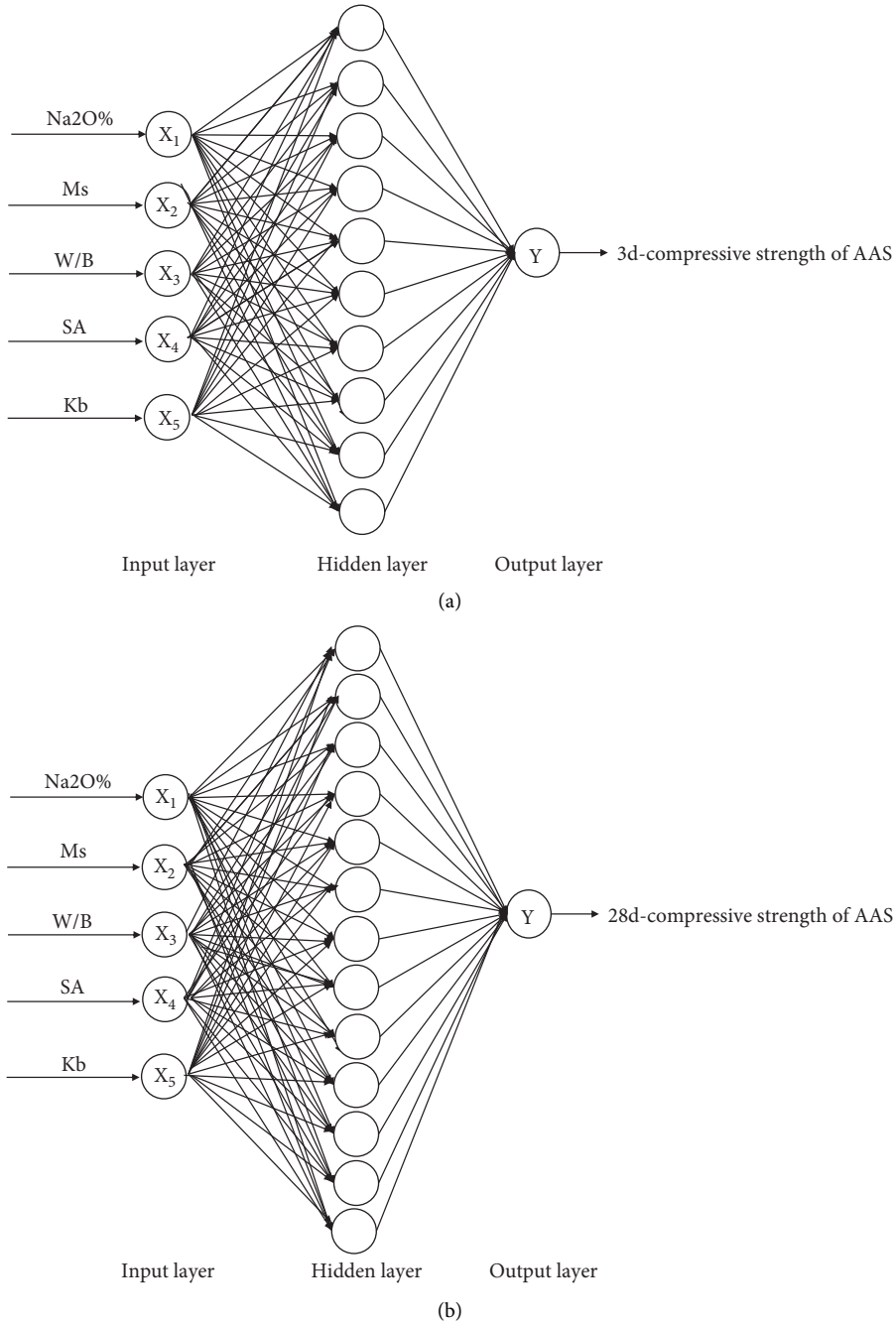

Figure 1: ANN model structures used in this study: (a) 5-10-1 structure for 3 d compressive strength. (b) 5-13-1 structure for 28 d compressive strength.

The slag used in the experimental work was from Qujing, Yunnan Province, China, whose K_b and SA were 0.96 and 405 m^2/kg, respectively. Its chemical compositions are given in Table 4.

Industrial water glass (with Na_2O% and SiO_2% of 11.49% and 31.25%, respectively) supplied by Kunming, Yunnan Province was used as activator. NaOH (with purity above 96%) from Fuchen (Tianjin) Chemical Reagent Co., Ltd. was used to adjust the modulus of the WG to the values required. Crushed limestone with size of 5–25 mm (continuous grading) and manufactured sand with fineness modulus of 2.82 were used as coarse and fine aggregates, respectively. Tap water was used for mixing.

By using the mix proportion given in Table 5, concrete specimens were manufactured according to Chinese standard JGJ/T 439–2018 [75]. After mixing, the concrete mixture was cast into molds with size of 100 mm × 100 mm × 100 mm in two layers. Vibration was carried out after each layer was cast. When the concrete surface was stiff, the specimens with molds were moved into curing room with temperature of 20 ± 2°C and RH ≥ 95%. The specimens were de-molded one day after mixing, and

Table 4: Chemical compositions of slag (%).

CaO	SiO_2	Al_2O_3	MgO	TiO_2	SO_3	MnO	Na_2O	K_2O	Fe_2O_3
38.26	31.40	15.71	6.90	2.94	1.43	1.23	0.96	0.53	0.38

Table 5: Mix proportions of concrete.

Mix no.	Na_2O%	Ms	W/B	Mix proportions (kg/m^3)					
				Slag	WG	NaOH	Water	Coarse aggregates	Fine aggregates
1	4.00	1.00	0.45	349.74	60.93	12.15	128.19	1123.24	748.83
2	4.00	1.50	0.45	344.21	89.95	9.05	107.79	1138.80	759.20
3	4.00	2.00	0.45	338.85	118.06	6.05	88.04	1153.87	769.25
4	6.00	1.00	0.45	336.35	87.89	17.52	109.24	1142.65	761.77
5	6.00	1.50	0.45	328.73	128.85	12.96	80.45	1164.49	776.33
6	6.00	2.00	0.45	321.45	168.00	8.61	52.95	1185.36	790.24
7	8.00	1.00	0.45	323.94	112.87	22.50	91.69	1160.62	773.75
8	8.00	1.50	0.45	314.58	164.41	16.54	555.47	1187.97	791.98
9	8.00	2.00	0.45	305.74	213.06	10.91	21.29	1213.78	809.19
10	6.00	1.50	0.40	328.73	128.85	12.96	61.45	1175.89	783.93
11	6.00	1.50	0.50	328.73	128.85	12.96	99.45	1153.09	768.73

then were moved into the curing room again for continuous curing to the ages required.

When the specimens reached curing ages of 3 d and 28 d, respectively, compressive strength test was carried out according to Chinese national standard GB/T 50081- 2019 [76]. The strength results to be reported are an average value of three duplicated specimens.

3. Results and Discussion

3.1. ANN. Regression of ANN modeling for prediction of 3 d and 28 d compressive strength of AAS is given in Figures 2 and 3, respectively. Correlation coefficient R is usually used to evaluate the correlation between the data samples. The closer the R-value is to 1, the stronger the correlation. From the figures, it can be seen that both the predictions have a good correlation between the data samples in general no matter training, testing, validation, or all of them are considered as the R-values are higher than 0.8. However, the correlation in the case of 28 d compressive strength is relatively lower in comparison with the 3 d one. It is known that 28 d compressive strength is the most elementary property of concrete, and therefore has been extensively reported in the literature. Consequently, large amounts of data samples on the 28 d compressive strength of AAS have been collected in this study, namely, 309 sets. This could have increased the scattering of the data as a result of different conditions of the specimen, such as different types and sizes of the specimen, different sources of slag, different aggregates, different curing conditions, used in the different studies.

Also, from MAE and RMSE error evaluation results, as given in Table 6, it can be seen that the error of the ANN models is at a low level, with MAE and RMSE values less than 20 MPa, in both the cases of 3 d and 28 d compressive strength, which means the models have sufficient accuracy.

Later, 3 d and 28 d compressive strengths of the 11 AAS concrete mixes were experimentally measured. Simultaneously, the material parameters used in the experimental work were put in the ANN model to run a prediction modeling. Comparison of the results measured and predicted is reported in Table 7, together with the error between them (100% × |predicted value-measured value|/measured value). From the table, it can be seen that in comparison to 28 d compressive strength, although the ANN model of 3 d compressive strength had an equivalent accuracy as discussed previously, it is less feasible to be employed to run the prediction. As stated previously, compared to the 309 sets of data that have been collected for the establishment of the 28 d compressive strength model, only 171 sets were available in the case of 3 d strength. Furthermore, the material parameters reported in the 171 data sets may not have covered the ones used in the experimental work, resulting in a lack of corresponding training, and finally in a high error between measurement and prediction. As can be seen from Table 1, few literatures consider the effects of 5 parameters on the 3D compressive strength of AAS at the same time. Therefore, as a result of insufficient training, the error of the mix 11 at 3 days is as high as 77.1%, while the larger database of 28 d compressive strength has supported effective training. Consequently, the error decreases dramatically to a low value of 4.6%. In this context, in order to improve feasibility of the ANN model for prediction, it is necessary to enlarge the scale of database enabling which could cover circumstances as full as possible, to ensure that a sufficient training could be implemented.

3.2. ACE. Relationship between input parameters X_1, $X_2 \cdots \cdots X_5$ and their corresponding response surface function $\varphi(X_1)$, $\varphi(X_2) \cdots\cdots \varphi(X_5)$ is shown in Figures 4 and 5. ACE fitting curves of compressive strength of AAS at curing ages of 3 d and 28 d were plotted in Figure 6, which have been

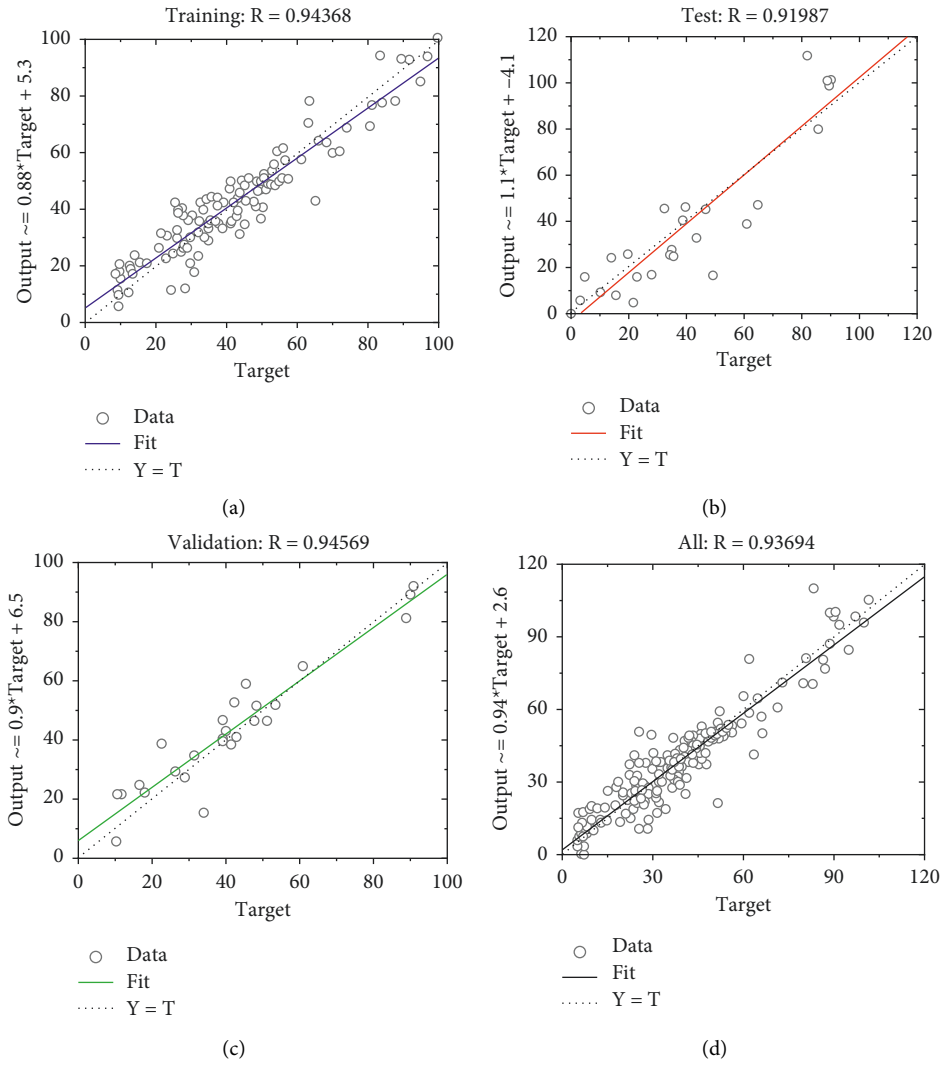

Figure 2: Regression of ANN modeling for prediction of 3 d compressive strength of AAS. (a) Training. (b) Testing. (c) Validation. (d) All.

adjusted by introducing correction coefficientλ as stated in Section 2.3. After trial-and-error, the values of λ were determined to be 0.90 and 0.85, respectively, for 3 d and 28 d compressive strength. Eventually, fitting goodness R^2 of 0.986 and 0.950 were obtained, respectively, in the case of 3 d and 28 d compressive strength, indicating that the ACE model has very high accuracy for both the cases. While probably due to the much bigger data size and the resulting increase in scattering, the ACE model for 28 d compressive strength is less accurate compared to the 3 d case, which could be seen from MAE and RMSE error evaluations as given in Table 6. However, the value is still acceptable for practical application.

In addition, from Figures 4 and 5, it can be seen that the relationship between X_1 (Na_2O%) and $\varphi(X_1)$ is much clearer compared to the others, and with the change of X_1 (Na_2O%), $\varphi(X_1)$ varies to a considerable scale. These indicate that among the five influencing factors, Na_2O%, Ms, W/B, SA, and K_b, Na_2O% took the largest weight-influencing compressive strength of AAS, followed by Ms > W/B > K_b > SA.

Similar to the ANN prediction, the ACE model was also run to predict the 3 d and 28 d compressive strength of the 11 AAS concrete mixes by inputting the material parameters used in the experimental work into the model. Comparison of the results measured and predicted is reported in Table 6, together with the error between them. Similarly, it is also found that no matter the mean error, max. error, or min. error, the value for 28 d compressive strength is lower than that for 3 d compressive strength, which indicates that compared to 3 d compressive strength, the ACE modeling was much more feasible to predict 28 d compressive strength, although the model for the latter was less accurate than the model for the former.

3.3. Comparison between ANN and ACE. From the discussion above it can be seen that when data size is relatively small, such as in the case of 3 d compressive strength (171 sets of data), although ANN model with a high precision could be established based on the given data size, its feasibility to predict nontrained data would be limited as ANN is a kind of statistics of known information in essence. While

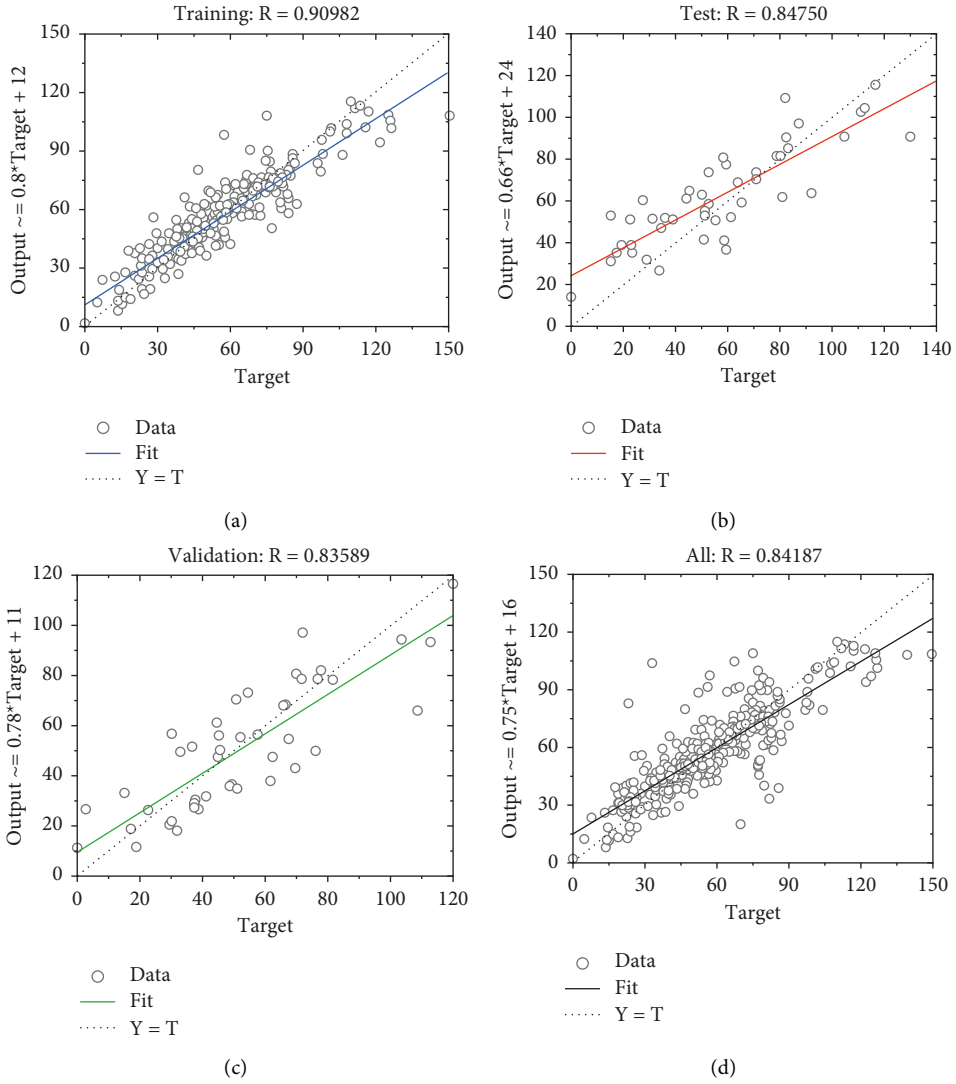

Figure 3: Regression of ANN modeling for prediction of 28 d compressive strength of AAS. (a) Training. (b) Testing. (c) Validation. (d) All.

Table 6: Error evaluation (MPa).

		ANN		ACE	
		Training	Testing	Training	Testing
3 d compressive strength	MAE	7.47	6.78	8.99	5.39
	RMSE	14.89	18.21	12.00	14.00
28 d compressive strength	MAE	15.64	5.79	14.87	7.32
	RMSE	14.89	10.95	18.70	15.79

ACE is based on fitting technique, its function could be close to the true values by adjusting the coefficient of the input parameters. As a result, from Table 6 it can be seen that in the case of 3 d compressive strength, nearly half of the error values of ACE prediction is at a very low level and the average one is also acceptable although very few predictions have yielded a high error value.

When data size is sufficiently large, such as in the case of 28 d compressive strength (309 sets of data), the error value between the results predicted and measured dramatically decreases as shown in Table 7, for both ANN and ACE, indicating a great improvement of their feasibility for the prediction. When applying ANN, there are more samples to train the model more efficiently. When a prediction is being processed, the related memory could be aroused to give a precise prediction. On the other hand, an increase in data size is also helpful to improve the precision of fitting, as a result of which the ACE error value decreases as well. However, it seems that there is an optimum data size for the fitting of ACE. When the size is beyond the upper bound, the

Table 7: Comparison between the strength measured and predicted.

Mix no.	3 d compressive strength (MPa)					28 d compressive strength (MPa)				
	Measured	ANN		ACE		Measured	ANN		ACE	
		Predicted	Error (%)	Predicted	Error (%)		Predicted	Error (%)	Predicted	Error (%)
1	24.2	27.3	12.8	23.3	3.7	50.5	47.4	6.1	51.4	1.8
2	21.2	29.2	37.7	23.7	11.8	51.0	53.0	3.9	59.4	16.5
3	23.0	31.2	35.6	28.4	23.5	51.2	56.2	9.8	57.2	11.7
4	27.7	29.4	6.1	32.2	16.2	54.4	51.4	5.5	58.7	7.9
5	33.7	31.8	5.6	32.6	3.3	60.0	57.1	4.8	65.7	9.5
6	35.1	35.1	0.0	38.0	8.3	59.6	60.1	0.8	63.8	7.0
7	37.8	27.5	27.2	36.5	3.4	61.0	54.9	10.0	61.7	1.1
8	33.8	29.4	13.0	32.6	3.6	62.3	60.6	2.7	68.2	9.5
9	38.2	30.2	20.9	42.5	11.2	60.2	63.5	5.5	66.4	10.3
10	44.1	39.4	10.6	20.5	53.5	65.9	59.9	9.1	68.4	3.8
11	13.1	23.2	77.1	10.9	16.8	56.2	53.6	4.6	60.7	8.0
Mean error (%)			22.4		14.1			5.7		7.9
Max. error (%)			77.1		53.5			10.0		16.5
Min. error (%)			0.0		3.3			0.8		1.1

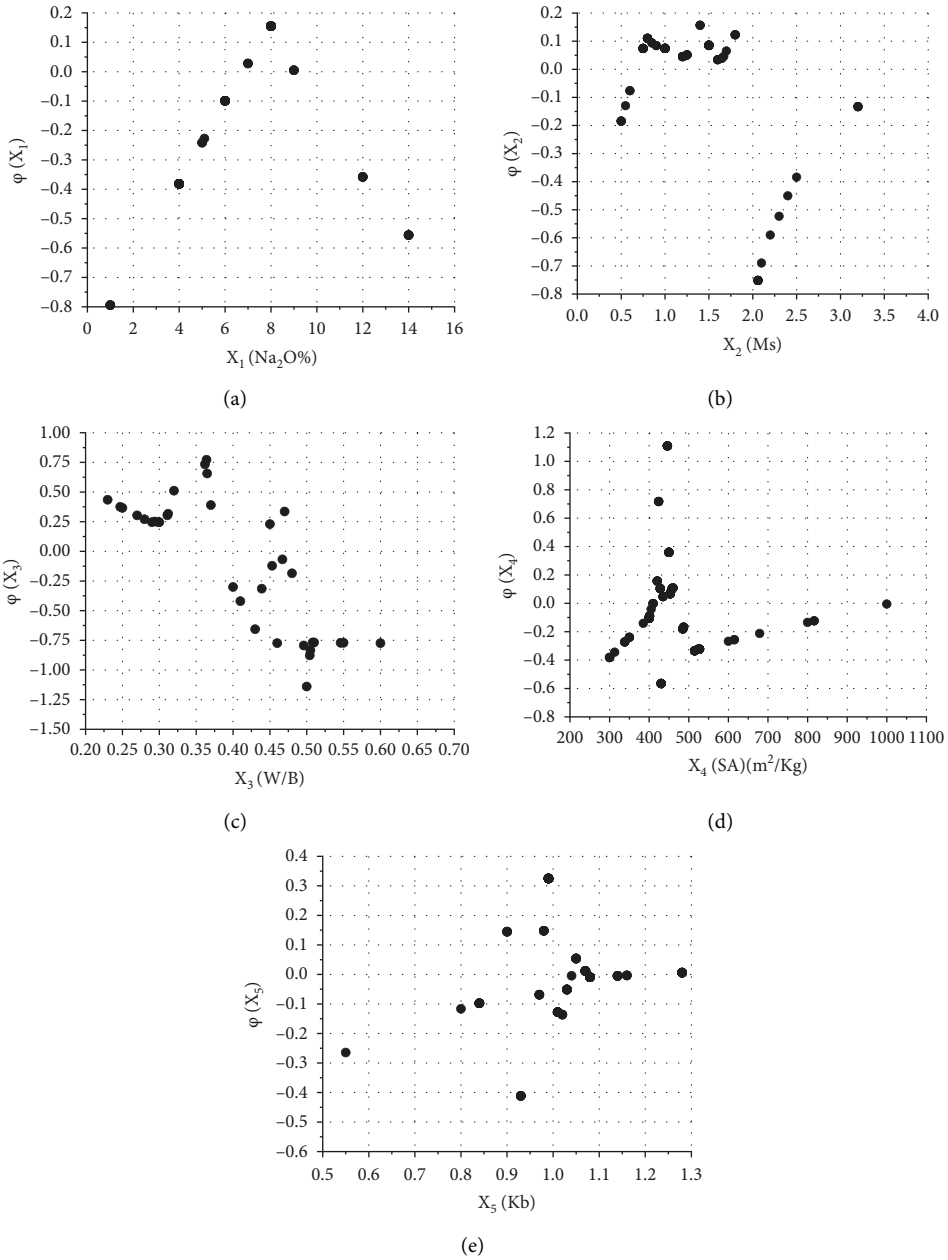

Figure 4: Relationship between input parameters and their corresponding response surface functions in the case of 3 d compressive strength. (a) X_1 (Na_2O%) and $\varphi(X_1)$. (b) X_2 (Ms) and $\varphi(X_2)$. (c) X_3 (W/B) and $\varphi(X_3)$. (d) X_4 (SA) and $\varphi(X_4)$. (e) X_5 (K_b) and $\varphi(X_5)$.

increase in fitting precision would be limited. Consequently, in this study, ACE performed not as well as ANN for the prediction of 28 d compressive strength, but it is worthy to note that the ACE error values are still in an acceptable range for practical application. Therefore, from the discussion above it can be seen that when massive data are available, it is more suitable to establish an ANN model for compressive strength prediction of AAS concretes. If data size was insufficient to support a precise ANN modeling, ACE could be considered as an alternative to yield an acceptable result.

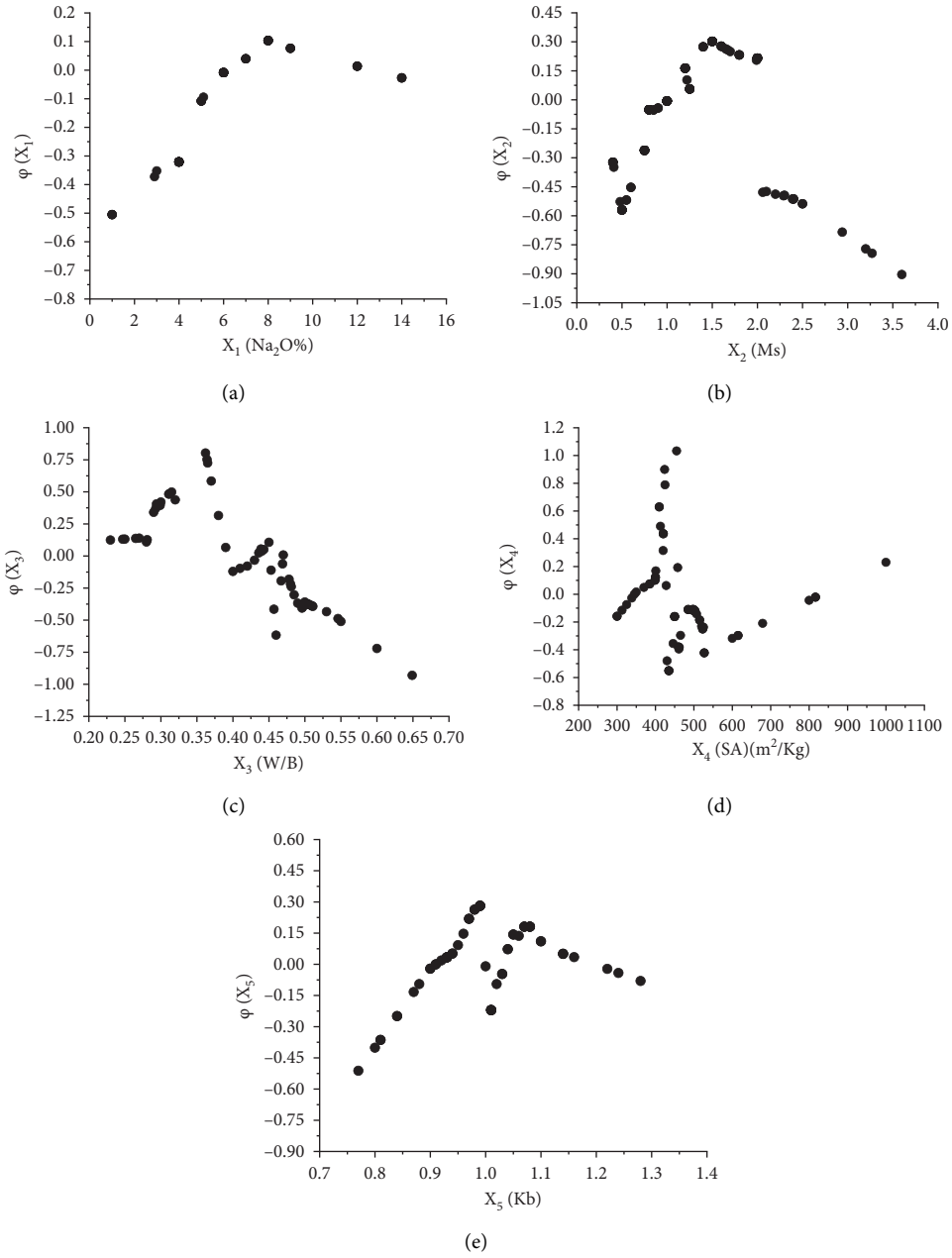

FIGURE 5: Relationship between input parameters and their corresponding response surface functions in the case of 28 d compressive strength. (a)X_1 (Na_2O%) and $\varphi(X_1)$. (b)X_2 (Ms) and $\varphi(X_2)$. (c)X_3 (W/B) and $\varphi(X_3)$. (d)X_4 (SA) and $\varphi(X_4)$. (e)X_5 (K_b) and $\varphi(X_5)$.

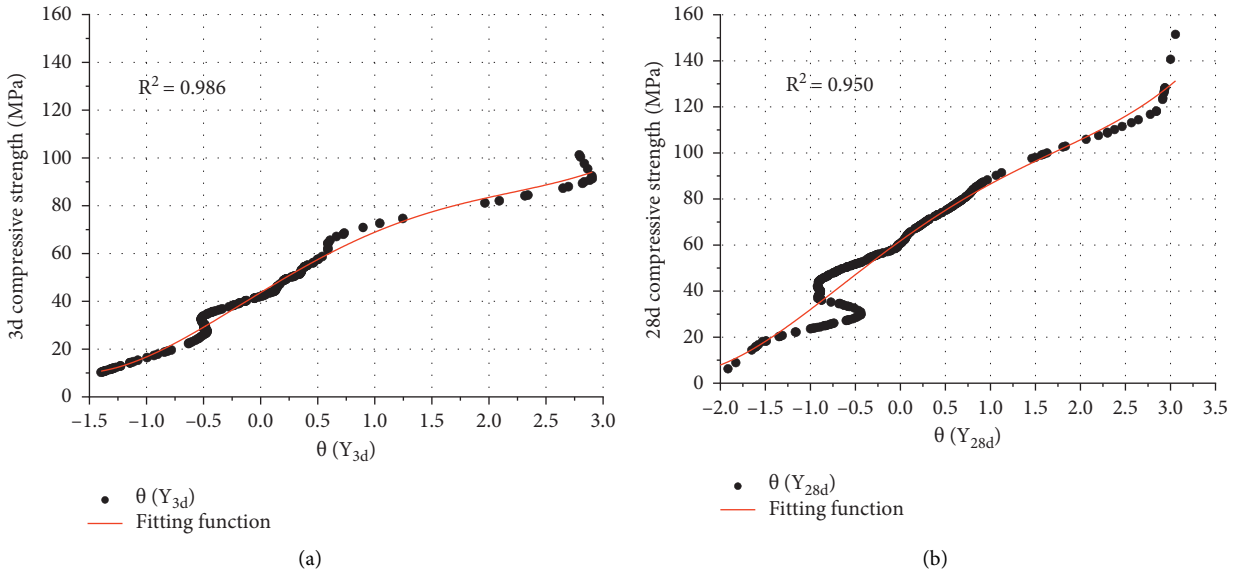

Figure 6: ACE fitting curves of compressive strength of AAS. (a) 3 d compressive strength. (b) 28 d compressive strength.

4. Conclusions

Based on the data collected and modeling used in this study, the following conclusions could be drawn:

(1) Both the ANN and the ACE models had adequate accuracy, no matter 3 d or 28 d compressive strength was considered.

(2) Compared to the 3 d compressive strength, due to increased data scattering and data size, both the ANN and the ACE models did not yield a higher accuracy in the case of 28 d strength. However, also due to the increase in data size, both the models were more feasible to implement a 28 d strength prediction as a result of sufficient learning and training during modeling.

(3) Based on the ACE analysis, among the five influencing factors, Na_2O%, Ms, W/B, SA, and K_b,, Na_2O % took the largest weight-influencing compressive strength of AAS, followed by Ms > W/B > K_b > SA.

(4) When massive data are available, it is more suitable to establish an ANN model for compressive strength prediction of AAS concretes. If data size was insufficient to support a precise ANN modeling, ACE could be considered as an alternative to yield an acceptable result.

Data Availability

All the data used to support the finding of this study have been included in the article.

Conflicts of Interest

The authors declare that they have no conflicts of interest.

Acknowledgments

This study was supported by National Natural Science Foundation of China (grant no. 52068038) and Yunnan Provincial Department of Science and Technology (grant no. 202101AT070089). The authors are grateful for the support of both institutions.

References

[1] B. Zhang, H. Zhu, Y. Cheng, G. F. Huseien, and K. W. Shah, "Shrinkage mechanisms and shrinkage-mitigating strategies of alkali-activated slag composites: A critical review," *Construction and Building Materials*, vol. 318, Article ID 125993, 2022.

[2] A. Bagheri, A. Nazari, and J. Sanjayan, "The use of machine learning in boron-based geopolymers: Function approximation of compressive strength by ANN and GP," *Measurement*, vol. 141, pp. 241–249, 2019.

[3] S. Nagajothi and S. Elavenil, "Influence of Aluminosilicate for the Prediction of Mechanical Properties of Geopolymer concrete - Artificial neural network," *Silicon*, vol. 12, no. 5, pp. 1011–1021, 2019.

[4] I. Faridmehr, M. L. Nehdi, G. F. Huseien, M. H. Baghban, A. R. M. Algaifi, and H. A. Algaifi, "Experimental and informational modeling study of sustainable self-compacting geopolymer concrete," *Sustainability*, vol. 13, no. 13, p. 7444, 2021.

[5] N. Shariatmadari, H. Hasanzadehshooiili, P. Ghadir, F. Saeidi, and F. Moharami, "Compressive strength of sandy soils stabilized with alkali-activated volcanic ash and slag," *Journal of Materials in Civil Engineering*, vol. 33, no. 11, Article ID 04021295, 2021.

[6] L. V. Zhang, A. Marani, and M. L. Nehdi, "Chemistry-informed machine learning prediction of compressive strength for alkali-

activated materials," *Construction and Building Materials*, vol. 316, Article ID 126103, 2022.

[7] T. Bakharev, J. G. Sanjayan, and Y. B. Cheng, "Alkali activation of Australian slag cements," *Cement and Concrete Research*, vol. 29, no. 1, pp. 113–120, 1999.

[8] C. Duran Atiş, C. Bilim, Ö. Çelik, and O. Karahan, "Influence of activator on the strength and drying shrinkage of alkali-activated slag mortar," *Construction and Building Materials*, vol. 23, no. 1, pp. 548–555, 2009.

[9] A. A. Ramezanianpour and M. A. Moeini, "Mechanical and durability properties of alkali activated slag coating mortars containing nanosilica and silica fume," *Construction and Building Materials*, vol. 163, pp. 611–621, 2018.

[10] A. M. Rashad, Y. Bai, P. Basheer, N. Collier, and N. Milestone, "Chemical and mechanical stability of sodium sulfate activated slag after exposure to elevated temperature," *Cement and Concrete Research*, vol. 42, no. 2, pp. 333–343, 2012.

[11] F. X. Wan, J. X. Lu, and S. L. Tian, "Experimental study on the high-temperature compressive strength of alkali-excited Kunshan slag cement," *Concrete and Cement Products*, no. 3, pp. 101–104, 2018.

[12] M. Dener, M. Karatas, and M. Mohabbi, "High temperature resistance of self compacting alkali activated slag/portland cement composite using lightweight aggregate," *Construction and Building Materials*, vol. 290, Article ID 123250, 2021.

[13] Y. J. Zhang, Y. L. Zhao, H. H. Li, and D. L. Xu, "Structure characterization of hydration products generated by alkaline activation of granulated blast furnace slag," *Journal of Materials Science*, vol. 43, no. 22, pp. 7141–7147, 2008.

[14] B. Fu, C. H. Yang, and J. X. Ye, "Microstructure and Mechanical Properties of Alkali-activated slag cement Pastes subjected to elevated temperatures," *Journal of Hunan University*, vol. 40, no. 08, pp. 90–96, 2013.

[15] B. Fu, C. H. Yang, and J. X. Ye, "Microstructure and Mechanical Properties of Alkali-Fly Ash-slag cement Pastes subjected to elevated temperatures," *Journal of Building Materials*, vol. 17, no. 06, pp. 1060–1065+1086, 2014.

[16] B. Fu, C. H. Yang, and Z. B. Cheng, "Influence of high temperature on microstructure ofalkali-acti vated slag cement pastes," *Journal of Huazhong University of Science and Technology*, vol. 41, no. 5, pp. 34–38, 2013.

[17] GB/T 203- 2008, "Granulated blast furnace slag powder for use in cement and concrete," *National Standard of the People's Republic of China*, 2008.

[18] Q. M. Ma, S. V. Nanukuttan, P. A. M. Basheer, Y. Bai, and C. Yang, "Chloride transport and the resulting corrosion of steel bars in alkali activated slag concretes," *Materials and Structures*, vol. 49, no. 9, pp. 3663–3677, 2016.

[19] J. Q. Liao and C. H. Yang, "Research on the preparation factor influencing the compressive strength of alkali activated slag cement concrete," *Fujian Building Materials*, no. 3, pp. 8–10+17, 2009.

[20] S. W. Zhang, X. M. Wan, T. J. Zhao et al., "Study on the optimization of mix ratio of alkali slag cementitious concrete," *New Building Materials*, vol. 44, no. 10, pp. 39–42, 2017.

[21] J. Xia, *Research on Mix Proportion of Alkali-Activated Slag Concrete*, Chongqing University, China, 2013.

[22] X. M. Wan, Y. Zhang, T. J. Zhao, S. W. Zhang, and Y. J. Cheng, "Mechanical properties of alkali excited slag concrete," *Material Report*, vol. 32, no. 12, pp. 2091–2095, 2018.

[23] D. Y. Kong and K. Meng, "Research on preparation and performance of alkali activated slag concrete," *Cement Engineering*, no. 02, pp. 83–86, 2017, (in Chinese).

[24] X. W. Sun and T. J. Wu, "Experimental Research of Alkali-activated slag cementitious Material," *Bulletin of the Chinese ceramic society*, vol. 33, no. 11, pp. 3036–3040, 2014.

[25] M. Tuyan, L. V. Zhang, and M. L. Nehdi, "Development of sustainable alkali-activated slag grout for preplaced aggregate concrete," *Journal of Cleaner Production*, vol. 277, Article ID 123488, 2020.

[26] A. E. Abubakr, A. M. Soliman, and S. H. Diab, "Effect of activator nature on the impact behaviour of Alkali-Activated slag mortar," *Construction and Building Materials*, vol. 257, Article ID 119531, 2020.

[27] M. C. Chi and Y. C. Liu, "Effects of Fly Ash/slag ratio and Liquid/binder ratio on strength of Alkali-Activated Fly Ash/slag Mortars," *Applied Mechanics and Materials*, vol. 377, pp. 50–54, 2013.

[28] K. Akçaözoğlu, S. Akçaözoğlu, and A. Açıkgöz, "Investigation of hydration temperature of alkali activated slag based concrete," *KSCE Journal of Civil Engineering*, vol. 22, no. 8, pp. 2994–3002, 2018.

[29] S. Liu, Q. Li, and W. Han, "Effect of various alkalis on hydration properties of alkali-activated slag cements," *Journal of Thermal Analysis and Calorimetry*, vol. 131, no. 3, pp. 3093–3104, 2018.

[30] S. A. Bernal, J. L. Provis, V. Rose, and R. Mejía de Gutierrez, "Evolution of binder structure in sodium silicate-activated slag-metakaolin blends," *Cement and Concrete Composites*, vol. 33, no. 1, pp. 46–54, 2011.

[31] S. A. Bernal, R. Mejía de Gutiérrez, A. L. Pedraza, J. L. Provis, E. D. Rodriguez, and S. Delvasto, "Effect of binder content on the performance of alkali-activated slag concretes," *Cement and Concrete Research*, vol. 41, no. 1, pp. 1–8, 2011.

[32] Z. G. Shi, C. J. Shi, S. Wan, N. Li, and Z. H. Zhang, "Effect of alkali dosage and silicate modulus on carbonation of alkali-activated slag mortars," *Cement and Concrete Research*, vol. 113, pp. 55–64, 2018.

[33] X. W. Ouyang, Y. W. Ma, Z. Liu, J. J. Liang, and G. Ye, "Effect of the sodium silicate modulus and slag content on fresh and hardened properties of alkali-activated fly ash/slag," *Minerals*, vol. 10, no. 1, p. 15, 2019.

[34] A. Wardhono, C. Gunasekara, D. W. Law, and S. Setunge, "Comparison of long term performance between alkali activated slag and fly ash geopolymer concretes," *Construction and Building Materials*, vol. 143, pp. 272–279, 2017.

[35] F. Puertas and M. Torres-Carrasco, "Use of glass waste as an activator in the preparation of alkali-activated slag. Mechanical strength and paste characterisation," *Cement and Concrete Research*, vol. 57, pp. 95–104, 2014.

[36] C. C. Wang, H. Y. Wang, B. T. Chen, and Y. C. Peng, "Study on the engineering properties and prediction models of an alkali-activated mortar material containing recycled waste glass," *Construction and Building Materials*, vol. 132, pp. 130–141, 2017.

[37] Z. Jiao, Y. Wang, W. Zheng, and W. Huang, "Pottery sand as fine aggregate for preparing alkali-activated slag mortar," *Advances in Materials Science and Engineering*, vol. 2018, pp. 1–10, 2018.

[38] N. Palankar, A. Ravi Shankar, and B. M. Mithun, "Durability studies on eco-friendly concrete mixes incorporating steel slag as coarse aggregates," *Journal of Cleaner Production*, vol. 129, pp. 437–448, 2016.

[39] M. Chi, "Effects of dosage of alkali-activated solution and curing conditions on the properties and durability of alkali-activated slag concrete," *Construction and Building Materials*, vol. 35, pp. 240–245, 2012.

[40] A. M. Humad, K. Habermehl-Cwirzen, and A. Cwirzen, "Effects of Fineness and chemical composition of blast Furnace slag on Properties of Alkali-Activated binder," *Materials*, vol. 12, no. 20, p. 3447, 2019.

[41] A. Wardhono, D. W. Law, and A. Strano, "The strength of alkali-activated slag/fly ash mortar blends at ambient temperature," *Procedia Engineering*, vol. 125, pp. 650–656, 2015.

[42] E. Acevedo-Martinez, L. Y. Gomez-Zamorano, and J. I. Escalante-Garcia, "Portland cement-blast furnace slag mortars activated using waterglass: - Part 1: effect of slag replacement and alkali concentration," *Construction and Building Materials*, vol. 37, pp. 462–469, 2012.

[43] W. A. Makhadmeh and A. Soliman, "Effect of activator nature on property development of alkali activated slag binders," *Journal of Sustainable Cement-Based Materials*, vol. 10, pp. 1–17, 2020.

[44] L. Coppola, D. Coffetti, E. Crotti, G. Gazzaniga, and T. Pastore, "The Durability of one-Part Alkali-Activated slag-based Mortars in Different Environments," *Sustainability*, vol. 12, no. 9, p. 3561, 2020.

[45] Y. L. Wang and H. Jing, "Comparison study of different series of alkali slag cement," *Journal of Henan polytechnic University (Natural science)*, vol. 35, no. 4, pp. 583–589, 2016.

[46] H. L. Ye, L. Huang, and Z. J. Chen, "Influence of activator composition on the chloride binding capacity of alkali-activated slag," *Cement and Concrete Composites*, vol. 104, Article ID 103368, 2019.

[47] Q. M. Ma, L. P. Huang, Z. L. Niu et al., "Effect of Alkali concentration and Modulus of Alkaline Activator on the compressive Properties and Hydration Products of Alkali Activated slag cementitious Material," *Bulletin of the Chinese ceramic society*, vol. 37, no. 6, pp. 2002–2007, 2018.

[48] Z. M. Xiao, D. T. Zhang, P. Chen, and B. L. Yan, "Effect of water glass on setting time and mechanical properties of water-glass based alkali slag cement," *Cement – lime*, vol. 4, pp. 13–15, 1994.

[49] X. Liao and J. H. Gu, "Relationship between alkali components (water glass) and strength and its development in alkali-slag cements," *Journal of Jinan University (Natural Science & Medicine Edition)*, no. 2, pp. 5–11, 1990.

[50] J. He and C. H. Yang, "Hydration Heat evolution and setting Performance of Alkali—slag cement Activated with W ater Glass," *Journal of Civil, Architectural & Environmental Engineering*, vol. 33, no. 03, pp. 147–152, 2011, (in Chinese).

[51] W. L. Zhang, C. H. Yang, T. Liu, B. Fu, and G. Cong, "Effect of Mix Activator on the Hydration of Alkali -Activated slag cements," *Bulletin of the Chinese ceramic society*, vol. 2, 2015.

[52] R. Tänzer, Y. Jin, and D. Stephan, "Alkali activated slag binder: effect of cations from silicate activators," *Materials and Structures*, vol. 50, no. 1, pp. 91–99, 2017.

[53] K. Vance, M. Aguayo, A. Dakhane, D. Ravikumar, J. Jain, and N. Neithalath, "Microstructural, mechanical, and durability related similarities in concretes based on OPC and alkali-activated slag binders," *International Journal of Concrete Structures and Materials*, vol. 8, no. 4, pp. 289–299, 2014.

[54] C. Bilim, O. Karahan, C. D. Atiş, and S. İlkentapar, "Influence of admixtures on the properties of alkali-activated slag mortars subjected to different curing conditions," *Materials & Design*, vol. 44, pp. 540–547, 2013.

[55] K. H. Yang and J. K. Song, "Workability loss and compressive strength development of cementless mortars activated by combination of sodium silicate and sodium hydroxide," *Journal of Materials in Civil Engineering*, vol. 21, no. 3, pp. 119–127, 2009.

[56] D. Krizan and B. Zivanovic, "Effects of dosage and modulus of water glass on early hydration of alkali-slag cements," *Cement and Concrete Research*, vol. 32, no. 8, pp. 1181–1188, 2002.

[57] A. Fernández-Jiménez, J. G. Palomo, and F. Puertas, "Alkali-activated slag mortars: mechanical strength behaviour," *Cement and Concrete Research*, vol. 29, no. 8, pp. 1313–1321, 1999.

[58] S. D. Wang, K. L. Scrivener, and P. L. Pratt, "Factors affecting the strength of alkali-activated slag," *Cement and Concrete Research*, vol. 24, no. 6, pp. 1033–1043, 1994.

[59] O. Burciaga-Díaz and J. I. Escalante-García, "Structure, Mechanisms of reaction, and strength of an Alkali-Activated blast-Furnace slag," *Journal of the American Ceramic Society*, vol. 96, no. 12, pp. 3939–3948, 2013.

[60] L. C. Lu, X. D. Shen, S. Yan, and X. Q. Wu, "Effect of fineness on the strength and hydration of alkali slag cements," *Cement – lime*, no. 2, pp. 15–18, 1995.

[61] M. Y. Yardımcı, S. Aydın, and M. Tuyan, "Flexural performance of alkali-activated slag cements under quasi-static and impact loading," *Journal of Materials in Civil Engineering*, vol. 29, no. 1, Article ID 04016192, 2017.

[62] F. Winnefeld, M. Ben Haha, G. Le Saout, M. Costoya, S. C. Ko, and B. Lothenbach, "Influence of slag composition on the hydration of alkali-activated slags," *Journal of Sustainable Cement-Based Materials*, vol. 4, no. 2, pp. 85–100, 2015.

[63] T. Bakharev, J. G. Sanjayan, and Y. B. Cheng, "Effect of admixtures on properties of alkali-activated slag concrete," *Cement and Concrete Research*, vol. 30, no. 9, pp. 1367–1374, 2000.

[64] A. Fernández-Jiménez, F. Puertas, I. Sobrados, and J. Sanz, "Structure of Calcium silicate Hydrates Formed in Alkaline-Activated slag: Influence of the type of Alkaline Activator," *Journal of the American Ceramic Society*, vol. 86, no. 8, pp. 1389–1394, 2003.

[65] S. Aydın and B. Baradan, "Effect of activator type and content on properties of alkali-activated slag mortars," *Composites Part B: Engineering*, vol. 57, pp. 166–172, 2014.

[66] S. Al-Otaibi, "Durability of concrete incorporating GGBS activated by water-glass," *Construction and Building Materials*, vol. 22, no. 10, pp. 2059–2067, 2008.

[67] Y. Tian, M. Shu, and Q. Jia, *Encyclopedia of Mathematical Geosciences*, Springer International Publishing, Berlin, Germany, pp. 1–4, 2022.

[68] S. N. Londhe, P. S. Kulkarni, P. R. Dixit, A. Silva, R. Neves, and J. de Brito, "Predicting carbonation coefficient using Artificial neural networks and genetic programming," *Journal of Building Engineering*, vol. 39, Article ID 102258, 2021.

[69] M. Ahmadi, A. Kheyroddin, and M. Kioumarsi, "Prediction models for bond strength of steel reinforcement with consideration of corrosion," *Materials Today Proceedings*, vol. 45, pp. 5829–5834, 2021.

[70] V. L. Tran and S. E. Kim, "A practical ANN model for predicting the PSS of two-way reinforced concrete slabs," *Engineering with Computers*, vol. 37, no. 3, pp. 2303–2327, 2021.

[71] B. Cai, L. F. Xu, and F. Fu, "Shear resistance prediction of post-fire reinforced concrete beams using artificial neural network," *International Journal of Concrete Structures and Materials*, vol. 13, no. 1, pp. 46–13, 2019.

[72] A. Ababneh, M. Alhassan, and M. Abu-Haifa, "Predicting the contribution of recycled aggregate concrete to the shear capacity of beams without transverse reinforcement using artificial neural networks," *Case Studies in Construction Materials*, vol. 13, Article ID e00414, 2020.

[73] D. F. Zhang, *MATLAB Neural Network Application Design-2nd edition*, China mechine press, Beijing, China, 2011.
[74] A. M. Hasofer and J. Qu, "Response surface modelling of monte carlo fire data," *Fire Safety Journal*, vol. 37, no. 8, pp. 772–784, 2002.
[75] JGJ/T 439- 2018, "Technical standard for application of alkali-activated slag concrete," *Ministry of Housing and Urban-Rural Development of the People's Republic of China*, 2018.
[76] GB/T 50081- 2019, "Standard for test methods of concrete physical and mechanical properties," *National Standard of the People's Republic of China*, 2019.

Hindawi
Advances in Civil Engineering
Volume 2022, Article ID 9348980, 11 pages
https://doi.org/10.1155/2022/9348980

Research Article

On Predictive Modeling for the Al_2O_3 Data Using a New Statistical Model and Machine Learning Approach

Mahmoud El-Morshedy,[1,2] **Zahra Almaspoor**,[3] **Gadde Srinivasa Rao**,[4] **Muhammad Ilyas**,[5] **and Afrah Al-Bossly**[1]

[1]*Department of Mathematics, College of Science and Humanities in Al-Kharj, Prince Sattam Bin Abdulaziz University, Al-Kharj 11942, Saudi Arabia*
[2]*Department of Mathematics, Faculty of Science, Mansoura University, Mansoura 35516, Egypt*
[3]*Department of Statistics, Yazd University, P.O. Box 89175-741, Yazd, Iran*
[4]*Department of Mathematics and Statistics, University of Dodoma, P.O. Box: 259, Dodoma, Tanzania*
[5]*Department of Statistics, University of Malakand, Dir (L), Chakdara, Khyber Pakhtunkhwa, Pakistan*

Correspondence should be addressed to Zahra Almaspoor; zahra.ferry21@gmail.com

Received 14 March 2022; Accepted 7 July 2022; Published 30 July 2022

Academic Editor: Ravindran Gobinath

In this article, we focused on predictive modeling for real data by means of a new statistical model and applying different machine learning algorithms. The importance of statistical methods in various research fields is modeling the real data and predicting the future behavior of data. For modeling and predicting real-life data, a series of statistical models have been introduced and successfully implemented. This study introduces another novel method, namely, a new generalized exponential-X family for generating new distributions. This method is introduced by using the T-X approach with the exponential model. A special case of the new method, namely, a new generalized exponential Weibull model, is introduced. The applicability of the new method is illustrated by means of a real application related to the alumina (Al_2O_3) data set. Acceptance sampling plans are developed for this distribution using percentiles when the life test is truncated at the pre-assigned time. The minimum sample size needed to make sure that the required lifetime percentile is determined for a specified customer's risk and producer's risk simultaneously. The operating characteristic value of the sampling plans is also provided. The plan methodology is illustrated using Al_2O_3 fracture toughness data. Using the same data set, we implement various machine learning approaches including the support vector machine (SVR), group method of data handling (GMDH), and random forest (RF). To evaluate their forecasting performances, three statistical measures of accuracy, namely, root-mean-square error (RMSE), mean absolute error (MAE), and Akaike information criterion (AIC) are computed.

1. Introduction

In the class of traditional/classical distributions, the Weibull model is an interesting model. It has been frequently implemented for dealing and modeling data in different sectors. The DF (cumulative distribution function) $V(x;\phi)$ of the two-parameter Weibull model is

$$V(x;\phi) = 1 - e^{-\sigma x^{\kappa}}, \cdots\cdots x \geq 0, \tag{1}$$

where $\phi = (\kappa, \sigma)$, $\kappa > 0$, and $\sigma > 0$.

The Weibull model and its different generalized/modified variants have been used by researchers for modeling data in numerous sectors. For example, (i) Ghorbani et al. [1] and Moreau [2] applied it to the medical science phenomena; (ii) Zaindin and Sarhan [3], Lai [4], Almalki and Yuan [5], and Singh [6] used it for reliability engineering applications; and (iii) Ahmad et al. [7] studied its applications in the finance sector.

The probability density function (PDF) $v(x;\phi)$ of the Weibull model is

$$v(x;\boldsymbol{\phi}) = \kappa\sigma x^{\kappa-1}e^{-\sigma x^{\kappa}}, \cdots\cdots x > 0, \tag{2}$$

with hazard function (HF) $h(x;\phi)$ given by

$$h(x;\boldsymbol{\phi}) = \kappa\sigma x^{\kappa-1}, \cdots\cdots x > 0. \tag{3}$$

From equation (3), we can see that the HF of the Weibull model can be (i) constant for $\kappa = 1$ (in this case, the Weibull captures the properties of the exponential model), (ii) increasing for $\kappa > 1$ (in this case, the Weibull captures the properties of the Rayleigh model), and (iii) decreasing for $\kappa < 1$.

The Weibull distribution provides impressive results when the failure behavior of the data is either increasing, decreasing, or constant (i.e., monotonic behavior). However, in many cases, the HF of the data behaves nonmonotonically [8]. In such scenarios, the Weibull model is not a popular distribution to use. In the literature, numerous authors have addressed different applications in various fields by developing a flexible version of the Weibull distribution with additional parameters (see Pham and Lai [9]; Nadarajah et al. [10]; and Wais [11]).

Here, we introduce a new method, namely, a new generalized exponential-X (for short "NGExp-X") family to obtain modified versions of the existing distributions. The NGExp-X family is introduced by implementing the exponential distribution with PDF e^{-t} and mixing it with the T-X distribution approach [12].

If X has the NGExp-X family, then its DF $F(x;\varphi,\delta,\phi)$ is given by

$$F(x;\varphi,\delta,\boldsymbol{\phi}) = 1 - \left(\frac{\varphi[1 - V(x;\boldsymbol{\phi})]}{\varphi + V(x;\boldsymbol{\phi})}\right)^{\delta}, \cdots\cdots x \in \mathbb{R}, \tag{4}$$

where $\varphi > 0, \delta > 0$ and $V(x;\phi)$ is a baseline DF with parameter vector ϕ.

In order to show that $F(x;\varphi,\delta,\phi)$ is a compact DF, we have the following two propositions.

Proposition 1. *For the expression $F(x;\varphi,\delta,\phi)$ in equation (1), we must prove that $\lim_{x\longrightarrow-\infty} F(x;\varphi,\delta,\phi) = 0$ and $\lim_{x\longrightarrow\infty} F(x;\varphi,\delta,\phi) = 1$.*

Proof.

$$\begin{aligned}
\lim_{x\longrightarrow-\infty} F(x;\varphi,\delta,\boldsymbol{\phi}) &= \lim_{x\longrightarrow-\infty}\left\{1 - \left(\frac{\varphi[1 - V(x;\boldsymbol{\phi})]}{\varphi + V(x;\boldsymbol{\phi})}\right)^{\delta}\right\},\\
&= 1 - \left(\frac{\varphi[1 - V(-\infty;\boldsymbol{\phi})]}{\varphi + V(-\infty;\boldsymbol{\phi})}\right)^{\delta},\\
&= 1 - \left(\frac{\varphi[1-0]}{\varphi+0}\right)^{\delta},\\
&= 1 - 1,\\
&= 0,
\end{aligned} \tag{5}$$

And

$$\begin{aligned}
\lim_{x\longrightarrow\infty} F(x;\varphi,\delta,\boldsymbol{\phi}) &= \lim_{x\longrightarrow\infty}\left\{1 - \left(\frac{\varphi[1 - V(x;\boldsymbol{\phi})]}{\varphi + V(x;\boldsymbol{\phi})}\right)^{\delta}\right\},\\
&= 1 - \left(\frac{\varphi[1 - V(\infty;\boldsymbol{\phi})]}{\varphi + V(\infty;\boldsymbol{\phi})}\right)^{\delta},\\
&= 1 - \left(\frac{\varphi[1-1]}{\varphi+1}\right)^{\delta},\\
&= 1 - 0,\\
&= 1.
\end{aligned} \tag{6}$$

□

Proposition 2. *The DF $F(x;\varphi,\delta,\phi)$ is differentiable and RC (right continuous).*

Proof. By taking the differentiation of equation (1), we get

$$\frac{\mathrm{d}}{\mathrm{d}x}F(x;\varphi,\delta,\phi) = f(x;\varphi,\delta,\boldsymbol{\phi}). \tag{7}$$

From the proofs of Propositions 1 and 2, it is obvious that the function $F(x;\varphi,\delta,\phi)$ provided in equation (4) is a valid DF.

For $x \in \mathbb{R}$, $\varphi > 0$, and $\delta > 0$, the PDF $f(x;\varphi,\delta,\phi)$ and HF $h(x;\varphi,\delta,\phi) = f(x;\varphi,\delta,\phi)/1 - F(x;\varphi,\delta,\phi)$ of the NGExp-X family are given by

$$f(x;\varphi,\delta,\boldsymbol{\phi}) = \frac{\delta\varphi^{\delta}(\varphi+1)v(x;\boldsymbol{\phi})[1 - V(x;\boldsymbol{\phi})]^{\delta-1}}{[\varphi + V(x;\boldsymbol{\phi})]^{\delta+1}}, \cdots\cdots v \in \mathbb{R}, \tag{8}$$

and

$$h(x;\varphi,\delta,\boldsymbol{\phi}) = \frac{\delta(\varphi+1)v(x;\boldsymbol{\phi})[1 - V(x;\boldsymbol{\phi})]^{-1}}{[\varphi + V(x;\boldsymbol{\phi})]}, \cdots\cdots v \in \mathbb{R}, \tag{9}$$

respectively. □

2. A New Generalized Exponential-Weibull Distribution

Let X be the proposed NGExp-Weibull distribution with parameters $\varphi > 0, \sigma > 0, \delta > 0$, and $\kappa > 0$, if its DF $F(x;\varphi,\sigma,\delta,\kappa)$ and PDF $f(x;\varphi,\sigma,\delta,\kappa)$ are given by

$$F(x;\varphi,\sigma,\delta,\kappa) = 1 - \left(\frac{\varphi e^{-\sigma x^{\kappa}}}{\varphi + 1 - e^{-\sigma x^{\kappa}}}\right)^{\delta}, \cdots\cdots v \geq 0, \tag{10}$$

and

$$f(x;\varphi,\sigma,\delta,\kappa) = \frac{\delta\kappa\sigma\varphi^{\delta}(\varphi+1)x^{\kappa-1}e^{-\delta\sigma x^{\kappa}}}{\left[\varphi + 1 - e^{-\sigma x^{\kappa}}\right]^{\delta+1}}, \cdots\cdots v > 0, \tag{11}$$

respectively.

Corresponding to $F(x;\varphi,\sigma,\delta,\kappa)$ and $f(x;\varphi,\sigma,\delta,\kappa)$, the SF $SF(x;\varphi,\sigma,\delta,\kappa) = 1 - F(x;\varphi,\sigma,\delta,\kappa)$, HF

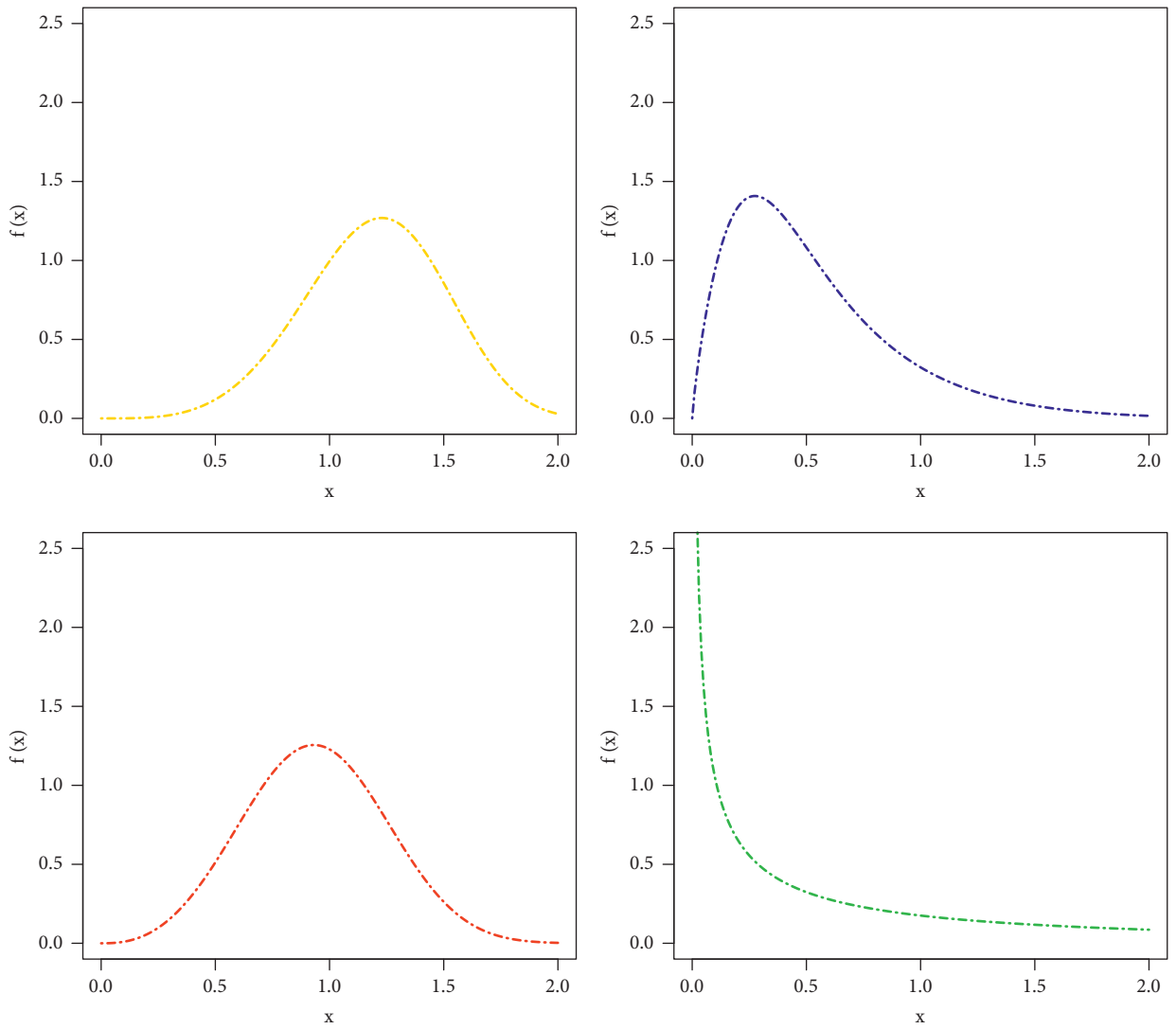

Figure 1: A visual behavior of $f(x;\varphi,\sigma,\delta,\kappa)$ for different values of $\varphi,\sigma,\delta>0$, and $\kappa>0$.

$h(x;\varphi,\sigma,\delta,\kappa)=f(x;\varphi,\sigma,\delta,\kappa)/S(x;\varphi,\sigma,\delta,\kappa)$, and CHF $H(x;\varphi,\sigma,\delta,\kappa)=-\log S(x;\varphi,\sigma,\delta,\kappa)$ are given by

$$S(x;\varphi,\sigma,\delta,\kappa)=\left(\frac{\varphi e^{-\sigma x^{\kappa}}}{\varphi+1-e^{-\sigma x^{\kappa}}}\right)^{\delta},\cdots\cdots x>0,$$
$$h(x;\varphi,\sigma,\delta,\kappa)=\frac{\delta\kappa\sigma(\varphi+1)x^{\kappa-1}}{\left[\varphi+1-e^{-\sigma x^{\kappa}}\right]},x>0, \tag{12}$$

and

$$H(x;\varphi,\sigma,\delta,\kappa)=-\log\left(\frac{\varphi e^{-\sigma x^{\kappa}}}{\varphi+1-e^{-\sigma x^{\kappa}}}\right)^{\delta},\cdots\cdots x>0, \tag{13}$$

respectively.

Different visual behaviors of $f(x;\varphi,\sigma,\delta,\kappa)$ for (i) $\kappa=4.5,\sigma=0.1,\delta=2.5,\varphi=4.5$ (gold curve), (ii) $\kappa=1.8,\sigma=1,\delta=1.2,\varphi=0.5$ (blue curve), (iii) $\kappa=3.5,\sigma=0.4,\delta=1.8,\varphi=3.9$ (red curve), and (iv) $\kappa=0.5,\sigma=0.4,\delta=1.8,\varphi=3.9$ (green curve) are presented in Figure 1.

From the visual illustration of $f(x;\varphi,\sigma,\delta,\kappa)$ in Figure 1, we can see that $f(x;\varphi,\sigma,\delta,\kappa)$ possess different behaviors. For example, it takes (i) the left-skewed form (gold curve), (ii) the right-skewed (blue curve), (iii) the symmetrical shape (red curve), and (iv) the reverse-J shape (green curve).

3. Modeling the Al_2O_3 Data Set

This section offers a practical illustration of the NGExp-Weibull distribution by analyzing data from the engineering sector. We implement the NGExp-Weibull distribution to analyze the Al_2O_3 (in the units of MPa m1/2) data set (see Nadarajah and Kotz) [13]. The data set is given by 5.5, 5, 4.9, 6.4, 5.1, 5.2, 5.2, 5, 4.7, 4, 4.5, 4.2, 4.1, 4.56, 5.01, 4.7, 3.13, 3.12, 2.68, 2.77, 2.7, 2.36, 4.38, 5.73, 4.35, 6.81, 1.91, 2.66, 2.61, 1.68, 2.04, 2.08, 2.13, 3.8, 3.73, 3.71, 3.28, 3.9, 4, 3.8, 4.1, 3.9, 4.05, 4, 3.95, 4, 4.5, 4.5, 4.2, 4.55, 4.65, 4.1, 4.25, 4.3, 4.5, 4.7, 5.15, 4.3, 4.5, 4.9, 5, 5.35, 5.15, 5.25, 5.8, 5.85, 5.9, 5.75, 6.25, 6.05, 5.9, 3.6, 4.1, 4.5, 5.3, 4.85, 5.3, 5.45, 5.1, 5.3, 5.2, 5.3, 5.25, 4.75, 4.5, 4.2, 4, 4.15, 4.25, 4.3, 3.75, 3.95, 3.51, 4.13, 5.4,5, 2.1,

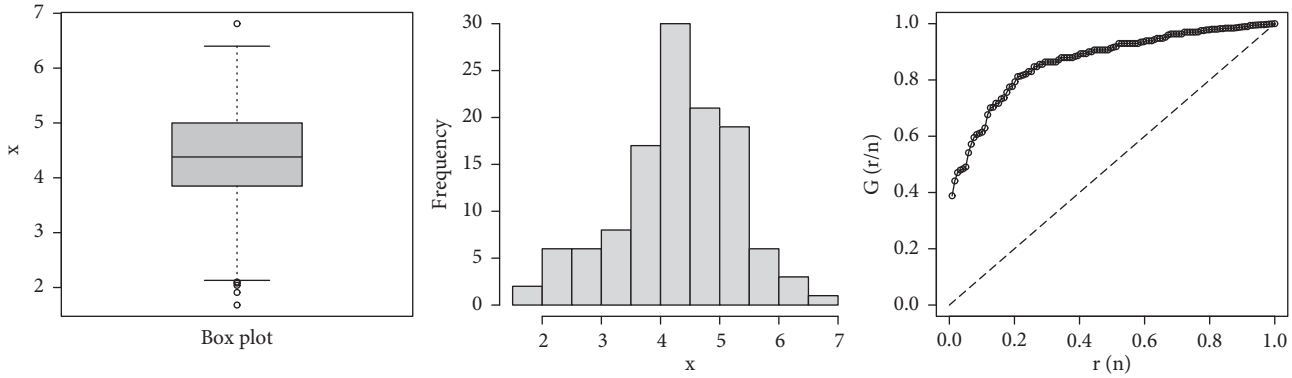

Figure 2: A visual sketching of the Al_2O_3 data.

Table 1: The numerical values of $\widehat{\kappa}, \widehat{\sigma}, \widehat{\varphi}, \widehat{\delta}, \widehat{\eta_1}, \widehat{\eta_2}$, and their SEs.

Model	$\widehat{\kappa}$	$\widehat{\sigma}$	$\widehat{\varphi}$	$\widehat{\delta}$	$\widehat{\eta_1}$	$\widehat{\eta_2}$
NGExp-Weibull	4.99058 (0.32556)	0.01412 (0.01143)	0.030667 (0.02670)	5.59645 (NaN)	—	—
Exp-Weibull	3.47923 (0.18832)	0.00696 (0.00236)	—	—	1.76624 (0.26376)	—
Kum-Weibull	2.25647 (0.39147)	0.01436 (0.00793)	—	—	2.64266 (0.49563)	12.99694 (14.37373)

4.6, 3.2, 2.5, 4.1, 3.5, 3.2, 3.3, 4.6, 4.3, 4.3, 4.5, 5.5, 4.6, 4.9, 4.3, 3, 3.4, 3.7, 4.4, 4.9, 4.9, and 5.

Corresponding to the Al_2O_3 data, the summary measures are as follows: minimum = 1.680, 1^{st} quartile = 3.850, median = 4.380, mean = 4.325, 1^{st} quartile = 5.000, maximum = 6.810, variance = 1.037332, range = 5.13, standard deviation = 1.018495, skewness = −0.4167136, and kurtosis = 5.13.

The box plot and histogram of the Al_2O_3 data are sketched in Figure 2. Additionally, the corresponding curve of the TTT (total test time) is also displayed in Figure 2.

The NGExp-Weibull model is applied to the Al_2O_3 data, and its results are compared with (i) the exponentiated Weibull (Exp-Weibull) model with DF given by $F(x;\kappa,\sigma,\eta_1) = (1-e^{-\sigma x^{\kappa}})^{\eta_1}, v \geq 0$, and (ii) Kumaraswamy Weibull (Kum-Weibull) model with DF given by $F(x;\kappa,\sigma,\eta_1,\eta_2) = 1-[1-(1-e^{-\sigma x^{\kappa}})^{\eta_1}]^{\eta_2}, v \geq 0$.

Furthermore, to figure out a suitable model for the Al_2O_3 data, three statistical tests with p-value are considered. These tests are given by (i) AD (Anderson–Darling) test given by $AD = -k - 1/k \sum_{a=1}^{k} (2a-1)[\log V(x_a) + \log\{1-V(x_{k-a+1})\}]$, (ii) CM (Cramer–von Mises) test expressed by $CM = 1/12k + \sum_{a=1}^{k} [2a - 1/2p - M(x_a)]^2$, and (*iii*) Kolmogorov–Smirnov (KS) test obtained as $KS = \sup_v [V_k(x) - V(x)]$.

Corresponding to the Al_2O_3 data, the values of $\widehat{\kappa}, \widehat{\sigma}, \widehat{\varphi}, \widehat{\delta}, \widehat{\eta}_1$, and $\widehat{\eta}_2$ are provided in Table 1. In the same table, the standard errors (SEs) (numerical values in the parentheses) of $\widehat{\kappa}, \widehat{\sigma}, \widehat{\varphi}, \widehat{\delta}, \widehat{\eta}_1$, and $\widehat{\eta}_2$ are also presented.

Corresponding to the Al_2O_3 data, the p-value along with the selected tests CM, AD, and KS of the fitted models is provided in Table 2. Based on the results of CM, AD, KS, and p value in Table 2, it is clear that the NGExp-Weibull model has the smallest values of CM, AD, and KS, and largest p-value. The values of these statistics show that the NGExp-Weibull model is the best competitor. In addition to the numerical illustration, a visual display of the performances of the NGExp-Weibull model is provided in Figure 3.

Table 2: The analytical measures of the fitted models for the Al_2O_3 data.

Model	CM	AD	KS	p-value
NGExp-Weibull	0.08555	0.52371	0.07204	0.56730
Exp-Weibull	0.16151	1.00382	0.09560	0.22600
Kum-Weibull	0.12816	0.79910	0.08058	0.42220

4. A New Acceptance Sampling Plans

In the usual practice of life testing experiment, the test will be terminated by the pre-assigned time t_0 and the number of failures observed. To establish a lower confidence limit on the mean life/percentile lifetime is the aim of the experiments. To protect the consumer's risk, the test has to establish the definite mean life with a certain probability. There are various methods for testing in the literature of acceptance sampling. Epstein [14] was first considered truncated life tests in the exponential distribution. Several authors described about truncated life tests for various distributions, for example, Soble and Tischendrof [15]; Gupta and Groll [16]; Gupta [17]; Baklizi and El-Masri [18]; Tsai and Wu [19]; Balakrishnan et al. [20]; and Kantam et al. [21].

In fact for life distributions, percentiles furnish more information than the mean life does. When the given life distribution is symmetric, the mean life, the median, and the 50th percentile are alike. Thus, developing acceptance sampling plans based on the mean life is a generalized case of developing the acceptance sampling plans based on percentiles of life distribution. Balakrishnan et al. [20] suggested that the acceptance sampling plans could be used for the quantiles and derived the formulae, whereas Lio et al. [22, 23] established for the acceptance sampling plans for any other percentiles of the Birnbaum–Saunders (BS) and

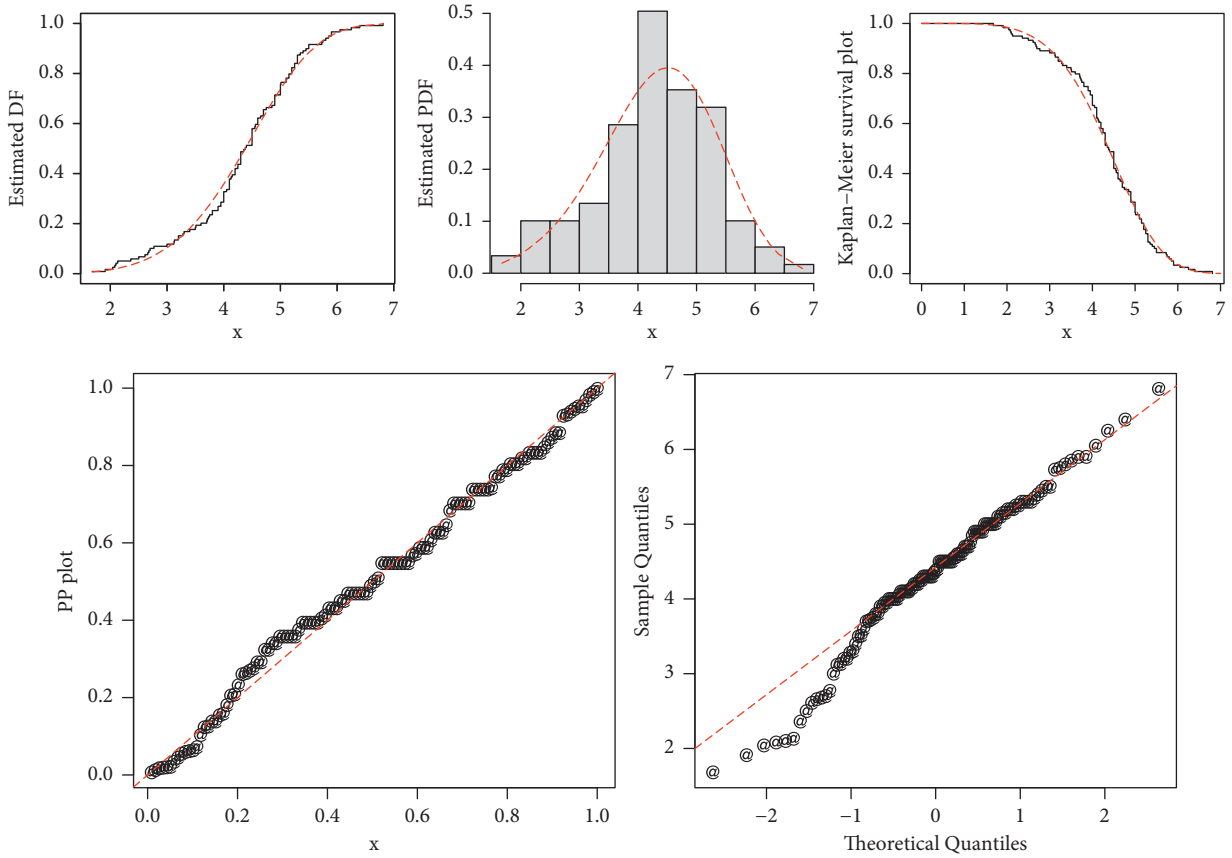

Figure 3: Visual performances of the NGExp-Weibull model for the Al_2O_3 data.

Burr type XII models. They have developed the acceptance sampling plans for percentile by replacing the scale parameter by the 100qth percentile.

Rao and Kantam [24] developed acceptance sampling plans from truncated life tests based on the log-logistic and inverse Rayleigh distributions for percentiles. Balamurali et al. [25] developed acceptance sampling plans based on median life for exponentiated half logistic distribution. Rao et al. [26] developed a new acceptance sampling plans based on percentiles for odds exponential log logistic distribution. This persuades to develop the acceptance sampling plans (ASP) based on the percentiles for NGExp-Weibull distribution, and it is a skewed distribution.

This section deals with study of new acceptance sampling plans (ASP) based on new distribution proposed in Section 2. The 100p-th percentile of NGExp-Weibull distribution is given by

$$t_p^k = -\frac{1}{\sigma}\log\left(\frac{(1-p)^{1/\delta}(1+\varphi)}{\varphi+(1-p)^{1/\delta}}\right). \tag{14}$$

The expression in equation (14) can also be written as

$$t_p^k = \frac{\tau_p}{\sigma}, \tag{15}$$

where

$$\tau_p^k = -\log\left(\frac{(1-p)^{1/\delta}(1+\varphi)}{\varphi+(1-p)^{1/\delta}}\right). \tag{16}$$

Hence, the quantile t_p given in equation (16) at a specified value of $\varphi = \varphi_0$, $\delta = \delta_0$, and $k = k_0$, the quantile t_p is a function of the scale parameter σ, and at a prespecified value of t_p, which say t_p^0, we may obtain the value of σ, which say σ_0 as $\sigma = \tau_p/t_p^k$. It is remarkable that σ_0 could rely on φ_0, δ_0, and k_0 to develop ASP for the NGExp-Weibull distribution determine that t_p exceeds t_p^0 equivalently σ exceeds σ_0.

At this juncture, the aim of the study was to obtain the minimum sample size needed to acquire percentile life if the life test ended at predestined time t_p^0 and if the amount of nonconformities noticed does not go beyond agreed acceptance number c. The judgment method is to accept a lot only if the given percentile of the lifetime is recognized with a pre-assigned high probability α that furnishes security to the consumer. The life testing arrives ended at the time at which $(c+1)^{th}$ failure is observed or at quantile of time t_p, whatsoever is prior.

The chance of accepting lot based on the number of failures is given by

$$L(q) = \sum_{i=0}^{c}\binom{n}{i}q^i(1-q)^{n-i}, \tag{17}$$

where n is the sample size, c is the acceptance number, and q is the chance of receiving a failure within the life test schedule time t_0. If the product lifetime follows an NGExp-Weibull distribution, then $q = F(t_0)$. Frequently, it would be suitable to define the testing conclusion time t_0 as $t_0 = \varsigma_p^0 t_p^0$ for a constant t_p^0 and the targeted 100p-th lifetime percentile, t_p^0. Suppose t_p is the true 100p-th lifetime percentile. Then, q can be transliterated as:

$$q = 1 - \left(\frac{\varphi \exp\left(-\left(\tau_p \left(\varsigma_p^0 \right)^k / \left(t_p / t_p^0 \right)^k \right) \right)}{\varphi + 1 - \exp\left(-\left(\tau_p \left(\varsigma_p^0 \right)^k / \left(t_p / t_p^0 \right)^k \right) \right)} \right)^{\delta}. \quad (18)$$

In this study, we adopt two points on the OC curve methodology by means of taking into account the both consumer's and producer's risks to obtain the design parameters of the proposed ASP. In this plan, the ratio of percentile lifetime to the lifetime, (t_p/t_p^0), is measured the quality intensity of the product. From producer's opinion, the chance of lot acceptance must be at least $1 - \alpha$ at the acceptable reliability level (ARL), that is, q_1. Hence, the producer requires that a lot must be accepted at different levels, say $t_p/t_p^0 = 2, 4, 6, 8, 10$ in equation (18). On the other hand, from consumer's point of view, the chance of rejection of a lot must be at most β at the lot of tolerance reliability level (LTRL), q_2. Thus, the consumer believes that a lot must be rejected when $t_p/t_p^0 = 1$.

Therefore, from equation (18), we get

$$L(q_1) = \sum_{i=0}^{c} \binom{n}{i} q_1^i (1 - q_1)^{n-i} \geq 1 - \alpha, \quad (19)$$

and

$$L(q_2) = \sum_{i=0}^{c} \binom{n}{i} q_2^i (1 - q_2)^{n-i} \leq \beta, \quad (20)$$

where q_1 and q_2 are given, respectively, by

$$q_1 = 1 - \left(\frac{\varphi \exp\left(-\left(\tau_p \left(\varsigma_p^0 \right)^k / \left(t_p / t_p^0 \right)^k \right) \right)}{\varphi + 1 - \exp\left(-\left(\tau_p \left(\varsigma_p^0 \right)^k / \left(t_p / t_p^0 \right)^k \right) \right)} \right)^{\delta}, \quad (21)$$

and

$$q_2 = 1 - \left(\frac{\varphi \exp\left(-\tau_p \left(\varsigma_p^0 \right)^k \right)}{\varphi + 1 - \exp\left(-\tau_p \left(\varsigma_p^0 \right)^k \right)} \right)^{\delta}, \quad (22)$$

where

$$\tau_p = -\log\left(\frac{(1-p)^{1/\delta_0} (1 + \varphi_0)}{\varphi_0 + (1 - p)^{1/\delta_0}} \right). \quad (23)$$

The design parametric measures for different values of parameters $\varphi = 2, \delta = 2,$ and $k = 2$ are constructed. The parameter of the suggested sampling design under the truncated life test at the pre-assigned time t_0 with $\varphi = 2, \delta = 2,$ and $k = 2$ is attained for the given producer's risk $\alpha = 0.05$ and test termination scheduled time t_0 with $\varsigma_p^0 = 1.0, 1.5, 2.0, 2.5, 3.0$ according to the consumer's confidence levels $\beta = 0.25, 0.10, 0.05, 0.01$ for 50^{th} percentile, and the OC values are determined, and the results are given in Tables 1–3. The design parameter value is tabulated in Tables 3 and 4, for $\varphi = 2, \delta = 2, k = 2$ and $\varphi = 0.5, \delta = 1.5,$ $k = 1.5$ with 50th percentiles, while Table 5 displays the design parameter for $\hat{\varphi} = 0.0307, \hat{\delta} = 5.59645$ and $\hat{k} = 4.9906$ is the maximum-likelihood estimates from the Al_2O_3 fracture toughness data set at 50^{th} percentile. It is noticed that from Tables 3–5 that the (a) when parametric values are increases the sample size decreases and (b) when the percentile ratio increases the sample size decreases.

4.1. Description of the Proposed Plan. To ensure that, the 50th percentile life of products under inspection is at least 1000 hours $\beta = 0.25$ under the assumption that the producer wants to enforce a single sampling plan at the percentile ratio (t_p/t_p^0). Researcher needs to run this life test for 1000 hours. If the lifetime of the product follows NGExp-Weibull distribution observed from the previous data with $\varphi = 2, \delta = 2,$ and $k = 2$. The best plan from Table 3 for stated demands such as $\beta = 0.25, \varphi = 2, \delta = 2, k = 2, (t_p/t_p^0),$ and $\varsigma_p^0 = 1.0$ is attained as $n = 12$ and $c = 4$ with the probability of acceptance, which is 0.9651. Most of the researchers are studied earlier based on one point on the operating characteristic curve method for assuring mean or percentile life time under various life distributions. The present study is deal with sampling plans based on two-point approach on the operating characteristic curve approach for ensuring percentile lifetime of the products under NGExp-Weibull distribution.

4.2. Real Data Illustration. Here, we consider the suggested ASP application for NGExp-Weibull distribution using Al_2O_3 fracture toughness (in the units of MPa m1/2) data set. The goodness of fit for the given model is shown in Table 2, and to emphasize the goodness of fit, we have proved the visuals in Figure 3. The MLEs of the parameters of NGExp-Weibull distribution for the Al_2O_3 fracture toughness data set are $\hat{\varphi} = 0.0307, \hat{\delta} = 5.59645, \hat{k} = 4.9906,$ and $\hat{\nu} = 1.7443$ and the Kolmogorov–Smirnov test we found that the maximum distance between the data and the fitted of the NGExp-Weibull distribution is 0.07204 with p-value 0.56730. This shows that Al_2O_3 fracture toughness data set is well fitted for NGExp-Weibull distribution with estimated parameters, and the plan parameters for these estimated parameters are given in Table 3.

Let us fix that the consumer's risk is at 25% when the true 50^{th} percentile is fracture toughness 2 units of MPa m1/2 and the producer's risk is 5% when the true 50^{th} percentile is fracture toughness 4 units of MPa m1/2. For $\hat{\varphi} = 0.0307,$ $\hat{\delta} = 5.59645, \hat{k} = 4.9906,$ the consumer's risk is 25%, $\varsigma_p^0 = 1,$ and $(t_p/t_p^0) = 2$. The minimum sample size $n = 5$ and acceptance number $c = 1$ are given from Table 3. Thus, the design can be implemented as follows: we select a sample of 5 fracture toughness units, and we will accept the lot when no more than 1 fracture toughness 2 units. Hence, by applying the proposed sampling plan, the fracture toughness lot has

Table 3: The plan parameters and OC values for NGExp-Weibull distribution for $\varphi = 2, \delta = 2$, and $k = 2$.

β	(t_p/t_p^0)	$\varsigma_p^0 = 1.0$			$\varsigma_p^0 = 1.5$			$\varsigma_p^0 = 2$			$\varsigma_p^0 = 2.5$			$\varsigma_p^0 = 3$		
		c	n	$L(q_1)$	c	n	$L(q_1)$	c	n	$L(q_1)$	c	n	$L(q_1)$	c	n	$L(q_1)$
0.25	2	4	12	0.9651	4	7	0.9573	6	8	0.9648	7	8	0.9673	11	12	0.9549
	4	1	5	0.9819	1	3	0.9736	1	2	0.9728	2	3	0.9855	2	3	0.9645
	6	1	5	0.9961	0	1	0.9555	1	2	0.9940	1	2	0.9860	1	2	0.9728
	8	0	3	0.9663	0	1	0.9747	2	1	0.9555	1	2	0.9953	1	2	0.9906
	10	0	3	0.9783	0	1	0.9837	2	2	0.9712	0	1	0.9555	1	2	0.9960
0.10	2	5	17	0.9518	6	11	0.9642	6	11	0.9673	10	13	0.9562	11	12	0.9549
	4	1	7	0.9641	1	4	0.9506	2	4	0.9843	2	2	0.9855	2	3	0.9645
	6	1	7	0.9921	1	4	0.9888	1	3	0.9829	1	2	0.9860	1	2	0.9728
	8	0	4	0.9554	1	4	0.9963	0	2	0.9555	1	2	0.9953	1	2	0.9906
	10	0	4	0.9712	0	2	0.9677	0	2	0.9712	0	1	0.9555	1	2	0.9960
0.05	2	6	21	0.9544	8	15	0.9719	9	13	0.9539	10	12	0.9562	17	19	0.9511
	4	1	8	0.9536	1	4	0.9506	2	4	0.9843	2	4	0.9527	2	3	0.9645
	6	1	8	0.9896	1	4	0.9888	1	3	0.9829	1	2	0.9860	1	2	0.9728
	8	0	8	0.9966	1	4	0.9963	1	3	0.9942	1	2	0.9953	1	2	0.9906
	10	0	5	0.9641	0	3	0.9519	1	3	0.9976	0	1	0.9555	1	2	0.9960
0.01	2	8	30	0.9523	10	20	0.9660	11	16	0.9616	13	16	0.9532	17	19	0.9511
	4	2	14	0.9778	2	7	0.9763	2	5	0.9655	2	4	0.9527	3	5	0.9570
	6	1	11	0.9803	1	6	0.9736	1	3	0.9675	1	3	0.9614	2	4	0.9843
	8	1	11	0.9934	1	6	0.9910	1	3	0.9888	1	3	0.9865	1	3	0.9736
	10	0	7	0.9501	1	6	0.9962	1	3	0.9952	1	3	0.9942	1	3	0.9885

Table 4: The plan parameters and OC values for NGExp-Weibull distribution for $\varphi = 0.5, \delta = 1.5$, and $k = 1.5$.

β	(t_p/t_p^0)	$\varsigma_p^0 = 1.0$			$\varsigma_p^0 = 1.5$			$\varsigma_p^0 = 2$			$\varsigma_p^0 = 2.5$			$\varsigma_p^0 = 3$		
		c	n	$L(q_1)$	c	n	$L(q_1)$	c	n	$L(q_1)$	c	n	$L(q_1)$	c	n	$L(q_1)$
0.25	2	7	18	0.9589	9	16	0.9618	9	13	0.9539	11	14	0.9582	5	18	0.9529
	4	2	7	0.9784	2	5	0.9667	2	4	0.9571	3	5	0.9664	4	6	0.9690
	6	1	5	0.9751	1	3	0.9753	2	4	0.9904	1	2	0.9651	2	3	0.9870
	8	1	5	0.9888	1	3	0.9888	1	3	0.9753	1	2	0.9837	1	2	0.9735
	10	0	2	0.9507	3	3	0.9941	1	3	0.9866	1	2	0.9912	1	2	0.9855
0.10	2	10	28	0.9540	13	24	0.9685	14	21	0.9608	18	24	0.9573	19	23	0.9593
	4	2	9	0.9551	3	8	0.9717	3	6	0.9697	4	7	0.9681	4	6	0.9690
	6	1	7	0.9512	1	4	0.9536	2	5	0.9784	2	4	0.9776	2	4	0.9571
	8	1	7	0.9775	1	4	0.9786	1	3	0.9753	1	3	0.9554	2	4	0.9849
	10	1	7	0.9879	1	4	0.9885	1	3	0.9866	1	3	0.9753	1	3	0.9599
0.05	2	12	35	0.9505	15	29	0.9591	18	28	0.9564	—	—	—	—	—	—
	4	3	13	0.9724	3	9	0.9555	4	9	0.9617	4	7	0.9681	5	8	0.9635
	6	2	11	0.9825	2	7	0.9784	2	6	0.9612	2	5	0.9517	2	4	0.9571
	8	1	8	0.9707	1	5	0.9657	1	4	0.9536	1	3	0.9554	2	3	0.9849
	10	1	8	0.9842	1	5	0.9813	1	4	0.9744	1	3	0.9753	1	3	0.9599
0.01	2	17	52	0.9533	—	—	—	—	—	—	—	—	—	—	—	—
	4	4	19	0.9725	4	13	0.9532	5	12	0.9586	6	11	0.9753	6	10	0.9610
	6	2	14	0.9895	2	9	0.9551	3	8	0.9836	3	7	0.9737	3	6	0.9697
	8	2	14	0.9886	2	7	0.9847	2	7	0.9784	2	6	0.9693	2	5	0.9667
	10	1	11	0.9704	1	7	0.9631	1	5	0.9593	1	4	0.9536	2	5	0.9855

Note. (—) indicates that the parameters cannot be found to satisfy conditions.

been rejected because there is more than one unit before the termination fracture toughness 4 units.

5. Data and Modeling Procedures

The Al_2O_3 forecasting is very crucial and attributes remarkable growth to the country's economy. Knowing its future trajectory is beneficial for the government and policymakers. Therefore, this section provides the multistep ahead forecast of Al_2O_3 by applying different machine learning algorithms, namely, support vector machine (SVM), group method of data handling (GMDH) neural network, and random forest (RF).

5.1. Support Vector Regression. The SVR method was first introduced by Cortes and Vapnik [27], and to date, it is frequently used for regression and classification problems. The SVR is based on statistical theory and structured risk minimization principle, due to which it circumvents the

Table 5: The plan parameters and OC values for NGExp-Weibull distribution for $\varphi = 0.0307, \delta = 5.59645$, and $k = 4.9906$.

β	(t_p/t_p^0)	$\varsigma_p^0 = 1.0$			$\varsigma_p^0 = 1.5$			$\varsigma_p^0 = 2$			$\varsigma_p^0 = 2.5$			$\varsigma_p^0 = 3$		
		c	n	$L(q_1)$	c	n	$L(q_1)$	c	n	$L(q_1)$	c	n	$L(q_1)$	c	n	$L(q_1)$
0.25	2	1	5	0.9950	1	2	0.9749	4	5	0.9688	18	19	0.9546	—	—	—
	4	0	3	0.9978	1	2	1.0000	0	1	0.9771	1	2	0.9954	1	2	0.9749
	6	0	3	0.9997	1	2	1.0000	0	1	0.9969	0	1	0.9907	0	1	0.9771
	8	0	3	0.9999	1	2	1.0000	0	1	0.9993	0	1	0.9978	0	1	0.9945
	10	0	3	1.0000	1	2	1.0000	0	1	0.9998	0	1	0.9993	0	1	0.9982
0.10	2	1	7	0.9898	1	2	0.9749	4	5	0.9688	18	19	0.9546	—	—	—
	4	0	4	0.9971	0	1	0.9945	0	1	0.9771	1	2	0.9954	1	2	0.9749
	6	0	4	0.9996	0	1	0.9993	0	1	0.9969	0	1	0.9907	0	1	0.9771
	8	0	4	0.9999	0	1	0.9998	0	1	0.9993	0	1	0.9978	0	1	0.9945
	10	0	4	1.0000	0	1	0.9999	0	1	0.9998	0	1	0.9993	0	1	0.9982
0.05	2	1	8	0.9867	1	2	0.9749	4	5	0.9688	18	19	0.9546	—	—	—
	4	0	5	0.9964	0	1	0.9945	0	1	0.9771	1	2	0.9954	1	2	0.9749
	6	0	5	0.9995	0	1	0.9993	0	1	0.9969	0	1	0.9907	0	1	0.9771
	8	0	5	0.9999	0	1	0.9998	0	1	0.9993	0	1	0.9978	0	1	0.9945
	10	0	5	1.0000	0	1	0.9999	0	1	0.9998	0	1	0.9993	0	1	0.9982
0.01	2	1	11	0.9750	2	4	0.9860	4	5	0.9688	—	—	—	—	—	—
	4	0	7	0.9949	0	2	0.9890	0	1	0.9771	1	2	0.9954	1	2	0.9749
	6	0	7	0.9993	0	2	0.9985	0	1	0.9969	0	1	0.9907	0	1	0.9771
	8	0	7	0.9998	0	2	0.9997	0	1	0.9993	0	1	0.9978	0	1	0.9945
	10	0	7	0.9999	0	2	0.9999	0	1	0.9998	0	1	0.9993	0	1	0.9982

problem of overfitting, and produces an accurate forecast. In practice, it can precisely approximate the linear and nonlinear problems in the real world [28]. The performance of SVR is based on the kernel function to be utilized. Kernel functions are utilized to carry out operations in the input space instead of higher-dimensional space. Various kernel functions are appeared in past studies, namely, linear, polynomial, splines, and sigmoid radial basis functions [29]. RBF has achieved great attention due to its outstanding performance in capturing nonlinear association [30, 31]. The SVR helps to disclose the margin of error, which is acceptable in a model [32, 33]. Let we have a set of training data, having output and input variables. Mathematically, the SVR seeks to find a function that fitted the data more appropriately. In other words, it minimizes the error between output variable and predicted values in the following way:

$$f(\delta) = (\Omega, (\delta)) + \beta, \tag{24}$$

where Ω is a weight parameter, (δ) represents the nonlinear function, and β is a constant parameter. In equation (25), the loss functions demonstrate the ε-insensitive model, where the loss tends to 0, if the difference between actual values and predicted values is less than c, and is illustrated by the Vapnik's e-insensitive loss function

$$\mathfrak{R}_\varepsilon(f(\delta), P) = \left\{ \begin{array}{cc} |f(\delta) - P| - \varepsilon & if\ |f(\delta) - P| \geq \varepsilon \\ 0 & \text{otherwise} \end{array} \right\}. \tag{25}$$

The problem of SVR is then constructed as the following optimization problem.

$$min_{\Omega,\beta,\aleph_j,\aleph_j^*} \frac{1}{2}\Omega + D\sum_{j=1}^{h}\left(\aleph_j + \aleph_j^*\right), \tag{26}$$

where $\aleph_j^*$ and $\aleph_j$ represent the slack variables describing the lower and upper training errors subject to the error tolerance ε, and D is a positive constant that discovers the extent of penalized loss when a training error occurs. In our case, we set the values of D and E are 1 and 0.01, respectively.

$$\Omega = \sum_{m=1}^{h}(\theta_m - \theta_m^*)Q(\delta_m, \delta). \tag{27}$$

The set of Lagrange multipliers including θ_m and θ_m^* is utilized for optimization problem solution. Thus, the approximate function is illustrated as follows:

$$P_t = \sum_{m=1}^{h}(\theta_m - \theta_m^*)Q(\delta_m, \delta) + \omega, \tag{28}$$

where δ_m represents the support vector, h represents the size of support vector, $Q(\delta_m, \delta)$ represents the kernel function, and ω represents the threshold value. Herein, the radial basis function (RBF) with a parameter π^2 is expressed as follows:

$$Q(\delta_m, \delta_n) = \exp\left(-\frac{\left\|\delta_m - \delta_n\right\|^2}{2\pi^2}\right), \tag{29}$$

where $\|\delta_m - \delta_n\|^2$ indicates the Euclidean distance between the two predictors in squared form, and π^2 indicates the width of RBF [34]. Hence, in this study, we focus on the RBF kernel function for SVR.

5.2. Random Forest. Breiman [35] developed a nonparametric approach known as random forest (RF). The development of the RF approach is based on decision tree algorithms; however, this is the modified form of classification and regression trees (CART). The RF is, therefore, to

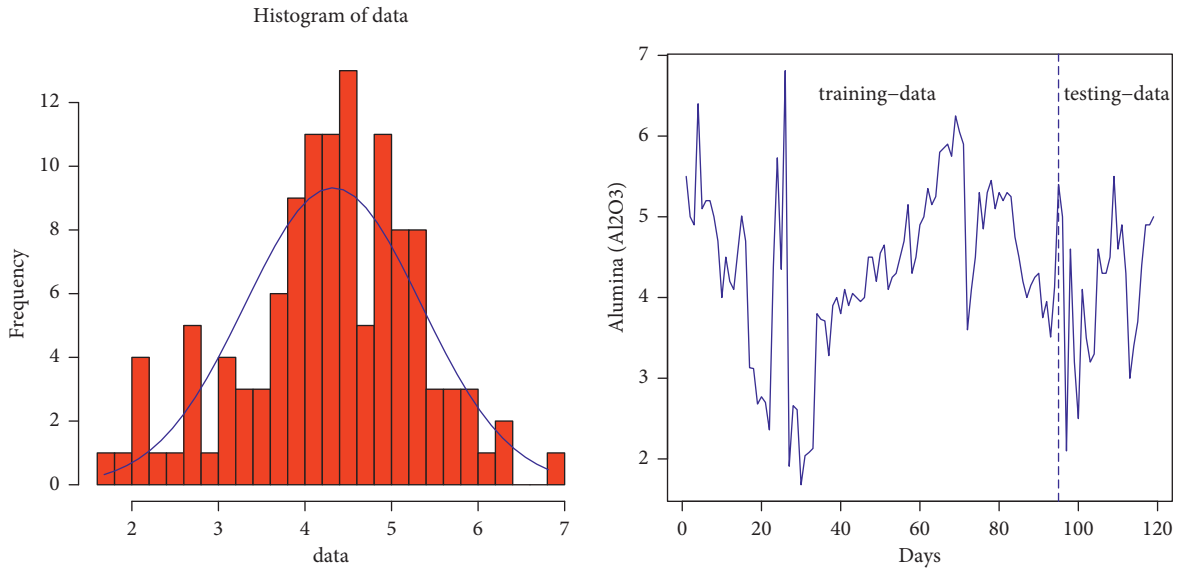

Figure 4: Histogram and line chart of Al_2O_3 data.

be utilized for handling both types of issues, classification, and regression. In general, the RF is a part of the supervised learning class and its output is based on decision trees' forest. The forecast for the RF approach is basically obtained by taking the mean of various trees. A large number of trees in the forest can help to improve the forecasting accuracy and prevent the problem of overfitting. The RF algorithm utilizes the popular procedure of bagging, also known as bootstrap aggregation, in order to train the tree learners. The random sample is taken repeatedly (M time) with replacement of the training set and estimates the trees to each repeated sample [32]. To estimate the RF, we utilize three hyperparameters including number of tress, number of nodes, and sample repetition. The number of tress and nodes is used as 500 and 3, respectively.

5.3. Group Method of Data Handling (GMDH). The GMDH neural network (GMDH-NN) was initially introduced by Ivakhnenko [36] in analyzing complex systems, which incorporates an output and a set of inputs. The core aim of GMDH-NN is simply to formulate a function in a feed-forward network based on second degree transfer function. The productive input variables, the set of neurons and layers within a hidden variable, and the optimal model framework are established automatically in the GDMH algorithm [37]. In our study, we select these parameters through error and trial approach, followed by Peng et al. [38]. The mapping amid target and input variables is carried out via GMDH-NN, and a nonlinear function is so-called Volterra series, given in equation (30) as follows:

$$\widehat{P} = \theta_o + \sum_{m=1}^{h} \theta_m y_m + \sum_{m=1}^{h}\sum_{n=1}^{h} \theta_{m,n} y_m y_n + \sum_{m=1}^{h}\sum_{n=1}^{h}\sum_{s=1}^{h} \theta_{m,n,s} y_m y_n y_s + \ldots. \tag{30}$$

For two variables, the Volterra series can be described in terms of second-degree polynomial in equation (31) as

$$M(y_m, y_n) = \theta_o + \theta_1 y_1 + \theta_2 y_2 + \theta_3 y_1^2 + \theta_4 y_4^2 + \theta_5 y_1 y_2, \tag{31}$$

where $M(y_m, y_n)$ denotes an output of the model, $y_i (i = 1, 2)$ denotes the input variables, and the corresponding weight is shown by θ.

The network neurons are recursively connected to each other through the partial quadratic equation, which reveals the nexus while estimating the unknown parameters using the training data. The key aim of GMDH is to find out the unknown coefficients provided in equation (31), as they demonstrate the least difference amid the actual data and forecasted values. The unknown parameters are computed utilizing the regression tool [39, 40]. Thus, under the rule of principle of least square error, the parameters of each quadratic equation are optimized in the following way:

$$E = \frac{\sum_{j=1}^{N} \left(P_j - W_j\right)^2}{N}. \tag{32}$$

We seek to reduce the squared difference (E) between predicted valued and actual values; in order to achieve an accurate forecast, we have

$$P = B\theta, \tag{33}$$

where P is the response variable, θ is the vector of unknown parameters to be estimated from the data at hand, and B is computed as follows:

$$B = \begin{bmatrix} 1 & \theta_{1p} & \theta_{1q} & \theta_{1p}^2 & \theta_{12}^2 & \theta_{1p}\theta_{1q} \\ 1 & \theta_{2p} & \theta_{2q} & \theta_{2p}^2 & \theta_{12}^2 & \theta_{2p}\theta_{2q} \\ 1 & \theta_{3p} & \theta_{3q} & \theta_{3p}^2 & \theta_{1q}^2 & \theta_{3p}\theta_{3q} \\ . & . & . & . & . & . \\ . & . & . & . & . & . \\ 1 & \theta_{Np} & \theta_{Nq} & \theta_{Np}^2 & \theta_{NQ}^2 & \theta_{Np}\theta_{Nq} \end{bmatrix}. \tag{34}$$

Table 6: The values of the error metrics.

Criteria	SVR	RF	GMDH
RMSE	0.070	0.090	0.233
MAE	0.031	0.064	0.159
AIC	−243.2	−128.8	−114.2

5.4. Out-of-Sample Al_2O_3 Forecasting. The Al_2O_3 data are utilized in this work to assess the predictive capability of different ML algorithms. The data consist of 119 observations. For estimation and prediction, the data set is decomposed into two parts: for model estimation, we use the data points from 1 to 95, and 96 to 119 for evaluating the models' multistep ahead out-of-sample predictive accuracy utilizing the expanding window methods. This study adopts popular three statistical measures, namely, root-mean-square error (RMSE), mean absolute error (MAE), and Akaike information criterion (AIC) to evaluate the forecasting accuracy of ML algorithms. The smaller the values of RMSE, MAE, and AIC, the better the forecast. Mathematically, they can be, respectively, illustrated as

$$MAE = \text{mean}\left(\left|\widehat{P}_t - P_t\right|\right), RMSE = \sqrt{\text{mean}\left(\widehat{P}_t - P_t\right)^2},$$
$$AIC = n\log\left(\frac{sse}{n}\right) + n * k, \tag{35}$$

where n shows the number of observations, sse indicates the sum of squared error, k indicates the number of parameters, P_t represents actual value of Al_2O_3, and $\widehat{P}_t$ represents the predicted values of Al_2O_3.

Figure 4 indicates the Al_2O_3 data trend, which does not follow any particular pattern and is highly uncertain. The Al_2O_3 data are plotted in Figure 4 where the vertical blue dotted line separates the estimation (80 percent) and out-of-sample forecasting (20 percent) parts. The accuracy measures for the Al_2O_3 data are reported in Table 6.

The accuracy measures for the Al_2O_3 data are reported in Table 6. The RMSE and MAE values for ML algorithms include GMDH, SVR, and RF. It can be observed that SVR beats the rival counterparts. The RMSE and MAE values associated with SVR are 0.07 and 0.031, the RF resulted in 0.09 and 0.064, and the GMDH resulted in 0.233 and 0.159, respectively. In addition, according to AIC, the best model is SVR among the all.

6. Concluding Remarks

In this piece of study, a new generalized exponential-X family of distributions is well thought-out as a real-life data model. The attempts in this paper lead to another approach to developing a new statistical model. Employing the proposed model, a new modification of the Weibull model called a new generalized exponential Weibull model is studied. The effectiveness of the new generalized exponential Weibull model is shown by considering the fracture toughness of the Al_2O_3 data set. A statistical product control application of the developed model is also studied by developing the new single acceptance sampling plan based on the NGExp-Weibull distribution. The plan parameters are determined such that both consumer's risk and producer's risk satisfy simultaneously. Some tables are given for industrial application purposes. The developed plan is exemplified by the Al_2O_3 fracture toughness data set, which is well fitted for the proposed NGExp-Weibull. Furthermore, using the same data set, we implemented several ML algorithms including SVR, GMDH, and RF. The out-of-sample forecast accuracy was assessed using three statistical measures of accuracy, namely, the RMSE, MAE, and AIC. After the analysis, we found that the SVR produces a more efficient forecast than the competitor counterparts. The findings clearly reveal that the predictive power of the SVR method is superior in a class of ML algorithms while predicting the Al_2O_3 data.

Data Availability

The data set is given in the main body of the paper.

Conflicts of Interest

The authors declare that there are no conflicts of interest.

References

[1] N. Ghorbani, J. Yazdani-Charati, K. Anvari, and N. Ghorbani, "Application of the Weibull accelerated failure time model in the determination of disease-free survival rate of patients with breast cancer," *Iranian Journal of Health Sciences*, vol. 4, no. 2, pp. 11–18, 2016.

[2] V. H. Moreau, "Using the Weibull distribution to model COVID-19 epidemic data," *Model Assisted Statistics and Applications*, vol. 16, no. 1, pp. 5–14, 2021.

[3] M. Zaindin and A. M. Sarhan, "Modified Weibull distribution," *Applied Sciences*, vol. 11, pp. 123–136, 2009.

[4] C. D. Lai, "Constructions and applications of lifetime distributions," *Applied Stochastic Models in Business and Industry*, vol. 29, no. 2, pp. 127–140, 2013.

[5] S. J. Almalki and J. Yuan, "A new modified Weibull distribution," *Reliability Engineering & System Safety*, vol. 111, pp. 164–170, 2013.

[6] B. Singh, "An additive Perks–Weibull model with Bathtub-shaped hazard rate function," *Communications in Mathematics and Statistics*, vol. 4, no. 4, pp. 473–493, 2016.

[7] Z. Ahmad, E. Mahmoudi, and G. Hamedani, "A class of claim distributions: properties, characterizations and applications to insurance claim data," *Communications in Statistics - Theory and Methods*, vol. 51, no. 7, pp. 2183–2208, 2020.

[8] C. D. Lai and M. Xie, *Stochastic Ageing and Dependence for Reliability*, p. 420, Springer, New York, 2006.

[9] H. Pham and C. D. Lai, "On recent generalizations of the Weibull distribution," *IEEE Transactions on Reliability*, vol. 56, no. 3, pp. 454–458, 2007.

[10] S. Nadarajah, G. M. Cordeiro, and E. M. M. Ortega, "The exponentiated Weibull distribution: a survey," *Statistical Papers*, vol. 54, no. 3, pp. 839–877, 2013.

[11] P. Wais, "A review of Weibull functions in wind sector," *Renewable and Sustainable Energy Reviews*, vol. 70, pp. 1099–1107, 2017.

[12] A. Alzaatreh, C. Lee, and F. Famoye, "A new method for generating families of continuous distributions," *Metron*, vol. 71, no. 1, pp. 63–79, 2013.

[13] S. Nadarajah and S. Kotz, "Strength modeling using Weibull distributions," *Journal of Mechanical Science and Technology*, vol. 22, no. 7, pp. 1247–1254, 2008.

[14] B. Epstein, "Truncated life tests in the exponential case," *The Annals of Mathematical Statistics*, vol. 25, no. 3, pp. 555–564, 1954.

[15] M. Soble and J. Tischendrof, "Acceptance sampling with new life test objectives," in *Proceedings of the 5th National Symposium on Reliability and Quality Control*, pp. 108–118, Philadelphia, Pennsylvania, 1959.

[16] S. S. Gupta and S. S. Gupta, "Gamma distribution in acceptance sampling based on life tests," *Journal of the American Statistical Association*, vol. 56, no. 296, pp. 942–970, 1961.

[17] S. S. Gupta, "Life test sampling plans for normal and log-normal distributions," *Technometrics*, vol. 4, no. 2, pp. 151–175, 1962.

[18] A. Baklizi and A. E. Q. El Masri, "Acceptance sampling based on truncated life tests in the Birnbaum Saunders model," *Risk Analysis*, vol. 24, no. 6, pp. 1453–1457, 2004.

[19] T. R. Tsai and S. J. Wu, "Acceptance sampling based on truncated life tests for Generalized Rayleigh distribution," *Journal of Applied Statistics*, vol. 33, no. 6, pp. 595–600, 2006.

[20] N. Balakrishnan, V. Leiva, and J. Lopez, "Acceptance sampling plans from truncated life tests based on the generalized birnbaum-Saunders distribution," *Communications in Statistics - Simulation and Computation*, vol. 36, no. 3, pp. 643–656, 2007.

[21] R. R. L. Kantam, K. Rosaiah, and G. S. Rao, "Acceptance sampling based on life tests: log-logistic model," *Journal of Applied Statistics*, vol. 28, no. 1, pp. 121–128, 2001.

[22] Y. L. Lio, T. R. Tsai, and S. J. Wu, "Acceptance sampling plans from truncated life tests based on the birnbaum–saunders distribution for percentiles," *Communications in Statistics - Simulation and Computation*, vol. 39, no. 1, pp. 119–136, 2009.

[23] Y. Lio, T. R. Tsai, and S. J. Wu, "Acceptance sampling plans from truncated life tests based on the Burr type XII percentiles," *Journal of the Chinese Institute of Industrial Engineers*, vol. 27, no. 4, pp. 270–280, 2010.

[24] G. S. Rao and R. R. L. Kantam, "Acceptance sampling plans from truncated life tests based on the log-logistic distributions for percentiles," *Economic Quality Control*, vol. 25, no. 2, pp. 153–167, 2010.

[25] S. Balamurali, M. Aslam, and M. S. F. Nezhad, "An acceptance sampling plan under frechet distribution assuring median life," *Research Journal of Applied Sciences, Engineering and Technology*, vol. 06, no. 24, pp. 4519–4523, 2013.

[26] G. S. Rao, K. Rosaiah, K. Kalyani, and D. C. U. Sivakumar, "A new acceptance sampling plans based on percentiles for odds exponential log logistic distribution," *The Open Statistics & Probability Journal*, vol. 7, no. 1, pp. 45–52, 2016.

[27] C. Cortes and V. Vapnik, "Support-vector networks," *Machine Learning*, vol. 20, no. 3, pp. 273–297, 1995.

[28] S. M. Awan, Z. A. Khan, M. Aslam, W. Mahmood, and A. Ahsan, "Application of NARX based FFNN, SVR and ANN Fitting models for long term industrial load forecasting and their comparison," in *Proceedings of the IEEE International Symposium on Industrial Electronics*, pp. 803–807, IEEE, Hangzhou, China, July 2012.

[29] P. S. Yu, T. C. Yang, S. Y. Chen, C. M. Kuo, and H. W. Tseng, "Comparison of random forests and support vector machine for real-time radar-derived rainfall forecasting," *Journal of Hydrology*, vol. 552, pp. 92–104, 2017.

[30] S. Ghosh, "SVM-PGSL coupled approach for statistical downscaling to predict rainfall from GCM output," *Journal of Geophysical Research*, vol. 115, no. 22, Article ID 22102, 2010.

[31] D. Raje and P. P. Mujumdar, "A comparison of three methods for downscaling daily precipitation in the Punjab region," *Hydrological Processes*, vol. 25, no. 23, pp. 3575–3589, 2011.

[32] N. Bibi, I. Shah, A. Alsubie, S. Ali, and S. A. Lone, "Electricity spot prices forecasting based on ensemble learning," *IEEE Access*, vol. 9, pp. 150984–150992, 2021.

[33] M. H. D. M. Ribeiro, R. G. da Silva, V. C. Mariani, and L. d. S. Coelho, "Short-term forecasting COVID-19 cumulative confirmed cases: perspectives for Brazil," *Chaos, Solitons & Fractals*, vol. 135, Article ID 109853, 2020.

[34] C. J. Lu, T. S. Lee, and C. C. Chiu, "Financial time series forecasting using independent component analysis and support vector regression," *Decision Support Systems*, vol. 47, no. 2, pp. 115–125, 2009.

[35] L. Breiman, "Random forests," *Machine Learning*, vol. 45, no. 1, pp. 5–32, 2001.

[36] A. G. Ivakhnenko, "Polynomial theory of complex systems," *IEEE transactions on Systems, Man, and Cybernetics*, no. 4, pp. 364–378, 1971.

[37] I. Ebtehaj, H. Bonakdari, A. H. Zaji, H. Azimi, and F. Khoshbin, "GMDH-type neural network approach for modeling the discharge coefficient of rectangular sharp-crested side weirs," *Engineering Science and Technology, an International Journal*, vol. 18, no. 4, pp. 746–757, 2015.

[38] Z. Peng, F. U. Khan, F. Khan et al., "An Application of Hybrid Models for Weekly Stock Market Index Prediction: Empirical Evidence from SAARC Countries," *Complexity*, vol. 2021, Article ID 5663302, 2021.

[39] R. Walton, A. Binns, H. Bonakdari, I. Ebtehaj, and B. Gharabaghi, "Estimating 2-year flood flows using the generalized structure of the Group Method of Data Handling," *Journal of Hydrology*, vol. 575, pp. 671–689, 2019.

[40] A. Gholami, H. Bonakdari, I. Ebtehaj, S. Shaghaghi, and F. Khoshbin, "Developing an expert group method of data handling system for predicting the geometry of a stable channel with a gravel bed," *Earth Surface Processes and Landforms*, vol. 42, no. 10, pp. 1460–1471, 2017.

Hindawi
Advances in Civil Engineering
Volume 2022, Article ID 4649660, 12 pages
https://doi.org/10.1155/2022/4649660

Research Article

Comparison of Compressive Strength of M30 Grade Concrete with Destructive and Nondestructive Procedures Using Digital Image Processing as a Technique

Sreenath Mahankali[1] **and Giridhar Valikala**[2]

[1]*Department of Civil Engineering, Jawaharlal Nehru Technological University Ananthapuramu, Ananthapuramu 515002, India*
[2]*Department of Civil Engineering, Kandula Srinivasa Reddy Memorial College of Engineering, Kadapa 516003, India*

Correspondence should be addressed to Sreenath Mahankali; mahankalisreenath.m@gmail.com

Received 3 April 2022; Revised 22 May 2022; Accepted 23 May 2022; Published 19 June 2022

Academic Editor: Ravindran Gobinath

Destructive, semidestructive, and nondestructive methods are used to assess the compressive strength of concrete and its substantial mechanical property. In the destructive method, samples of concrete are crushed and treated under compression to determine its compressive strength. As such, the impact is seen on test results like the method of casting and compaction. The tests on concrete become limited in the destructive method and are confined to predict compressive strength, flexural strength, etc. To overcome its limitations and to study concrete matrix, semidestructive and nondestructive test methods came into limelight. Among nondestructive methods, strength prediction can be carried out using Schmidt's rebound hammer test, ultrasonic pulse velocity test, image analysis techniques, radioactive tests, etc. Consequently, an advanced technique to predict the strength of the structural element using digital image processing technique has been introduced, and one can have a glimpse of the enlarged image, which quantifies and is used to assess the strength. The various characteristic features associated with the image help to calculate the strength of the structural element. A high-pixel camera is used to take images of concrete cube samples, and they are analyzed with digital image processing techniques and a tool in MATLab or directly by making use of ImageJ software. In addition, digital image processing techniques are being implemented in various fields such as medical, industrial, remote sensing, and engineering. The present paper proposes to cast $150 \times 150 \times 150$ mm-sized M30 grade concrete cube samples and to study their strength after a period of 7 days and subsequently after 28 days. Destructive and nondestructive methods are used, and the samples are analyzed with digital image processing techniques using ImageJ software. The observed findings are discussed in the paper.

1. Introduction

Concrete is an incredibly vital construction material known for its durability and possesses several attributes that make it the best option for use in buildings and structures. The concrete is widely available, is inexpensive, and enjoys quite significant properties. Destructive, semidestructive, and nondestructive tests are available today to assess the properties of concrete [1]. Certain mechanical properties of concrete can be measured with conventional nondestructive methods such as rebound hammer test and ultrasonic pulse velocity test. In the case of rebound hammer test, after analyzing the data for more than 65 years, it has been concluded that the estimated compressive strength determined with the rebound hammer is higher than that of the destructive procedures [2]. Factors such as compaction, curing environment of concrete, temperature variations, and water-cement ratio influence the rebound index, which ultimately impacts the compressive strength of concrete. Therefore, it is imperative to modify or limit or develop the nondestructive test standards [2]. However, in the case of ultrasonic pulse velocity test, a few factors like its dry state or saturated condition and the type of cement used influence the results to a certain extent [3]. In recent times, structural health monitoring (SHM) became the buzzword in the field of structural engineering, which includes the study of both

concrete and steel. Various NDT techniques such as sweep frequency approach, infrared techniques, camera-based techniques, and sensor techniques are available to monitor the quality of structures of both concrete and steel. Among all, use of sensors is the best approach, which gives caution in case of any invisible damages like cracks and corrosion of bars and further monitors the strength of the structures [4, 5].

Different types of NDT techniques can be performed on various elements of construction, but all methods will not arrive at accurate results. For instance, the ultrasonic pulse velocity test and acoustic test are more suitable and accurate for historical stone masonry; radar methods and penetrating radiation methods may be used in case of brick material; and the ultrasonic pulse velocity test may be used for concrete [6]. Assessment of strength is influenced by hardness, resistance against penetration, rebound capacity, and ability to transmit ultrasonic pulses and X-rays. At present, ANN (artificial neural network) and IP (image processing) are in use to solve engineering problems, and as noticed here, there exists high correlation between ANN, IP, and actual test results, where the variance is between 97.18 and 99.87%. It is therefore proved that combination of the above techniques will always lead to satisfactory outcomes [7]. The difference between the test results offered by destructive and nondestructive tests declined within 28 days. In the ultrasonic pulse velocity test, results declined with respect to the increase in W/C ratio because it increases porosity in the concrete samples and the dynamic modulus of elasticity decreased with an increase in W/C ratio [8]. NDT techniques like rebound hammer and ultrasonic pulse velocity tests were conducted in nuclear power plants where High Strength Concrete whose Compressive Strength was more than 40 MPa, and the results were acceptable with the strength correction factor [9]. In recent times, rebound hammer results have become accurate by applying artificial neural networks in predicting compressive strength of in situ concrete [10].

Digital image processing is one of the important areas of electronics and computer science engineering as the two significant tech brothers revolutionized all the fields, and with digitalization, many developments are being noticed. Growth of digital image processing has led to numerous innovations in the area of digital imaging. In reality, many engineering fields are predominantly using analog techniques and slowly paving way to advanced digital imaging. Civil engineering is one of the oldest engineering sectors, and entwined with digital technology, it has been producing unpredictable results. Recently, many inventions were proposed in civil engineering with digital image processing techniques [11]. The compressive strength of concrete, especially concrete made up of cement replacement materials (CRMs), i.e., fly ash and silica fumes, is predicted with image processing and artificial neural networks (ANNs) modeling. The predicted compressive strength is found to be very accurate up to 98.65% in destructive tests [12]. The image processing algorithms were proposed and applied to assess the strength, and the error rate was about a mere 1-2% [13]. Digital image processing can be used to detect the construction progress by adopting a suitable algorithm, which can detect the structural elements and their defaults at site [14]. In building materials, digital image processing techniques were applied to determine the quality of the marble stone in industry. In marble industry, quality, texture, and basic composition of stone can be verified and classified through image processing techniques [15]. Image analysis techniques are used to decide the strength and durability of the age-old historic constructions. Historic stones were captured on the digital camera, and the images were analyzed on the system using digital image processing techniques. The results were compared using the direct compression test. The two test results were similar, with an error margin of + -2% [16]. In GIS and remote sensing, images of a certain large area are captured using satellites and digital image techniques are applied to the images to generate digital thematic maps [17].

In case of tests on coarse aggregate, the shape of coarse aggregate can be determined with digital images. The coarse aggregate is spread over an area, and digital images are taken; furthermore, the images are analyzed to determine the particle size of the coarse aggregate. The flakiness of coarse aggregate can also be determined by the same process [18, 19]. The cement content in concrete, which plays a key role in attaining good compressive strength, can be predicted by image analysis using ImageJ software, which helps in estimating the chlorine content in cement [20]. The compressive strength of concrete can also be predicted by using digital image processing techniques; the outer surface of the concrete is captured on a high-resolution digital camera, images are converted to greyscale, and the histogram of the image is generated. By analyzing this picture using the MatLab technique, the compressive strength of the concrete is predicted and compared with that of the conventional method [21]. Besides concrete, digital image processing techniques are used even in other specializations of civil engineering, like environmental engineering, in predicting pH value and settling velocity of water [22, 23].

Accordingly, the above case studies helped the authors to progress toward digital image processing techniques to be used in predicting the compressive strength of concrete along with conventional destructive and nondestructive procedures. This paper aims to study compressive strength property of M30 grade concrete with nondestructive tests such as rebound hammer test, SonReb method (combination of rebound number and ultrasonic pulse velocity), and a new approach digital image processing as one of the techniques, and the results are compared with the destructive procedure. Pros and cons of the nondestructive tests and the suitability of using digital image processing techniques in predicting the compressive strength of concrete have been discussed. The test procedures are as follows.

2. Materials

For the experimentation procedures, ordinary Portland cement of grade 53 is used. Preliminary experiments on cement were conducted, and the initial and final settings of

(a) (b)

(c)

Figure 1: (a) Compression testing machine. (b) Schmidt's rebound hammer test apparatus with a digital display. (c) Pundit's ultrasonic pulse velocity test.

cement were 60 and 480 min, respectively. Standard consistency of the cement sample is 32% with a fineness of 3.5%. All the properties of cement are satisfactory as per Indian Standard Code 12269-1987 [24]. Locally available sand has been procured for experimentation, and it is confirmed to Zone-II according to Table 4 of Indian Standard Code 383-1970 [25]. The specific gravity test is conducted on the fine aggregate, and the result is found to be 2.63. Locally available crushed granite is used as the coarse aggregate in the experimentation, and its specific gravity is 2.62. Potable water from the local sources, which is suitable for mixing and curing of concrete, has been used for experimentation.

3. Analyzing Digital Images

In recent era, drastic changes have been taking place in the digital world. Even in the civil engineering field, analysis of digital images has replaced the regular conventional method of assessment with interdisciplinary studies. Conventional images or photos have to be captured during the casting and testing, but these cannot be analyzed properly. Digital images can be captured during the casting and testing of concrete samples, analyzed, and used for various purposes like prediction of strength, study of bonding, study of ITZ (interfacial transition zone), and finding permeability of concrete. Every system has a basic component from which the whole system is made up of, and just like atom is the basic unit of matter, "pixel" is the basic component of the digital image. A digital image is a combination of number of unit cells called "pixels." Usually, digital camera specifications are defined in "megapixels." For example, the digital camera has specifications of 1 megapixel which implies that the image, which is captured, consists of 1 mega (10^6) number of pixels, to say that the image has 1 million of pixels and each pixel has a pixel number. For a color image, there will be RGB colors. Each color has 8 bytes (red = 2^8, green = 2^8, and blue = 2^8). The pixel number varies from 1 to $2^8 \times 2^8 \times 2^8$, i.e., from "0" to "16777215" (numbering starts from "0" onwards), but analyzing such a large number of data may be tedious and conclusions cannot be drawn in profound form. So, the color image must be transformed to greyscale, and after this conversion, the pixel number varies from 1 to 2^8. The pixel number can vary from 0 to 255. As a rule, "0" value indicates black and "255" indicates white. Grey tones with different shades are formed among these values.

Steps for analyzing the image using ImageJ software:

(i) Opening ImageJ software

(ii) Adding or uploading the digital image to the software

(iii) Cropping the image by cutting down the unnecessary edges of the image

(iv) Converting the RGB color image into greyscale image

(v) Analyzing the image and extracting the histogram of the image

Table 1: Classification of concrete by the ultrasonic pulse velocity test [28].

Range of ultrasonic pulse velocity results (km/s)	Classification of concrete
>4.5	Excellent
3.5–4.5	Good
3.0–3.5	Medium
<3.0	Doubtful

4. Methodology to Determine the Compressive Strength of Concrete

4.1. Destructive Tests. The destructive test procedure is one of the oldest and conventional methods to determine the various strengths and study the quality of concrete after destruction. Mechanical properties of concrete can be determined by destructive tests such as compressive strength test, splitting tensile strength test, and flexural strength test, which are regular type of destructive tests on concrete. Among all these tests, compressive strength test is frequently performed on concrete cubes and cylinders. The analog testing procedure consists of casting cubes or cylinders of different grades of concrete samples and curing them in a water tank. The sample is tested using the compression test machine (CTM) shown in Figure 1(a), and the uniform rate of loading is applied until the specimen crushes.

4.2. Nondestructive Tests. The nondestructive test implies the prediction of properties of concrete without any damage or destroying the specimen sample or structure, and there are different types of tests based on the principles. Some of the NDT techniques are Schmidt's rebound hammer test, Pundit's ultrasonic pulse velocity test, combined ultrasonic-rebound hammer test, and digital image processing method. The advantages of the NDT techniques are as follows:

(i) Man force required for NDT techniques is very less compared to destructive tests

(ii) Preparatory works in destructive testing require more labor than in NDT

(iii) No portion or very small portion of the structure is damaged in NDT compared to destructive testing

(iv) Probability of structural damage is very low, which may cause the need for reinforcement

(v) In special cases like thin walls and dense reinforced concrete structures, sample extraction in destructive test has no scope, whereas NDT can overcome such hurdles in reality

(vi) Handy tools and less-expensive equipment may be used for nondestructive tests compared to destructive tests

However, the advantages are valuable only if those results lead to accuracy in reality [26].

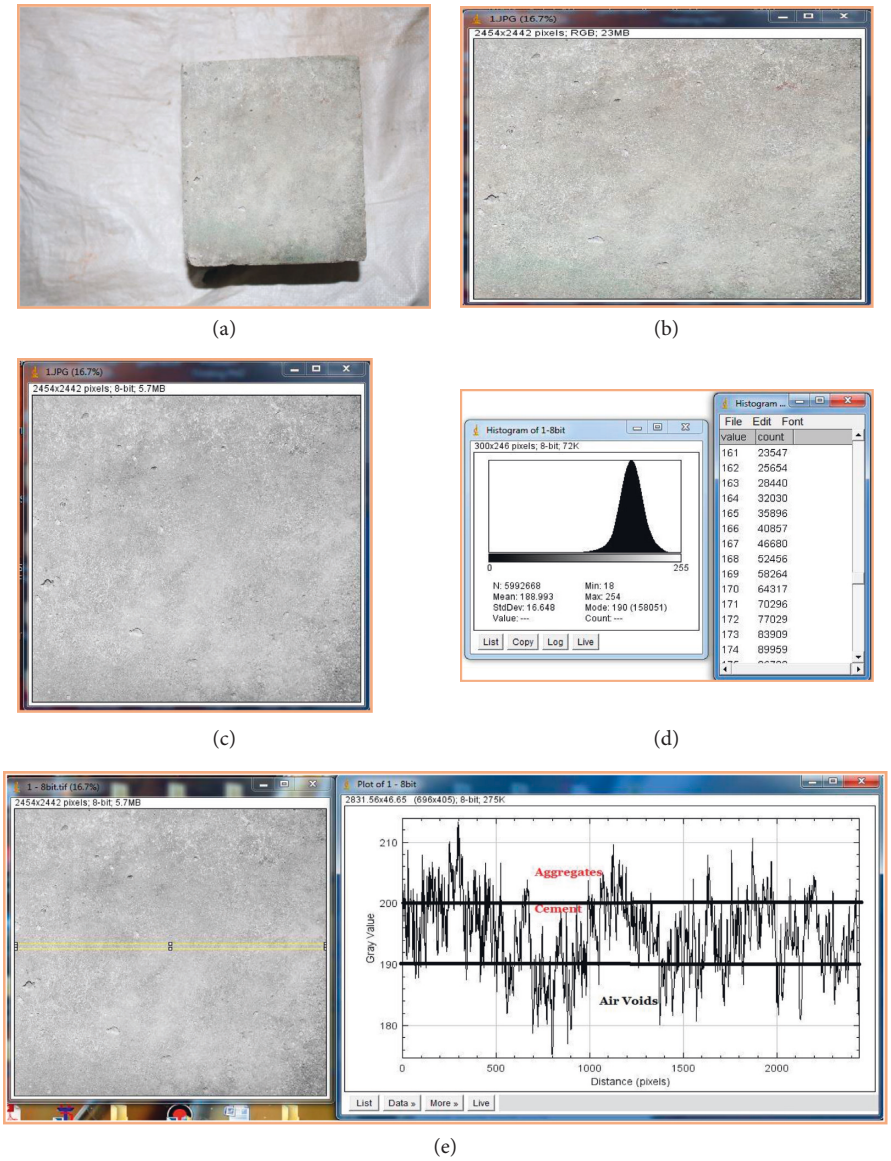

FIGURE 2: Digital image of (a) a concrete cube, (b) the concrete cube after cropping in RGB color, (c) the concrete cube after converting into greyscale, (d) the histogram, and (e) the profile of the rectangular section of the cube surface.

4.2.1. Schmidt's Rebound Hammer Test. Among all the nondestructive tests on concrete, Schmidt's rebound hammer test is the most commonly used test carried out on concrete, as shown in Figure 1(b). The rebound hammer test directly relates to the compressive strength of concrete, and the test results can be obtained instantly. The basic principle behind this test is the rebound nature of an elastic mass (concrete in the present scenario), which depends on the hardness of the surface against which the mass impinges. The energy which is absorbed by the concrete is directly related to its compressive strength property. Even though the test procedure is simple, the test involves complex problems of impact and is associated with stress-wave propagation [26].

4.2.2. Pundit's Ultrasonic Pulse Velocity Test. The ultrasonic pulse velocity method, as shown in Figure 1(c), is one of the NDTs (nondestructive tests) conducted on concrete specimens to determine the mechanical properties of concrete without any destruction. In this method, the time taken by ultrasonic pulse to pass through the concrete is recorded, which ultimately gives the velocity of the ultrasonic pulse in that particular concrete specimen. This method is a litmus test for any concrete specimen, by which one can determine whether the concrete has good properties or not in terms of density, homogeneity, uniformity, etc. In this method, ultrasonic waves are passed through the concrete cube specimen and ultrasonic waves or sound waves, which travel through a medium having frequency more than 20000 Hz, cannot be detected by human ear. Humans can hear sounds with frequency ranging from 20 Hz to 20,000 Hz. The ultrasonic pulse velocity test is more significant as it studies the internal structure of the concrete specimen. The results of

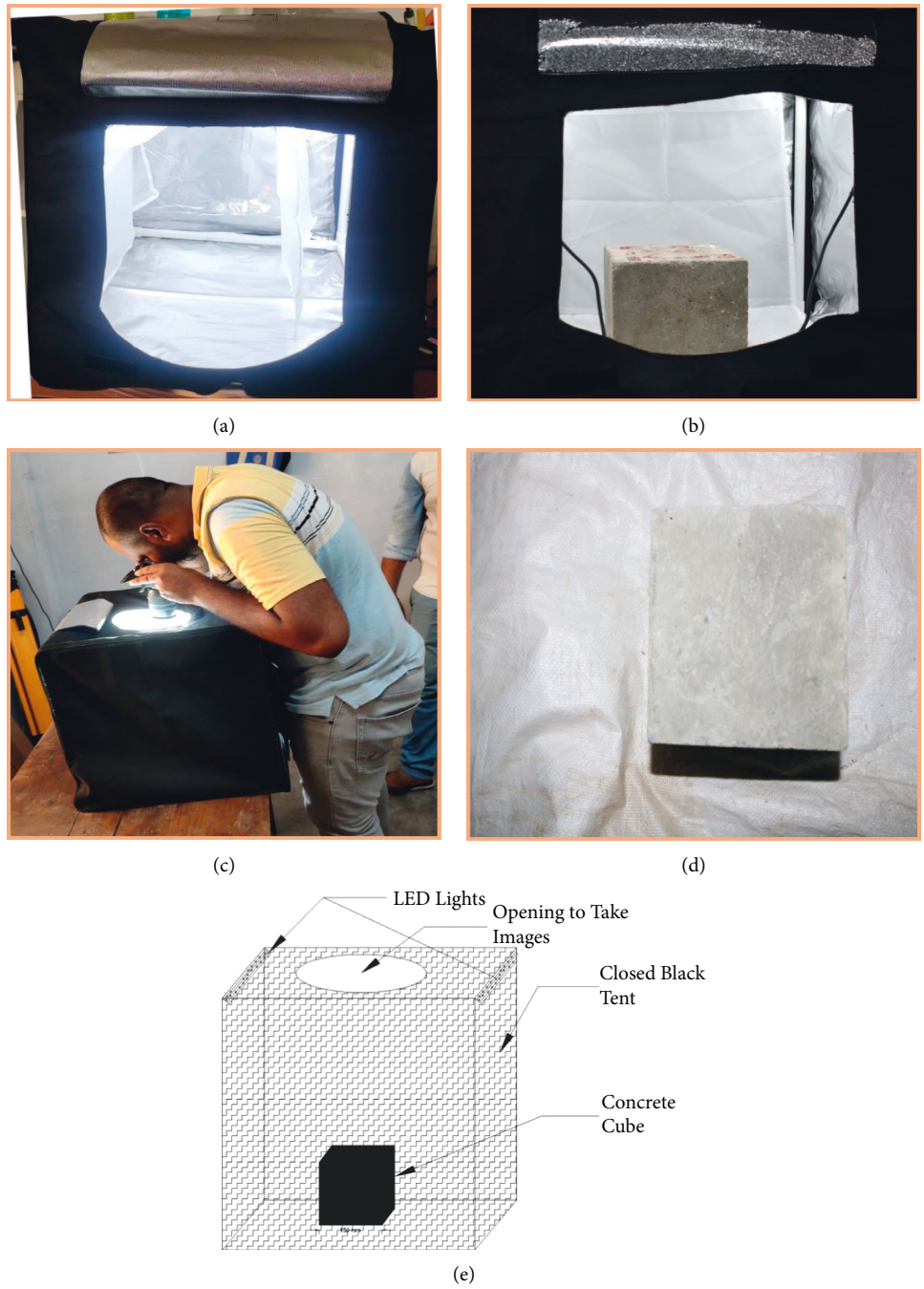

Figure 3: (a) Test setup to take digital images: (b) concrete cube after placing in the setup; (c) capturing images of concrete cube surfaces from the top; (d) the digital image captured; (e) block diagram of the test setup for capturing digital images.

ultrasonic pulse velocity test reflect whether the compaction of concrete is done properly or not at the time of casting. Poor results imply that a honeycomb type of structure is formed in the concrete.

(1) *Analysis of Ultrasonic Pulse Velocity Test Results.* According to the Indian Standard Code 13311 (Part 1) 1992 [27], based on the range of results to justify its quality, the concrete can be classified as excellent, good, medium, and doubtful based on ultrasonic pulse velocity result as shown in Table 1 [28].

4.2.3. SonReb Method. The SonReb method is one of the important methods used to predict the compressive strength of concrete. The name itself implies that the method is a combination of both ultra"Son"ic pulse velocity and "Re-b"ound hammer tests. The principle involved in the SonReb method is rebound number (RN) and the ultrasonic pulse velocity as input and the compressive strength as output. The SonReb method is significant as it is a combination of both the rebound hammer test and ultrasonic pulse velocity test. The rebound hammer test gives the strength of the concrete

specimen near the surface, whereas the ultrasonic pulse velocity test reflects the interior properties of concrete. So, by considering various correction factors, the SonReb method achieves accuracy.

Many authors contributed different empirical formulas to correlate the compressive strength of concrete with rebound number (RN) and ultrasonic pulse velocity. There are numerous types of relationships, such as linear, polynomial, power, exponential, and logarithmic, based on which empirical formulas are developed [29–31]. The following are some of the most reliable equations among all methods [32]:

$$f_{ck} = 7.695 \times 10^{-11} \times (RN)^{1.4} \times (V)^{2.6}, \quad (1)$$

$$f_{ck} = 1.2 \times 10^{-9} \times (RN)^{1.058} \times (V)^{2.446}, \quad (2)$$

$$f_{ck} = 0.0286 \times (RN)^{1.246} \times (V)^{1.85}. \quad (3)$$

f_{ck} = compressive strength of concrete (N/mm^2), RN = rebound number, and V = ultrasonic pulse velocity (in m/s).

Based on the given three formulations, another formulation is proposed based on Technical Standards of Tuscany region, which is the mean value calculated by the three formulations and the mean value is considered as SonReb results in this paper.

4.2.4. Digital Image Processing Method. The digital image processing test is one of the latest techniques to determine the compressive strength of the concrete without any destruction. There are several relationships between the compressive strength and all the other mechanical properties of concrete. In this technique, the concrete surface is captured with in a closed setup to avoid errors of light reflection by using a high-resolution digital camera as shown in Figure 2(a). A digital image, which has been captured, is analyzed with MATLab, SCILab, ImageJ etc., for digital image analysis processing. The image is to be cropped up to the clear surface cutting down the unrelated things in the background as shown in Figure 2(b). As explained above, a digital image is a grouping of very small units called pixels. Each pixel has a pixel value depending upon light intensity while light rays strike the object. As specified in the earlier description, a color image has a very large variation of data and in order to have feasibility to analyze data, the image should be converted into greyscale as shown in Figure 2(c) [16]. After conversion into grey scale, the image is analyzed using the appropriate software and histograms as shown in Figure 2(d). A histogram is the graphical representation of the number of pixels in the whole image representing the same pixel value. By histogram data, 0 = 0 pixels, 1 = 2 pixels, 2 = 5 pixels... 255 = 3254 pixels are extracted. Then, the threshold pixel number is to be determined for air voids, cement, and aggregates. For this purpose, the grey value of a small section is to be obtained across the concrete cube surface image as shown in Figure 2(e). So, the concrete composition of air voids, cement, and aggregates in percentages is obtained. By these values, compressive strength of concrete is determined by the application of empirical formulas, which were obtained by previous researchers by conducting numerous experiments [21, 33].

$$f_{ck} = \frac{(\text{aggregate})^{0.021}}{(\text{cement})^{-1.004}} - (\text{air voids})^{-1.251}. \quad (4)$$

f_{ck} = compressive strength of concrete in N/mm^2.

(1) Flowchart for 'Prediction of Compressive Strength of Concrete by Digital Image Processing Technique

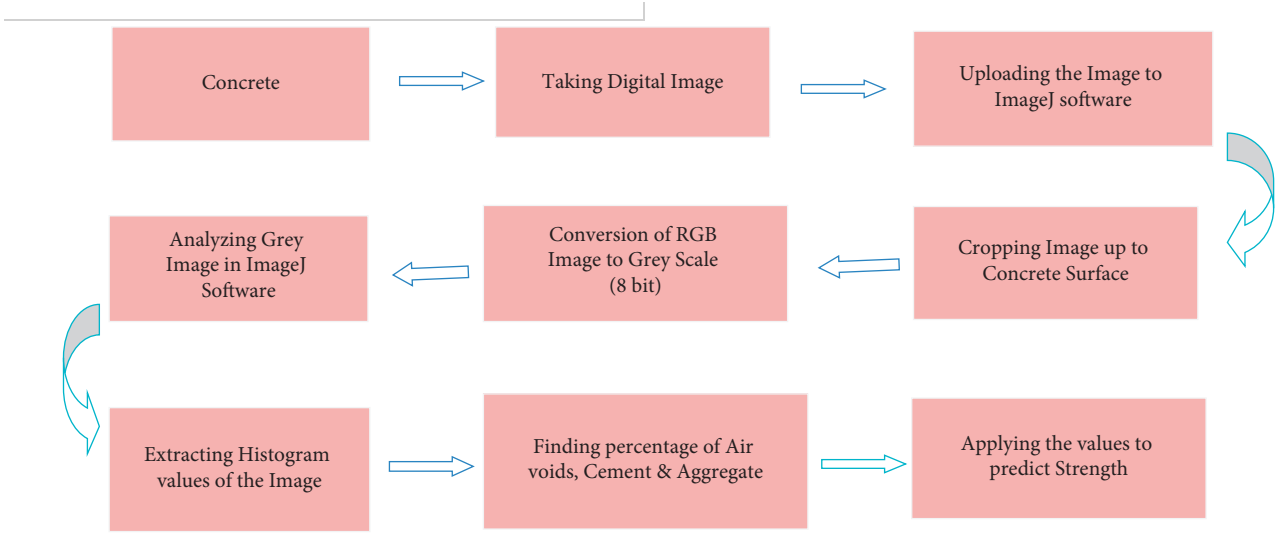

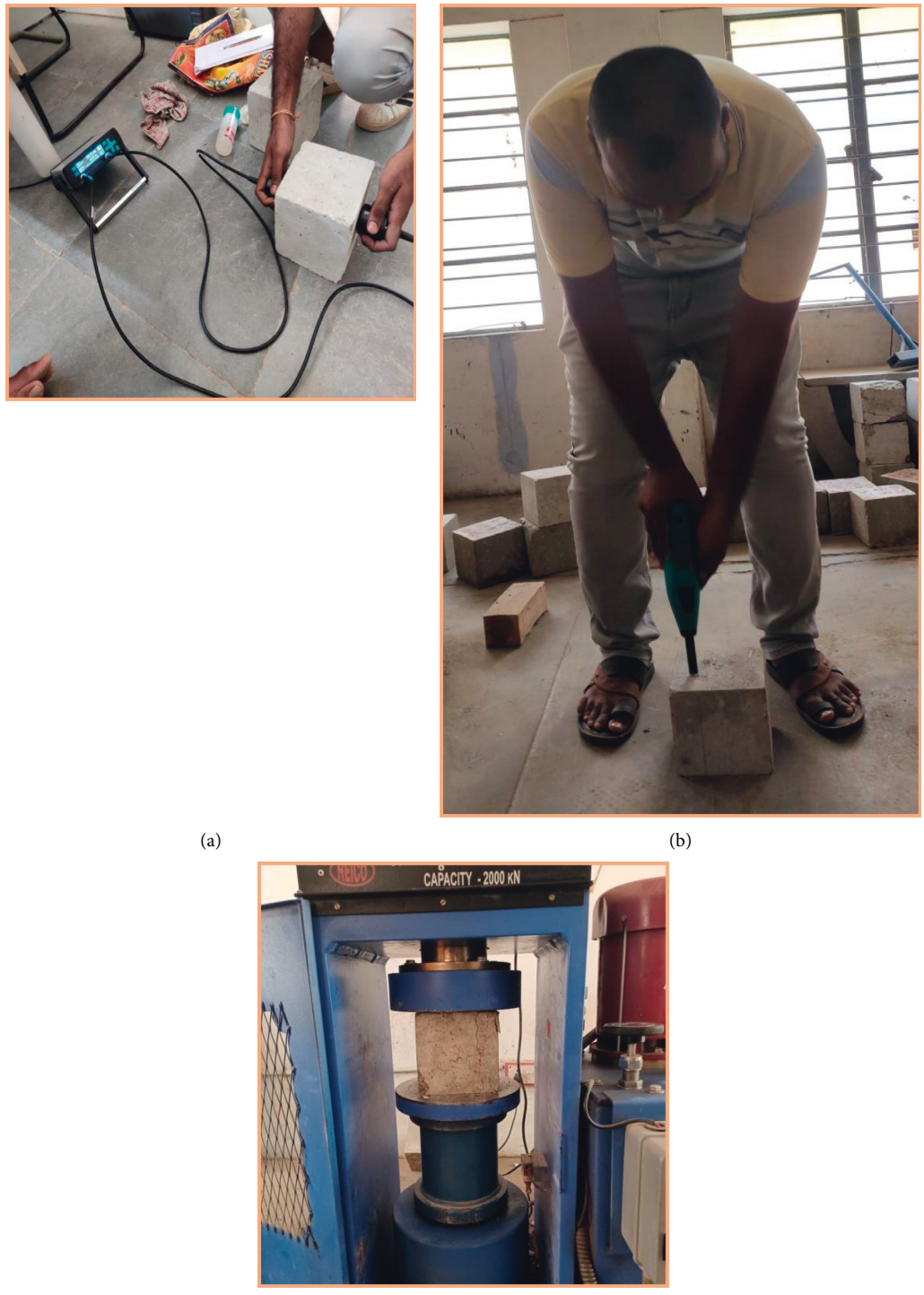

(a) (b) (c)

Figure 4: Testing of concrete cube samples: (a) ultrasonic pulse velocity, (b) rebound hammer test, and (c) crushing under CTM.

5. Experimental Program

5.1. Design Mix. According to the Indian Standard Code 10262–2009 [34], a mixed design is prepared for M30 grade concrete with proportion 0.45 : 1 : 1.46 : 2.26 (water: cement: fine aggregate: coarse aggregate) by weight. To obtain better workability at the time of mixing of concrete, graded aggregates are used in two fractions as 60% of 20 mm and 40% of 12.5 mm of coarse aggregate in concrete composition.

5.2. Sample Preparation and Curing. Weigh batching is followed as per the mixed design proportion of M30 grade concrete, and twelve cube samples of size 150 × 150 × 150 mm are cast. As per the Indian Standard Code 456-2000 [35], six

Table 2: Comparison of compressive strength obtained by destructive and nondestructive tests.

Sample no.	No. of days of curing	Compressive strength by CTM (in N/mm^2)	Rebound hammer		Ultrasonic pulse velocity test	Compressive strength as per the SonReb method	Image analysis
		f_{ck} in N/mm^2	RN	f_{ck} in N/mm^2	Velocity (m/s)	f_{ck} in N/mm^2	f_{ck} in N/mm^2
1	7 days	20.444	21	14.5	4545.5	21.72	22.95
2	7 days	17.778	20	14.0	4622.5	21.27	16.90
3	7 days	19.555	20	14.0	4713.5	22.25	19.49514
4	7 days	19.111	21.5	16.5	4651.5	23.56	18.82616
5	7 days	18.889	23.5	18.5	4587	25.41	17.96898
6	7 days	19.555	24	19.5	4492	24.84	25.56
	Average	**19.222**		**16.166**		**23.175**	**20.28**
7	28 days	32.444	30.5	29.00	4833.5	39.36	27.26081
8	28 days	36.889	30.0	28.00	4792	37.81	32.54504
9	28 days	28.444	25.50	22.50	4870	32.20	26.6878
10	28 days	37.7778	24.00	19.50	4818	29.19	33.91921
11	28 days	39.111	27.00	24.00	4757	32.70	34.9321
12	28 days	31.111	27.50	25.00	4788	33.95	31.1603
	Average	**34.298**		**24.40**		**34.20**	**31.08**

$*f_{ck}$ = compressive strength of concrete in N/mm^2.

Table 3: Comparative difference between destructive and nondestructive tests.

No. of curing days	Destructive test	Nondestructive tests					
		Rebound hammer		SonReb method		Image analysis	
			% diff		% diff		% diff
7 days	19.222	16.166	**−15.89%**	23.175	**+20.56%**	20.28	**+0.055%**
28 days	34.298	24.40	**−28.85%**	34.20	**−0.0028%**	31.08	**−9.382%**

*% diff indicates the percentage difference between average compressive strength of destructive and particular nondestructive tests.

samples were tested at the age of 7 days of curing and the other six samples were tested at the age of 28 days of curing.

6. Testing Procedures

As mentioned in the methodology and as per Indian Standard Code 456-2000 [34], after the completion of the curing period, the samples were tested in CTM by the destructive nature and the results are tabulated in Table 2. Before destruction, NDT were completed and carried over to the destruction of concrete cube samples.

6.1. Nondestructive Test Procedures. The given steps were followed during the test procedure.

6.1.1. Capture of Digital Images and Analysis. Digital images of test samples are to be captured in a separate environment having no other effects which may influence the histogram of the image. For this purpose, a special environment is created as shown in Figure 3(a). The special environment consists of a tent having opening on the side and top and two LED lights to have equal focus while taking images. The cured specimens are shifted into the tent and placed on a flat surface as shown in Figure 3(b). Digital images are taken on all six sides of the cube specimen in order to avoid and nullify errors, as shown in Figure 3(c). As explained in the methodology, the captured images are analyzed using ImageJ software. Figure 3(d) shows the digital image of the concrete cube sample after 28 days of curing.

6.1.2. Schmidt's Rebound Hammer Test. After capturing digital images of the specimens, samples are to be examined by Schmidt's rebound hammer test. It works on the principle of the surface hardness of the concrete sample. Hence, Schmidt's rebound hammer is to be handled carefully to extract the rebound number (RN) of the sample. In the test procedure, it is mandatory to select a better surface on the concrete for the testing operation. A fixed amount of energy is applied on the concrete surface by pushing the hammer against the concrete surface. The plunger through which the energy is applied on the concrete must be permitted to strike perpendicularly on the test surface. There should not be any inclination to the surface of the sample during the application of plunger as any slight angle of inclination may also influence results. After the application of energy, the rebound hammer is locked by pressing a button provided and the rebound number as generated on the rebound hammer is noted as shown in Figure 4(b). There is no direct relation between the hardness of the surface to the compressive strength of concrete, but an empirical relation is developed as determined by previous research, where the compressive strength is determined by establishing a relationship between the rebound number (RN) and the compressive strength of concrete. The test is repeated to avoid mistakes

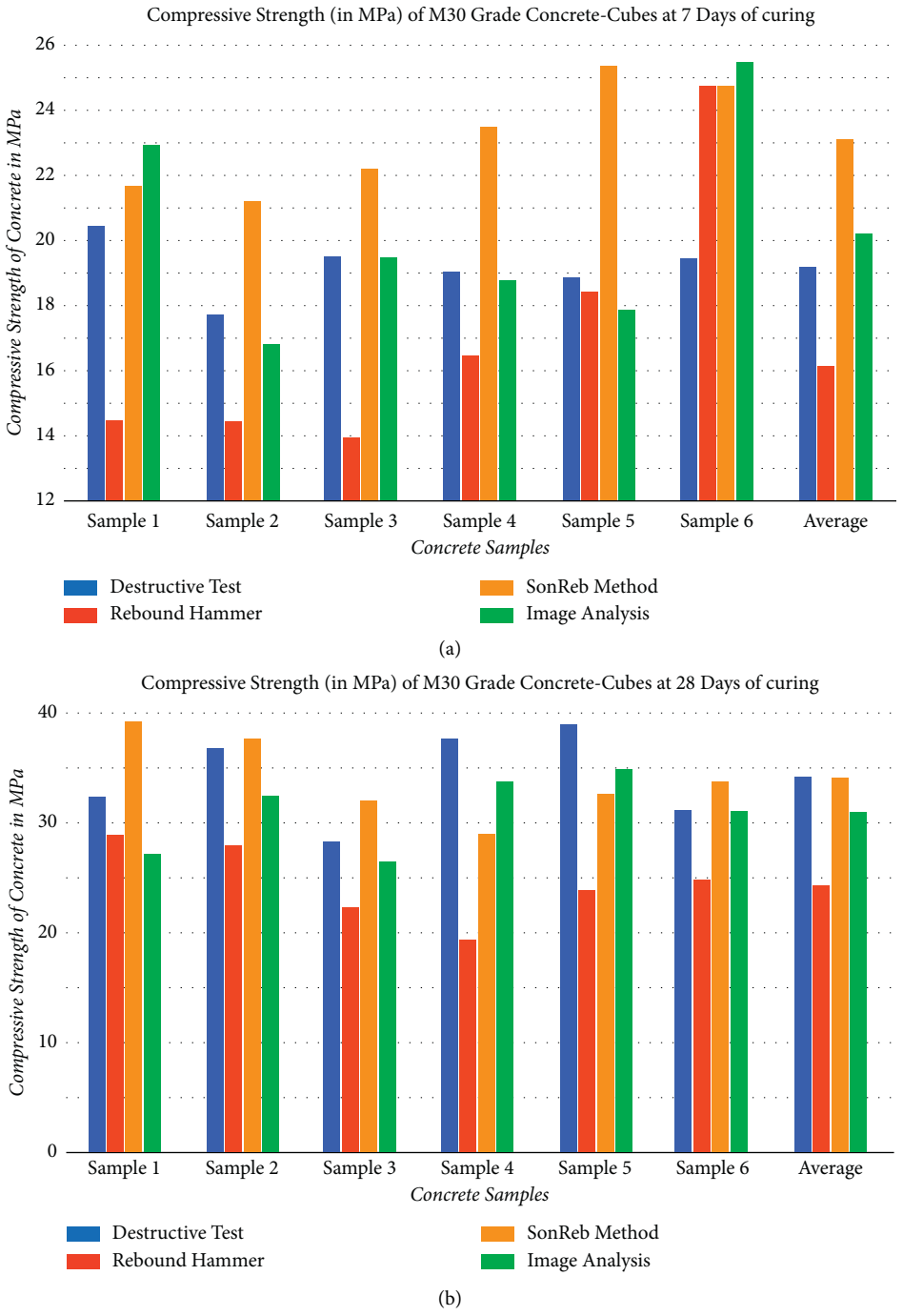

Figure 5: Results of compressive strength (in MPa) of M30 grade concrete obtained by destructive method, rebound hammer test, SonReb method, and digital image processing. (a) 7 days of curing and (b) 28 days of curing.

and errors in the process of testing and to reach the accurate compressive strength of concrete [36].

6.1.3. Pundit's Ultrasonic Pulse Velocity Test. For the ultrasonic pulse velocity test, Pundit's ultrasonic pulse velocity testing machine is used, which consists of an electrical pulse generator and two transducers having one transmitting transducer and another receiving transducer. The amplifier, an electromagnetic timing device, is used to determine the velocity of wave propagation. Meanwhile, the concrete specimen cube is placed on the table surface. Two transducers are to be rubbed initially with grease or petroleum jelly or kaolin or liquid soap. The concrete surface is made smooth at the place of application of transducers, and ultrasonic waves are propagated through the concrete specimen from the transmitter transducer to the receiver transducer. The sound waves propagate through the concrete medium, and the time taken for travelling is noted down to be displayed on the electronic timing device

attached to the apparatus. The length of the specimen and time are noted down from the device. The velocity of the propagating waves is calculated and recorded as shown in Figure 4(a). There is no direct relation between compressive strength of concrete and ultrasonic pulse velocity, but the SonReb method correlates rebound hammer results with ultrasonic pulse velocity results and is helpful in determining the compressive strength. Results of the SonReb method are calculated as per the formula specified in equations (1)–(3), and their average values are presented in Table 2.

6.2. Destructive Test Procedures. Destructive testing conducted on the compressive testing machine (CTM) is as per Indian Standard Code 516 [37]. Samples are to be tested by using CTM, and the compressive strength has been tabulated in Table 2. The crushed sample is shown in Figure 4(c).

7. Results and Discussion

After curing for 7 and 28 days, six samples of M30 grade concrete cube specimens have been casted and tested for the study. All types of tests as discussed above are conducted step by step, and the results are summarized and presented in Tables 2 and 3. Graphs comparing the compressive strength of concrete (f_{ck}) cubes in all the test procedures of 7 days and 28 days are shown in Figures 5(a) and 5(b).

8. Conclusions

Interlinking of different applications as discussed in the present study has proved to save time and money, and precise incremental results have been obtained. Civil engineering is one of the oldest branches of engineering, and application of other engineering branches into civil engineering has been shown as a new approach to solve many civil engineering problems. There are many conventional experiments in civil engineering, which can be interconnected technologically by using digital image processing techniques, a solution for numerous problems. In the present study, twelve M30 grade concrete samples are casted. Of the twelve, six samples are tested at the age of 7 days of curing and the rest of the samples are tested at the age of 28 days. Conclusions drawn based on the results of destructive and NDT procedures are as follows:

(1) The rebound hammer test, which works on the principle of surface hardness, is the most effective procedure for testing samples at 7 days compared to 28 days.

(2) Gradual increase in the results of ultrasonic pulse velocity can be seen from 7 days to 28 days samples. It may be because of the reaction occurring in the C-S-H gel from 7 to 28 days.

(3) The SonReb method is one of the finest methods interlinking both RBH and ultrasonic pulse velocity results with compressive strength and bestows accurate results when results are considered in average.

(4) Digital image processing techniques are helpful in the prediction of the compressive strength of concrete by analyzing the surface images.

(5) "ImageJ" software, one of the free software packages, is user-friendly and most flexible to extract histograms of digital images.

(6) A unique pattern is observed in all histograms when grouped as 7 days and 28 days.

(7) Relationship (4) used for predicting the compressive strength of concrete by digital image processing is satisfactory in obtaining results.

(8) Compressive strength results obtained by digital image processing techniques are almost similar to the results obtained by destructive procedures and SonReb method.

(9) The average compressive strength of concrete samples at 28 days is almost equal to the results of the SonReb method with a difference of −0.0028% and results of the image analysis method with −9.382% difference.

(10) The image analysis method fetches accurate results as it studies the concrete surfaces to the maximum extent using modern digital image processing techniques.

(11) Digital image processing techniques can be applied to higher grades of concrete cube samples in order to generalize the procedure towards emerging of a new nondestructive test of concrete.

Data Availability

Necessary data are included within the manuscript.

Conflicts of Interest

The authors declare that they have no conflicts of interest regarding the publication of this paper.

Acknowledgments

The authors acknowledge JNTU Ananthapuramu and the KSRM College of Engineering for helping them during the research and preparation of the manuscript.

References

[1] K. Schabowicz, "Nondestructive testing of materials in civil engineering," *Materials*, vol. 12, no. 19, p. 3237, 2019.

[2] H. R. Kumavat, N. R. Chandak, and I. T. Patil, "Factors influencing the performance of rebound hammer used for nondestructive testing of concrete members: a review," *Case Studies in Construction Materials*, vol. 14, Article ID e00491, 2021.

[3] J. P. Godinho, T. F. De Souza Júnior, M. H. F. Medeiros, and M. S. A. Silva, "Factors influencing ultrasonic pulse velocity in concrete," *Revista IBRACON de Estruturas e Materiais*, vol. 13, no. 2, pp. 222–247, 2020.

[4] P. Kot, M. Muradov, M. Gkantou, G. S. Kamaris, K. Hashim, and D. Yeboah, "Recent advancements in nondestructive

testing techniques for structural health monitoring," *Applied Sciences*, vol. 11, no. 6, p. 2750, 2021.

[5] M. Mohammadreza Hamidian, "Application of Schmidt rebound hammer and ultrasonic pulse velocity techniques for structural health monitoring," *Scientific Research and Essays*, vol. 7, no. 21, 2012.

[6] A. Hussain and S. Akhtar, "Review of nondestructive tests for evaluation of historic masonry and concrete structures," *Arabian Journal for Science and Engineering*, vol. 42, no. 3, pp. 925–940, 2017.

[7] G. Dogan, M. H. Arslan, and M. Ceylan, "Concrete compressive strength detection using image processing based new test method," *Measurement*, vol. 109, pp. 137–148, 2017.

[8] M. Jedidi and M. Kaouther, "Destructive and non- destructive testing of cConcrete structures," *Jordan Journal of Civil Engineering*, vol. 8, pp. 432–441, 2015.

[9] M. Ju, K. Park, and H. Oh, "Estimation of compressive sStrength of high sStrength cConcrete using non-destructive technique and cConcrete core sStrength," *Applied Sciences*, vol. 7, no. 12, p. 1249, 2017.

[10] Y. R. Wang, Y. L. Lu, and D. L. Chiang, "Adapting artificial intelligence to improve in situ cConcrete compressive sStrength estimations in rebound hammer tests," *Frontiers in Materials*, vol. 7, p. 365, 2020.

[11] A. A. Salunkhe, R. Gobinath, S. Vinay, and L. Joseph, "Progress and trends in image processing applications in civil engineering: opportunities and challenges," *Advances in Civil Engineering*, vol. 2022, pp. 1–17, Article ID 6400254, 2022.

[12] M. I. Waris, J. Mir, V. Plevris, and A. Ahmad, "strength-Predicting compressive strength of CRM samples using Image processing and ANN," *IOP Conference Series: Materials Science and Engineering*, vol. 899, no. 1, Article ID 012014, 2020.

[13] M. Baygin, S. G. Ozkaya, and M. A. Ozdemir, "A new approach based on image processing for measuring compressive sStrength of structures," *International Journal of Intelligent Systems and Applications in Engineering*, no. Special Issue, pp. 21–25, 2018.

[14] Y. Wu and H. Kim, "Digital imaging in assessment of construction project progress," in *Proceedings of the 21st International Symposium on Automation and Robotics in Construction*, Jeju Island, South Korea, January 2004.

[15] O. Akkoyun, "An evaluation of image processing methods applied to marble quality classification," in *Proceedings of the 2010 2nd International Conference on Computer Technology and Development*, November 2010.

[16] S. G. Ozkaya, M. Baygin, M. A. Ozdemir, and I. Kazaz, "Image processing based analysis of the compressive strength for the stones used in historical masonry structures," *International Journal of Computer Systems Science and Engineering*, vol. 6, no. 10, pp. 216–222, 2017.

[17] F. F. Sabins Jr and J. M. Ellis, *Remote Sensing: Principles, Interpretation, and Applications*, Waveland Press, Illinois, IL, USA, 2020.

[18] C. F. Mora, A. K. H. Kwan, and H. C. Chan, "Particle size distribution analysis of coarse aggregate using digital image processing," *Cement and Concrete Research*, vol. 28, no. 6, pp. 921–932, 1998.

[19] A. K. H. Kwan, C. F. Mora, and H. C. Chan, "Particle shape analysis of coarse aggregate using digital image processing," *Cement and Concrete Research*, vol. 29, no. 9, pp. 1403–1410, 1999.

[20] C. Boschmann Käthler, U. M. Angst, M. Wagner, and B. Elsener, "Image analysis for determination of cement content in concrete to improve accuracy of chloride analyses," *Cement and Concrete Research*, vol. 99, pp. 1–7, 2017.

[21] C. Başyiğit, B. Çomak, Ş Kilinçarslan, and I. Serkan Üncü, "Assessment of concrete compressive strength by image processing technique," *Construction and Building Materials*, vol. 37, pp. 526–532, 2012.

[22] A. Beycıoğlu, B. Çomak, and D. Akcaabat, "Evaluation of pH value by using image processing," *Acta Physica Polonica A*, vol. 132, no. 3-II, pp. 1142–1144, 2017.

[23] D. Kim, Y. Son, and J. Park, "Prediction of settling velocity of nonspherical soil particles using digital image processing," *Advances in Civil Engineering*, vol. 2018, pp. 1–8, 2018.

[24] Is 12269, *Specifications for 53 Grade Ordinary Portland Cement*, Bureau of Indian Standards, New Dehli, India, 1987.

[25] Is 383, *Specification for Coarse and fine Aggregates from Natural Sources for concrete*, Bureau of Indian Standards, Old delhi, India, 1970.

[26] T. Akashi and S. Amasaki, "Study of the stress waves in the plunger of a rebound hammer at the time of impact," *Symposium Papers*, vol. 82, pp. 17–34, 1984.

[27] Is 13311-1, *Method of Nnondestructive Testing of Concret, Part 1: Ultrasonic Pulse Velocity*, Bureau of Indian Standards, New Delhi, 1992.

[28] M. J. Kumar, K. J. Rao, B. D. Kumar, and V. S. Reddy, "Effect of polyethylene glycol on the properties of self-curing concrete," *International Journal of Engineering & Technology*, vol. 7, pp. 529–532, 2018.

[29] M. T. Cristofaro, S. Viti, and M. Tanganelli, "New predictive models to evaluate concrete compressive strength using the SonReb method," *Journal of Building Engineering*, vol. 27, Article ID 100962, 2020.

[30] G. Concu, B. de Nicolo, L. Pani, N. Trulli, and M. Valdés, "Prediction of cConcrete compressive sStrength by means of combined non-destructive testing," *Advanced Materials Research*, vol. 894, pp. 77–81, 2014.

[31] N. Pereira and X. Romão, "Assessing concrete strength variability in existing structures based on the results of NDTs," *Construction and Building Materials*, vol. 173, pp. 786–800, 2018.

[32] L. Nobile, "Prediction of concrete compressive strength by combined nondestructive methods," *Meccanica*, vol. 50, no. 2, pp. 411–417, 2015.

[33] C. Başyiğit, B. Çomak, and Ş. Kilinçarslan, "A new approach to compressive strength assessment of concrete: image processing technique," *AIP Conference Proceedings*, vol. 1476, pp. 65–69, 2012, https://doi.org/10.1063/1.4751567.

[34] Bureau of Indian Standard, *Concrete Mix Proportioning-Guidelines*, , pp. 1–40, Second Revision, 2019.

[35] I S 456, *Plain and Reinforced concrete-code of Practice*, Bureau of Indian Standards, New Dehli, India, 2000.

[36] F Aydin and M Saribiyik, "Correlation between Schmidt Hammer and destructive compressions testing for concretes in existing buildings," *Scientific Research and Essays*, vol. 5, no. 13, pp. 1644–1648, 2010.

[37] Is 516, *Method of Tests for Strength of Concrete*, Bureau of Indian Standards, New Dehli, India, 1959.

Hindawi
Advances in Civil Engineering
Volume 2022, Article ID 6400254, 17 pages
https://doi.org/10.1155/2022/6400254

Review Article

Progress and Trends in Image Processing Applications in Civil Engineering: Opportunities and Challenges

Ashwini A. Salunkhe,[1,2] **R. Gobinath**,[1] **S. Vinay**,[1] **and Leo Joseph**[3]

[1]*Department of Civil Engineering, SR University, Warangal, Telangana 506371, India*
[2]*Department of Civil Engineering, DIT, Pimpri Pune, Maharashtra 411018, India*
[3]*Department of Electronics and Communication Engineering, SR University, Warangal, Telangana 506371, India*

Correspondence should be addressed to Ashwini A. Salunkhe; rsalunkhee@gmail.com

Received 14 December 2021; Accepted 22 March 2022; Published 5 May 2022

Academic Editor: Wei-Yao Guo

Technological advancements in electronic storage have been trending for cloud computing. The revolution of this computer technology with machine learning and artificial intelligence has created prodigious platforms to the various disciplines of science and technology. Civil engineering is the oldest discipline, and due to the never-ending demand of this domain, it is rapidly adapting to newer computer techniques like image processing, deep learning, big data analysis, neural networks, building information modeling (BIM), unmanned aerial vehicle (UAV) system, digital image correlation (DIC), and many more. In the current paper, we portrayed the primary research and achievements of AI and image processing applications in the civil domain. The paper is divided in two parts. The first part provides analysis of existing methods along with examples relevant to the civil domain where it is incorporated. The second part elaborates scientometric study constituting 605 documents (Science Direct database) published in the last two decades. The bibliometrics are further used for producing analytical frameworks based on publications, citations, top journals, top institutions, and funding sources. This study serves as a guide for readers to identify research gaps and use the review for potential future study.

1. Introduction and Background

Paper forms have been a fundamental mode of transferring and storing data, but with technology advancements electronic storage has been trending for cloud computing. The revolution of this computer technology has created prodigious platforms to the various fields of science and technology which make researchers extend these techniques across all fields. However, when it comes to using digitalization to provide trustworthy data and enhance decision-making processes, the construction industry lags behind other industries [1]. According to Committee for European Construction Equipment (CECE), the civil industry is the least digitized sector. The climatic, environmental, economic, and sociopolitical challenges within civil projects make it difficult in digitization within the construction industry. Since last decade, computer-based monitoring systems and simulations using image processing, AI, ML, and others have piqued the interest among civil engineering community as a cost-effective and unobtrusive solution for image and video data collection and analysis in many construction organizations [1–13]. As a result, several applications were targeted by previous researchers in 3D imaging technologies for construction management, progress monitoring [9, 10], safety [14], and quality control [15, 16]. This review paper concisely emphasises imaging trends and techniques used for applications in civil engineering.

Computer vision has evolved into a broad subject that includes everything from capturing raw data to extracting picture patterns and interpreting data [17]. Image processing involves analysis improving the pictorial information for better interpretation. Digital image processing (DIP) is concerned with performing systematic analysis of images

using computers, whereas computer vision is concerned with creating models, data extraction, and information from photos [18]. DIP and computer vision technologies have been coupled in a wide range of research and project-based applications [19–21]. Figure 1 outlines evolution of image processing and its applications in diverse fields, starting from newspaper printing in 1920, while modern image processing with computing technology began in 1960 in the field astronomy, remote sensing, etc. [22]. Further developments were achieved in medical imaging, industrial inspection, and forensic applications in the early 2000s. In the twenty-first century, computer-based applications and image processing have become the need for a wide range of applications across all disciplines.

Mirsalar Kamari used a hand drafted and computer drawing for development of pattern recognition algorithm to understand structural notations marks from building pictures, and the knowledge was linked to analyze performance of structures. Here programming interface provides the freedom to integrate algorithms with software [23].

Wei et al. carried out feasibility studies on using 3D imaging for construction and infrastructure management [24]. Likewise, Mróz et al. (2020) modelled the usefulness of digital image correlation (DIC), for testing concrete's susceptibility to fire spalling [25]. While Zhang et al. verified the feasibility of DIC for quantifying displacement and strain fields in gravel particle breakage process under uniaxial process [26], del Rey Castillo et al. (2019) modelled the behaviour of fiber reinforced polymer (FRP) for obtaining displacement and strain field with DIC, where displacement measurement was satisfactory, but strain correlation showed dependency on direction of fibers (coincident with parallel direction of fibers and divergent for any other direction) [27].

Globally, the interaction of new technologies is changing continuously, and with AI and ML systems it must cope with a variety of difficulties such as optimization and precise prediction. The advancement of image processing is providing innovative solutions to key challenges, achieving more reliable results at lower cost and time, opening new possibilities, and enabling the acquisition of accurate information from hypothesis testing systems. With digital cameras and sensors of high resolution, connectivity, and network communication, it is easy to upload the clicked photographs of construction activities [10] which are used for planning, monitoring, etc.

Therefore, comprehensive guidance from literature review on DIP applications in civil engineering is presented herein. The purpose of this paper is to introduce the audience to the research by describing the potential of image processing in civil engineering. The following is a brief description of the sections in this paper. The advancement of image processing is generating a new philosophy in civil engineering, which is explored in Section 2. Section 3 provides a detailed scientometric study of two-decade publications in this field, while Section 4 examines this research in terms of language, citations, top journals, top institutions, and funding agencies. Finally, Section 5 discusses the challenges and future scope of image processing before concluding with Section 6 with extracted outcomes and scope.

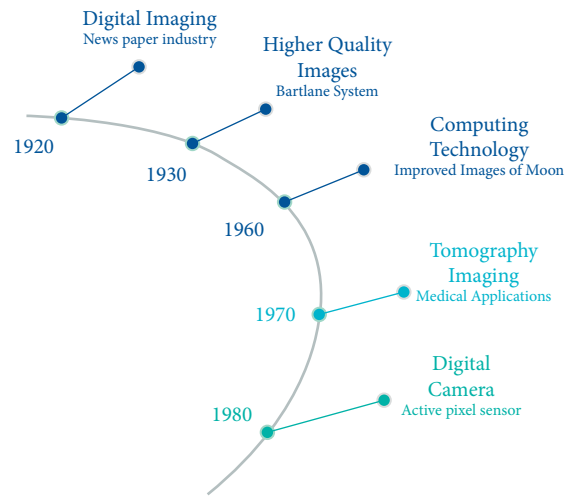

Figure 1: Evolution of image processing.

2. Civil Engineering Approach in Image Processing

The recent surge in the high demand for development and thrust for rapid infrastructure development has created an impact in modern technological advancements in this domain. Many researchers are working on finding the solutions to the problems raised at that society, technical expertise, and managers. Traditional methods for inspection or supervision involve visual assessment. However, a thorough inspection can disclose information that can be used to make various connections in order to determine structural integrity. This provides countless subdivisions to develop image processing applications (Figure 2).

2.1. Remote Sensing and GIS in Geological Applications. Remote sensing (RS) and GIS are linked feature extraction and analysis of ground surface data without coming in physical contact with the surface. It is utilised for urban planning, resource distribution, planning of water retention structures, detecting changes, hazards monitoring and mapping extent, estimating the damages [28], and so on. Despite the advances in RS technology, the applications in infrastructure and construction industry are limited [29]. Geotechnical information is imported for effective decision making [30]. In tunnel work, 2D geotechnical maps provide information of location and directions of weak planes. Particularly, complexity of tunnel work location and use of heavy machines like TBM (tunnel boring machines) make remote monitoring necessary. To overcome costly and time-consuming investigation, the image processing approach is adopted by researchers.

Image acquisition of tunnel facing, its processing is used for rock mass rating, geological features (faults, joints, etc.), and interpolation technique on two consecutive images established in 3D visualization [31].

In this context, Schindler et al. performed a virtual reality environment with 4D visualization by satellite and terrestrial based settlement data [7].

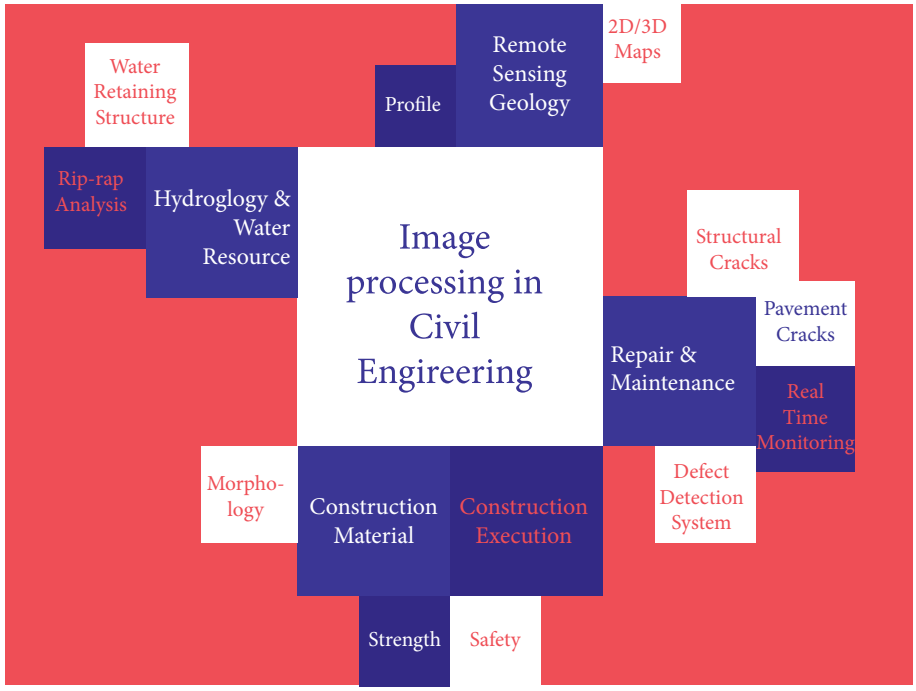

Figure 2: Image processing applications in civil engineering.

One of the studies focused on the 1st of its trial on rock face characterization using images. The images on the rock surface provide comprehensive geological mapping. Additional rock mass parameters obtained by mapping are useful for tunnel stability estimation and support steps [32].

2.2. Hydrology and Water Resource Engineering. Management of earth's water mass distribution and its interaction with natural and engineering material is essential for sustainable development. Computing technology offers a framework for interpretation as well as simulating the behaviour of water bodies along with their surroundings.

Land use land cover (LULC) classification [33], changes detection [11, 12, 34–38], and its impact on water reservoirs were studied by Musaoglu, Moniruzzaman to help authorities and decision makers in changing quality conditions of reservoirs [39, 40].

Chang et al. studied river behaviour using image processing technique on river-bed digital photographs. An image processing method was applied by fusing feedback pulse couple neural network (FPCNN) [41–44] and multilevel thresholding for image segmentation and grain size distribution [41]. In a similar context, Robert et al. have used image processing to establish granulometry of riprap. Along with rivers, the design of geotextile filters for water/soil retaining structures, drains, etc. requires morphological data where digital image processing is effectively applied for nonwoven geotextiles by Shobha in 1993 [19].

Moreover, for applications in stream gauging, Lewis et al. evaluated the potential of unmanned aerial system (UAS) for quantifying flow in rivers [45].

2.3. Constructional Material. Construction engineering starts with study of construction material properties to acquire desired strength as per design requirement. The behaviour of any material is dependent on its morphological properties, and image processing is a very powerful tool to gather this information [46]. Digital image correlation (DIC) was used by McCormick et al., and Suleiman et al. measured deformation and strain by analyzing a pair of images of specimen surfaces taken before and after under various loading conditions [47, 48]. Image analysis for civil engineering materials, in the process of sampling and counting particles using specific methods for estimation of quantitative parameters, is useful for analyzing functions related to size distribution and anisotropy [46]. DIC has versatile abilities in adapting to any scalable applications allowing it to extend use in structural health monitoring [49].

Aggregate gradation: in the construction sector, few are the key building materials such as cement, steel, and sand. Aggregates are one of the essential materials, and they play a vital role in asphalt pavements. Rutting of pavement gives major distress in pavement where aggregate gradation characteristics have a significant role in improving its performance [50]. The time-consuming methods aggregate gradation gives the motivation to the simple approach of image processing techniques. The method comprises curve fitting and image processing techniques to detect aggregates

from cross-section images of cylindrical samples [51]. Anding et al. applied intelligent image processing algorithms in optical identification and analysis of mineral aggregates from construction and demolition waste [52].

2.4. Construction Execution and Safety. Execution work where there is major involvement of people and machinery together deals with site conditions, simultaneous activities, safety aspects, real-time progress, etc. Nowadays, drone technology is becoming very effective in making various surveys. Although the technology was introduced in risk assessment, disaster monitoring, etc., it is becoming famous in civil engineering works as well. The data gathered from these surveys can be analysed for civil engineering applications. Liu et al. used unmanned aerial vehicles (UAV) for construction execution [53]. The leading safety concerns at construction sites have attracted the researchers for smart techniques of safety assessment. This approach conducts dynamic measurement in the field of civil engineering through morphological operators for image filtering and a feature extraction technique: Hough Transform [14].

2.5. Repair and Maintenance. Every constructed structure, at some point of period, will require care in order to extend its lifespan. This part of the period focuses on the maintenance work of structures. Infrastructure challenges for constructing and maintaining the work include checking, making reports, and if required deciding what actions to be taken. Hence, the maintenance part requires the involvement of more people. In the major civil structures like bridges, high rise buildings, roads, etc., the crucial job is detecting the current state of structure and necessary maintenance. Due to vastness of the section, it is further categorized into two parts.

2.5.1. Assessment of Structural Cracks. All structural assessment starts with crack detection, location, pattern, etc. However, the current evaluation techniques depend on people which attract more error and cost of execution. Valença et al. have developed image processing and laser scanning method to survey the cracks in bridges, while Kong et al. used DIP for fatigue crack detection in infrastructure [54]. Valença [55] used MCrack-TLS which is a combination of two technologies: image processing for crack detection (MCrack) and terrestrial laser scanning (TLS). In this technique, images are captured with different equipment depending on the location and type of structure, and further laser scanning helps to orthorectify the images for processing. Fangfei invented a comprehensive evaluator of defect detection in civil engineering structure [56]. The detailed module is shown in Figure 3.

2.5.2. Pavement Crack Monitoring and Analysis. Under pavement monitoring, asphalt resurfacing or overlay is a basic method of asphalt repair, and asphalt chip seals are the most common preventative maintenance technique employed by transportation/road agencies around the world. This requires precise percent aggregate in a thin bitumen sheet to avoid bleeding or aggregate loss. Ozdemir invented a standard procedure that uses digital image analysis to quantify the percent aggregate embedment in the bitumen layer [57].

Further pavement monitoring entails the traditional assessment of pavement cracks via manual observation. To overcome the errors and drawbacks of conventional methods, a new automated method has been proposed for evaluation of crack sealing performance [58] while Chun in 2015 developed a semiautomatic method for asphalt pavement crack detection based on crack ratio [59]. Pavement surface drainage is a major concern to avoid hydroplaning in wet weather conditions. Mataei et al. created a pavement evaluation system that simulates the surface saturation condition from acquired images, and image processing generates indices to assess drainage quality [60].

Uneven background illumination makes it challenging for automatic pavement defects detection and segmentation. For this, Oliveira and Correia (2014) recommended an image normalization approach [61]. This maintains the average intensities of the defect-containing regions while balancing the average intensities of defects-free regions. Figure 4 depicts image preprocessing for pavement. It is clear that background noise and sealed cracks are filtered to a large extent while pothole regions are kept for enabling further segmentation. The image-closing operator is one of the morphological operators used to improve segmented pothole shapes. This operator is illustrated in Figure 3 for extracting pothole shapes from pavement.

The visual appearance of an object by the projective integral (PI) method is a one-dimensional pattern acquired by the addition of a set of pixels along the representative direction. PI is used to characterize the different forms of cracks based on the arithmetic mean computation of row or column pixels [63]. Figure 5 shows PI for longitudinal, transverse, and alligator forms of cracks and also a state of no crack.

An image of adhesive loss and pull-out failure was used to identify the distress of a sealed crack. As shown in Figure 6, the complement of the image has developed to represent a region of distress, further converting it to grayscale image for efficient computation which is further used to represent gradient mask by distinguishing texture of other regions from a uniform texture to sealed crack. A dilation operation is conducted on this for simplifying the sealed crack region from the background region (similar to morphological operation). The hole-filling method fills the noisy holes left over from the dilation process in the noncrack region. The finished image is binarized into black and white and compared to the binarized original image, resulting in the display of failure zones in sealed fractures.

2.5.3. Real-Time Monitoring. The large scale civil engineering structure itself demands maximum monitoring to reduce risk of failure or disaster management by providing early warnings. In this context, Vasileva et al. and Fukuda et al. came up with real-time and long-term remote

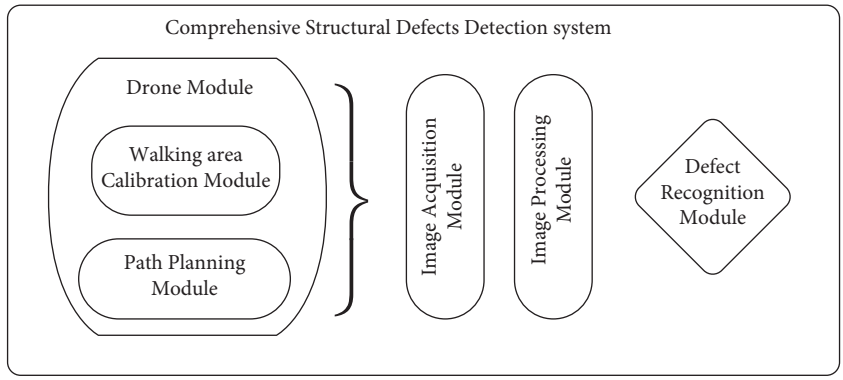

Figure 3: Defect detection system.

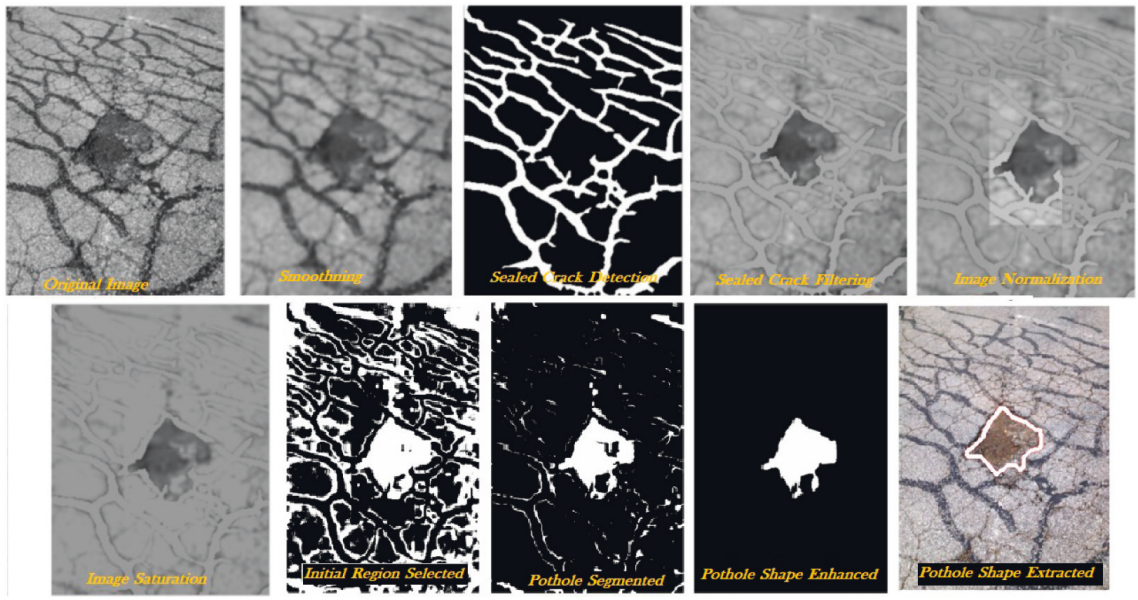

Figure 4: Example of pothole extraction by 2D image pre- and postprocessing [62].

monitoring of dynamic responses of major civil structures [5, 6]. Fukuda et al. used structure of target panel (predefined marks) transferring the signal in terms of movement captured by a connected camcorder. These signals are extracted in dynamic responses by the digital image processing software to compute displacement in real time while Vasileva et al. used FGPA (Field Programmable Gate Array) for high performance. Furthermore, Ehrhart et al. developed dynamic deformation monitoring by total station (for 3D movements) and image assisted total station (IATS) to compute absolute 3D coordinates and calculate structure's natural frequencies [3]. However, to extract vibration behaviour of structure, sensors like accelerometers are used. The method uses IATS and marked targets fixed to the object. Total station telescope camera enabled real-time video streams with 10fps and 2"/px angular resolution. The electronic distance measurement (EDM) integrated in the total station gives precision to transform angular terms received from image processing to length units. The accuracy in case of dynamic application achieved better than 0.2 mm and for static applications better than 0.05 mm possible [4].

In 2018, Huang used stiffness coefficient and numerical analysis of a loaded structure for the life prediction module [65]. This evaluation system in predicting the life of structure involves a drone module for collecting data through image which is processed under image acquisition module.

3. Review of Image Processing Tools and Algorithms

The summary of image processing tools researchers have used with their usefulness in their study is shown in Table 1. In summary, notable researchers in the field of material image processing have used wavelet transformation methods, although the method has the limitation that particle diameters cannot change by more than a factor of two in area analysis [66]. This necessitates particle separation prior to picture acquisition. In addition, the researchers' software selection scenario reveals a preference for MATLAB software. This could be due to the image processing library's built-in tools, which include standard algorithms, visualization functions, and applications.

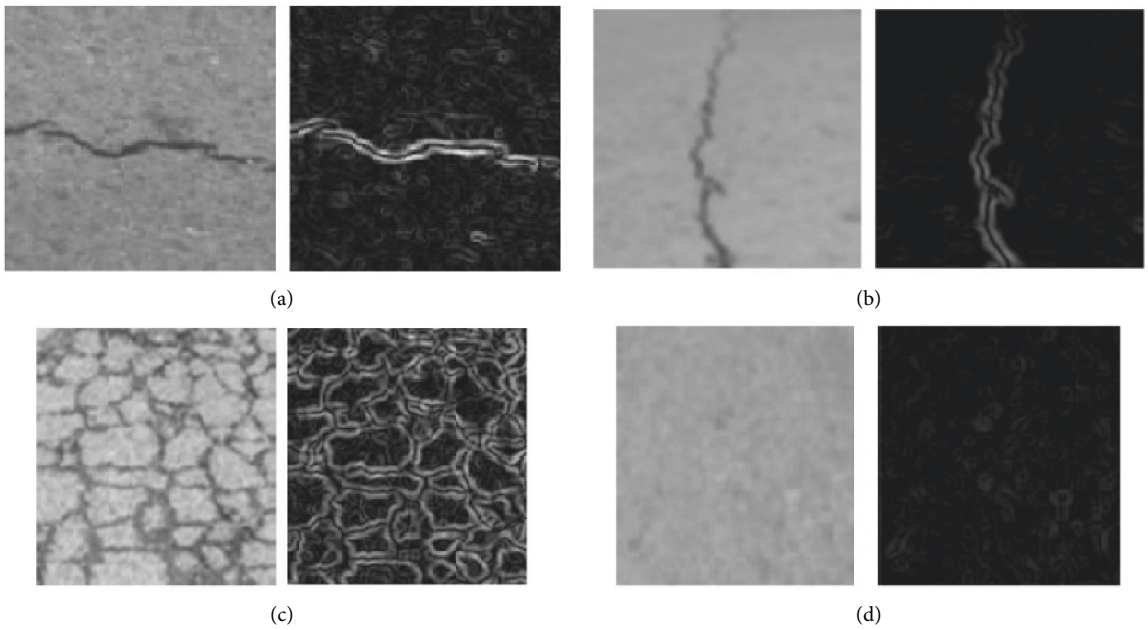

Figure 5: Images and SF response for various forms of cracks [64]. (a) Transverse crack. (b) Longitudinal crack. (c) Alligator crack. (d) No crack.

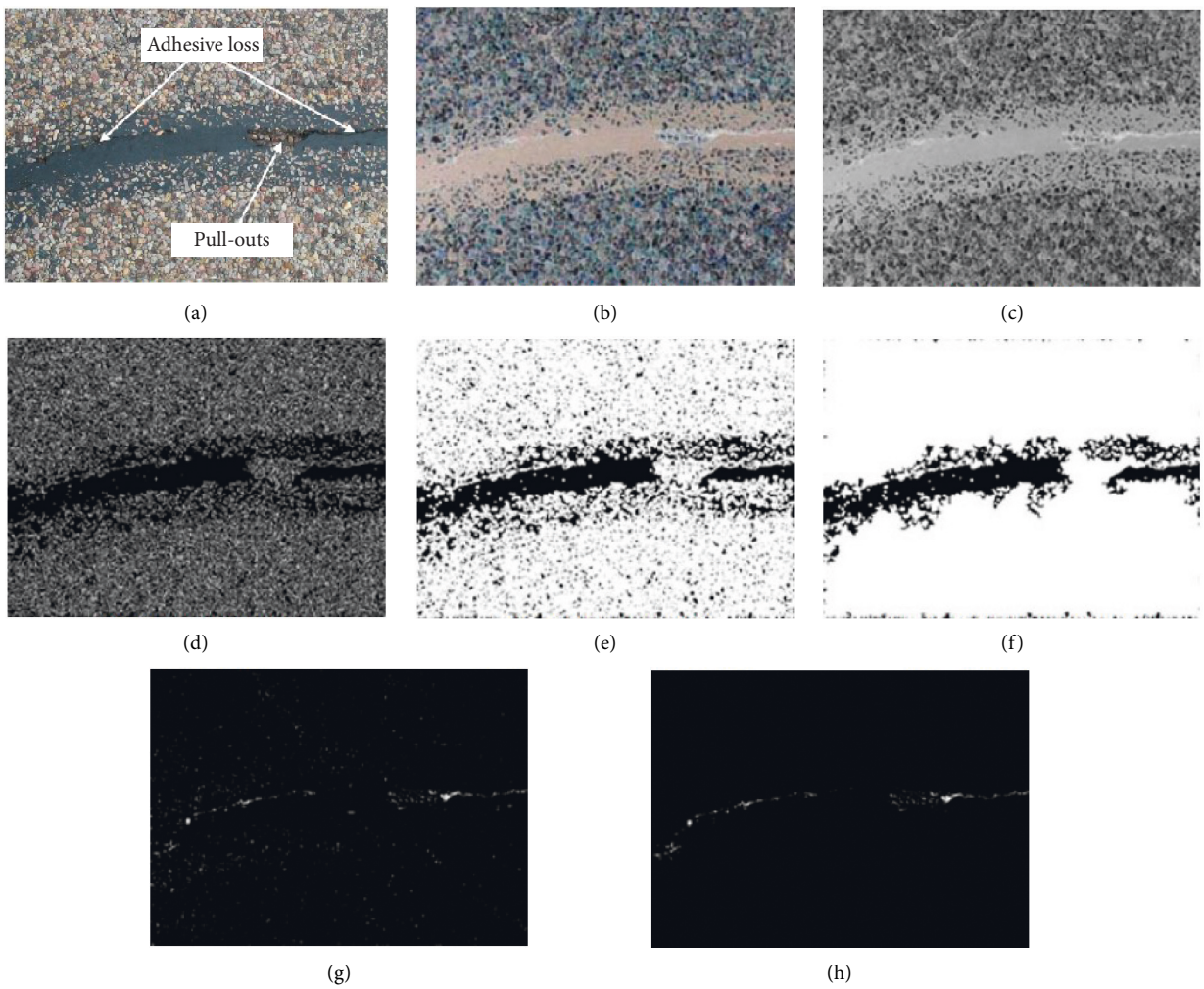

Figure 6: Crack sealing performance analysis from image processing (distress region extraction of sealed cracks) [58]. (a) Original figure. (b) Complement of image. (c) Grayscale image. (d) Binary gradient mask. (e) Dilated gradient mask. (f) Binary image with holes filled. (g) Binary image from the original figure. (h) Final extraction of the distress of a sealed crack.

Table 1: Image processing tools in civil engineering applications.

Researchers	Tools and techniques	Tool application	Usefulness in research
Sou-Sen Leu et al. (2005) [31]	Borland C++, Slice dicer	Borland C++ developed an image processing subsystem while Slice dicer integrated 3D reconstruction and visualization in the main system	Technique can effectively guide aspirants to visualize geological features from tunnel excavation
Yoshio Fukuda et al. (2010) [5]	Digital camcorder and a notebook computer equipped with DirectShow technology (Microsoft corporation) software using C++ language	Image processing modules were implemented with DirectShow software. The module helps to detect geometric patterns with trigonometric transforms	System is capable for real-time dynamic response measurement and ideal for monitoring civil engineering structures
Nick McCormick et al. (2012) [47]	ARAMIS software	The deformation measurement was initially done on integer and further targeted in subpixel interpolation by 2D spline fitting and Newton Raphson technique	Full-field deformation measurements of civil structures with DIC is effective and can be tested for various sites with sensors
Morteza Vadood et al. (2013) [51]	MATLAB R2006a	Distance and modified watershed transform methodology with Canny's filter	The method effectively detects aggregate gradation
Katharina Anding et al. (2013) [52]	Halcon 8.0.3	A machine vision software with feature algorithms for supervised learning classifier	Algorithms integrated for sorting optical aggregates in construction demolition waste (CDW)
Peter Liu et al. (2014) [53]	Unmanned aerial vehicle (UAV), ground controlling station (GCS)	UAV acquires aerial perspective info and GCS software performs simulations function	Potential use of UAV in mapping methods, geometric analysis, and civil engineering applications
Hyon-Sohk Ohm et al. (2014) [66]	MATLAB R2013a	Image analysis method using wavelet transformation coded in software gives sediment size distribution	Sedimaging and sieving test for nine soils give identical results on soil gradation plot by both methods
Behrouz Mataeia et al. (2017) [60]	Innovative device & software	Device consists of several parts: imaging, saturation, constant lighting, temperature recorder, and movement arrangement. Image processing software using sharelet transform	Pavement surface drainage quality was examined and classified into "good," "normal," and "bad"
Can Wang et al. (2018) [67]	Particle flow code (PFC) 3D (version 5)	Software allows three-dimensional mapping of restitution tests for mapping segregated mixture	Material heterogeneity from digital image processing generates discrete element model which helps to examine influence of particle properties on segregation
Saghafi et al. (2019) [68]	Img. Pro. Plus 6	Software measurement feature counts total aggregate loss by summing up pixels with loss area	Abrasion of slurry seal mixtures was investigated to find out loss of aggregate and bitumen
Faria Borges et al. (2019) [69]	SkyScan reconstruction software (CTAn)	Software was capable of scanning hundreds of 2D images and combined to project 3D image	Algorithm generated supervised information (grain size, void ratio, and soil tortuosity) through material microtomography for sandy material
Bidgoli et al. (2020) [70]	MATLAB R2014a	MATLAB code was developed to determine the percentage of pixels for each surface fracture	Damage investigation between binder and aggregate was done by moisture susceptibility of asphalt mixture by registration image-processing method
Detcev et al. (2014)	Eight digital cameras and two projectors	Camera was used for capturing concrete beam which is being deformed by actuator loading. Projectors were used for performing 3D reconstruction and point cloud processing for deflection measurement	Precise deflection measurement of concrete beam loaded by hydraulic actuator

Image processing starts with the image acquisition process either with powerful camera capturing images [19, 47, 48] or video recording [66, 67]. The typical image analysis procedure can be summarized: (i) image acquisition, (ii) image preprocessing, (iii) image enhancement, (iv) image segmentation, (v) image postprocessing, and (vi) detection or prediction. Image preprocessing can be done with various algorithms with image graying like single component method, maximum weighted method, best weighted average method [2], etc. Further image filtering

processes usually retain useful characteristics of image by removing noise. It can be done by mean filtering method, median filtering method, and morphology filtering method. Segmentation process labels every pixel for a certain characteristic which is useful for object recognition, edge detection, etc. Table 2 provides the summary of such algorithms and their briefing for getting insights of algorithms.

4. Scientometric Analysis of Image Processing Applications in Civil Engineering

Scientometrics is the analysis of quantitative qualities and qualities of science and scientific study. The location of emphasis is on inquiries which concentrate on the processes and mechanisms of science that are explored using statistical mathematical approaches. Scientometrics is the area of study that is concerned with the collection, analysis, and evaluation of academic publications. The application of the methodologies used in bibliometrics (i.e., scientometrics) is a subfield of bibliometrics. There are several concerns in major research that need to be examined, including the study of the influence of research articles and academic journals, the comprehension of scientific citations, and the utilisation of research measurements in policy and management. Although there is some overlap, in practice there is a strong overlap between the areas of scientometrics and other scientific topics such as information systems, information science, science of science policy, sociology of science, and metascience. There have been critics who suggest that an overreliance on scientometrics has established a system of perverse incentives, which has produced a publish or perish atmosphere that encourages low-quality research. In 1969, Vasily Nalimov, in his capacity as the Chairman of the Russian Academy of Sciences' Institute of Scientific Information, proposed that the field of scientometrics be renamed Naukometriya, which translates to "Scientometrics" in English [54, 75–77]. In modern scientific methodology, nearly all of the effort is focused on the work of Derek J. de Solla Price and Eugene Garfield. Later on, this individual established the Scientific Index and started the Institute for Scientific Information (also known as ISI). This is commonly used for scientometric analysis. In 1978, the Scientometrics journal was launched for committed researchers only. The expansion in the industrialization of science led to an increase in publications and research outputs, as well as the rise of computers, which allowed for effective analysis of the data. While the focus of the sociological study of science was on the conduct of scientists, the focus of the scientometric study was on examination of publications [78]. Similarly, science and technology analytics are referred to as the scientific and empirical examination of science and its outcomes.

In this work, we had tried to analyze the progress of research in the image processing applications vertical to understand the quantum of research work being undertaken in various levels and its field implications. We had used SCOPUS core collection, a product of Elsevier Co for the analysis fully to understand how much research work is in progress. A multilevel bibliometric information retrieval was done on SCOPUS website on single day June 4, 2021, to avoid bias caused by updates of open databases. First, a search was made on SCOPUS with the following query:

((TITLE-ABS-KEY(image processing) AND TITLE-ABS-KEY(civil engineering)) AND PUBYEAR >1999)

The search comprises a total of 605 documents, containing various open access journals and articles in which all peer-reviewed scholarly articles are online and available without restriction. The distribution is shown in Figure 7.

The documents are collected with details of year of publication, type of document like conference, editorial, book chapters, etc., keywords, name of author(s) with affiliation(s), and country. The bibliometric analysis was carried out for identifying trends, leading authors, funding agencies, and countries. The major key points in the publication datasets which relate to the civil engineering field were "deformation," "construction equipment," "concrete crack," "structural health monitoring," "building material," etc. as shown in Figure 8(a). For the dataset, key points with computer techniques were "digital image correlation," "algorithm," "data processing," "image enhancement," "image segment," etc. as shown in Figure 8(b).

5. Database Analysis

5.1. Type of Document Analysis with Language. For the +20-year period of 2000 to 2021, researchers globally published 604 documents related to image processing in civil engineering. Using this SCOPUS data, we performed categorial analysis based on year of publication, type of document, language, and country origin. Figure 9 shows that research conducted over two decades has consistently contributed the most to conference papers, followed by articles. Data shows that the highest record was 370 (61.25828%) documents from conference paper followed by articles 173 (28.64238%), followed by conference review 37 (6.12582%) and review 11 (1.82119). The remaining 13 documents (2.152317%) were published as book, book chapters, editorial erratum, and short survey which constitute 1392 citations due to one Springer book having the highest citation of 1343. The maximum number of papers 574 (95.03%) was published in English language followed by Chinese 22 (3.64%). Hence, around 98.67% are in these two languages out of total documents findings. The remaining 1.49% were scattered in 5 different languages "GJSPT" around the globe constituting the language with papers: German (3), Japanese (2), Spanish (2), Portuguese (1), and Turkish (1). However, one of the papers is available in two languages, English and Japanese. By looking at the overall scenario in Figure 9, it can be concluded that image processing in the civil engineering field comprises the maximum number of papers in English language with very few documents from other 6 languages.

5.2. Publication Analysis. In the publication analysis process, bibliometrics allows us to perform statistical projection in acquiring reliable indicators. Along with the number of research publications, citations have been one of the most

Table 2: Algorithmic analysis for civil engineering application.

References	Application	Algorithm	Brief
[29, 58, 59, 61, 64]	Intelligent approach in pavement crack classification	Image processing and machine learning algorithms	Image processing tool: nonlocal means, steerable filter, projective integral, and image thresholding machine learning tool: support vector machine and artificial colony bee
[2]	Crack detection algorithm for crack skeleton	Zhang-Suen skeleton extraction algorithm	OTSU automatic threshold, gamma filtering, and gamma image enhancement
[71]	Damage evaluation through tunnel crack	Image threshold segmentation algorithm based on fuzzy set	Image analysis with cracks characteristic
[22, 46]	Image analysis for civil engineering materials	Probabilistic models: tessellation and polyphase	Image acquisition, extraction of feature, segmentation, and binary image treatment
[72]	Interphase contact angle for unsaturated geomaterial	Image-based contact angle measurement	Zero-intercept approach compared with liquid pixel approach and regression approach
[73]	Aggregate gradation	Laser imaging and neural network	Wavelet transform to extract features of material gradation
[51]	Separate aggregate from bitumen mastic and split joint aggregate	Numerical and image processing techniques such as fitting equation and colour space system	Binary images with colour space method can accurately and easily remove bitumen from cross-sections images compared to the shape method. Then, the distance and modified watershed transform was applied on the obtained binary images, and the aggregate gradation was extracted from images
[52]	Optical identification of recycled aggregates from CDW	Intelligent image processing algorithms	Feature extraction and machine learning classifiers
[66]	Size distribution of coarse-grained soil (0.075–2.0 mm)	Image analysis based on wavelet transformation	Wavelet transformation decomposes soil image of kth pixel size into k decomposition level to produce size distribution
[57]	Quantifying aggregate embedded in asphalt binder	Peak valley method, embedment of each aggregate method, and surface coverage area method	A digital image analysis to calculate percent aggregate embedded in asphalt
[4, 5]	Displacement measurement system for real-time monitoring for large civil structures	Image processing algorithm for target panel detection	Geometry of target panel analysis by position of white spots on panel
[2, 4, 47, 74]	Measurement of deformation of structure	Processing pair of images under different loading conditions	High resolution cameras for displacement measurement

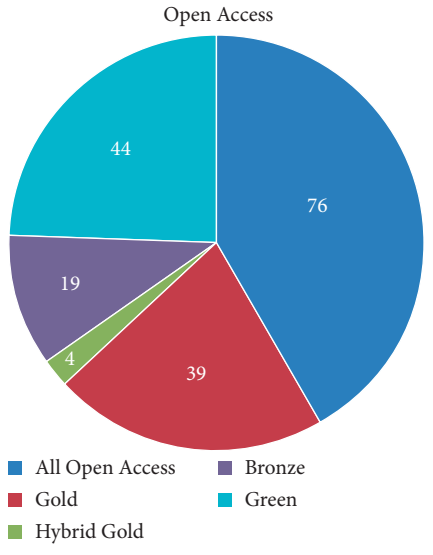

Figure 7: Journal distribution.

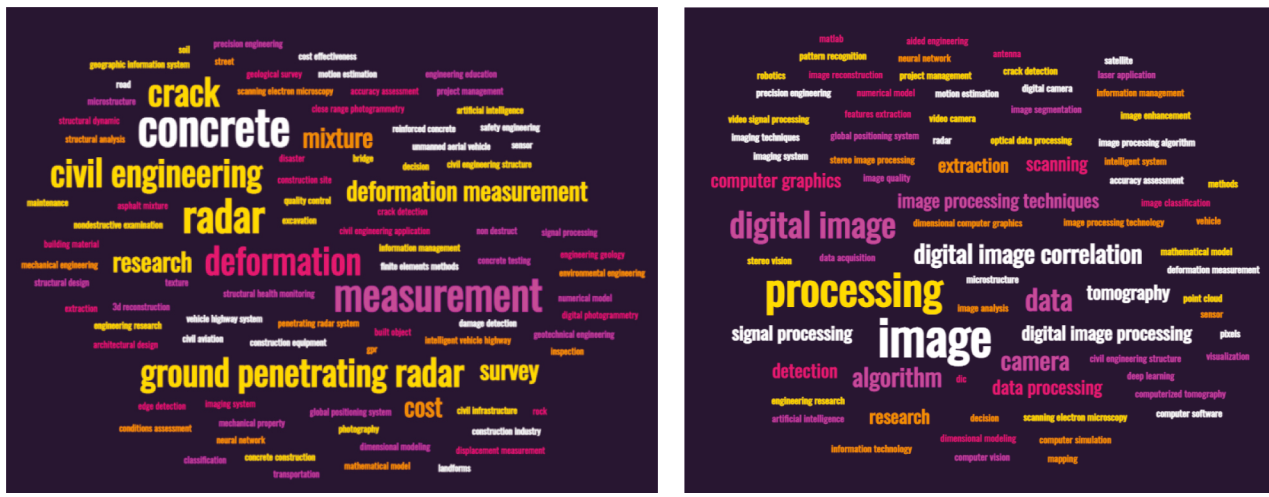

(a) (b)

Figure 8: (a) Key points related to civil engineering. (b) Key points related to image processing.

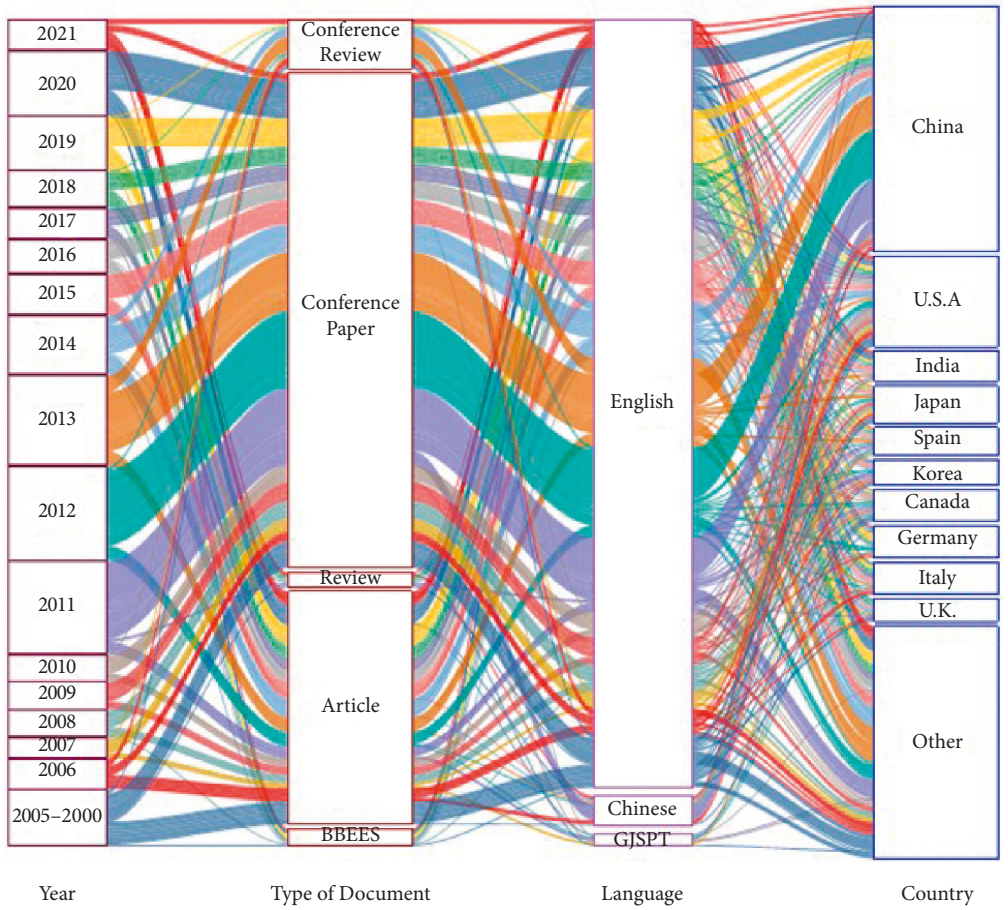

Figure 9: Publication overview with language and country for the period from 2001 to 2021.

important indicators for research quality. Citations are a form of scientific performance metric that measures the impact of an article. Figure 10 depicts the multiple axis (4Y) combination to one axis (X) for better understanding of publication and citation trends from research output in image processing in civil engineering during the period 2000–2021. The median for the publications is 22, while the deviation value for publication is 20. The average publications were 27 per year, and the highest number of documents published was 70 in 2012. It indicates that the global growth

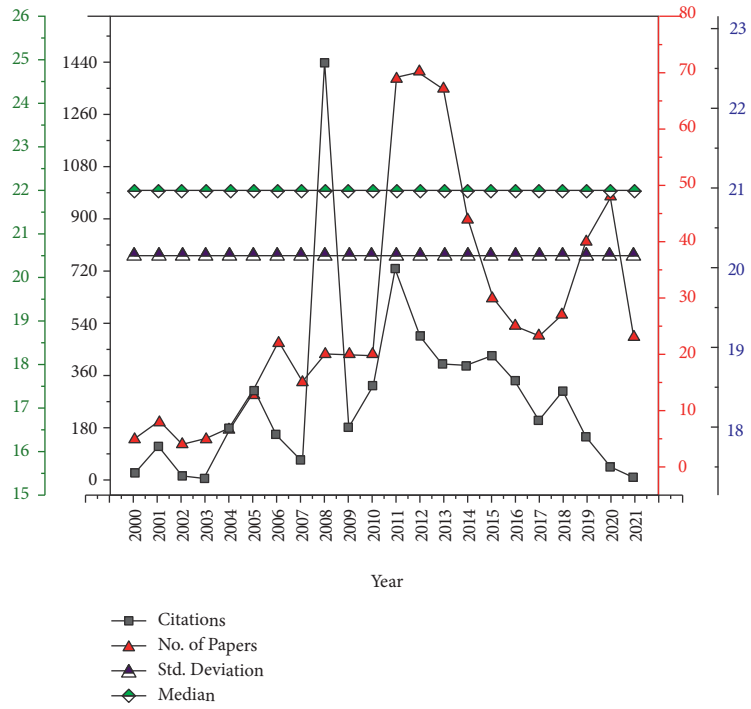

Figure 10: Publication trend from 2000 to 2021.

rate is constant in the period from 2000 to 2008. The data output shows stagnant growth in the first 10 years, and suddenly it reached a peak in 2011, which stayed there for the next 2 years.

5.3. Top Journals Contributing More Research. Targeted at analyzing the research contribution from top sources, Figure 11 shows most article contributed journals ranking in the top ten list. Journal named "Applied Mechanics & Materials" is conducting the most rigorous research in the field of image processing for civil engineering. The scientific explanation could be that they prefer to publish comprehensive volumes on specific topics rather than individual papers by authors. With around 30+ papers gap, the remaining sources come into the view like SPIE proceedings (dedicated to advancing the science and application of light and light-based technologies), Advanced Materials Research, etc.

5.4. Top Universities or Institutions. The world of scientific research has become more collaborative with research papers by authors from multiple affiliations (same or different country, continent). This affiliation represents research integrity of paper and also the place of research conducted. China and the United States of America (USA) continue to be the most prolific vendors in generating quality research output. Figure 12 shows the ranking of top 15 affiliations by researchers, where 60% of researchers' affiliations are with universities from China, followed by USA (20%).

5.5. Top Funding Sources. Research funding is a common feature for all mature innovation systems. The data presented in Figure 13 does not focus on the quantity of money that agencies have given, but rather on the number of research entities that have been supported. The majority of the articles in this scientometric study were funded by China's National Natural Science Foundation, which promotes and finances basic research and applied research in China. The second largest agency is from the USA, "National Science Foundation," which supports fundamental research in the nonmedical field of science and engineering.

6. Challenges and Future Suggestions (Gap and Issues)

Technical reliability of image processing addresses the uncertainty of construction sites, severity of weather conditions, and real-time image acquisition for smooth application in the civil domain. Despite the fact that civil engineering has a plethora of subdivisions, some of them have excelled in image processing applications. Some of these subdivisions come from "infrastructure repair and maintenance," which has been extensively researched by researchers in conjunction with computer vision. For deep understanding between the research gap and presenting it in a narrative manner, a network visualization graph of keywords is helpful. Network visualization graph in Figure 14 features the relevance for major image processing research work carried out on the basis of keywords. The graphics use colour, geometry for interfacing, and overall reasoning. The thematic study results in major work in areas of remote

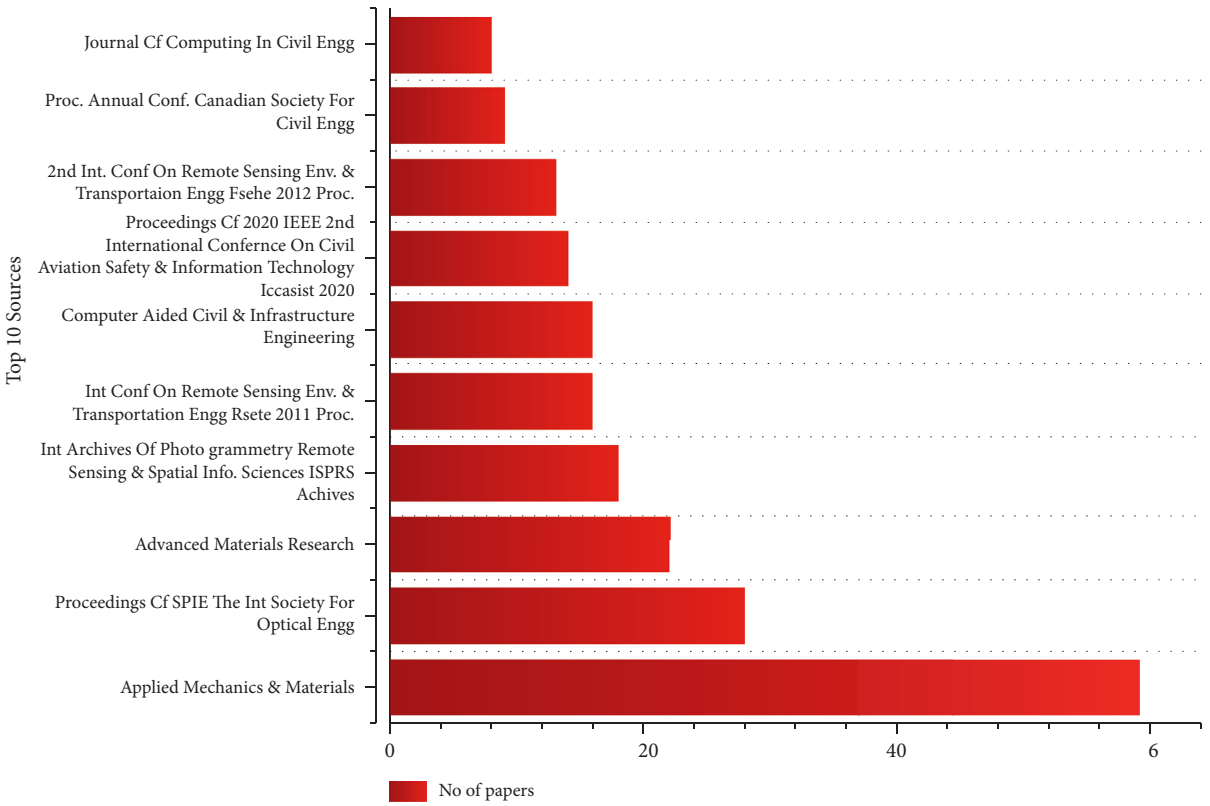

Figure 11: Top 10 sources for 2001 to 2021.

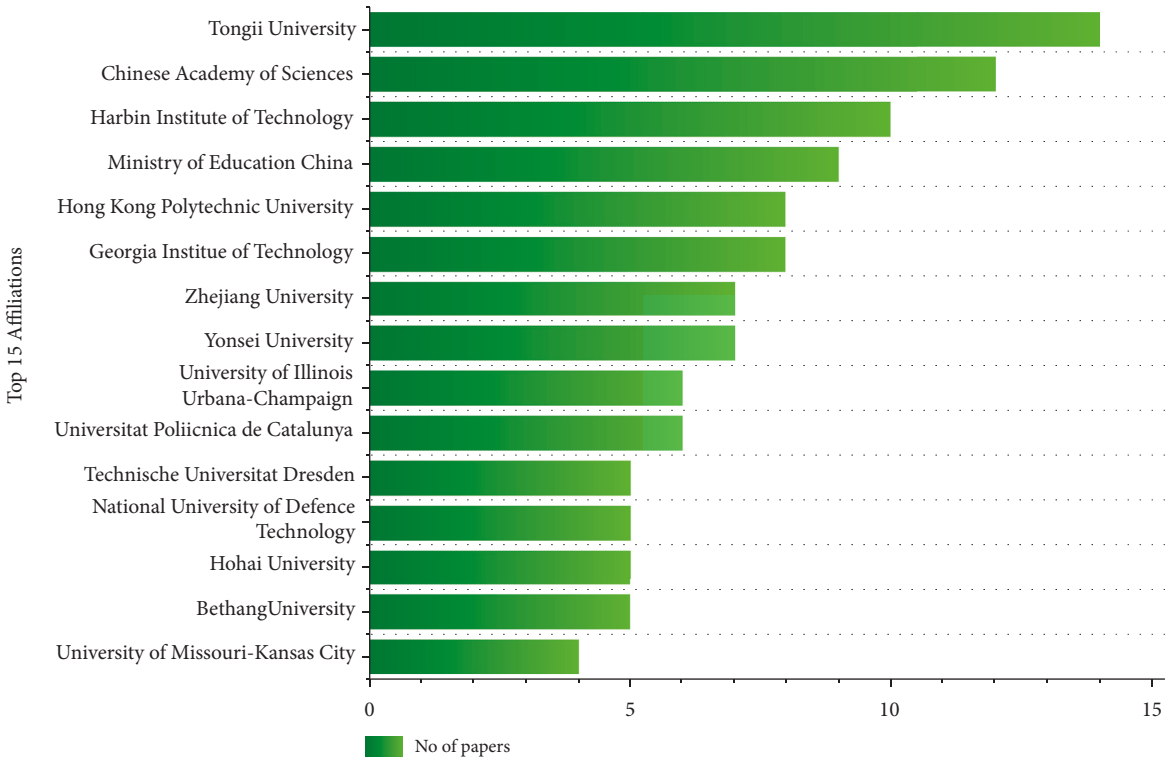

Figure 12: Top 15 affiliations for 2001 to 2021.

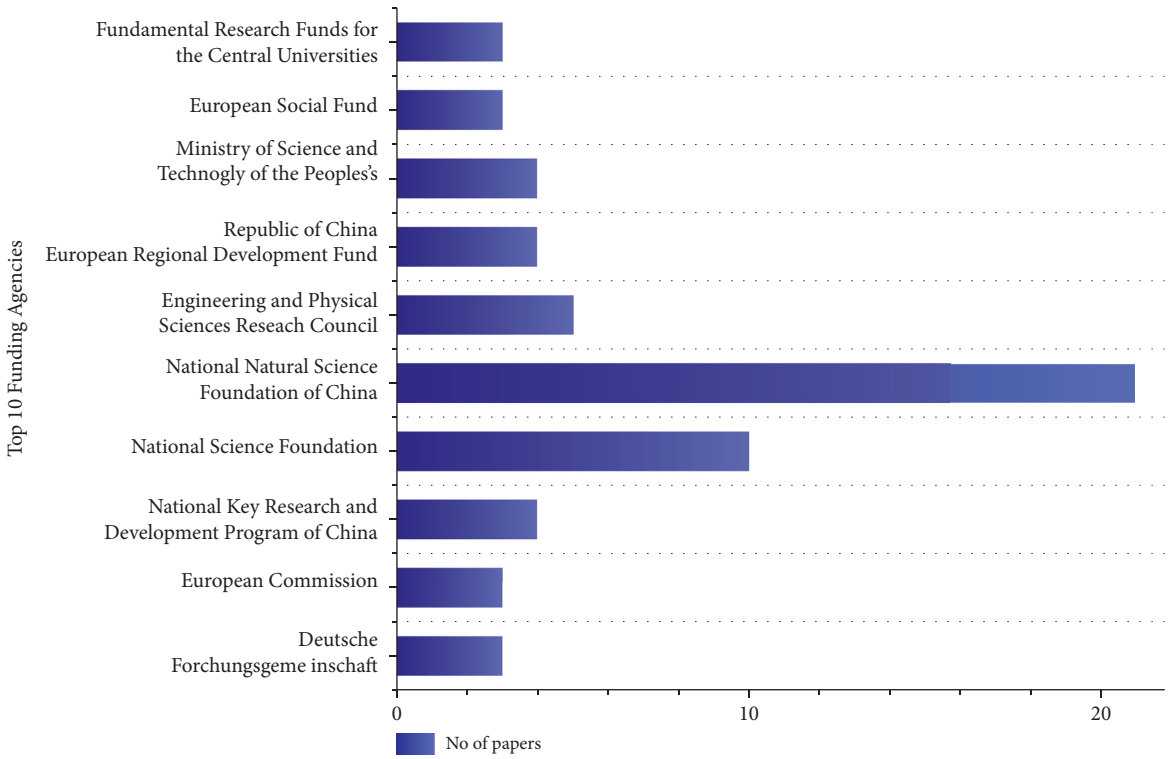

Figure 13: Top 10 funding agencies for 2001 to 2021.

sensing, motion or deformation estimates, and disaster analysis. However, due to technical limitations such as restricting the image frame and depth to which data extraction is necessary, some domains such as geotechnical engineering and concrete technology remain unexplored.

On one hand, civil work is responsible for developing the most efficient structures using modern equipment in order to deal with harsh site circumstances, while on the other hand, it is also responsible for maintaining and repairing ageing infrastructure [73]. The versatile nature of civil work makes it more complex to develop one tool or algorithm for a particular job and standardize for future similar works. As civil engineering activities are carried out in the field, a picture frame for this sort of work comprises a lot of noise and extraneous items, making it challenging for image acquisition and training the model for object detection. This makes image classification difficult, as each class requires hundreds of images. For better performance of the model, large amounts of data with accurate labelling are required. As a result, it is crucial to operate on the best hardware that supports the complex operations and processing of images.

7. Extraction Outcome and Potential Scope

In civil engineering, computer vision refers to artificial intelligence and machine learning, and further it can be closely related to image processing. The imaging applications give opportunity to civil engineers for the challenges of handling simultaneous work. From this automation, major benefits can be acquired by construction material companies. Various image processing techniques have been developed and used in the civil engineering field, yet so many areas are untouched.

This paper provides an up-to-date review of image processing applications in the field of civil engineering. Image acquisition that has been used in controlled indoor setup and on-site equipment is described. Developing trends toward portable devices like digital camera, UAV, and mobile camera to acquire images are noted. From the research carried out in this article, it can be seen that digital imaging research in the context of civil engineering has heavily focused on object tracking like crack identification, classification, etc., and activity recognition like displacement or deformation, etc. The benefit of this approach is that it allows you to analyze the deformations without direct physical contact with structure. The applications of automation from image processing can save time and cost in some tedious jobs like material characterization in CDW, measuring strain, strength, and displacements. The future scope of this study can be considered as the use of handy tools (mobile camera) for image acquisition, transferring, and processing image data. In addition, one of the potential areas is making an image cloud database for civil engineering work. This will help multiple aspirants to easily access data and collaborate for the work in developing algorithms for more better results.

Finally, this research paper is projection of progress and trends of image processing in virtue of civil engineering. This will help researchers to get background, challenges, and future scope of using image processing work in civil engineering.

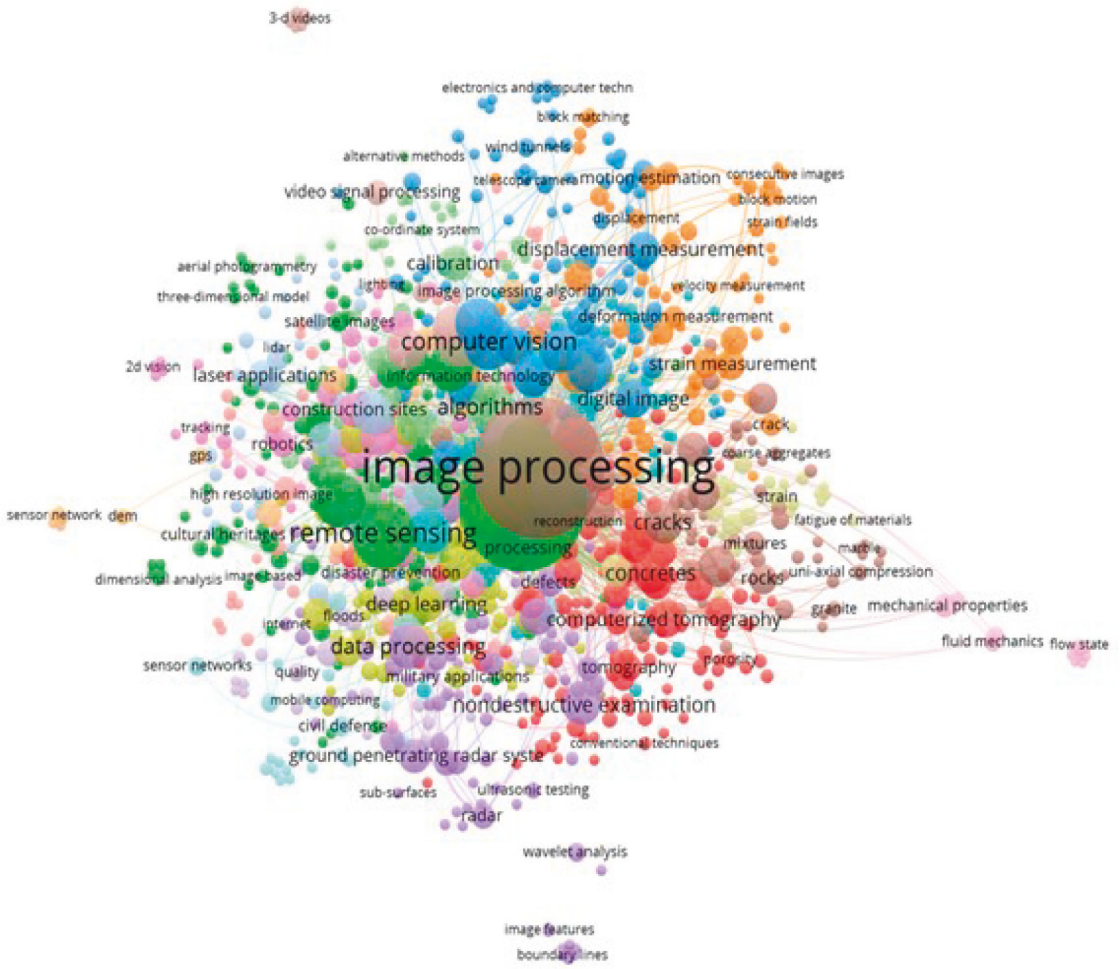

Figure 14: Network of keyword interrelation.

Data Availability

The data are available upon request to the corresponding author.

Conflicts of Interest

The authors declare that they have no conflicts of interest.

References

[1] K. Ali, A. Woldesenbet, and S. Rokooei, "Integration of augmented reality building information modeling, and image processing in construction management: a content analysis," in *Proceedings of the AEI 2017. American Society of Civil Engineers*, Oklahoma, Oklahoma, April 2017.

[2] X. Yu, X. Wang, X. Da, and J. Zhao, "Crack detection algorithm of complex bridge based on image process," in *Proceedings of the 20th COTA International Conference of Transportation Professionals*, Xi'an, China, August 2020.

[3] M. Ehrhart and L. Werner, "Development and evaluation of a long range image-based monitoring system for civil engineering structures," in *Proceedings of the Structural Health Monitoring and Inspection of Advanced Materials Aerospace, and Civil Infrastructure 2015*, SPIE, San Diego, CA, USA, March 2015.

[4] M. Ehrhart and L. Werner, "Image-based dynamic deformation monitoring of civil engineering structures from long ranges," in *Proceedings of the Image Processing: Machine Vision Applications VIII*, SPIE, San Francisco, CA, USA, February 2015.

[5] Y. Fukuda, M. Q. Feng, and M. Shinozuka, "Cost-effective vision-based system for monitoring dynamic response of civil engineering structures," *Structural Control and Health Monitoring*, Wiley, vol. 17, no. 8, pp. 918–936, 2010.

[6] A. V. Vasileva, A. S. Vasilev, and I. A. Konyakhin, "Vision-based system for long-term remote monitoring of large civil engineering structures: design, testing, evaluation," *Measurement Science and Technology*, IOP Publishing, vol. 29, no. 11, Article ID 115003, 2018.

[7] S. Schindler, F. Hegemann, C. Koch, M. König, and P. Mark, "Radar interferometry based settlement monitoring in tunnelling: visualisation and accuracy analyses," *Visualization in Engineering*, vol. 4, 2016.

[8] J. S. Bohn and J. Teizer, "Benefits and barriers of construction project monitoring using high-resolution automated

cameras," *Journal of Construction Engineering and Management*, vol. 136, no. 6, pp. 632–640, 2010.

[9] J. Yang, M.-W. Park, P. A. Vela, and M. Golparvar-Fard, "Construction performance monitoring via still images, time-lapse photos, and video streams: now, tomorrow, and the future," *Advanced Engineering Informatics*, vol. 29, no. 2, pp. 211–224, 2015.

[10] M. Golparvar-Fard, F. Peña-Mora, and S. Savarese, "Automated progress monitoring using unordered daily construction photographs and IFC-based building information models. ASCE," *Journal of Computing in Civil Engineering*, vol. 29, no. 1, 2015.

[11] H. Bashir and S. S. Ahmad, "Exploring geospatial techniques for spatiotemporal change detection in land cover dynamics along Soan River, Pakistan," *Environmental Monitoring and Assessment*, vol. 189, no. 5, p. 222, 2017.

[12] R. M. Ramachandran and C. S. Reddy, "Monitoring of deforestation and land use changes (1925-2012) in Idukki district, Kerala, India using remote sensing and GIS," *Journal of the Indian Society of Remote Sensing*, vol. 45, no. 1, pp. 163–170, 2017.

[13] A. Woldesenbet, H. D. Jeong, and H. Park, "Framework for integrating and assessing highway infrastructure data," *Journal of Management in Engineering*, vol. 32, no. 1, Article ID 04015028, 2016.

[14] B. Ferrer, J. C. Pomares, R. Irles, J. Espinosa, and D. Mas, "Image processing for safety assessment in civil engineering," *Applied Optics*, vol. 52, no. 18, p. 4385, 2013.

[15] L. Y. Chen, M.-Y. Wang, C.-C. Chao, and W. Lo, "Assessment of asphalt concrete pavement quality by using infrared thermal imaging technology," *Journal of Marine Science and Technology*, vol. 23, no. 3, pp. 331–338, 2015.

[16] Q. Chen and Y. Chen, "Construction material concrete quality detection method based on ultrasonic tomography technology," in *Proceedings of the 2020 IEEE International Conference on Industrial Application of Artificial Intelligence (IAAI)*, Harbin, China, December 2020.

[17] K. K. Patel, A. Kar, S. N. Jha, and M. A. Khan, "Machine vision system: a tool for quality inspection of food and agricultural products," *Journal of Food Science & Technology*, vol. 49, no. 2, pp. 123–141, 2011.

[18] O. H. Babatunde, L. Armstrong, J. Leng, and D. Dean, "A survey of computer-based vision systems for automatic identification of plant species," *Journal of Agricultural Informatics 6 Journal of Agricultural Informatics*, vol. 6, 2015.

[19] Q. Huang and S. K. Bhatia, "Application of digital image processing in morphological analysis of geotextiles," in *Proceedings of the Digital Image Processing: Techniques and Applications in Civil Engineering American Society of Civil Engineers National Science Foundation Engineering Foundation*, Kona, Hawaii, USA, March 1993.

[20] R. Chaney, K. Demars, D.-J. Jang, J. Frost, and J.-Y. Park, "Preparation of epoxy impregnated sand coupons for image analysis," *Geotechnical Testing Journal*, vol. 22, no. 2, p. 153, 1999.

[21] A. H. Aydilek, S. H. Oguz, and T. B. Edil, "Digital image analysis to determine pore opening size distribution of nonwoven geotextiles," *Journal of Computing in Civil Engineering*, vol. 16, pp. 280–290, 2002.

[22] E. Masad and K. Sivakumar, "Advances in the characterization and modeling of civil engineering materials using imaging techniques," *Journal of Computing in Civil Engineering*, vol. 18, no. 1, p. 1, 2004.

[23] O. G. Mirsalar Kamari, "Segmentation and analysis of a sketched truss frame using morphological image processing techniques," in *Proceedings of the International Conference On Civil Engineering, Architecture and Cityscape*, Shanghai, China, December 2016.

[24] Y. Wei, V. Kasireddy, and B. Akinci, "3D imaging in construction and infrastructure management: technological assessment and future research directions," in *Advanced Computing Strategies for Engineering. EG-ICE 2018*, I. Smith and B. Domer, Eds., vol. 10863, Lecture Notes in Computer Science, Berlin, Germany, Springer, 2018.

[25] K. Mróz, M. Tekieli, and I. Hager, "Feasibility study of digital image correlation in determining strains in concrete exposed to fire," *Materials*, vol. 13, no. 11, p. 2516, 2020.

[26] Z. Zhang, Y. Zheng, J. Zheng, and B. Li, "Feasibility of using high-speed imaging and digital image correlation techniques to analyze particle breakage process," in *Proceedings of the Geo-Congress 2020*, pp. 114–122, Minneapolis, Minnesota, February 2020.

[27] E. del Rey Castillo, T. Henry, M. Ingham, M. Griffithc, and J. Inghama, "Digital image correlation (DIC) for measurement of strains and displacements in coarse, low volume-fraction FRP composites used in civil infrastructure," *Composite Structures*, vol. 212, pp. 43–57, 2019.

[28] Z. Q. Chen and T. C. Hutchinson, "Urban damage estimation using statistical processing of satellite images: 2003 Bam Iran earthquake," in *Proceedings of the Color Imaging X: Processing, Hardcopy, and Applications SPIE, San Jose, CA, USA*, January 2005.

[29] D. F. Laefer, "Harnessing remote sensing for civil engineering: then, now, and tomorrow," in *Applications of Geomatics in Civil Engineering*, J. Ghosh and I. da Silva, Eds., vol. 33, Lecture Notes in Civil Engineering, Berlin, Germany, Springer, 2020.

[30] U. C. Benz, P. Hofmann, G. WillhauckIris, L. felder, and M. Heynen, "Multi-resolution, object-oriented fuzzy analysis of remote sensing data for GIS-ready information," *ISPRS Journal of Photogrammetry and Remote Sensing*, vol. 58, no. 3–4, 2004.

[31] S.-S. Leu and S.-L. Chang, "Digital image processing based approach for tunnel excavation faces," *Automation in Construction*, Elsevier BV, vol. 14, no. 6, pp. 750–765, 2005.

[32] A. Gaich and G. Pischinger, "3D images for digital geological mapping," *Geomechanics and Tunnelling*, Wiley, vol. 9, no. 1, pp. 45–51, 2016.

[33] M. W. Naikoo, M. Rihan, M. Ishtiaque, and F. Shah, "Analyses of land use land cover (LULC) change and built-up expansion in the suburb of a metropolitan city: spatio-temporal analysis of Delhi NCR using landsat datasets," *Journal of Urban Management*, vol. 9, no. 3, pp. 347–359, 2020.

[34] W. A. Bagwan and R. Sopan Gavali, "Dam-triggered land use land cover change detection and comparison (transition matrix method) of urmodi river watershed of Maharashtra, India: a remote sensing and GIS approach," *Geology, Ecology, and Landscapes*, pp. 1–9, 2021.

[35] S. Jayakumar and D. I. Arockiasamy, "Land use/land cover mapping and change detection in part of Eastern Ghats of Tamil Nadu using remote sensing and GIS," *Journal of the Indian Society of Remote Sensing*, vol. 31, no. 4, pp. 251–260, 2003.

[36] P. K. Mishra, A. Rai, and S. C. Rai, "Land use and land cover change detection using geospatial techniques in the Sikkim Himalaya, India," *The Egyptian Journal of Remote Sensing and Space Science*, vol. 23, no. 2, pp. 133–143, 2020.

[37] T. D. T. Oyedotun, "Land use change and classification in Chaohu Lake catchment from multi-temporal remotely sensed images," *Geology, Ecology, and Landscapes*, vol. 3, no. 1, pp. 37–45, 2019.

[38] C. Paiboonvorachat and T. J. Oyana, "Land-cover changes and potential impacts on soil erosion in the nan watershed, Thailand," *International Journal of Remote Sensing*, vol. 32, no. 21, pp. 6587–6609, 2011.

[39] N. Musaoglu, A. Tanik, and V. Kocabas, "Identification of land-cover changes through image processing and associated impacts on water reservoir conditions," *Environmental Management*, vol. 35, no. 2, pp. 220–230, 2005.

[40] M. Moniruzzaman, P. K. Thakur, P. Kumar et al., "Decadal urban land use/land cover changes and its impact on surface runoff potential for the dhaka city and surroundings using remote sensing," *Remote Sensing*, vol. 13, no. 1, p. 83, 2020.

[41] F.-J. Chang and C.-H. Chung, "Estimation of riverbed grain-size distribution using image-processing techniques," *Journal of Hydrology*, vol. 440-441, pp. 102–112, 2012.

[42] M. Ye, "A novel image fusion algorithm based on local contrast and improved PCNN model," in *Advanced Materials Research,* vol. 108-111, pp. 21–26, Trans Tech Publications, Ltd, 2010.

[43] L. Jiang, D. Zhang, and L. Che, "Texture analysis-based multi-focus image fusion using a modified Pulse-Coupled Neural Network (PCNN)," *Signal Processing: Image Communication*, vol. 91, Article ID 116068, 2021.

[44] Y. Liu, X. Chen, Z. Wang, Z. J. Wang, R. K. Ward, and X. Wang, "Deep learning for pixel-level image fusion: recent advances and future prospects," *Information Fusion*, vol. 42, pp. 158–173, 2018.

[45] Q. W. Lewis, E. M. Lindroth, and B. L. Rhoads, "Integrating unmanned aerial systems and LSPIV for rapid, cost-effective stream gauging," *Journal of Hydrology*, vol. 560, pp. 230–246, 2018.

[46] M. Coster and J.-L. Chermant, "Image analysis and mathematical morphology for civil engineering materials," *Cement and Concrete Composites*, Elsevier BV, vol. 23, no. 2-3, pp. 133–151, 2001.

[47] N. McCormick and J. Lord, "Digital image correlation for structural measurements," *Proceedings of the Institution of Civil Engineers - Civil Engineering*, Thomas Telford Ltd, vol. 165, no. 4, pp. 185–190, 2012.

[48] A. Suleiman and A. Ahmadreza Hedayat, "Digital image correlation and its application in an undergraduate civil engineering materials laboratory," 2014, https://1library.net/document/yjv3jkpy-digital-image-correlation-application-undergraduate-engineering-materials-laboraa.

[49] T. Ramos, A. Furtado, S. Eslami et al., "2D and 3D digital image correlation in civil engineering - measurements in a masonry wall," *Procedia Engineering*, Elsevier BV, vol. 114, , pp. 215–222, 2015.

[50] A. Golalipour, E. Jamshidi, Y. Niazi, Z. Afsharikia, and M. Khadem, "Effect of aggregate gradation on rutting of asphalt pavements," *Procedia - Social and Behavioral Sciences*, Elsevier BV, vol. 53, pp. 440–449, 2012.

[51] M. Vadood, M. S. Johari, and A. R. Rahaei, "Introducing a simple method to determine aggregate gradation of hot mix asphalt using image processing," *International Journal of Pavement Engineering*, Informa UK Limited, vol. 15, no. 2, pp. 142–150, 2013.

[52] K. Anding, D. Garten, and E. Linß, "Application of intelligent image processing in the construction material industry," *ACTA IMEKO*, vol. 2, no. 1, p. 61, 2013.

[53] P. Liu, A. Y. Chen, Y.-N. Huang et al., "A review of rotorcraft Unmanned Aerial Vehicle (UAV) developments and applications in civil engineering," *Smart Structures and Systems*, Techno-Press, vol. 13, no. 6, pp. 1065–1094, 2014.

[54] X. Kong and J. Li, "Non-contact fatigue crack detection in civil infrastructure through image overlapping and crack breathing sensing," *Automation in Construction*, vol. 99, pp. 125–139, 2019.

[55] J. Valença, I. Puente, E. Júlio, H. González-Jorge, and P. Arias-Sánchez, "Assessment of cracks on concrete bridges using image processing supported by laser scanning survey," *Construction and Building Materials*, vol. 146, pp. 668–678, 2017.

[56] F. Dong, "Evaluation and Detection System for Apparent Defects of Civil Engineering Structure. CN 109738460 A," Xijing University, Xi'an, China, 2019.

[57] U. Ozdemir, M. E. Kutay, D. Hibner, M. Lanotte, and Y. S. Kumbargeri, "Quantification of aggregate embedment in chip seals using image processing," *Journal of Transportation Engineering, Part B: Pavements*, vol. 144, no. 4, Article ID 04018047, 2018.

[58] H. Kim, S. Hamid, S. H. Han, and H. Nam, "Evaluation of asphalt pavement crack sealing performance using image processing technique," in *Proceedings of the 23rd International Symposium on Automation and Robotics in Construction. International Association for Automation and Robotics in Construction (IAARC)*, Tokyo, Japan, October 2006.

[59] P.-jo Chun and K. Hashimoto, "Development OF semi-automatic asphalt pavement crack detection system using image processing and machine learning approach," *Journal of Japan Society of Civil Engineers Ser. E1*, vol. 71, 2015.

[60] B. Mataei, F. Moghadas Nejad, M. Zahedi, and H. Zakeri, "Evaluation of pavement surface drainage using an automated image acquisition and processing system," *Automation in Construction*, Elsevier BV, vol. 86, , pp. 240–255, 2018.

[61] H. Oliveira and P. L. Correia, "CrackIT —\(\mathsemicolon\) an image processing toolbox for crack detection and characterization," in *Proceedings of the 2014 IEEE International Conference on Image Processing (ICIP). IEEE*, Paris, France, October 2014.

[62] S. Li, C. Yuan, D. Liu, and H. Cai, "Integrated processing of image and GPR data for automated pothole detection," *Journal of Computing in Civil Engineering*, vol. 30, no. 6, Article ID 04016015, 2016.

[63] A. Cubero-Fernandez, F. J. Rodriguez-Lozano, R. Villatoro, J. Olivares, and M. Jose, "Efficient pavement crack detection and classification," *EURASIP Journal on Image and Video Processing*, vol. 2017, Article ID 39, 2017.

[64] N.-D. Hoang, Q.-L. Nguyen, and D. Tien Bui, "Image processing-based classification of asphalt pavement cracks using support vector machine optimized by artificial bee colony," *Journal of Computing in Civil Engineering*, vol. 32, no. 5, Article ID 04018037, 2018.

[65] Z. Huang, "Evaluation and Detection System for Apparent Defects of Civil Engineering Structure. CN 108956638 A," Hunan University of Arts and Science, Changde, China, 2018.

[66] O. Hyon-Sohk and D. Roman, "Hryciw. Size distribution of coarse-grained soil by sedimaging," *Journal of Geotechnical and Geoenvironmental Engineering*, vol. 140, Article ID 04013053, 2014.

[67] C. Wang, A. Deng, and A. Taheri, "Digital image processing on segregation of rubber sand mixture," *International Journal of Geomechanics*, vol. 18, no. 10, Article ID 04018138, 2018.

[68] M. Saghafi, S. Mohammad Asgharzadeh, A. Fathi, and A. Hosseini, "Image processing method to estimate the wearing condition of slurry seal mixtures," in *Proceedings of the International Airfield and Highway Pavements Conference 2019*, Chicago, Illinois, July 2019.

[69] L. P. de Faria Borges, R. M. de Moraes, S. Crestana, and A. L. B. Cavalcante, "Geometric features and fractal nature of soil analyzed by X-ray microtomography image processing," *International Journal of Geomechanics*, vol. 19, no. 8, Article ID 04019088, 2019.

[70] M. Arbabpour Bidgoli, P. Hajikarimi, M. R. Pourebrahimi, K. Naderi, A. Golroo, and F. Moghadas Nejad, "Introducing adhesion-cohesion Index to evaluate moisture susceptibility of asphalt mixtures using a registration image-processing method," *Journal of Materials in Civil Engineering*, vol. 32, no. 12, Article ID 04020376, 2020.

[71] L. Zhao and L. Niu, "Study on key techniques of image processing and automatic recognition of tunnel cracks," in *Proceedings of the Inernational Conference of Logistics Engineering and Management 2012*, Chengdu, China, October 2013.

[72] M. M. Nejad, K. N. Manahiloh, and C. L. Meehan, "Applying the techniques of microstructural image processing toward measuring interface angles in unsaturated geomaterials," in *Proceedings of the Geotechnical Frontiers 2017*, Orlando, Florida, March 2017.

[73] H. Kim, A. F. Rauch, and C. T. Haas, "Automated quality assessment of stone aggregates based on laser imaging and a neural network," *Journal of Computing in Civil Engineering*, vol. 18, pp. 58–64, 2004.

[74] I. Detchev, A. Habib, F. He, and M. El-Badry, "Deformation monitoring with off-the-shelf digital cameras for civil engineering fatigue testing," in *Proceedings of the The International Archives of the Photogrammetry, Remote Sensing and Spatial Information Sciences*, pp. 195–202, Riva del Garda, Italy, June 2014.

[75] V. Chitra, "Growth of literature on lung cancer a scientometric analysis," http://hdl.handle.net/10603/137718 Thesis, Alagappa University, Karaikudi, India, 2014, http://hdl.handle.net/10603/137718 Thesis.

[76] Eugene Garfield, "From the science of science to scientometrics visualizing the history of science with HistCite software," *Journal of Informetrics*, vol. 3, no. 3, pp. 173–179, 2009.

[77] D. Kh. Valeev and V. G Golubtsov, "Legal scientometrics and civil studies," *Methodological Problems of Civil Studies*, STATUT Publishing House LLC, Moscow, Russia, 2018.

[78] L. Leydesdorff and S. Milojevic, ""Scientometrics" arXiv: 1208.4566 (2013), forthcoming," in *International Encyclopedia of Social and Behavioral Sciences Subsection 85030*, M. Lynch, Ed., Elsevier, Amsterdam, Netherlands, 2015.

[79] P. Jacquot and M. Facchini, "Interferometric imaging: involvement in civil engineering," *Journal of Computing in Civil Engineering*, vol. 13, pp. 61–70, 1999.

Hindawi
Advances in Civil Engineering
Volume 2022, Article ID 2908616, 14 pages
https://doi.org/10.1155/2022/2908616

Research Article

Research and Model Prediction on the Performance of Recycled Brick Powder Foam Concrete

Hongyang Xie, Jianjun Dong, Yong Deng, and Yiwen Dai

College of Civil Engineering and Architecture, Nanchang Hangkong University, Nanchang, Jiangxi 330063, China

Correspondence should be addressed to Jianjun Dong; 1911085213105@stu.nchu.edu.cn

Received 7 January 2022; Accepted 24 February 2022; Published 30 March 2022

Academic Editor: Ravindran Gobinath

In order to achieve resource conservation, protect the environment and realize the sustainable development of the construction industry, the low energy resource utilization of construction waste was explored. In this paper, the effect of air bubble swarm admixture, recycled brick powder admixture, water to material ratio, and HPMC content on the physical and mechanical properties of recycled brick powder foam concrete was investigated by conducting a 4-factor, 5-level orthogonal test with recycled brick powder as fine aggregate, and the effect of each factor on the physical and mechanical properties of recycled brick powder foam concrete was derived, and the optimum ratio of recycled brick powder foam concrete was determined by analysing the specific strength. Five machine learning models, namely, back propagation neural network improved by particle swarm optimization (PSO-BP), support vector machine (SVM), multiple linear regression (MLR), random forest (RF), and back propagation neural network (BP), were used to predict the compressive strength of recycled brick powder foam concrete, and the PSO-BP model was found to have obvious advantages in terms of prediction accuracy and model stability. The experimental results and prediction models can provide experimental and theoretical references for the research and application of recycled brick powder foam concrete.

1. Introduction

With the development of urbanization, the amount of construction and demolition waste is increasing rapidly. In China, about 1.8 billion tons of construction waste are generated every year [1]. In the past, construction waste was often dumped or landfilled, which not only wasted land and resources but also polluted the environment. Xiao et al. [2] reported that, about 80% of construction waste was reusable construction waste, such as waste concrete, bricks, and glass. Therefore, it has become an effective way to use construction waste as recycled aggregate for cement-based materials. Recycled concrete aggregates are equipped with similar properties to natural aggregates, which have been widely used in concrete production. Previous studies [3–5] have reported that recycled brick powder (RBP) has similar characteristics as supplementary cementitious materials, such as high content of SiO_2 and Al_2O_3. However, waste clay brick aggregates are of high crushing value and water absorption, which limits their large-scale application in concrete. Therefore, the effective utilization of clay bricks recovered from construction waste has become a top priority.

Foam concrete takes the cement-based cementitious materials, admixtures, and so on, as the main cementing materials. The admixtures and water, or some granular lightweight aggregates, are added to make slurry. It is a lightweight concrete material that contains a large number of tiny, independent, and evenly-distributed bubbles formed by casting and curing at the construction site or in the factory [6]. In recent years, foam concrete has been widely used in the field of civil engineering as a building material with excellent performance. Foam concrete consumes a large amount of cementitious material [7], with more expensive costs and lower strength than structural concrete. Reducing the amount of cementitious materials while maintaining its light weight and increasing strength is an important direction for studying the mix ratio of foam concrete [8].

Studies have shown that adding fillers and improving the pore structure can effectively increase the strength of foamed concrete [9–13]. Domestic and foreign scholars have explored the possibility of replacing cementitious materials with various materials [14–18]. However, few reports have emerged on using recycled brick powder as a filler for foam concrete.

In this paper, recycled brick powder was prepared based on the waste clay bricks produced by demolishing houses in rural areas. Based on the test of ordinary foam concrete, recycled brick powder and hydroxypropyl methyl cellulose ether (HPMC) foam stabilizer was added to explore the influence of bubble group content, recycled brick powder content, water-to-material ratio, and HPMC content on the compressive strength of recycled brick powder foam concrete. The pore size distribution and microscopic morphology were observed, the parameter sensitivity of various factors were analyzed through neural network and machine learning theory, and the compressive strength of recycled brick powder foam concrete cubes was predicted.

2. Experiment Overview

2.1. Raw materials

2.1.1. Cement. The cement should also have high strength and not compromise the stability of the foam, based on compliance with the Chinese standard "General Silicate Cement" (GB175-2007) [19]. Conch brand P.O.42.5 ordinary Portland cement was used in this experiment. The chemical composition and basic properties of the cement are shown in Table 1.

2.1.2. Recycled Brick Powder. Crush the waste clay bricks to Table 2 particles of about 4.75 mm with a hammer crusher and use a ball mill to grind them for one hour to obtain regenerated recycled brick powder particles of 10 to 80 μm. Figure 1 shows the waste clay bricks, and Figure 2 shows the recycled brick powder.

2.1.3. Foaming Agent. The HT composite foaming agent produced by Henan Huatai Building Materials Co., Ltd., was used, while its physical properties are shown in Table 3.

The foaming agent performance test was carried out in accordance with the Chinese standard "Technical Regulations for Air-bubble Mixed Lightweight Soil Filling Engineering," and the results showed that the HT compound foaming agent diluted 30 times had the lowest water secretion and the smallest settling distance. The preparation process is shown in Figure 3.

2.1.4. Foam Stabilizer. HPMC produced by Fuqiang Fine Chemical Co., Ltd., was adopted, and its physical performance indicators are shown in Table 4. Figure 4 shows a photograph of the hydroxypropyl methyl cellulose ether (HPMC).

Table 1: Chemical composition of cement.

Component	SiO_2	Fe_2O_3	Al_2O_3	CaO	MgO	SO_3
Content (%)	22	4.2	5.2	63	1.5	2.2

Table 2: Basic properties of cement.

Item	Index	Results	Judgement
Initial set time (min)	≥60	176	Qualified
Final set time (min)	≤600	310	Qualified
3d flexural strength (MPa)	≥3.5	4.2	Qualified
28d flexural strength (MPa)	≥6.5	7.1	Qualified
3d compressive strength (MPa)	≥17	22.3	Qualified
28d compressive strength (MPa)	≥42.5	48.2	Qualified

Figure 1: Waste clay bricks.

Figure 2: Recycled brick powder.

2.2. Calculation of mix Ratio. The commonly-used methods of concrete mix design comprised the volume method and mass method. Due to the light mass of bubbles, the volume method was adopted in this research after a comprehensive consideration [20]. According to formula (5.2.1-1) in the Chinese standard "Technical Specification for Foamed Mixture Lightweight Soil Filling Engineering," the mix ratio calculation is conducted, and the expression is as follows:

Table 3: Physical performance indicators of HT composite foaming agent.

HT	Appearances	Density (g/cm^3)	Solid content (%)	pH value	Dilution ratio	Settlement distance for 1 h (mm)	Bleeding rate for 1 h (%)
	Dark brown	1.05	23.8	9.2	15~30	≤50	≤70

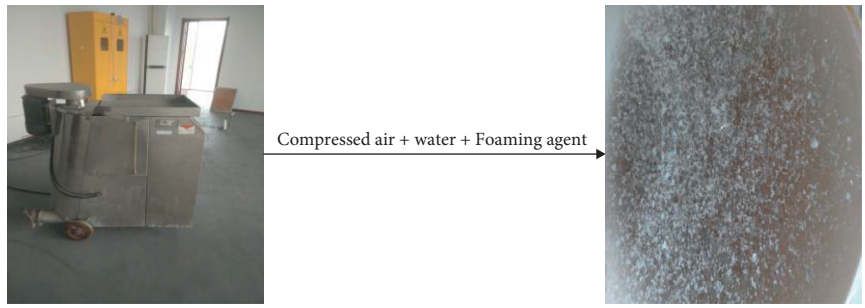

Figure 3: Foam preparation process.

Table 4: Physical performance indicators of HPMC.

Indicator results	Appearances	Viscosity (Pa s)	PH value	Water content (%)
	White powder	150	6.5	2.1

Figure 4: HPMC.

$$\frac{m_c}{\rho_c} + \frac{m_w}{\rho_w} + \frac{m_f}{\rho_f} + \frac{m_f}{\rho_f} = 1. \quad (1)$$

In the formula, m_c: cement dosage per cubic meter of foam concrete (kg); ρ_c: cement density (kg/m^3); m_w: water consumption per cubic meter of foamed concrete; ρ_w density of water (kg/m^3), taking 1000 kg/m^3; m_f.: amount of air foams per cubic meter of foam concrete (kg); ρ_f.: density of air foams (kg/m^3); m_m: mixture amount of foam concrete per cubic meter (kg); ρ_m: density of the admixture (kg/m^3).

2.3. Mixture Ratio Data of Ordinary Foam Concrete. To explore the performance difference between recycled brick powder foam concrete and ordinary foam concrete, ordinary foam concrete test blocks were made as a control group. The ordinary foam concrete adopted the orthogonal test of two factors and five levels, and the change range of the bubble swarm content was 3% to 7%, while the change range of the water-cement ratio was 0.45 to 0.65. The data is shown in Table 5.

2.4. Test Pieces Preparation and Test Methods. Ordinary foam concrete specimens were made according to the following process: (1) Accurately weigh the quality of cement; (2) Add water of accurate quality into the mixer, and then quickly stir for 150 seconds; (3) Add the foaming agent aqueous solution to the cement foaming integrated machine, pressurize the air to foam, prepare to measure the mass of the bubble group, and quickly add it to the cement slurry of construction waste, and stir for 120 seconds. When the mixing is uniform and no bubbles have emerged on the surface of the slurry, the fluidity test is conducted immediately. After meeting the requirements of 160 to 200 mm, quickly pour it into a 100 mm × 100 mm × 100 mm mold, and gently flip the mold to prevent irregular test blocks: (4) After standing for 36 hours, scrape the surface of the mold and remove it with an air gun. To fulfill the strength requirements, it needs to be stored in a standard curing room with a temperature of 20 ± 2°C and a humidity of 95% or more, as well as normal curing for 28 days.

The process of making recycled brick powder foam concrete specimens (1) was as follows: Accurately weigh the quality of cement, recycled brick powder and HPMC, and drily mix with a mixer for 150 seconds. The process from (2) to (4) was the same as that of the control group. The preparation process for the recycled brick powder foam concrete specimens in this paper is shown in Figure 5.

Table 5: Mixture ratio data of ordinary foam concrete.

Group number	Bubble volumes (%)	Water cement ratio	Cement (g)	Bubble groups (g)	Water (g)
1	3	0.45	728.55	21.86	327.85
2	3	0.50	702.95	21.09	351.48
3	3	0.55	679.08	20.37	373.49
4	3	0.60	656.78	19.70	394.07
5	3	0.65	635.90	19.08	413.34
6	4	0.45	635.90	25.44	286.16
7	4	0.50	616.30	24.65	308.15
8	4	0.55	597.88	23.92	328.83
9	4	0.60	580.52	23.22	348.31
10	4	0.65	564.15	22.57	366.70
11	5	0.45	564.15	28.21	253.87
12	5	0.50	548.73	27.44	274.37
13	5	0.55	534.02	26.70	293.71
14	5	0.60	520.13	26.01	312.08
15	5	0.65	506.95	25.35	329.52
16	6	0.45	506.95	30.42	228.13
17	6	0.50	494.42	29.67	247.21
18	6	0.55	482.49	28.95	265.37
19	6	0.60	471.12	28.27	282.67
20	6	0.65	460.28	27.62	298.18
21	7	0.45	460.28	32.22	207.13
22	7	0.50	449.93	31.50	224.97
23	7	0.55	440.03	30.80	242.02
24	7	0.60	430.56	30.14	258.34
25	7	0.65	421.48	29.50	273.96

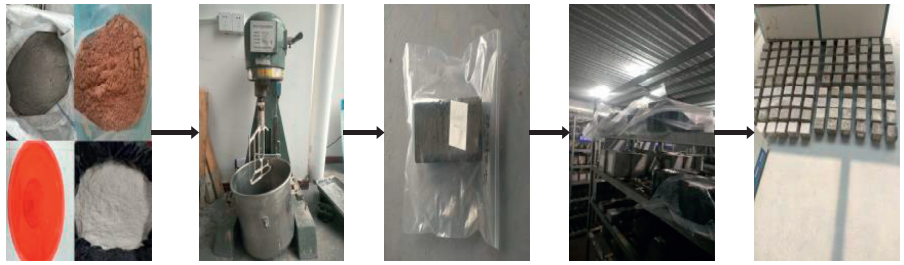

Figure 5: Test piece preparation process for recycled brick powder foam concrete.

The dry density of the control and experimental group specimens were measured according to the Chinese standard "Foam Concrete" [21]; the determination of the compressive strength of the control group and the experimental group could refer to the Chinese standard "Standard for Test Methods of Mechanical Properties of Ordinary Concrete" and "Test methods of Autoclaved aerated Concrete" [22].

2.5. Orthogonal Mix Ratio Design. Recycled brick powder foam concrete adopted an orthogonal test of 4 factors and 5 levels, that was, the orthogonal test table was L25 (4^5). The four factors of bubble group content, recycled brick powder content, water-to-material ratio, and HPMC content were used, respectively, for experimental research. The specific level factor data is shown in Table 6.

3. Experimental Results and Analysis

3.1. Orthogonal Experiment Results. The orthogonal test results of recycled brick powder foam concrete are shown in Table 7.

The orthogonal test results of ordinary foam concrete are shown in Table 8.

According to the orthogonal test results in Tables 7 and 8, the compressive strength is analyzed through the extremely poor method [23]. The larger the range value is, the greater the influence of this factor on the compressive strength would be. The results are shown in Tables 9 and 10.

The influence order of various factors on the compressive strength of recycled brick powder foam concrete can be obtained from Table 9 as follows: bubble volume > recycled brick powder volume > the ratio of water to

Table 6: Orthogonal test factor level of experimental group.

Level	Factor			
	Bubble volumes (A) (%)	Recycled brick powder volume (B) (%)	Water to material ratio (C) (%)	HPMC content (D)
1	3	10	0.45	0.03
2	4	20	0.5	0.04
3	5	30	0.55	0.05
4	6	40	0.6	0.06
5	7	50	0.65	0.07

Table 7: Orthogonal test results of recycled brick powder foam concrete.

Group number	Dry density (kg/m^3)	28 d compressive strength (MPa)	Specific strength ($N{\cdot}m{\cdot}kg^{-1}$)	Group number	Dry density (kg/m^3)	28 d compressive strength (MPa	Specific strength ($N{\cdot}m{\cdot}kg^{-1}$)
1	1171.10	6.07	5185.30	14	710.85	0.84	1186.89
2	1210.25	5.80	4792.61	15	838.75	2.37	2830.70
3	988.00	5.76	5833.35	16	806.80	2.11	2621.41
4	1072.75	4.55	4241.30	17	952.50	2.82	2955.64
5	1039.45	3.09	2975.81	18	857.60	2.47	2882.64
6	997.15	5.17	5183.17	19	647.65	1.74	2686.56
7	854.25	4.23	4947.38	20	889.40	1.25	1404.43
8	680.85	3.11	4570.76	21	769.50	2.15	2794.67
9	937.55	2.26	2410.22	22	975.85	2.58	2645.59
10	1071.20	3.04	2838.83	23	851.15	1.51	1777.36
11	988.20	5.31	5369.92	24	675.20	1.96	2901.14
12	1008.45	2.76	2736.92	25	786.60	0.96	1226.04
13	721.45	1.46	2020.72				

Table 8: Orthogonal test results of ordinary foam concrete.

Group number	Dry density (kg/m^3)	28 d compressive strength (MPa)	Specific strength ($N{\cdot}m{\cdot}kg^{-1}$)	Group number	Dry density (kg/m^3)	28 d compressive strength (MPa)	Specific strength ($N{\cdot}m{\cdot}kg^{-1}$)
1	743.55	2.290	3079.82	14	591.6	1.182	1997.97
2	722.38	2.229	3085.63	15	590.3	1.014	1717.77
3	707.6	1.998	2823.63	16	644.1	1.734	2692.13
4	714.9	2.012	2814.38	17	628.7	1.548	2462.22
5	639.4	1.668	2608.70	18	584.1	0.949	1624.72
6	536.0	0.880	1641.79	19	599.7	1.212	2021.01
7	735.2	2.109	2868.61	20	550.3	0.919	1670.00
8	797.1	2.408	3020.95	21	608.4	1.229	2020.05
9	648.6	0.853	1315.14	22	500.1	0.875	1749.65
10	567.4	0.830	1462.81	23	672.7	1.462	2173.33
11	713.8	1.657	2321.38	24	592.8	1.073	1810.05
12	638.2	1.471	2304.92	25	567.4	0.951	1676.07
13	615.9	1.631	2648.16				

Table 9: Analysis of extreme differences in compressive strength of recycled brick powder foam concrete.

	Bubble volumes	Recycled brick powder volume	Water to material ratio	HPMC content
K1	5.06	4.16	3.00	2.77
K2	3.56	3.64	3.32	2.88
K3	2.55	2.86	3.70	3.11
K4	2.08	2.27	2.70	3.16
K5	1.83	2.14	2.36	3.17
Extreme difference value R	3.22	2.02	1.35	0.40
Rank	1	2	3	4

Table 10: Analysis of extreme differences in compressive strength of ordinary foam concrete.

	Bubble volumes	Water cement ratio
K1	2.04	1.56
K2	1.42	1.65
K3	1.39	1.69
K4	1.27	1.27
K5	1.12	1.08
Extreme difference value R	0.92	0.61
Rank	1	2

material > HPMC content. Table 10 shows that the amount of bubble exerts a greater effect on the compressive strength of ordinary foam concrete.

The data in Tables 9 and 10 is visualized, as shown in Figure 6.

Figure 6(a) shows that the compressive strength of recycled brick powder foam concrete and ordinary foam concrete both show a decreasing trend with the increase of the amount of air bubble, which drop by 63.6% and 45.1%, respectively. The increase in the bubble volume poses a significant effect on reducing the compressive strength of recycled brick powder foam concrete. The main reasons are as follows: (1) the increase in the bubble volume is accompanied by the decrease in the amount of cementitious material, which are the main source of the strength of recycled brick powder foam concrete; (2) the increase in the bubble volume will increase the pore volume and produce numerous harmful pores, which will make the pore distribution in the specimen uneven and reduce the strength.

Figure 6(b) shows that the compressive strength of recycled brick powder foam concrete is decreased by 48.6% with the increase in the amount of recycled brick powder. The main reasons are as follows: (1) the increase in the amount of recycled brick powder is accompanied by the decrease in the amount of cement, which leads to the reduction of C-S-H hydration products and the decrease in strength; (2) the reduction of cement content has led to the deformation of a dense skeleton in part of the recycled brick powder; (3) the main component of recycled brick powder is glassy SiO_2, which is an inert material. Although it contains a small amount of Al_2O_3, most of the substances do not participate in the early hydration reaction of cement-based materials, while the increase in the substitution rate will reduce the strength; (4) the mixture of recycled brick powder poses a dilution effect on the cement and increased the effective water-cement ratio.

Figure 6(c) shows that the compressive strength of recycled brick powder foam concrete and ordinary foam concrete are increased at first and then decreased with the increase in water-to-material ratio. The reasons are as follows: (1) when the water-to-material ratio is within the range of 0.45 to 0.55, the compressive strength of recycled brick powder foam concrete is increased with the increase of the water-to-material ratio. As recycled brick powder is of a certain pozzolanic activity, the water demand is more than that of virgin materials. As the amount of water is increased, the pozzolanic activity of recycled brick powder helps in generating more C-S-H gel, which further improves the microstructure of recycled brick powder foam concrete, thereby increasing its strength [24]. (2) When the water-to-material ratio is between 0.60 and 0.65, the compressive strength of recycled brick powder foam concrete is decreased as the water-to-material ratio is increased, which is mainly due to the following: (1) the amount of water is excessive. Due to the different densities, the denser components in the recycled brick powder are left underneath, and the bubbles and remaining cementitious materials are on the top, leading to delamination; (2) excessive water thickens the bubble group liquid film, which will accelerate the bleeding under the action of gravity, leading the bubble group to bursting prematurely or forming numerous harmful holes, thereby reducing the strength.

Figure 6(d) shows that the compressive strength of recycled brick powder foam concrete is increased with the increase of HPMC content, while the increasing rate is gradually slowed. The reasons are as follows: with the increase in the HPMC content, the performance of the bubble group is improved, the shape of the pores, the distance between the holes, and the pore diameter are all improved. Moreover, the bubble group is uniformly distributed in the slurry. Therefore, the strength is improved. However, as the strength of recycled brick powder foam concrete is mainly derived from cementitious materials, the upward trend tends to be flat.

3.2. Determination of the Optimal Mix Ratio. The specific strength is the ratio of the strength of a material to its dry density, and it is an important indicator to measure the light weight and high strength of the material [21]. The greater the specific strength is, the better the light-weight and high-strength performance of the material would be [25]. Table 7 shows that the specific strength of the test blocks under the mix ratios in the 3rd group is the largest, as the level of recycled brick powder foam concrete that fulfilled the requirements of light weight and high strength is $A_1B_3C_3D_3$. That is, the optimal mixing ratio is 3% of the bubble group content, 30% of the recycled brick powder content, 0.55 of the water-to-material ratio, and 0.05% of the HPMC content. It can be concluded from Table 8 that the specific strength of the test block is the largest under the mix ratios in the 2nd group, that is, the optimal mix ratio of ordinary foam concrete is 3% of the bubble group content and 0.50 water-cement ratio.

For the optimal mix ratio of recycled brick powder foam concrete, the water-to-cement ratio is 0.55, while for the optimal mix ratio of ordinary foam concrete, the water-cement ratio is 0.50. That is, adding recycled brick powder requires more water to promote the complete hydration of the cementitious material. The dry density of the 3rd group of specimens in Table 7 is 988 kg/m^3, while the 28 d compressive strength is 5.76 MPa; The dry density of the 2nd group of specimens in Table 8 is 722.38 kg/m^2, and the 28 d compressive strength is 2.229 MPa. The compressive strength of recycled brick powder foam concrete with 28 d compressive Strength is 2.58 times that of ordinary foam concrete, while the compressive strength of dry density

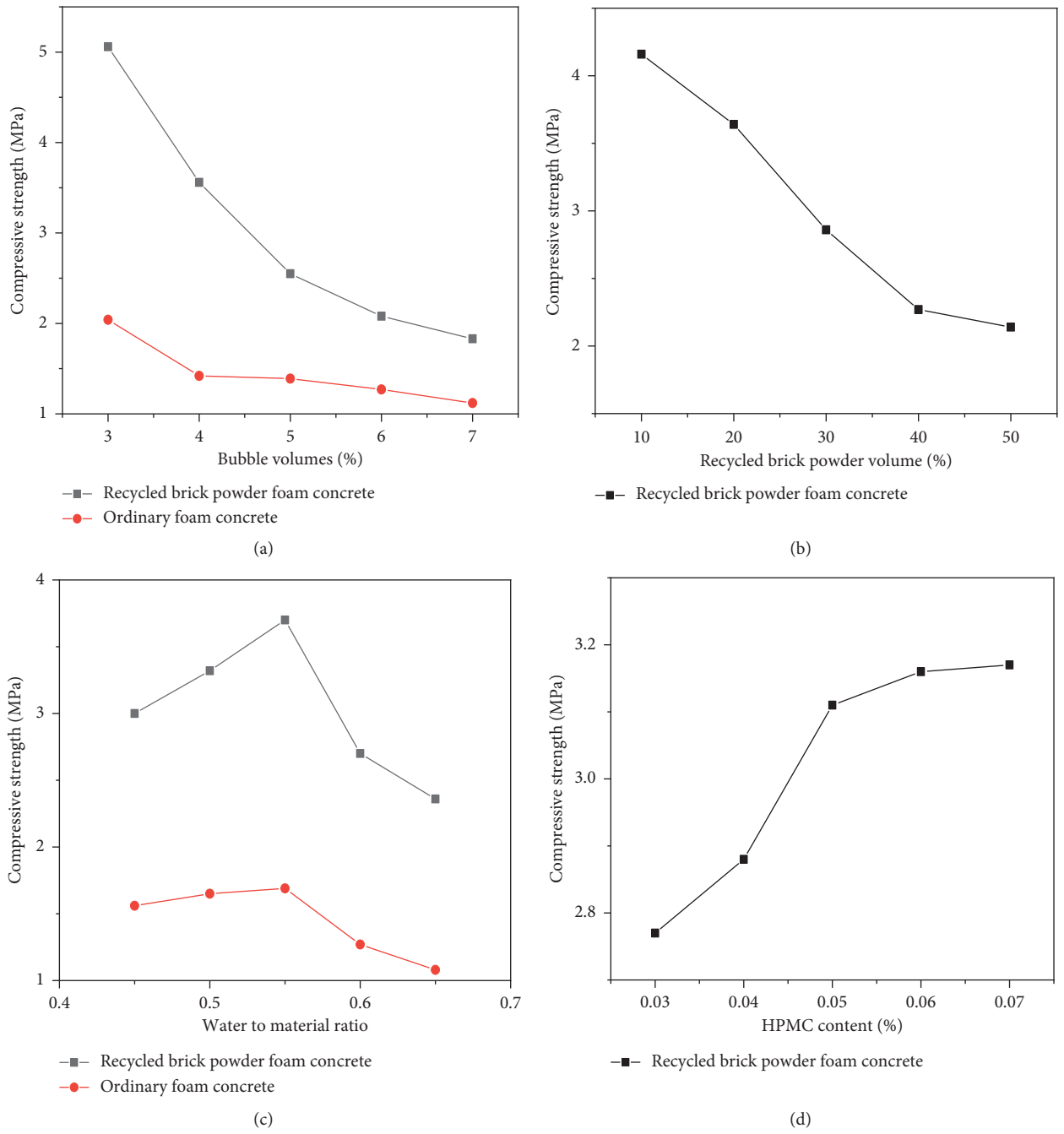

Figure 6: Changes in the influence of various factors on compressive strength.

recycled brick powder foam concrete is 1.37 times that of ordinary foam concrete. Although the addition of recycled brick powder will increase the dry density of foam concrete, the increase in compressive strength is even greater.

3.3. Microscopic Morphology Analysis. The optimal mix ratio test piece can be observed by the SU8100 scanning electron microscope, and the test results are shown in Figure 7.

The pore diameter of the samples was measured by the NanoMeasure software. Figure 3 shows that the average pore diameter of the ordinary Figure 8 foam concrete is 109.73 μm, and the average pore diameter of the recycled brick powder foam concrete is about 72.17 μm, a reduction of 34.2%. The pore wall thickness in Figure 7(b) is obviously greater than that in Figure 7(a). Obvious micro-filling effects can be found. Therefore, the added recycled brick powder refines the pores, increases the compactness of the concrete matrix, and improves the compressive strength of the recycled brick powder foam concrete. When the multiplying factor is 50x, the pore diameter is large with obvious connecting holes in Figure 8(a). In Figure 8(b), the pore diameter is smaller, the pore structure is more uniform, the wall between the pores is dense, the communicating pores

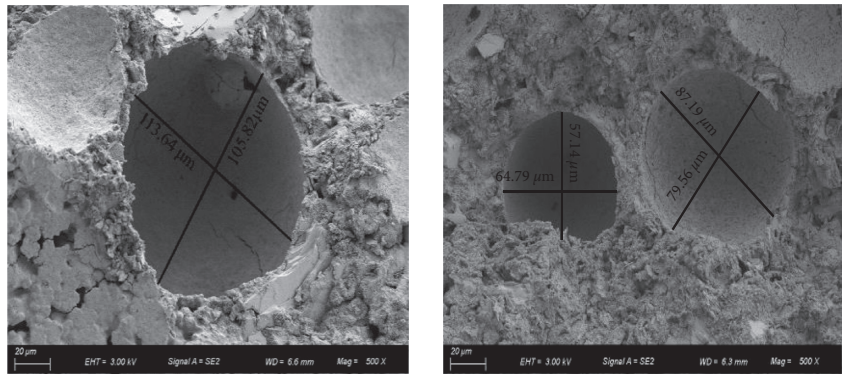

Figure 7: Photograph of 28 d hydration of the specimen when scanned by electron microscope at 500x.

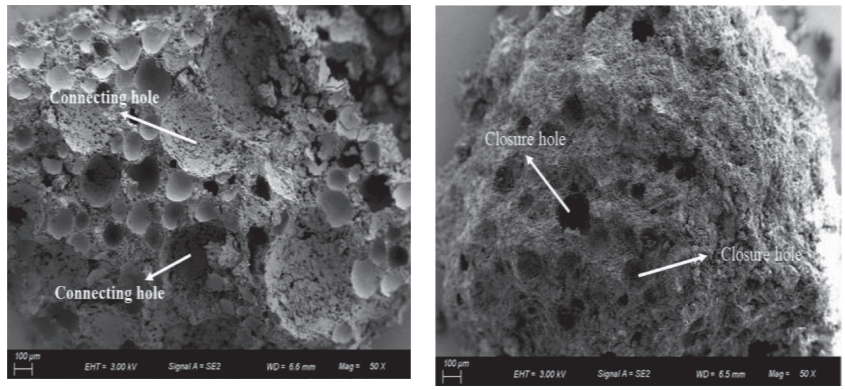

Figure 8: Photograph of 28 d hydration of the specimen when scanned by electron microscope at 50x.

are less, and the closed pores are more. As a foam stabilizer, HPMC reduces the occurrence of harmful pores such as connecting holes in the test piece, and makes the pore distribution more uniform.

3.4. Correlation Analysis of Various Factors and Recycled Brick Powder Foam Concrete. To investigate the correlation between the compressive strength of recycled brick powder foam concrete and the bubble volumes, the amount of recycled brick powder, the water-to-material ratio, and the HPMC content, the Pearson correlation coefficient was used for analysis. The Pearson correlation coefficient [26] (also known as covariance correlation or Bravais–Pearson correlation) describes the degree of correlation between two fixed-ratio, linearly correlated variables (measurement value series) that are not less than affected by their units (also known as tightness). The Pearson correlation coefficient is calculated based on the covariance and product of mean difference of two variables, and its calculation formula is as follows:

$$r = \frac{\operatorname{cov}(x, y)}{S_x \bullet S_y} = \frac{\sum_i^n \left((x_i - \overline{x}) \bullet (y_i - \overline{y})\right)}{n \bullet S_x \bullet S_y}. \quad (2)$$

In the formula: $\operatorname{cov}(x, y)$ is the covariance of variables x and y; S_x and S_y are the variances of variables x and y; n is the number of variables; $\overline{x}$ and $\overline{y}$ are the mean values of variables x and y, respectively. The value of the correlation coefficient is generally between −1 and 1. The greater the absolute value of the correlation coefficient is, the stronger the correlation of 2 variables would be. If the absolute value of the correlation coefficient is close to 1, it indicates that a perfect linear correlation exists between the two variables; if it is close to 0, no linear correlation exists between the two variables [27].

In the Figure 9, $X1$, $X2$, $X3$, and $X4$ represent the volume of bubble volumes, the volume of recycled brick powder, water-to-material ratio, and HPMC content, respectively. $Y1$ represents the compressive strength of recycled brick powder foam concrete. The order of correlation is as follows: bubble volume > recycled brick powder volume > the ratio of water to material > HPMC content, which is consistent with the results from the orthogonal test analysis. The amount of bubble volume poses a significant effect on the compressive strength of recycled brick powder foam concrete.

3.5. PSO-BP (Back Propagation Neural Network Improved by Particle Swarm Optimization) Prediction. For the recycled brick powder foam concrete, due to the increase in its components, the hydration reaction mechanism is not

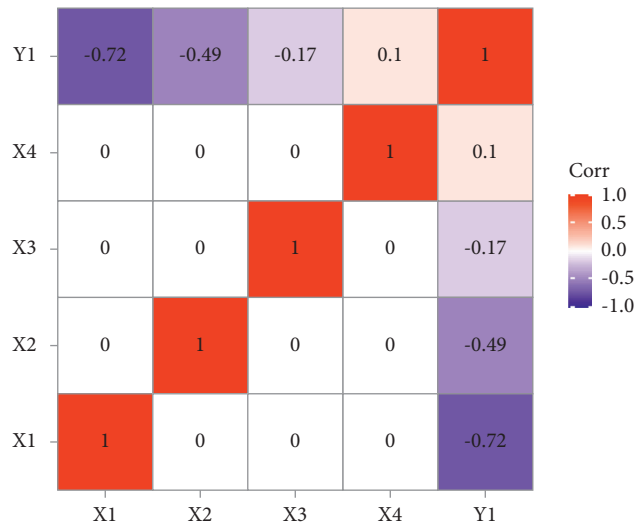

Figure 9: Heat map of the correlation between each factor and the compressive strength of the cube.

completely clear. The influencing factors are complex and interactive, which manifests as a specific high-dimensional nonlinear law [28]. The BP neural network is an effective method to solve high-dimensional nonlinear problems. Among them, the PSO-BP [29] neural network defines the initial weights and thresholds of the BP neural network as the particles in the particle swarm optimization algorithm. All particles form a group, and the optimal solution is found through cooperation and information-sharing between individuals in the group. The defects of multiple local extreme points in the BP neural network and difficulty in establishing mathematical models can be avoided. The PSO-BP model consists of the following steps [29].

Step 1. Enter the mix ratio and compressive strength data of recycled brick powder foam concrete and randomly assign 70% of the data as the training set and 30% of the data as the test set.

Step 2. Initialize the parameters of the BP neural network.

Step 3. The initial weights and thresholds are extracted from the BP neural network, encoded as a set of particles in the PSO (group size N). Initialize the number of iterations t, maximum number of iterations $t_{\max}$, inertia weight W, and acceleration factor $c1$ and $c2$.

Step 4. Assume the position of each particle X_i and the velocity of each particle V_i in space.

Step 5. Evaluate the fitness value of all particles and obtain the best personal solution *pbest* and the best group solution *gbest*.

Step 6. Use *pbest* and *gbest* to correct the velocity of each particle $V_i(t+1)$.

Step 7. Correct the position of each particle $X_i(t+1)$.

Step 8. Repeat Step 4 to Step 6 until $t \geq t_{\max}$.

Step 9. The optimized position *gbest* can be obtained.

Step 10. The optimized BP neural network model is trained with the training set, and the accuracy of the model is verified with the test set.

The establishment process of the PSO-BP neural network in this paper is shown in Figure 10.

Taking cement quality, bubble group quality, recycled brick powder quality, water and HPMC quality as input independent variables, and the compressive strength of recycled brick powder foam concrete as output dependent variables, a 5-1-11-1 PSO-BP neural network was established. The prediction of the cubic compressive strength of recycled brick powder foam concrete and the strength of the specimen are compared as shown in Figure 11.

Figure 11 shows that the predicted compressive strength of the PSO-BP model is close to the actual value, that is, the prediction result of the PSO-BP model is more accurate, with small errors and high fitting accuracy.

3.6. Model Performance Comparison. The prediction performance of the PSO-BP model was compared with various models, including the support vector machine (SVM), multiple linear regression (MLR), random forest (RF), and artificial neural network (BP) models. The fitting effect is shown in Figure 12.

Figure 12 shows that most of the scattered data of the prediction model of PSO-BP are concentrated in and around the 100% regression line. While SVM, MLR, RF and BP scattered point data are very discrete, the data in Figure 11 is fitted according to the form of $y = a_0 x + a_1$.. Compared with the four models in the control group, the a_0 value of the PSO-BP model is closer to 1 and a_1 values are closer to 0. The

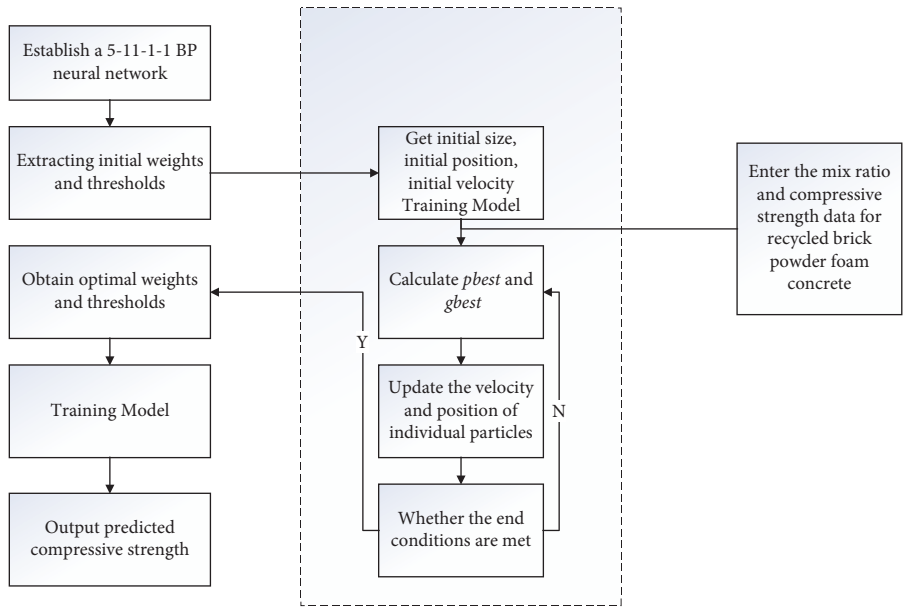

Figure 10: Establishment process of PSO-BP neural network.

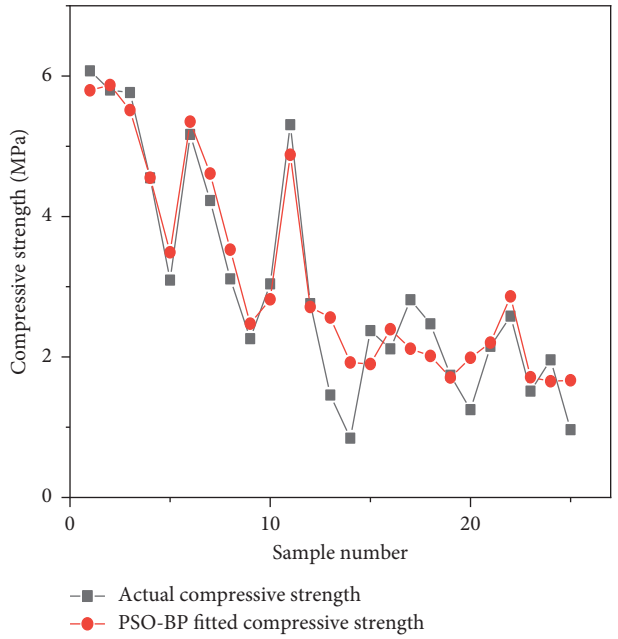

Figure 11: PSO-BP model fitting effect diagram.

prediction accuracy of the PSO-BP model is higher and the error is smaller.

3.7. Statistical Indicators of the Model. In this paper, five statistics were selected to evaluate the prediction accuracy of the PSO-BP model and the control model, as the coefficient of determination (R^2), the mean square error (RMSE), the mean error (MAE), the calculation formula of the average absolute deviation percentage error (RMAE), and benefit coefficient (E) [30–32]. The calculation formula is shown in Table 11.

According to the evaluation index formula describes in Table 11, the calculation results are shown in Table 12.

The coefficient of determination R^2 is widely used in regression problems to estimate the correlation between the target value and the predicted value; RMSE and MAE are two standards used to measure the average error between the target and the predicted output; RMAE represents the average percentage size of the total absolute deviation error between the target value and the predicted output; the efficiency coefficient E (%) represents the prediction accuracy of the model. The value of R^2 is close to 1, the values of RMSE, MAE, and RMAE are close to 0, and the value of E is

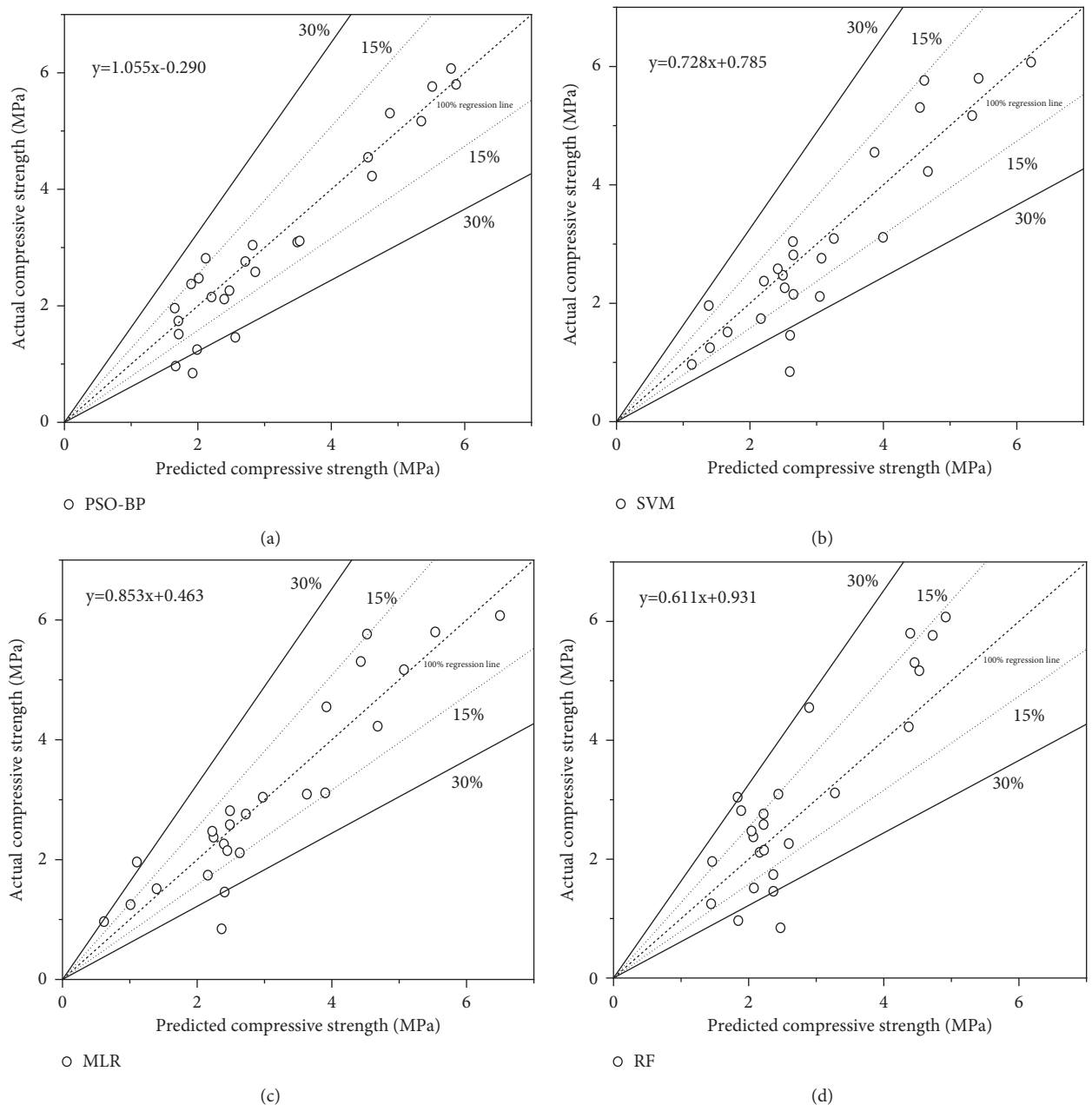

Figure 12: Continued.

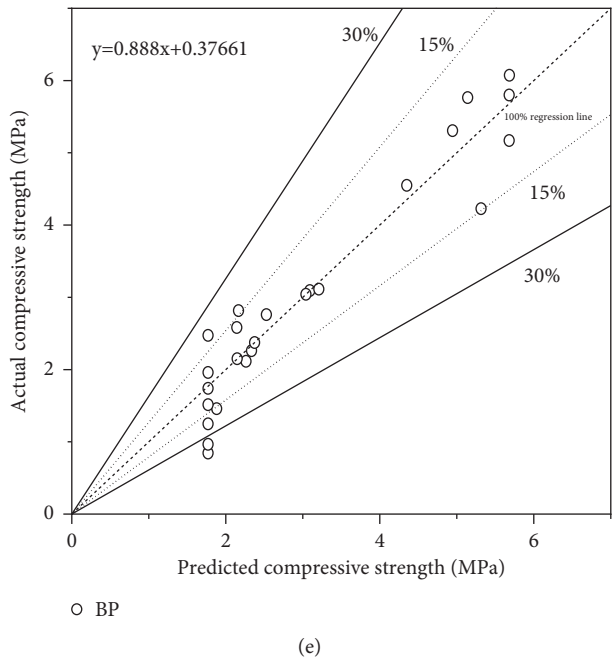

(e)

Figure 12: Scattered distribution diagram of predicted and actual values of each model.

Table 11: Calculation formula of statistical indicators.

Measure	Calculation
Coefficient of determination ($R2$)	$R^2 = 1 - 1/N \sum_{i=1}^{N} (Y_i - \overline{Y})^2 / 1/N \sum_{i=1}^{N} (Y_i - \overline{Y})^2$
Root mean square error (RMSE)	$\mathrm{RMSE} = \sqrt{1/N \sum_{i=1}^{N} (Y_i - \overline{Y})^2}$.
Mean absolute error (MAE)	$\mathrm{MAE} = 1/N \sum_{i=1}^{N} abs(Y_i - y_i)$.
Root mean absolute error (RMAE)	$\mathrm{RMAE} = 100 \bullet MAE/\overline{y}$
Coefficient of efficiency (E)	$E(\%) = 1 - \sum_{i=1}^{N} (Y_i - \overline{Y})^2 / \sum_{i=1}^{N} (Y_i - \overline{Y})^2$.

y_i was the actual target value, $\overline{y}$ was the average value of y_i; Y_i was the predicted value, $\overline{Y}$ was the average of Y_i; and N was the number of model data.

Table 12: R^2, RMSE, MAE, RMAE, and E (%) results of different models.

Model	R^2	RMSE	MAE	RMAE	E (%)
PSO-BP	0.957	0.466	0.352	11.673	90.867
SVM	0.782	0.634	0.482	15.979	77.391
MLR	0.853	0.599	0.464	15.399	85.296
RF	0.611	0.827	0.689	22.858	71.945
BP	0.888	0.472	0.372	12.325	87.094

more than 90%, which mean that the accuracy of the model is higher [33]. Table 12 has shown that the PSO-BP prediction model is of higher R^2 and E (%) values than other models, as well as lower RMSE, MAE, and RMAE values. That is, the PSO-BP model can accurately predict the compressive strength of recycled brick powder foam concrete.

As can be seen from Figure 13, the relative error values of the PSO-BP model are mostly concentrated around the value of 0, and its performance is relatively stable, while the relative error values of the other models fluctuate widely. Combined with Figure 13 and Table 12, it can be seen that the PSO-BP model can make more accurate predictions and its performance is significantly better than the rest of the models.

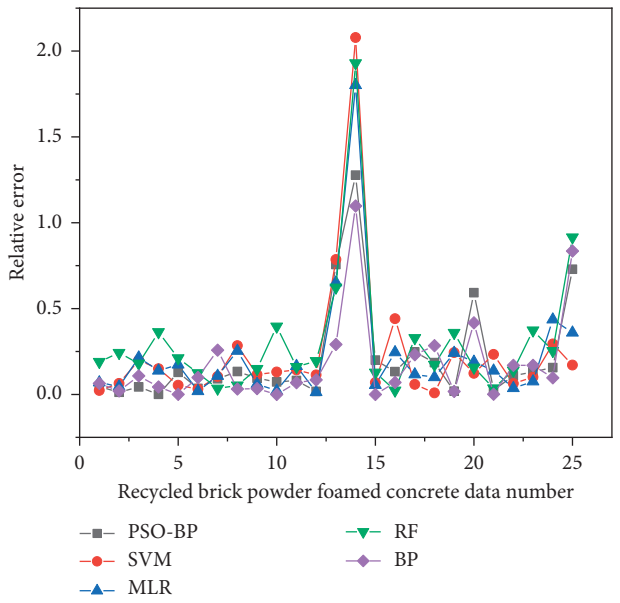

Figure 13: Relative error plots for each model.

4. Conclusion

In this paper, experimental research on the mechanical properties of recycled brick powder foam concrete was carried out, and a neural network model was established to accurately predict the compressive strength based on the compressive strength data of recycled brick powder foam concrete, and the main conclusions reached are as follows.

(1) The range analysis was conducted on the orthogonal test data of recycled brick powder foam concrete, and the results have shown that the influence of various factors on the compressive strength of recycled brick powder foam concrete in descending order is the bubble volumes, the amount of recycled brick powder, water-to-material ratio, and HPMC content.

(2) Comparing the specific strength of each group of recycled brick powder foamed concrete finds that the optimal mixing ratio of recycled brick powder foam concrete fulfilling the requirements of light weight and high strength is 3% bubble group content, 30% recycled brick powder content, 0.55 water-to-material ratio, and 0.05% HPMC content.

(3) With the increase in the bubble volumes, the compressive strength of recycled brick powder foam concrete is decreased, while the reduction effect is significant; with the increase in the amount of construction waste, the compressive strength of recycled brick powder foam concrete exhibits a slow decline; with the increase in the water-to-material ratio, the overall compressive strength of recycled brick powder foam concrete is increased and decreased; with the increase in HPMC content, the compressive strength of recycled brick powder foam concrete is gradually increased, but the increased amount is not as huge.

(4) Two improvements of the compressive strength of recycled brick powder foam concrete is analyzed from a microscopic point of view. One is that the added recycled brick powder refines the pores and increases the compactness of the concrete matrix. Moreover, the foam stabilizer HPMC reduces the damage of the bubble group during the preparation of the test piece and reduces the generation of harmful holes, such as connecting holes.

(5) The PSO-BP model predicts the compressive strength of recycled brick powder foam concrete with high prediction accuracy and data reliability. It provides an effective method for exploring the changing law of the strength of recycled brick powder foam concrete under multiple factors.

While the work in this paper is beneficial to the progress of subsequent foam concrete research, the following issues remain to be further explored due to the time and conditions of the tests and some human uncontrollable factors.

(1) Although the pore structure of recycled brick powder foam concrete has been observed by electron microscopy scanning in this paper, only a few specimens have been studied and future experiments related to the pore structure need to be designed in order to derive the specific influence of pore structure characteristics on the performance of recycled brick powder foam concrete.

(2) Due to time and equipment constraints, a large database was not constructed for neural network model training. With the continuous research on recycled brick powder foam concrete, a large amount of experimental data should be used to train the neural network model in the future, thus supporting the application of the constructed neural network model to engineering practice.

Data Availability

The data supporting the conclusion of the article are shown in the relevant figures and tables in the article.

Conflicts of Interest

The authors declare that there are no conflicts of interest regarding the publication of this article.

Acknowledgments

This work was financially supported by the Science and Technology Research Project of Jiangxi Provincial Education Department (GJJ205301) and Nanchang Hangkong University Postgraduate Innovation Special Fund (YC2020-095), and its support is gratefully appreciated.

References

[1] T. Liu, Z. Wang, D. Zou, A. Zhou, and J. Du, "Strength enhancement of recycled aggregate pervious concrete using a cement paste redistribution method," *Cement and Concrete Research*, vol. 122, pp. 72–82, 2019.

[2] J. Xiao, Z. Ma, and T. Ding, "Reclamation chain of waste concrete: a case study of Shanghai," *Waste Management*, vol. 48, pp. 334–343, 2016.

[3] B. Chen, "Preparation and Performance of Sintered Clay Brick Powder Mixed Building Materials," Master's Degree Thesis, Tai'an, China, 2020.

[4] M. Liu, *Properties of the Foam concrete Containing Recycled Powder Derived from Construction and Demolition Waste*, Yangzhou, China, 2021.

[5] B. Chen, J. H. Zhai, and A. L. Zhai, "Study on preparation and strength influencing factors of recycled clay brick powder autoclaved bricks," *New Building Materials*, vol. 47, no. 2, pp. 95–99, 2020.

[6] M. Tang, L. X. Xu, and Z. J. Yan, *Foam concrete Materials and Engineering Applications*, China Construction Industry Press, Beijing, China, 2013.

[7] X. M. Zhang, P. Z. Huang, and Q. Y. Cui, "Study on performance of foam concrete with recycled micro powder from Construction Waste," *China Concrete and Cement Products*, no. 5, pp. 96–98, 2020.

[8] S. Zhang, R. Y. Li, X. Dong, Z. Lan, and L. Z. xiong, "Recycled fine powder effectively replace the part of cement to prepare foamed concrete," *Bulletin of the Chinese ceramic society*, vol. 37, no. 9, pp. 2948–2953, 2018.

[9] L. Y. Chen, A. Yang, F. Hong, Y. J. Ma, J. Wang, and H. X. Qiao, "Influence of different fly ash content on the performance and pore size of foamed concrete," *Concrete*, no. 8, pp. 137–140, 2021.

[10] Q. Sun, H. Wang, J. Chen, Y. L. An, J. W. Lan, and H. B. Liu, "Study on properties of original fly ash-iron tailings foam concrete," *China Concrete and Cement Products*, no. 5, pp. 100–104, 2021.

[11] X. M. Wei, C. Dong, J. J. Feng, and J. B. Yang, "Experimental study on the performance of double-doped fly ash slag foam concrete," *China Concrete and Cement Products*, no. 7, pp. 63–66, 2019.

[12] Y. L. Hu, J. G. Hao, X. M. Zhao, H. L. Peng, W. B. Yang, and P. W. Gao, "Relationship between properties and pore structure of foamed lightweight concrete," *Journal of Nanjing University of Science and Technology*, vol. 43, no. 3, pp. 363–366, 2019.

[13] F. X. Li, Q. J. Yu, Y. F. Luo, and J. X. Wei, "Mathematical description and analysis on characteristics of pore structure for foam concrete," *Journal of Southwest Jiaotong University*, vol. 53, no. 6, pp. 1205–1210, 2018.

[14] Q. J. Li, D. Ouyang, Q. Zhao, K. K. Huang, W. W. Lin, and J. H. Xiong, "Influence of the municipal waste residues on the properties of foamed concrete," *China Concrete and Cement Products*, vol. 11, pp. 90–93, 2021.

[15] J. Y. Guo and Y. J. Yan, "Experimental research on properties of foam concrete with large amount of fly ash microbead," *New Building Materials*, vol. 46, no. 1, pp. 79–81, 2019.

[16] T. J. Chandni and K. B. Anand, "Utilization of recycled waste as filler in foam concrete," *Journal of Building Engineering*, vol. 19, pp. 154–160, 2018.

[17] S.-C. Ng and K.-S. Low, "Thermal conductivity of newspaper sandwiched aerated lightweight concrete panel," *Energy and Buildings*, vol. 42, no. 12, pp. 2452–2456, 2010.

[18] A. Benazzouk, O. Douzane, K. Mezreb, B. Laidoudi, and M. Quéneudec, "Thermal conductivity of cement composites containing rubber waste particles: experimental study and modelling," *Construction and Building Materials*, vol. 22, no. 4, pp. 573–579, 2008.

[19] GB 175-2007, *General Silicate Cement*Standardization Administration of the People's Republic of China, Beijing, China, 2007.

[20] X. F. Wang, Z. S. An, T. Xie, F. Li, K. Cui, and Z. L. Liu, "Study on recycled foam concrete for construction waste," *Construction Technology*, vol. 47, no. S2, pp. 45–48, 2018.

[21] F. X. Yang, M. H. Shi, Y. Y. Niu et al., "Research the mix proportion of foam concrete based on orthogonal experiment," *The 28th National Academic Conference on Structural Engineering*, vol. 3, 2019.

[22] J. Y. Yu, *Research on Foamed Light Weight Soil Subgrade in BinLai Expressway Reconstruction and Expansion Project*, Master's Degree Thesis, Jinan, 2018.

[23] X. M. Wang, "Stress-Strain Behavior of FRP-Confined Waste Brick-Containing Concrete," Doctoral Thesis, Hangzhou, 2020.

[24] F. Wang, "The Mix Proportion Optimal Design of High Strength and High Performance Concrete Based on Specific Strength," Doctoral Thesis, Xian, 2014.

[25] Y. H. Hao, Y. R. Li, L. D. Qin, H. Sun, and Z. X. Wu, "Experiment of the mixture ratio of magnesium-based foam concrete," *Advanced Engineering Sciences*, vol. 53, no. 6, pp. 72–80, 2021.

[26] J. H. Wang, S. Yang, F. C. Liu, W. U. Xianguo, and Z. Haowei, "Prediction of early crack resistance of concrete based on random forest algorithm," *Journal of Xinyang Normal University*, vol. 34, no. 1, pp. 158–165, 2021.

[27] Y. Hu, L. S. Zhang, F. Y. Yuan, T. J. Li, X. G. Wu, and T. T. Deng, "Prediction of concrete strength based on random forest," *Construction Technology*, vol. 49, no. 17, pp. 89–94, 2020.

[28] X. H. Liao, X. Huang, J. L. Shi et al., "Forecast model about compressive strength of recycle aggregate concrete base on BP neutral network," *Journal of Nanjing Forestry University (Natural Sciences Edition)*, vol. 34, no. 5, pp. 105–108, 2010.

[29] C. Zhu, J. Zhang, Y. Liu, D. Ma, M. Li, and B. Xiang, "Comparison of GA-BP and PSO-BP neural network models with initial BP model for rainfall-induced landslides risk assessment in regional scale: a case study in Sichuan, China," *Natural Hazards*, vol. 100, no. 1, pp. 173–204, 2020.

[30] Z. M. Yaseen, R. C. Deo, A. Hilal et al., "Predicting compressive strength of lightweight foamed concrete using extreme learning machine model," *Advances in Engineering Software*, vol. 115, pp. 112–125, 2018.

[31] O. Hamidi, L. Tapak, H. Abbasi, and Z. Maryanaji, "Application of random forest time series, support vector regression and multivariate adaptive regression splines models in prediction of snowfall (a case study of Alvand in the middle Zagros, Iran)," *Theoretical and Applied Climatology*, vol. 134, no. 3-4, pp. 769–776, 2018.

[32] A. Ashrafian, F. Shokri, M. J. Taheri Amiri, Z. M. Yaseen, and M. Rezaie-Balf, "Compressive strength of Foamed Cellular Lightweight Concrete simulation: new development of hybrid artificial intelligence model," *Construction and Building Materials*, vol. 230, Article ID 117048, 2020.

[33] H.-B. Ly, T.-A. Nguyen, H.-V. Thi Mai, and V. Q. Tran, "Development of deep neural network model to predict the compressive strength of rubber concrete," *Construction and Building Materials*, vol. 301, Article ID 124081, 2021.

Hindawi
Advances in Civil Engineering
Volume 2022, Article ID 5297864, 18 pages
https://doi.org/10.1155/2022/5297864

Research Article

Finite Element and Vulnerability Analyses of a Building Failure due to Landslide in Kaithakunda, Kerala, India

Rajkumar Andrewwinner[1] and Sembulichampalayam Sennimalai Chandrasekaran[2]

[1]*Department of Structural and Geotechnical Engineering, School of Civil Engineering, Vellore Institute of Technology, Vellore, Tamil Nadu 632014, India*
[2]*Centre for Disaster Mitigation and Management (CDMM), Vellore Institute of Technology, Vellore, Tamil Nadu 632014, India*

Correspondence should be addressed to Sembulichampalayam Sennimalai Chandrasekaran; chandrasekaran.ss@vit.ac.in

Received 3 December 2021; Accepted 23 February 2022; Published 17 March 2022

Academic Editor: Ravindran Gobinath

Rainfall-induced landslide is one of the major natural disasters in the Western Ghats of India. Kerala state in southern India received unprecedented heavy rainfall from July to August 2018. The rainfall received was higher than the average for the past 100 years. The present study discusses the investigation of vertical cut failure at Kaithakunda, located in Malappuram district, Kerala, India. It was due to the series of medium rainfall followed by a short period of extremely heavy rainfall. The heavy rainfall triggered the slope failure, which led to the damage of the building and the death of three residents of the building. The index and engineering properties of the soil were evaluated from the laboratory tests. The tests revealed that the soil was silty sand (SM) with low permeability. Tests on the mineral composition and microstructure fabric nature of the soil revealed that the soil was formed due to the weathering action of the parent charnockite rock. The finite element analysis of the slope was carried out using PLAXIS 3D. The analysis was carried out in two stages. The original slope before the vertical cut was modelled as the first stage. The vertical cut was modelled in the second stage to study the actual site condition before failure. The failure occurs due to the increase in pore water pressure in the soil, thereby reducing the matric suction and shear strength of the soil. The vulnerability of the building located near the cut slope is studied using the Support Vector Method to investigate the effect of material on the failure. The results showed the importance of the material properties in the increase of building resistance to 20%.

1. Introduction

Rainfall-induced landslide is a major threat to mountainous slopes all around the globe. The uprising frequency of development in landslide-prone areas increases the risk of landslides [1, 2]. India is among the top ten countries with the highest percentage of landslide fatalities for the years 2003, 2007, and 2008 [3, 4]. When rainfall exceeds the nominal rainfall in the monsoon season, the risk for landslides also increases [5]. The main factors for the initiation of landslides are antecedent rainfall and infiltration, as described by [6]. The leading cause of the rainfall-induced landslide is the increase in pore pressure and the reduction in mean effective stress in the slopes [7–13]. Two mechanisms are observed in rainfall-induced landslides [14]. First is the development of positive pore pressures in the soil-bedrock interface and hence the soil in the interface fails [15]. The second mechanism is due to the wetting of the soil in the slope, which causes the reduction in matric suction resulting in shallow landslides [16, 17].

Kerala is the third densely populated state in peninsular India. Nearly 47% of its land area is surrounded by the Western Ghats [18]. Kerala is divided into three distinct regions geographically: eastern highlands, central low lands, and coastal midlands. Precambrian and Pleistocene are the predominant geological formations covering most mountainous terrain with khondalite, gneisses, and charnockite rocks [19]. The landslides in the Western Ghats are mainly due to the climatic condition and the depth of the loose unconsolidated soil due to weathering. The soil stratum

consists of unconsolidated colluviums, lateritic soils, and lithomargic clay over Charnockite and Gneisses [19].

Very heavy rainfall in 2018 Southwest monsoon resulted in floods and landslides across Kerala. According to the Geological Survey of India (GSI), more than 67 major landslides and hundreds of minor landslides are reported. Among the 14 districts in the state, 13 of them were affected due to landslides of various types, scales, and dimensions [20]. More than 400 people died due to floods and landslides [21]. Average rainfall of 771 mm was recorded from the period of 1st to 20th August, and it is 140% more than the normal amount of rainfall [22], which caused many landslides and debris flow resulting in fatalities and heavy loss to infrastructure.

Nemmara landslide in Palakkad district, Peringavu and Kaithakunda landslides in Malappuram district, Karinchola landslide in Kozhikode district, and Upputhode landslide in Idukki district are some of the significant landslides that occurred during the 2018 southwest monsoon. The present study discusses the detailed investigation of the Kaithakunda slide by geotechnical characterization of the soil slope and the influence of weathering in the slope and slope stability analysis using a 3D finite element model.

The physical vulnerability of the building to slope failure is essential for the risk definition [23]. It is the degree of loss of an element or a given set of elements in a hazard area [24]. For assessing the structural loss, the vulnerability of the building at risk is obtained by analyzing the damage degree from the type and intensity of landslide [25]. Studies were carried out to find the vulnerability using vulnerability curves and matrices, but they neglected the building properties that led to the vulnerability [26]. There are studies related to finding the residual lateral thrust on the footing sides of the wall through nominal codal provisions but no deterministic studies to find the parameters required for the probabilistic analysis are carried out till now [26, 27]. There are very few studies related to the vulnerability of buildings in the cut slope, and hence a detailed study of the vulnerability of the buildings is needed. This study helps in vulnerability assessment in terms of mechanics and its effect on vertical cut slope failure. The method used will be helpful to planners and engineers on the variables that make the structure vulnerable during cut slope failures.

2. Building Failure in Kaithakunda

The slope failure occurred at Kaithakunda (11°10′ 59.59″N, 75°53′ 48.37″E) located in Malappuram district, Kerala state of India (Figure 1). The slide occurred at 1 AM on August 16, 2018, and damaged a house, as shown in Figures 2(a) and 2(b). It led to the death of 3 people [28]. The failure of the slope is observed as a vertical cut failure, as shown in Figures 2(c) and 2(d). Figures 2(e) and 2(f) show the mudslide into the house that led to the death of three people. The overall plan of the area and the longitudinal section of the slope are shown in Figures 3(a) and 3(b), respectively.

The building is a load-bearing structure and the material used for the construction is laterite block obtained from the local area. The building is a single-storey building with two columns to support the front porch of the building. Figure 2(b) shows the tilting of the column in the portico of the building and wide cracks in the building. As can be observed from Figure 3(b), the building was constructed after cutting the original slope vertically for about 11.5 m. No stabilization measure was adopted for the vertical cut. The building was located 3 m from the vertical cut. The vertical cut of the slope extended up to 20 m in width. At the top of the cut, another building applied the surcharge load on the vertical cut. The main reason for the occurrence of the slide is the heavy rainfall experienced in the area. The rainfall occurred in two stages, with the 1st stage of very light rainfall between June and July 2018. The second stage of rainfall occurred from August 1 to August 14. The third stage consists of very heavy rainfall during and August 15–16, 2018.

3. Rainfall Data

The rainfall in Kerala consists of two monsoons, namely, the Southwest monsoon and Northeast monsoon. The Southwest monsoon starts in early June and ends in August. The Northeast monsoon starts in October and ends in November [29]. The location of rain gauge stations in the Malappuram and Kozhikode districts is depicted in Figure 4(a). Two rain gauge stations are located near the site: one at Karipur Airport in Malappuram district and the other at Kozhikode in Kozhikode district. Rainfall data from the rain gauge station at Karipur airport is considered for further analysis due to its proximity to the site. Cumulative rainfall of Malappuram district during the Southwest monsoon 2018 is compared with the average cumulative rainfall data of the previous 50 years, as shown in Figure 4(b) [22]. Cumulative rainfall data for the event year (2018) is 2600 mm, 44% higher than 50 years average rainfall (1800 mm). Daily rainfall recorded at Karipur airport during August 2018 is depicted in Figure 4(c). The landslide occurred at 1 AM on August 16, 2018. As can be observed from Figure 4(c), the daily rainfall on the event day is 175 mm. The importance of antecedent rainfall in triggering the landslide can be observed as the heavy rainfall on the event day was preceded by heavy rainfall on the 14th and 15th of August 2018.

4. Tests on Soil Samples

The top layer of the soil extends up to a depth of 6 m from the ground surface. The second layer extends from 6 m to the bedrock. The top layer is highly weathered in nature and reddish compared to the second layer of soil, which is white. The slip surface is found in both the top and second layers of the soil, as can be seen from Figure 2(d). The geological map of the Malappuram district, as developed by the Geological Survey of India [30], is depicted in Figure 5. The figure indicates the occurrence of charnockite rock in the study area [31]. The geology and geomorphology of the site location indicate that the soil is formed due to the weathering action of the parent charnockite rock.

The soil samples were collected from the slip plane: one at 1.5 m depth in the topsoil and the other at 6.5 m depth in

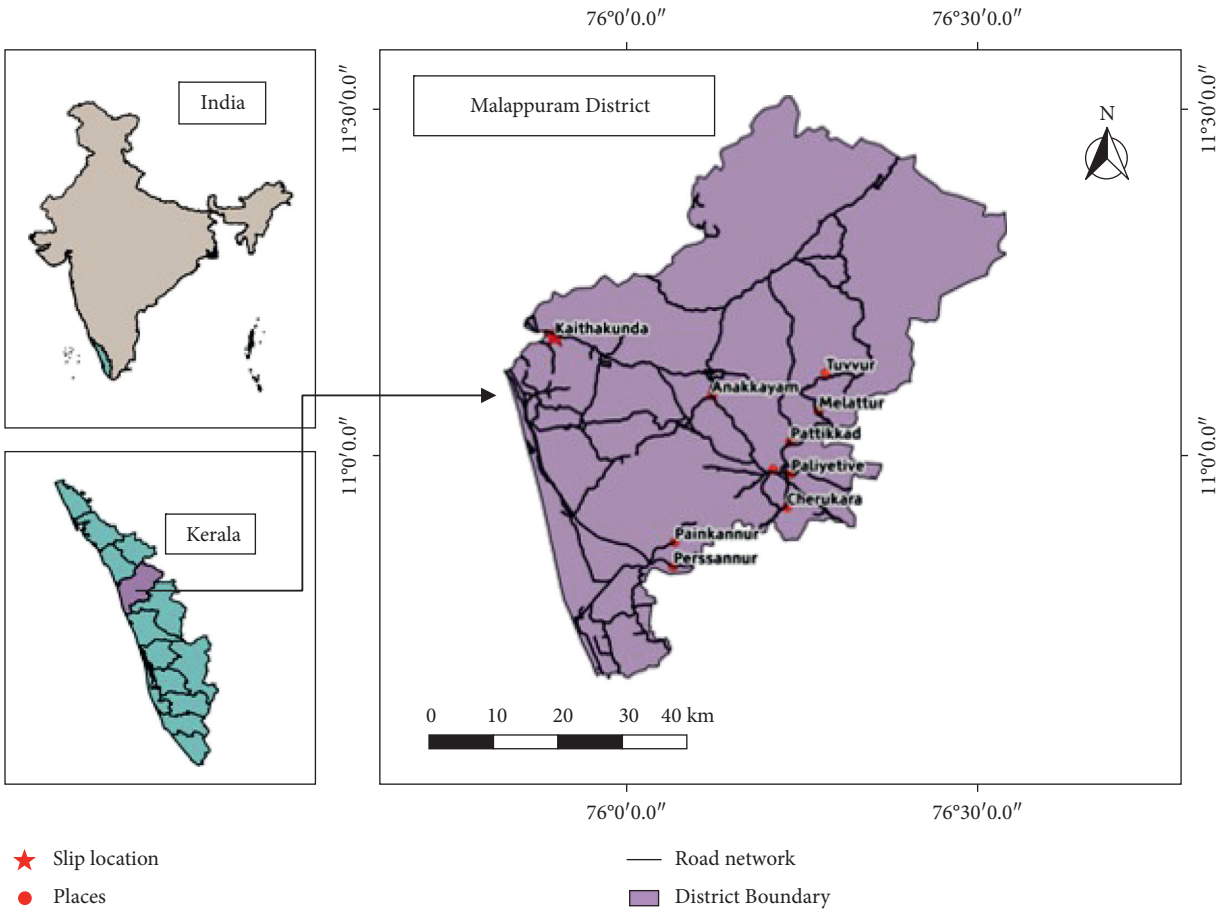

Figure 1: Geographical location of slope failure at Kaithakunda, Malappuram district, Kerala, India.

the second layer (Figure 2(d)). The characteristics of the soil layer are found through laboratory tests. Index and engineering properties of the soil samples are evaluated by carrying out laboratory tests as per ASTM standards. Sedimentation analysis was carried out to identify the amount of clay and silt content.

The mineral composition and the microfabric nature of the soil were identified by X-ray Diffraction (XRD), Field Emission Scanning Electron Microscopy (FE-SEM), and Energy-Dispersive X-ray spectrum (EDX).

5. Analysis Using the Finite Element Method

The finite element analysis is carried out using PLAXIS 3D. The analysis is carried out in three phases.

5.1. Analysis of the Original Slope. To understand the behaviour of the natural slope, the analysis is carried out on a model of the original slope. Figure 6 shows the model of the original slope with two layers of soil and one layer of rock. Slope with dimensions of 104 m length, 30 m width, and 33 m height is considered in the analysis. The properties of soil and rock are presented in Table 1. The soil is modelled as 10-node tetrahedral elements. The soil is modelled as Mohr–Coulomb elastic perfectly plastic model [32]. The hydraulic boundary condition (X, Y), Z_{min} are considered as open for the analysis and all other directions with respect to Z are closed. The undrained shear strength of the soil is modelled using effective stress analysis with the effective shear strength parameters. Fully coupled flow deformation analysis is carried out to study the coupled effect of flow and deformation in the unsaturated soil due to the change in hydraulic boundary conditions with respect to time [33]. The initial stage of the calculation is carried out with gravity loading for the attainment of the geostatic equilibrium of the slope [34].

5.2. Infiltration Analysis. For the infiltration analysis, the soil condition is taken as unsaturated and Soil Water Characteristic Curve (SWCC) is considered to describe the hydraulic parameters of the groundwater flow in the unsaturated soil. The infiltration analysis is carried out by the van Genuchten method [35]. S_e is the effective saturation and is given by

$$S_e = \frac{S - S_{res}}{S_{sat} - S_{res}}.\text{and,}$$
$$S_e = \left[\frac{1}{1 + (\varphi/\alpha)^n}\right]^l. \quad (1)$$

FIGURE 2: View of building failure. (a) View of the damaged house with vertical cut. (b) Elevation of damaged building. (c) Sliding part of the failed cut. (d) View of vertical cut failure. (e) Detailed view of the damaged portion. (f) Outside view of the damaged portion.

And S_{res} is the residual saturation in the soil and S_{sat} is the full saturation level in the soil. Soil saturation is a decreasing function of the matrix potential. van Genuchten (1980) provides the relation between effective saturation and matric suction potential, where φ is the matric suction potential and α, n, and l are the curve fitting parameters. This

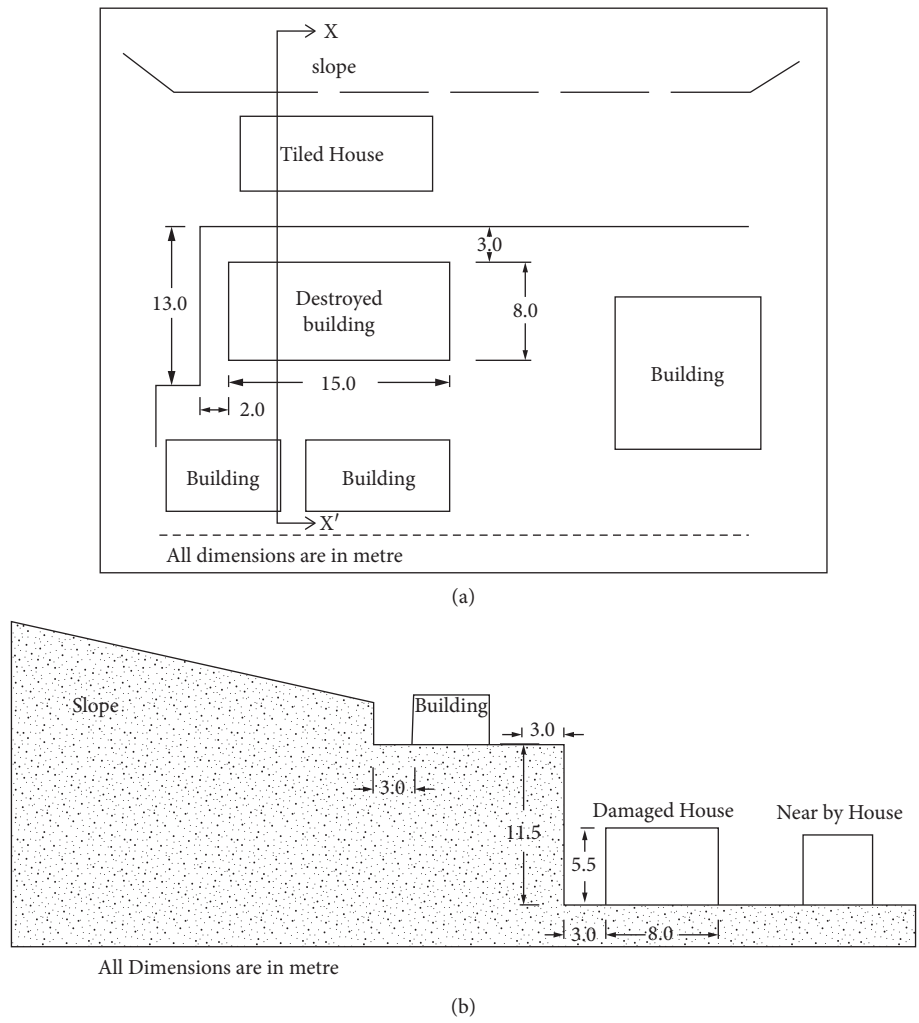

Figure 3: Geometry of the slope with vertical cut and buildings: (a) plane and (b) longitudinal section.

can be found out by Soil Water Characteristic Curve (van Genuchten, 1980). Based on the suggestion of [36], the typical capillary curve for silty material and sand was obtained from [37]. The van Genuchten parameters for sandy silt and sand were obtained from the unsaturated soil hydraulic database (UNSODA) [38, 39]. The van Genuchten fitting parameters (α, n, l) of the topsoil and bottom soil are 0.010, 0.45, 0.089 and 0.029, 0.47, 0.069, respectively.

5.3. Analysis of Vertical Cut. Finite element analysis of the site condition that existed before failure (Figure 3(b)) is carried out to evaluate the mechanism of failure. Figure 7 shows the geometry of the model before slope failure. It shows the vertical cut in the slope and the building located very close to it. The structure is a single-storey building with load-bearing walls. The building is modelled as a plate element. Beam elements are used to transfer the load from the roof to the plates (load-bearing walls) (Figure 7). The foundation of the building is considered as a plate element to transfer the load to the soil. The plate and beam elements are modelled with a unit weight of Reinforced Cement Concrete (RCC). The width and length of the building are taken as 8 m and 15 m, respectively (Figures 8, 2(a), and 3(a)). The beam and plate elements are considered with a minimum thickness of 125 mm and 75 mm, respectively. The effect of a tiled roof building located above the vertical cut (Figure 3(b)) is considered as a surcharge load (20 kN/m^2) in the analysis.

The modelling and properties of soil and the method of analysis were already discussed in the previous section. Infiltration analysis was carried out to study the effect of slope on the building. The rainfall data were used for infiltration in surface groundwater flow boundary conditions. The rainfall data obtained from the Indian Meteorological Department (IMD) are shown in Figures 4(b) and 4(c). The analysis was carried out in three stages. The first stage considered continuous rainfall of low intensity (cumulative rainfall of 1770 mm) from June to July 2018. The second stage considered intense rainfall from the 1st of August to the 14th of August 2018. The rainfall recorded during the second stage (August 1–14) is 2800 mm. Since the failure of the slope was observed on August 16, the third stage of analysis was carried out by considering the rainfall that occurred on the 15th and 16th of August with a very high intensity of 187.5 mm/day (Figure 4(b)).

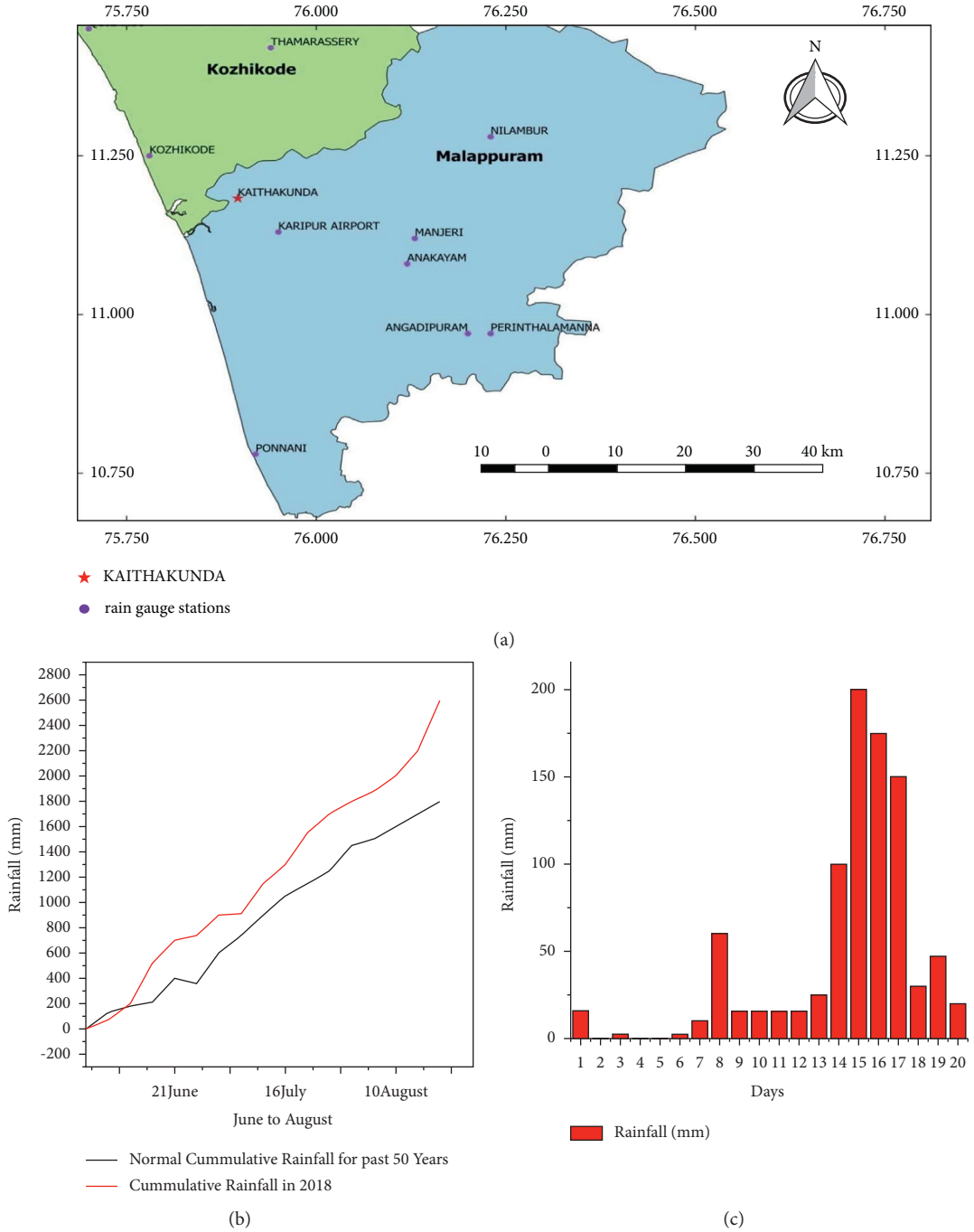

Figure 4: Rainfall data. (a) Rain gauge stations near Kaithakunda. (b) Cumulative rainfall for south-west monsoon 2018 (after IMD 2018). (c) Daily rainfall recorded at Karipur airport in August 2018 (after IMD 2018).

6. Vulnerability of the Building Located near the Vertical Cut

To evaluate the vulnerability of buildings during vertical cut failure, the forces acting on the building are required to be calculated. Factors such as geological and structural features of buildings play a vital role in physical vulnerability. The vulnerability based on indicators is used to define the vulnerability of the building. The process used in this analysis is the calculation of the residual thrust force of the slope failure through Finite Element Analysis (FEA). In FEA, the residual force acting on the sides of the building is calculated by considering the interface elements between the soil and the structure [40]. The building thrust force, height, length, width, and material properties of the building are used as indicators to find the vulnerability of the building for this particular type of soil surroundings [41–44]. The indicators are selected based on the available characteristics and the results from the deterministic model.

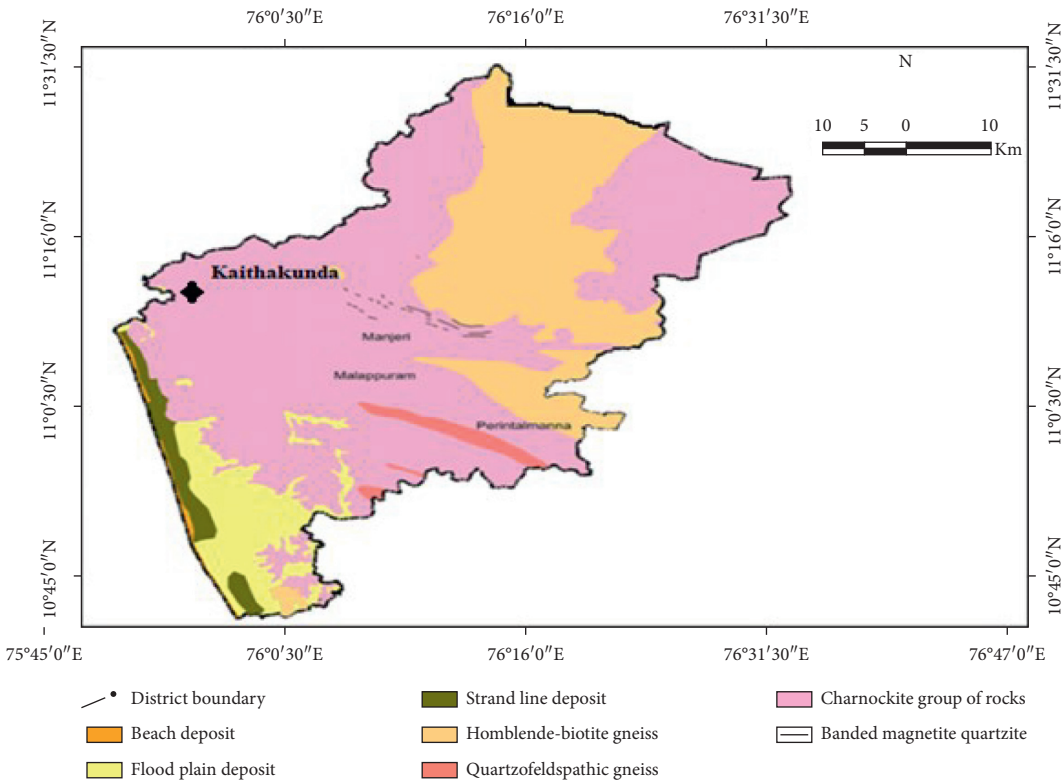

Figure 5: Geological map of Malappuram district (after GSI 2005).

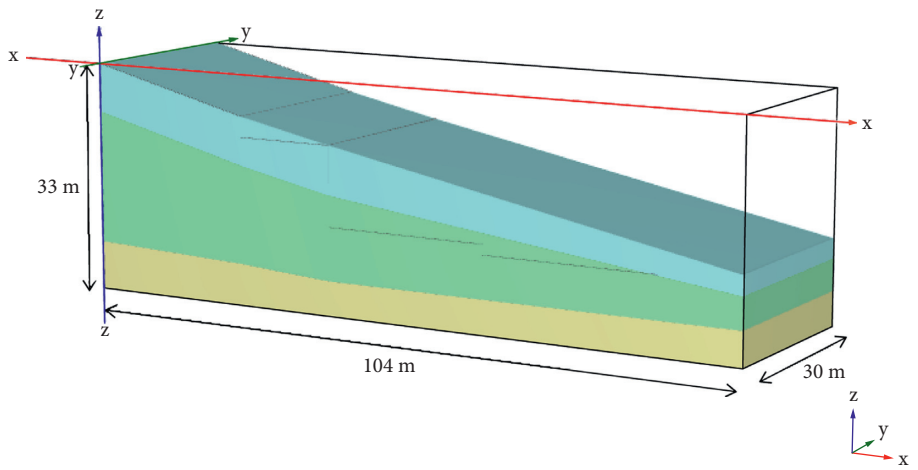

Figure 6: Finite element representation of the original slope geometry.

Table 1: Properties of soil and rock.

Property	Layer 1—soil	Layer 2—soil	Layer 3—rock
Specific gravity (G)	2.48	2.57	—
Liquid limit (w_1) (%)	49	49	—
Plastic limit (w_p) (%)	34	29	—
Plasticity index (I_p) (%)	15	20	—
Soil classification	SM	SM	Soft rock
Coefficient of permeability (k) (m/s)	5.54×10^{-8}	1.88×10^{-7}	—
Effective cohesion (c') (kN/m^2)	10.90	9.86	0
Effective friction angle (φ') (°)	20.06	22.10	55
Elastic modulus (E) (kN/m^2)	14×10^3	16×10^3	70×10^3
Poisson's ratio (ν)	0.325	0.325	0.35
Dry unit weight (γ) (kN/m^3)	18.55	19.90	26
Dilatancy angle (ψ) (°)	0	0	0

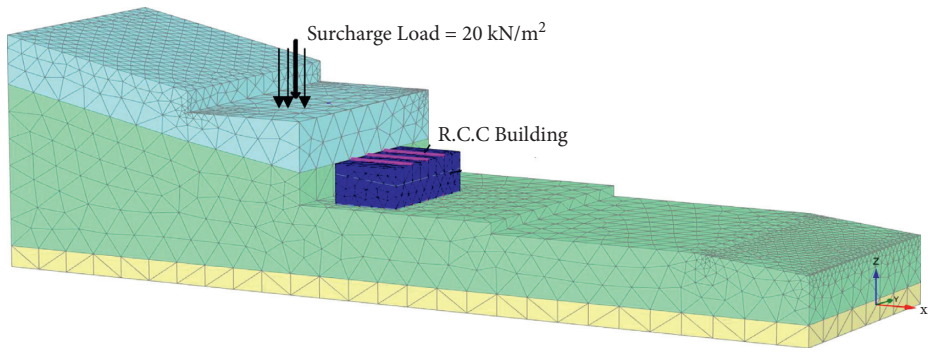

Figure 7: The geometry of the model existing site condition before failure.

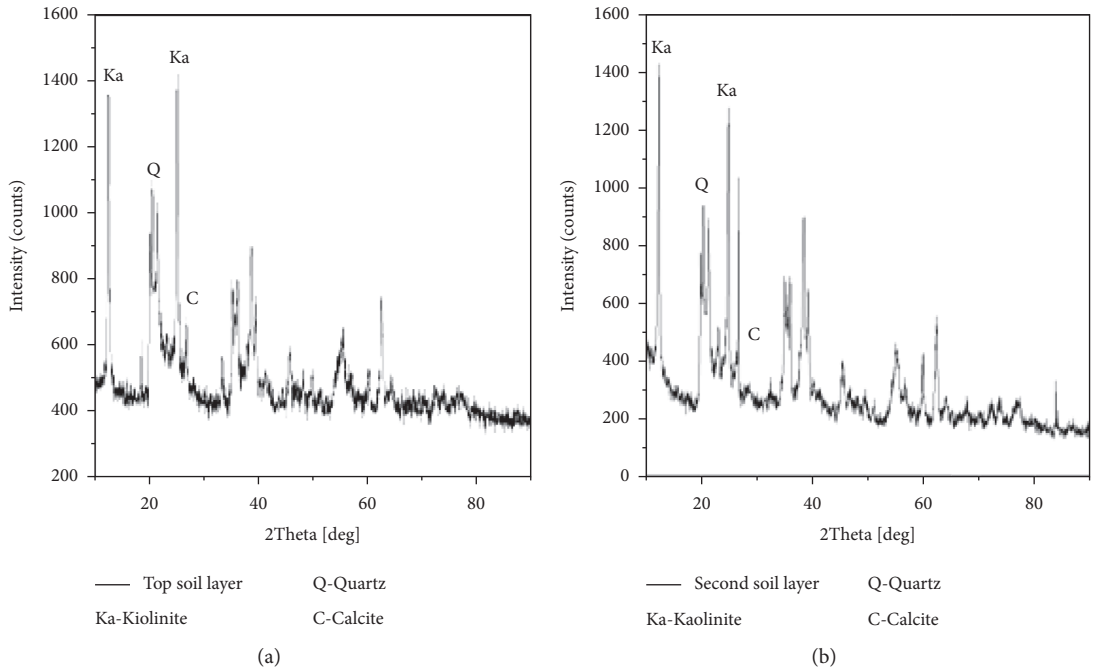

Figure 8: X-ray diffraction pattern for (a) the topsoil layer and (b) the bottom soil layer.

The undrained soil parameters are given as input for the deterministic analysis in the numerical model. The groundwater infiltration was carried out using the rainfall data for June–August 2018. The vulnerability of the building based on the inclination of the building is used in the study. Thus, when the vulnerability value reaches 1, then the building is subjected to failure and when the vulnerability is less than 0.2, it is safe [26, 27].

Vulnerability based on the inclination of the building is used to define the degree of damage to the building [45]. The inclination is calculated with respect to the deflection of the building. Analytically, the Timoshenko function of deflection for a uniform loaded beam is used to find the deflection [27, 46].

$$y_m = \frac{5qL^4}{384EI} + \frac{3qL^2}{16GA}, \tag{2}$$

where y_m is the maximum deflection of the beam, q is the lateral thrust of the structure, and L and W are the length and width of the structure. E and G denote the elastic and shear modulus of the building material.

6.1. Inclination and Lateral Thrust Calculation. The inclination of the building is the ratio of horizontal deflection to the vertical height of the wall. The inclination of the building is defined as

$$i = \frac{y_m}{H}, \tag{3}$$

where i is the inclination of the building, y_m is the horizontal deflection of the building, and H is the vertical height of the building. According to [47], the allowable deflection is 1.6 cm, and this is classified as safe.

The lateral thrust is calculated from the finite element model by considering the interface between the structure and the soil. Interfaces are used to study the interaction between the structure and soil [33, 47]. The interface describes the friction between the structure and the soil, which is usually 2/3 of the soil friction angle. The interface element helps to obtain the effective horizontal stress acting on the structure, which are the lateral Earth pressures acting on the structure [33].

6.2. Damage Degree of Inclination. The ratio of the inclination of the building to the threshold value (i_m) is defined as the damage degree, which is the physical vulnerability (v) [48, 49]. The degree of damage can be evaluated by parameters such as cracks, inclination, and maintenance cost [50, 51]. The vulnerability in the vertical cut slope failure is developed with the inclination, which is defined as the function of building lateral thrust, building material properties, dimension of the building, and the height of the building. Vulnerability of building is given by [27]

$$v = \begin{cases} \dfrac{i}{i_m} = \dfrac{1\left(5qL^4/384EI + 3qL^2/16GA\right)}{Hi_m}, & \begin{pmatrix} i < i_m \\ i \geq i_m \end{pmatrix} \\ 1, \end{cases} \quad (4)$$

where i_m is the permissible inclination of the building. According to Kotlicki and Wysokinski, the permissible value of deflection is 25 mm for the masonry building with reinforced concrete slabs and beams, and the i_m value is limited to 0.008.

The vulnerability (v) is from 0 to 1, where 1 indicates severe damage and 0 indicates being safe. The deformation of the building is calculated with the help of unsaturated soil parameters and hence the soil deformation is studied to give real-time vulnerability of the building.

6.3. Vulnerability Using the Support Vector Method. The optimization or calibration of the parameters used for the vulnerability analysis is analyzed through the Support Vector Method (SVM) in machine learning. Khalil et al. compared different machine learning techniques for approximating groundwater models, which are complex whereas SVM was found to reduce the error in the fitting of the indicators. SVM solves both optimization and regression problems. Many of the SVM applications have predicted very good results [52–56].

In this study, SVM is used to predict the vulnerability of buildings in the vertical cut slope failure. For the regression problem, two subsets are used, and they are as follows: (1) training subsets to construct the model and (2) a testing subset to estimate the model performance [57]. The training, testing, and normalization techniques are used for the prediction. The input parameters are q (lateral thrust of the structure), H (height of the structure), E (elastic modulus of the building material), L and W (length and width of the structure), and v (vulnerability) is the output of the model. RStudio platform is used for conducting the regression analysis in this study.

7. Results and Discussion

7.1. Properties of Soil. The particle size distribution curve for the soil samples is shown in Figure 9. Properties of soil evaluated from lab tests are presented in Table 1. Both soils are identified as silty sand (SM) as per USCS classification [58]. Hydraulic conductivity of the soil sample is evaluated as per the Indian Standard Code [59] and the permeability values for both the soil samples are in the range of 10^{-7} to 10^{-8} m/s. The Proctor compaction test is carried out to determine the maximum dry density of the soil. Consolidated drained (CD) direct shear tests on the soil samples are conducted as per [60]. The effective shear strength parameters obtained from the tests are presented in Table 1.

7.1.1. Weathering Characteristics. Figure 10 depicts FE-SEM images of both layers of soil. Figure 10(a) indicates that the topsoil layer was governed by silt/clay size clusters with voids on the soil particle surface and a highly porous structure due to the high weathering. The degree of weathering reduces with the increase in depth as the presence of clay minerals and pore volume decreases (Figure 10(b)). The FE-SEM images of both soil layers show the presence of kaolinite clay mineral with many pores in it, which is well supported by EDX and XRD analysis, as shown in Figures 8 and 11. EDX and XRD results indicate the presence of kaolinite clay mineral ($Al_2Si_2O_5(OH)_4$) along with quartz and calcium carbonate ($CaCO_3$) in the topsoil (Figures 8(a) and 10(a)) [61, 62]. The presence of calcium carbonate in the soil indicates the weathering process in the soil [62, 63]. The second layer of soil has a very less amount of kaolinite clay due to the incomplete weathering process (weathering degree-VI according to [64]) in the soil [63, 65] (Figures 8(b) and 11(b)).

Charnockite rocks are the parent rocks present in the Malappuram district and the weathering action of the rocks results in laterite soil, which is reddish brown [66]. The second layer of the sample is white due to the formation of calcium carbonate ($CaCO_3$) in the soil (Figure 2(d)). Charnockite is a felsic rock present in the lower crust containing minerals, such as orthopyroxene and garnet [67]. The property of the bedrock is shown in Table 1. Most of the laterite soil in the region covers up to 25mm depth and is underlain by charnockite rocks [68]. Due to the granulite facies metamorphic event, the felsic magmas are hydrated to form the charnockite rock [67].

7.2. Results of Finite Element Analysis

7.2.1. Original Slope. Rainfall data from June to August 2018 (Figure 4(b)) were considered for the infiltration analysis. The rainfall with low intensity and high intensity were carried out in separate stages (the cumulative rainfall of the first stage (June to July 2018) is 1770 mm and the second stage (August 1–14) is 2800 mm). At the end of the first

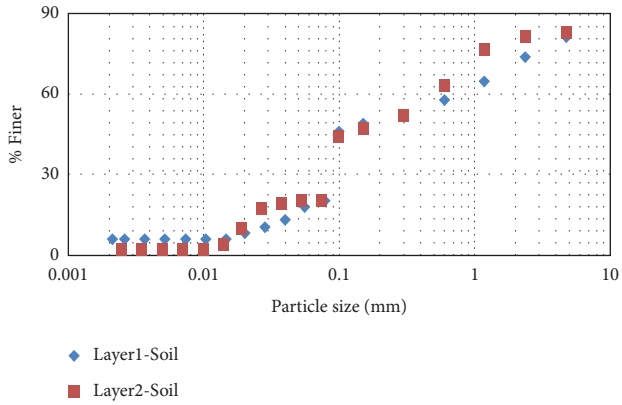

Figure 9: Particle size distribution curve.

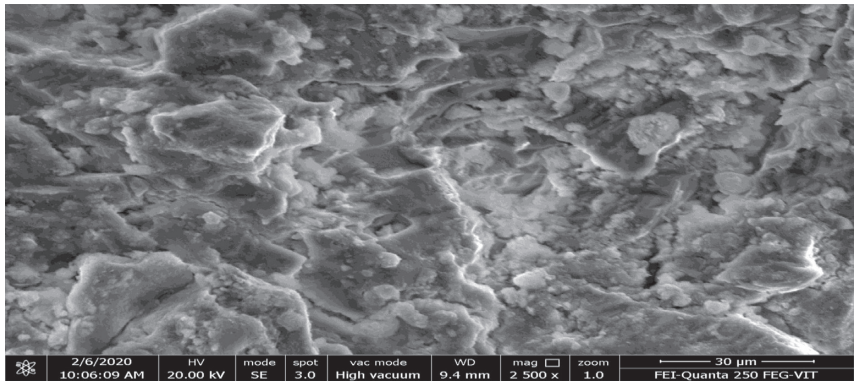

(a)

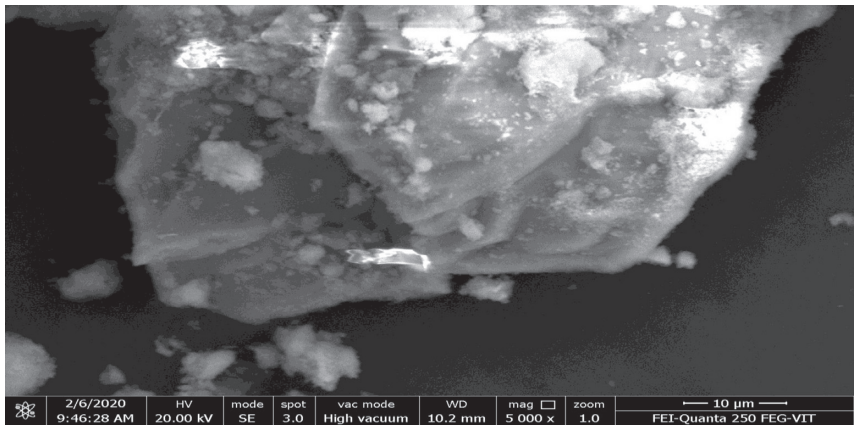

(b)

Figure 10: FE-SEM images of (a) topsoil and (b) second-layer soil.

stage, there was no significant displacement. The pore water pressure and the displacement of the original slope at the end of the second stage are shown in Figures 12(a) and 12(b), respectively. The pore pressure, as observed in Figure 12(a), indicates that the matric suction of the soil is more and hence negligible displacement in the slope, as shown in Figure 12(b) [69]. This indicates the stability of the original slope.

7.2.2. Results of Vertical Cut Analysis. The details of the beam and plate elements are given in Table 2. The deformed mesh is shown in Figure 13(a). The deformed mesh indicates the caving of the vertical cut. The shape of the deformed mesh indicates the failure of the vertical cut. The displacement profile of the slope (Figure 13(b)) indicates that the maximum displacement occurred at the top of the vertical cut. It depicts the slip surface of failure as observed

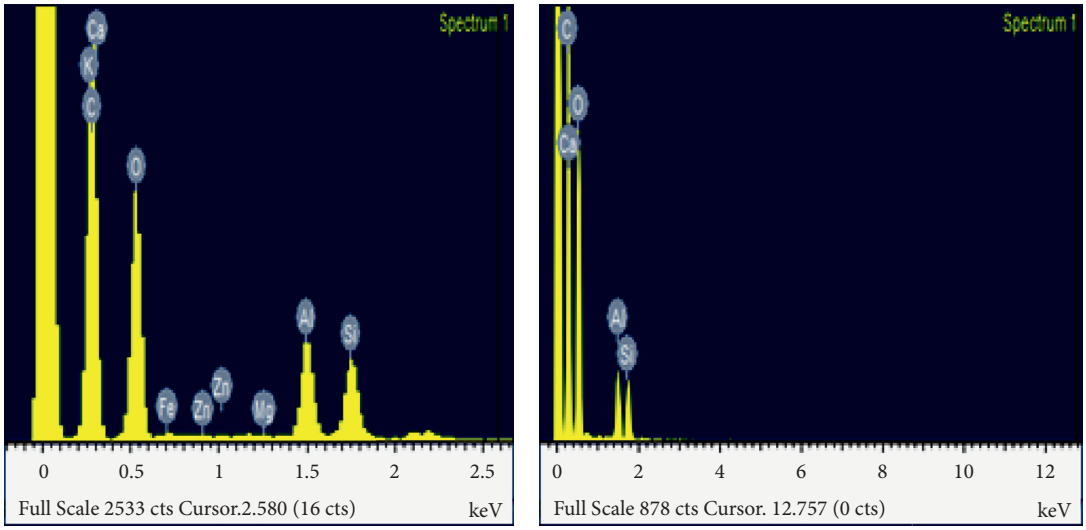

Figure 11: Energy-dispersive X-ray spectrum. (a) The topsoil layer and (b) the bottom soil layer.

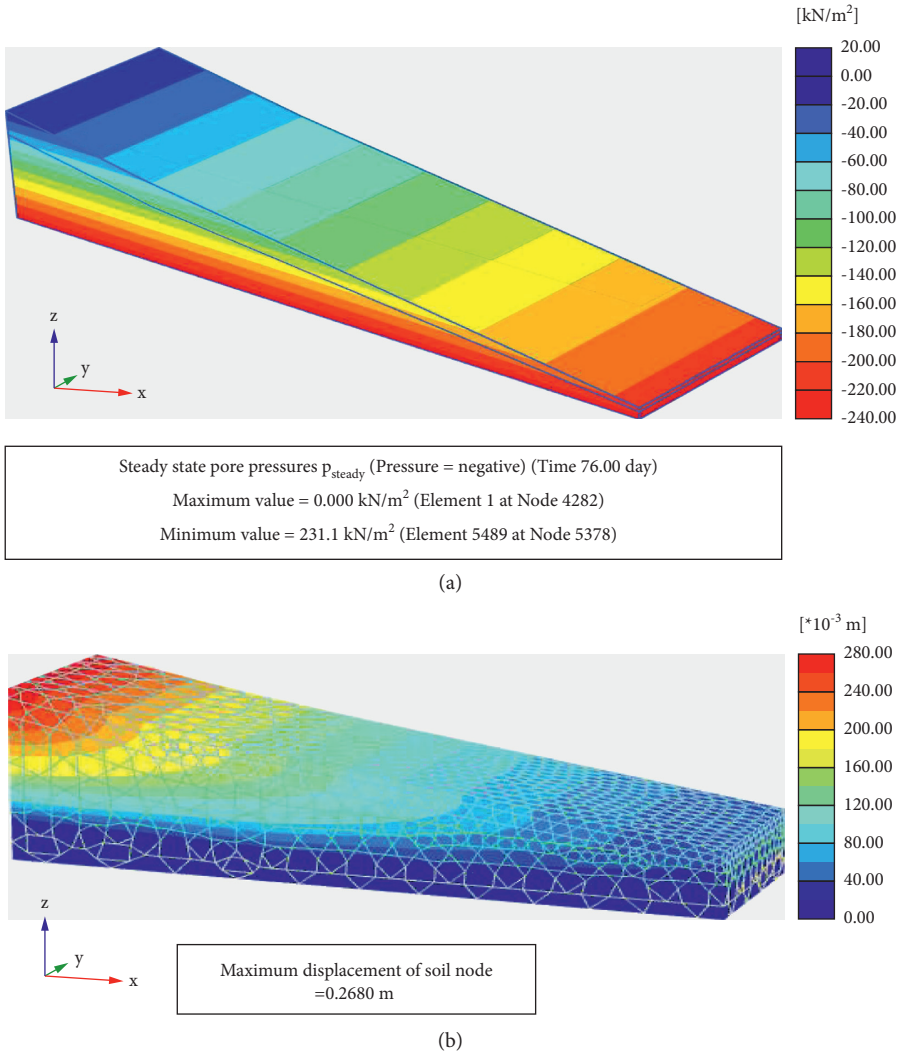

Figure 12: Finite element representation of the original slope. (a) Pore water pressure development. (b) Displacement contour.

Table 2: Building properties.

Property	Building	
	Plates	Beam
Density (kN/m^3) (γ)	25	25
Elastic modulus (kN/m^2) (E)	30×10^6	30×10^6
Poisson's ratio (ν)	0.2	0.2

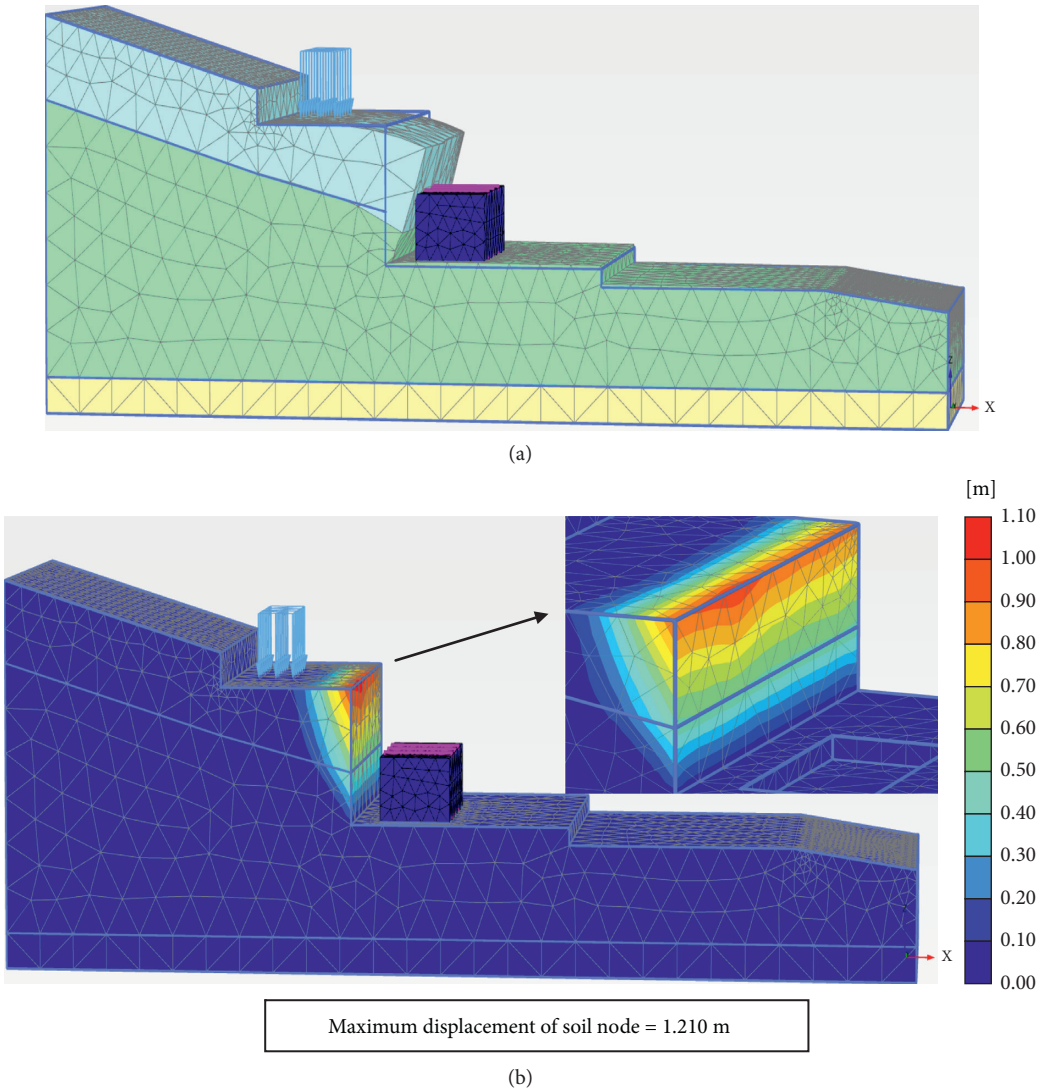

Figure 13: View of vertical cut failure. (a) Deformed mesh. (b) Displacement profile for vertical cut.

from the field (Figure 2(c)) and indicates the displacement of the soil node as 1.20 m.

Figure 14(a) shows the maximum displaced nodal position of the model. The calculation is carried out with infiltration analysis and the maximum value of the displaced soil node is found to be 1.210 m at the position of the node (40, 9.737, −8.9), as shown in Figure 14(a). The figure shows that the maximum displacement of the soil from its original position before deformation is 4.1 m. The rotation of the soil node is found to be 4.667 degrees. As the distance between the vertical cut and the building is 3 m (Figure 3(b)), the displacement of soil, flow pattern, and plastic points of soil observed from Figures 13(a), 13(b) and 14(a) and 14(b), the sliding soil reaches the building, which caused tilting and severe damage of the building (Figures 2(e) and 2(f)) and hence the building wall is deformed to a distance of 45 cm from its original position, which is visible from Figure 2(d). Figure 14(b) shows the plastic points of the model slope with the failure points occurring at the toe of the cut and it progresses to the topsoil layer. The tension cut-off point refers to the movement of the soil due to the failure. The red cube indicates the development of failure stress in the failure

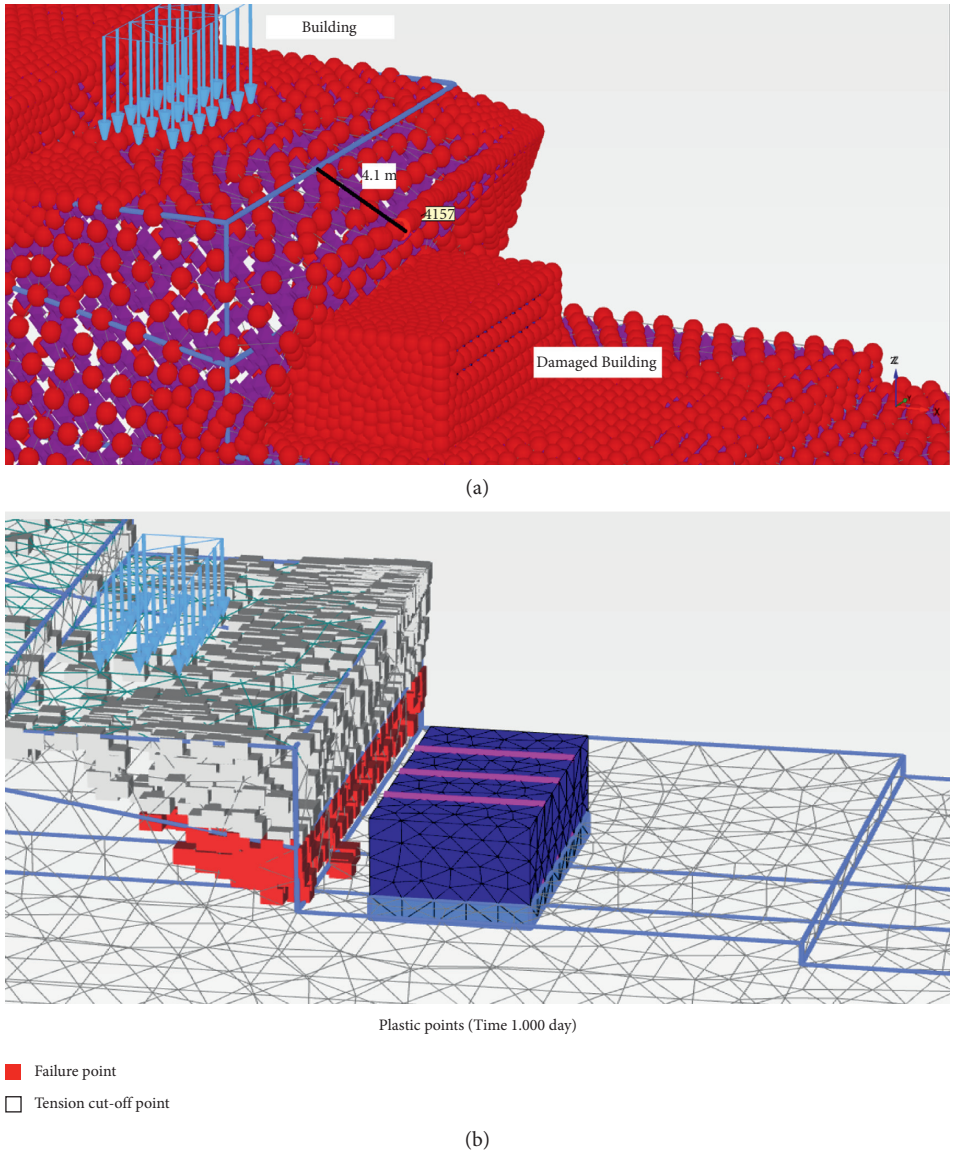

Figure 14: Detailed view of (a) maximum displaced node (node no. 4157) and (b) plastic points in the model.

envelope and the tension point is a point that fails in tension [33]. The results indicate that the soil displacement at the top of the vertical cut is more. As can be observed from Figures 3(b), 13(a), 14(a), and 15(a), the saturation level of soil cross section close to the vertical cut at $X = 39.55$ m and $Z = -8.9$ m indicates that the soil at the top level is saturated more. It can be observed from the figure that the saturation level of soil reaches up to 100% of the soil located at the top of the vertical cut. The saturation contour at a level of −20.90 m indicates the saturation level of nearly 65% and this leads to the increase in pore water pressure and a decrease in the effective stress as shown in Figure 15(b).

The effective stress for the soil at various stages of rainfall indicates the reduction in stresses due to the increase in pore pressure, and it can be visible that the effective stresses decrease and reach constant value for all three stages (Figures 15(b) and 15(c)) [12]. The pore water pressure for different stages of rainfall is depicted in Figure 15(d). The first stage of rainfall indicates the suction pressure is more due to the unsaturated state of soil and hence the slope is stable. This is due to the increased shear strength of the soil. The second stage (August 1–14) and the third stage (August 15–16) denote the fact that the pore water pressure increases at the top of the soil due to the increase in saturation level (Figure 15(a)). The increase in the pore water pressure at the third stage results in the reduction of effective stress (Figure 15(b)) and thereby, it reduces the shear strength of the soil at the vertical cut. This leads to the failure of the slope, as shown in Figures 13(a) and 13(b). The values from the numerical analysis were validated against the analytical values (Bishop's effective stress) used in the PLAXIS 3D software to emphasize the importance of the reduction in the effective stress at the end of the third stage. Figure 15(c) shows a slight variation from the numerical analysis in the analytical formula and this is due to the assumption that

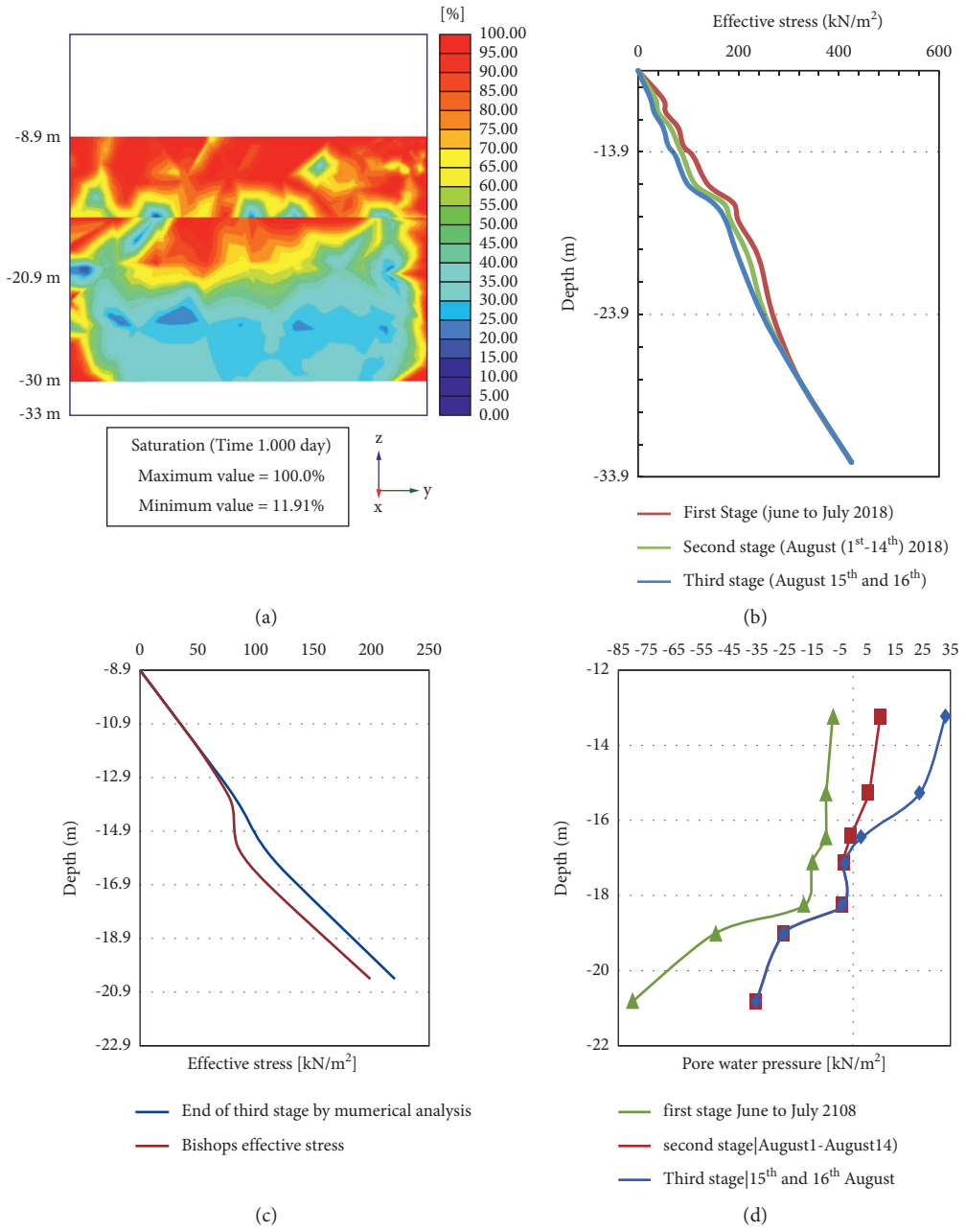

Figure 15: Results of numerical analysis. (a) Saturation level of the soil cross section at $x = 39.55$ m and $Z = 8.9$ m at vertical cut. (b) Effective stress at various stages. (c) Effective stress validated with the analytical method from PLAXIS 3D. (d) Pore water pressure of the soil at various stages.

pore air pressure used in PLAXIS is zero at the reference level [33].

The slope is stable at the end of the first stage of rainfall (Figure 15(d)) and this is due to the increase in matric suction in the soil. This is well supported by the increase in the effective strength of soil (Figure 15(b)). During the second stage of rainfall, the slope gets saturated and thereby, the pore water pressure increases. The increase in pore water pressure causes the effective stress to be reduced. The third stage causes the slope to be saturated (saturation up to 80%) for a depth of 8 m from the ground surface of the vertical cut. This causes the soil to develop an intense increase in pore water pressure (Figure 15(d)) of 35 kN/m^2, which is accompanied by a decrease in effective stress of 25 kN/m^2. This reduction in the effective stress of the slope results in its failure (Figure 13(a)). The displacement of the soil is found to be 4.1 m from the top of the vertical cut (Figures 14(a) and 14(b)) and hence the displaced soil from the vertical cut caused the building to fail as observed from Figures 2(e) and 2(f).

7.3. Results of Vulnerability Analysis. The model used for the analysis uses the polynomial kernel, which has an R^2

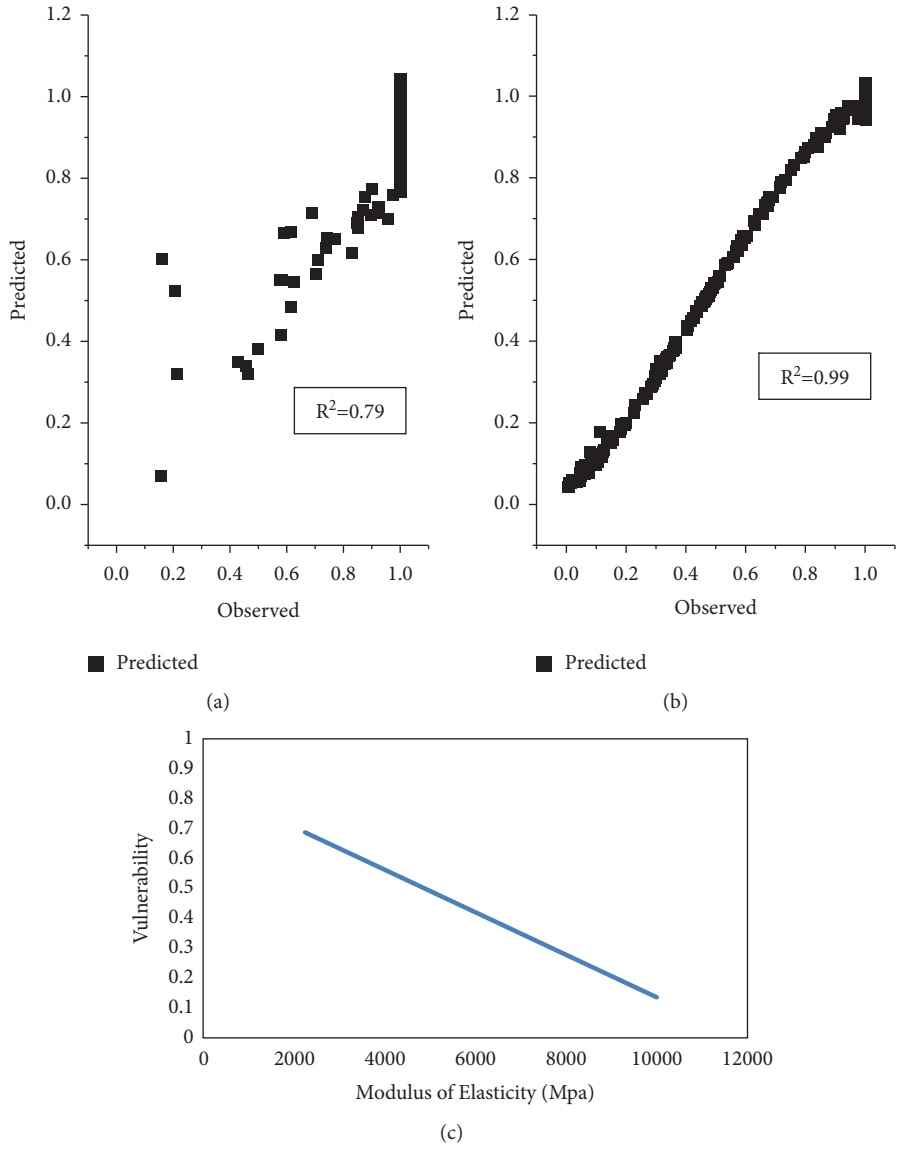

Figure 16: SVM model. (a, b) Performance of testing dataset of $E = 2{,}250$ MPa and 10,000 MPa. (c) Variation of the vulnerability of the building for modulus of elasticity.

accuracy of 0.93 in training and 0.79 in testing (Figures 16(a) and 16(b)). The testing data is less than the training data, which shows that the SVM model does not overfit the model and helps in attaining valuable predictions [57]. The input parameters such as the lateral Earth thrust and the angle of inclination of the building are calculated from the finite element analysis. The length and the width of the building are set as 15 m and 10 m for the analysis. The elastic modulus of the building is set for the masonry building parameters. Table 3 shows the parameters used for the model. The tests were carried out to find the performance of the building when they have different heights and elastic modulus of the building.

The test was conducted to find the efficiency in the material properties ($E = 10000$ MPa) and R^2 accuracy of the building performance is found to be 0.99 for both training and testing (Figures 16(a) and 16(b)). The modulus of elasticity of RCC is considered to study the vulnerability of the building. The results showed that the vulnerability of the building decreased due to the increased material properties with all other properties being the same as before iteration.

Reference [70] provides guidelines for the selection of the site for buildings in the hilly region. The building considered in this study was built at a distance of 3 m from the vertical cut. The vertical cut height is 11 m, which is more than the codal provisions and, hence, is not safe. The building had a height of 4 m and the lateral thrust force acting on the wall is 1200 kN/m^2. The vulnerability according to equation (4) shows the vulnerability is 1. Figure 16(c) shows the relation between vulnerability and elastic properties of the building. It shows the vulnerability value of different building elastic properties ranging from 2250 MPa to 10000 MPa. The building height considered for the analysis is 3 m and the lateral thrust acting on the

Table 3: Parameters used in the model.

Parameters	Unit	Range
Lateral Earth thrust (q)	kN/m^2	0 to 1200
Height of the building (H)	m	3
Length of the building (L)	m	15
Width of the building (W)	m	10
Elastic modulus (E)	MPa	2250 to 10000
Ratio of inclination of the building	No unit	0 to 1

building is 300 kN/m^2. The value of vulnerability reduces from 0.7 to 0.3 and the building resistance is increased to 20%. This is the case observed in this study for an inclination value of 0.01. This study shows that proper guidelines are to be framed, designed and the construction of the building should be according to the codal provisions.

8. Conclusions

The numerical investigation and vulnerability analysis of the building failure due to the vertical cut slope failure were carried out. The parameters used for the numerical investigation were obtained from the laboratory investigations and it revealed that the soil along the slip plane is silty sand (SM) and has a very low permeability coefficient. The low permeability of the soil is explained using Field Emission Scanning Electron Microscopy (FE-SEM), Energy-Dispersive X-ray spectrum (EDX), and X-ray diffraction analysis (XRD). FE-SEM images of both soil layers show the presence of kaolinite clay mineral with a large number of pores in it, which is well supported by EDX and XRD. EDX and XRD results indicate the presence of kaolinite clay mineral ($Al_2Si_2O_5(OH)_4$) along with quartz and calcium carbonate ($CaCO_3$) in the topsoil. The presence of calcium carbonate in the soil confirms the weathering process in the soil. The second layer of soil has a significantly less amount of kaolinite clay due to the incomplete weathering process in the soil. Thus, the topsoil experiences a low coefficient of permeability. The reddish colour in the topsoil explains the presence of ferrous content in the soil. The ferrous content helps in the attainment of soil/strength in the dry season due to the formation of ferrous aluminium silicates.

The vertical cut slope failure mechanism is studied based on the transient seepage condition and coupled analysis to identify soil deformation behaviour based on the flow condition. This helps in studying the effect of slope failure in the building. The analysis is carried out by considering the actual rainfall in three stages. The first stage of rainfall is considered from June to July 2018. Results from the first stage revealed that the matric suction of the soil is more and hence there is a negligible displacement in the slope. Analysis results from the second stage of rainfall (1 to 14 August 2018) emphasize the significance of antecedent rainfall in increasing the degree of saturation and pore pressure, thus leading the slope from stable to unstable. The third stage involves heavy rainfall during 15th and 16th of August 2018, with an average rainfall intensity of 187.5 mm/day. The large excess rainfall during the event day increases the pore water pressure and saturation of the soil above the slip surface to 35 kN/m^2 and 80%, respectively. The increase in the saturation of the soil and the reduction in matric suction led to the reduction in the effective stress and shear strength of the soil. Thus, the cut slope failure occurred and damaged the building located nearby. Results from the numerical analysis match reasonably well with the failure pattern observed at the site.

The vulnerability of the building is studied with the physical parameters obtained from the finite element analysis and it is predicted using the Support Vector Method of regression. The testing data showed that the predicted value and the observed value of vulnerability fitted very efficiently. The values showed the importance of the material properties in the increase in building resistance to 20%. This showed there should be proper guidelines and the building should be built according to codal provisions to avoid such a failure in the future.

Any one of the vertical cut stabilization measures needs to be considered before the construction of a building near the vertical cut. Soil nailing, Reinforced Earth (RE) walls, and slope stabilizing piles are useful stabilization measures.

Data Availability

Necessary data are included in the manuscript.

Conflicts of Interest

The authors declare that they have no conflicts of interest regarding the publication of this paper.

References

[1] P. R. Orense, S. Shimoma, K. Maeda, and I. Towhata, "Instrumented model slope failure due to water seepage," *Journal of Natural Disaster Science*, vol. 26, no. 1, pp. 15–26, 2004.

[2] D. Petley, "Global patterns of loss of life from landslides," *Geology*, vol. 40, no. 10, pp. 927–930, 2012.

[3] D. B. Kirschbaum, R. Adler, Y. Hong, S. Hill, and A. Lerner-Lam, "A global landslide catalog for hazard applications: method, results, and limitations," *Natural Hazards*, vol. 52, no. 3, pp. 561–575, 2010.

[4] D. Kirschbaum and T. Stanley, "Satellite-based assessment of rainfall-triggered landslide hazard for situational awareness," *Earth's Future*, vol. 6, no. 3, pp. 505–523, 2018.

[5] T. H. Nilsen and B. L. Turner, *Influence of Rainfall and Ancient Landslide Deposits on Recent Landslides (1950-71) in Urban Areas of Contra Costa County*, California, California, USA, 1975.

[6] R. H. Campbell, *Soil Slips, Debris Flows, and Rainstorms in the Santa Monica Mountains and Vicinity*, southern California, California, USA, 1975.

[7] S. A. Anderson and N. Sitar, "Analysis of rainfall-induced debris flows," *Journal of Geotechnical Engineering*, vol. 121, pp. 544–552, 1995.

[8] R. M. Iverson, M. E. Reid, and R. G. LaHusen, "Debris-flow mobilization from landslides," *Annual Review of Earth and Planetary Sciences*, vol. 25, no. 1, pp. 85–138, 1997.

[9] S. S. Chandrasekaran, R. Sayed Owaise, S. Ashwin, R. M. Jain, S. Prasanth, and R. B. Venugopalan, "Investigation on infrastructural damages by rainfall-induced landslides during

November 2009 in Nilgiris, India," *Natural Hazards*, vol. 65, no. 3, pp. 1535–1557, 2013.

[10] S. Vadivel and C. S. Sennimalai, "Failure mechanism of long-runout landslide triggered by heavy rainfall in achanakkal, nilgiris, India," *Journal of Geotechnical and Geoenvironmental Engineering*, vol. 145, Article ID 04019047, 2019.

[11] V. Senthilkumar, S. S. Chandrasekaran, and V. B. Maji, "Geotechnical characterization and analysis of rainfall-induced 2009 landslide at Marappalam area of Nilgiris district, Tamil Nadu state, India," *Landslides*, vol. 14, no. 5, pp. 1803–1814, 2017.

[12] V. Senthilkumar, S. S. Chandrasekaran, and V. B. Maji, "Rainfall-induced landslides: case study of the marappalam landslide, nilgiris district, Tamil nadu, India," *International Journal of Geomechanics*, vol. 18, pp. 1–13, 2018.

[13] R. Andrewwinner and S. S. Chandrasekaran, "Investigation on the failure mechanism of rainfall-induced long-runout landslide at Upputhode, Kerala state of India," *Land*, vol. 10, no. 11, p. 1212, 2021.

[14] D C. Brain and Z. Dobroslav, "Stability analyses of rainfall induced landslides," *Journal of Geotechnical and Geoenvironmental Engineering*, vol. 130, pp. 362–372, 2004.

[15] G. Wang and K. Sassa, "Factors affecting rainfall-induced flowslides in laboratory flume tests," *Géotechnique*, vol. 51, no. 7, pp. 587–599, 2001.

[16] H. ., D. G. Fredlund Rahardjo, *Soil Mechanics for Unsaturated Soils*, Wiley, New Jersey, USA, 1993.

[17] H. Rahardjo, T. T. Lim, M. F. Chang, and D. G. Fredlund, "Shear-strength characteristics of a residual soil," *Canadian Geotechnical Journal*, vol. 32, no. 1, pp. 60–77, 1995.

[18] S. L. Kuriakose, S. Devkota, D. G. Rossiter, and V. G. Jetten, "Prediction of soil depth using environmental variables in an anthropogenic landscape, a case study in the Western Ghats of Kerala, India," *Catena*, vol. 79, no. 1, pp. 27–38, 2009.

[19] K. S. Sajinkumar, S. Anbazhagan, A. P. Pradeepkumar, and V. R. Rani, "Weathering and landslide occurrences in parts of Western Ghats, Kerala," *Journal of the Geological Society of India*, vol. 78, no. 3, pp. 249–257, 2011.

[20] T. R. Martha, P. Roy, K. Khanna, K. Mrinalni, and K. Vinod Kumar, "Landslides mapped using satellite data in the Western Ghats of India after excess rainfall during August 2018," *Current Science*, vol. 117, no. 5, pp. 804–812, 2019.

[21] K. M. R. Hunt and A. Menon, "The 2018 Kerala floods: a climate change perspective," *Climate Dynamics*, vol. 54, no. 3-4, pp. 2433–2446, 2020.

[22] IMD, *Malappuram District Rainfall for Last Five Years* , vol. 25, Accessed, Oct, 2018.

[23] D. Varnes, "Landslide hazard zonation: a review of principles and practice," *Natural Hazards*, vol. 3, no. 19, p. 63, 1984.

[24] *UNDRO UNDRO News*, UNDRO, PP ,Geneva : Geneva, July/Aug. 1984.

[25] C. J. van Westen, T. W. J. van Asch, and R. Soeters, "Landslide hazard and risk zonation-why is it still so difficult?" *Bulletin of Engineering Geology and the Environment*, vol. 65, no. 2, pp. 167–184, 2006.

[26] C. N. Subasinghe and A. Kawasaki, "Assessment of physical vulnerability of buildings and socio-economic vulnerability of residents to rainfall induced cut slope failures: a case study in central highlands, Sri Lanka," *International Journal of Disaster Risk Reduction*, vol. 65, Article ID 102550, 2021.

[27] Q. Chen, L. Chen, L. Gui et al., "Assessment of the physical vulnerability of buildings affected by slow-moving landslides," *Natural Hazards and Earth System Sciences*, vol. 20, no. 9, pp. 2547–2565, 2020.

[28] The HINDU, "Rain continues to pound Malappuram," https://www.thehindu.com/news/national/kerala/rain-continues-to-pound-malappuram/article24696358.ece.

[29] S. L. Kuriakose, V. G. Jetten, C. J. van Westen, G. Sankar, and L. P. H. van Beek, "Pore water pressure as a trigger of shallow landslides in the western Ghats of Kerala, India: some preliminary observations from an experimental catchment," *Physical Geography*, vol. 29, no. 4, pp. 374–386, 2008.

[30] "GSI," *GSI Available Online*, May 10, 2020.

[31] K. S. Akhil and D. Venkat Reddy, "Geological and Geotechnical Investigations of Calicut Granite of Kerala State - A Case in Study," in *Proceedings of the National Conference on Technological Innovations for Sustainable infrastructure*, Calicut, India, March 2015.

[32] M. R. Mitchell, R. E. Link, O. F. Usluogullari, and C. Vipulanandan, "Stress-strain behavior and California bearing ratio of artificially cemented sand," *Journal of Testing and Evaluation*, vol. 39, no. 4, pp. 103165–6103645, 2011.

[33] "PLAXIS-3D CONNECT edition V21.01," *PLAXIS 3D-Reference Manual*, pp. 1–600, 2021.

[34] D. Kyung and J. Lee, "Interpretative analysis of lateral load-carrying behavior and design model for inclined single and group micropiles," *Journal of Geotechnical and Geoenvironmental Engineering*, vol. 144, pp. 1–11, 2018.

[35] M. T. van Genuchten, "A closed-form equation for predicting the hydraulic conductivity of unsaturated soils," *Soil Science Society of America Journal*, vol. 44, no. 5, pp. 892–898, 1980.

[36] R. D. Hart, C. L. Detournay, and P. A. Cundall, "Continuum and distinct element modeling in geo-engineering," in *Proceedings of the Proceedings First FLAC/DEM Symposium*, vol. 25, MN, USA, 2008.

[37] J. Bear, *Hydraulics of Groundwater*, McGraw-Hill Book Co., New York, 1979.

[38] F. J. Leij, "The UNSODA unsaturated soil hydraulic database: user's manual," *National Risk Management Research Laboratory, Office of Research and*, vol. 96, 1996.

[39] J. H. M. Wösten and M. T. van Genuchten, "Using texture and other soil properties to predict the unsaturated soil hydraulic functions," *Soil Science Society of America Journal*, vol. 52, no. 6, pp. 1762–1770, 1988.

[40] M. Alam, O. Chaallal, and B. Galy, "Flexible temporary shield in soft and sensitive clay: 3D FE modelling of experimental field test," *Modelling and Simulation in Engineering*, vol. 2021, pp. 1–15, Article ID 6626750, 2021.

[41] M. Papathoma-Köhle, "Vulnerability curves vs. vulnerability indicators: application of an indicator-based methodology for debris-flow hazards," *Natural Hazards and Earth System Sciences*, vol. 16, no. 8, pp. 1771–1790, 2016.

[42] M. Silva and S. Pereira, "Assessment of physical vulnerability and potential losses of buildings due to shallow slides," *Natural Hazards*, vol. 72, no. 2, pp. 1029–1050, 2014.

[43] M. Papathoma-Köhle, B. Neuhäuser, K. Ratzinger, H. Wenzel, and D. Dominey-Howes, "Elements at risk as a framework for assessing the vulnerability of communities to landslides," *Natural Hazards and Earth System Sciences*, vol. 7, no. 6, pp. 765–779, 2007.

[44] A. Puissant, M. Van Den Eeckhaut, M. Kappes et al., "Index-oriented methodologies for landslide consequence analysis: an application to a mountain community in the French alps," in *Landslide Science and Practice: Volume 7: Social and Economic IMPact and Policies*, C. Margottini, P. Canuti, and K. Sassa, Eds., vol. 18, pp. 159–167, Springer, Berlin, Heidelberg, 2013.

[45] J. B. Burland and C. P. Wroth, "Settlement of buildings and associated damage," in *Proceedings of the Settlement of Structures, Proceedings of the Conference of the British Geotechnical Society*, pp. 611–654, Hertsford, England, January 1975.

[46] S. P. Timoshenko, *Strength of Materials Pt. 1, Pt. 1*, Van Nostrand, New York, USA, 1955.

[47] J. B. G. A. Calejo, *3d Modelling of Sheet Pile Corner in Difficult Ground Conditions*, Universidade Do Porto, Porto, Portugal, 2015.

[48] C. Tarbotton, F. Dall'Osso, D. Dominey-Howes, and J. Goff, "The use of empirical vulnerability functions to assess the response of buildings to tsunami iMPact: CoMParative review and summary of best practice," *Earth-Science Reviews*, vol. 142, 2015.

[49] H.-s. Kang and Y.-t. Kim, "The physical vulnerability of different types of building structure to debris flow events," *Natural Hazards*, vol. 80, no. 3, pp. 1475–1493, 2016.

[50] C. Chiocchio, G. Iovine, and M. Parise, "A proposal for surveying and classifying landslide damage to buildings in urban areas," *Eng. Geol. Environ. Proc. sympsium, Athens, 1997*, vol. 1, no. 1997, pp. 553–558, 1977.

[51] A. H. Cooper, "The classification, recording, databasing and use of information about building damage caused by subsidence and landslides," *The Quarterly Journal of Engineering Geology and Hydrogeology*, vol. 41, no. 3, pp. 409–424, 2008.

[52] Y. B. Dibike, S. Velickov, D. Solomatine, and M. B. Abbott, "Model induction with support vector machines: introduction and applications," *Journal of Computing in Civil Engineering*, vol. 15, 2001.

[53] T. Asefa, M. W. Kemblowski, G. Urroz, M. McKee, and A. Khalil, "Support vectors-based groundwater head observation networks design," *Water Resources Research*, vol. 40, no. 11, 2004.

[54] X. Zhang, R. Srinivasan, and M. Van Liew, "Approximating SWAT model using artificial neural network and support vector machine," *JAWRA Journal of the American Water Resources Association*, vol. 45, no. 2, pp. 460–474, 2009.

[55] V. Budamala and A. B. Mahindrakar, "Adaptive hybrid architecture for enhancement of the complex hydroclimatic system and assessment of freshwater security," *Journal of Hydroinformatics*, vol. 23, no. 5, pp. 950–965, 2021.

[56] V. Budamala and A. Baburao Mahindrakar, "Enhance the prediction of complex hydrological models by pseudo-simulators," *Geocarto International*, vol. 36, no. 9, pp. 1027–1043, 2021.

[57] P. Samui, "Slope stability analysis: a support vector machine approach," *Environmental Geology*, vol. 56, no. 2, pp. 255–267, 2008.

[58] "ASTM D2487-11," in *Proceedings of the Standard Practice for Classification of Soils for Engineering Purposes (Unified Soil Classification System)*, p. 5, American Society for Testing Materials, 2011.

[59] *IS2720(17) Indian Standard Methods of Tests for Soils: Laboratory Determination of Permeability Bur*, Indian Stand., New Delhi, 1986.

[60] P. Samui, "Slope stability analysis: A support vector machine approach. Environ," *Geol*, vol. 56, pp. 255–267, 2008.

[61] ASTM D2487-11, *Proceedings of the Standard Practice for Classification of Soils for Engineering Purposes (Unified Soil Classification System)*, American Society for Testing and Materials, West Conshohocken, PA, USA, 2011.

[62] IS2720 Part-17, *Indian Standard Methods of Tests for Soils: Laboratory Determination of Permeability*, Bureau of Indian Standards, New Delhi, India, 1986.

[63] B. F. Mallory and D. N. Cargo, *Physical Geology*, Article ID 007085047X, 1979.

[64] "BS5930-1999 Code of practice for site investigations (formerly CP 2001)," *International Journal of Rock Mechanics and Mining Science & Geomechanics Abstracts*, vol. 18, p. 106, 1981.

[65] "Weathering of rocks," *Developments in Geotechnical Engineering*, vol. 10, pp. 146–162, 1976.

[66] K. S. Sajinkumar and S. Anbazhagan, "Geomorphic appraisal of landslides on the windward slope of Western Ghats, southern India," *Natural Hazards*, vol. 75, no. 1, pp. 953–973, 2015.

[67] J. L. R. Touret and J. M. Huizenga, "Charnockite microstructures: from magmatic to metamorphic," *Geoscience Frontiers*, vol. 3, no. 6, pp. 745–753, 2012.

[68] "GSI Systematic geological mapping and preliminary mineral investigation in parts of Kozhikode taluk, Kozhikode district,Manjeri and Tirur taluks," *Malappuram district, Kerala state*, vol. 5973, pp. 1–23, 1973.

[69] M. E. José and H. Laureano, "Effect of degree of weathering on dynamic properties of residual soils," *J. Geotech. Eng*, vol. 122, pp. 988–997, 1996.

[70] *IS14243-2 Guidelines For Selection and Development of Site for Building in hill Areas*, Part 2: Selection and development, 1995.

Hindawi
Advances in Civil Engineering
Volume 2022, Article ID 3601914, 12 pages
https://doi.org/10.1155/2022/3601914

Research Article

Hybridizing Grid Search and Support Vector Regression to Predict the Compressive Strength of Fly Ash Concrete

Fei Tang,[1] Yanqi Wu ,[2] and Yisong Zhou[3]

[1]*School of Architectural Engineering, Xinyang Vocational and Technical College, Xinyang 464000, China*
[2]*School of Civil Engineering, Southeast University, Nanjing 211189, China*
[3]*School of Civil Engineering, Xinyang College, Xinyang 464000, China*

Correspondence should be addressed to Yanqi Wu; yanqiwu@seu.edu.cn

Received 23 December 2021; Accepted 8 February 2022; Published 23 February 2022

Academic Editor: Ravindran Gobinath

Support vector regression (SVR) has been applied to the prediction of mechanical properties of concrete, but the selection of its hyperparameters has been a key factor affecting the prediction accuracy. To this end, hybrid machine learning combines the SVR model and grid search (GS), namely, the GS-SVR model was proposed to predict the compressive strength of concrete and sensitivity analysis in this work. The hybrid model was trained and tested on a total of 98 datasets retrieved from literature, and the model performance was compared with the original SVR model under the same datasets. The obtained results in terms of R of 0.981, MSE of 3.44, RMSE of 1.85, MAE of 1.17, and MAPE of 0.05 demonstrate that the GS-SVR model proposed can be a candidate method for compressive strength prediction in subsequent related studies. Additionally, a graphical user interface (GUI) was developed to conveniently provide some initial estimates of the outcomes before performing extensive laboratory or fieldwork. Finally, the effect of each variable on the compressive strength in a random environment was analyzed.

1. Introduction

As the most consumed material in the construction industry, cement has brought great convenience to the construction industry. But the bad news is that it also puts enormous pressure on the environment. Since the production and utilization of cement are accompanied by a large amount of greenhouse gas emissions, many scholars have started to focus on research related to mineral admixtures that can be used to replace cement [1–5]. Among them, the use of fly ash as an auxiliary cementitious material for the production of a large amount of fly ash concrete is one of the important ways to reduce environmental pollution and realize the resourcefulness of fly ash. Moreover, it is also an effective means for concrete producers to enhance and improve the performance of concrete in all aspects, reduce the use of cement, and lower the cost of concrete [6, 7]. The incorporation of fly ash not only ensures the quality of concrete and reduces the cost of manufacturing concrete but also improves the compatibility, durability, and strength, thus becoming the most widely used alternative and receiving great attention [8].

The importance of concrete materials for the construction industry needs no more introduction [9–11]. Concrete is used as a construction material worldwide due to its various properties such as strength, durability, stiffness, and fire resistance. Among these properties, compressive strength is considered to be the most important one because it seriously affects the safety and durability of concrete members. Understanding the early behavior of concrete allows appropriate measures to be taken to avoid problems such as cracking and deformation of concrete members, formwork failure, and rework. In addition, early strength prediction and monitoring are important for assessing construction safety, determining structural maturity, and predicting later strength development. The main reason for different compressive strength values of concrete is that concrete is a nonhomogeneous material consisting of binders, aggregates, water, and admixtures. In such a complex mix, it is difficult to find or predict the compressive

strength of concrete accurately. The compressive strength of concrete can be assessed in the laboratory by crushing a standard size cylinder or cube. However, such laboratory tests are supposed to be inefficient and uneconomical, as well as labor-intensive and time-consuming. Traditional methods of concrete strength prediction are mainly based on a statistical analysis of linear or nonlinear regression equations, but obtaining accurate equations is difficult and requires a great deal of skill and experience. Due to the large number of concrete ingredients, it seems difficult to establish an explicit equation between the compressive strength and each ingredient as a way to predict its compressive strength.

To address these issues, machine learning techniques are used to predict the compressive strength of concrete. In fact, with the development of artificial intelligence, various machine learning algorithms such as artificial neural network (ANN), support vector machines (SVM), random forest, and extreme learning machine (ELM) have been applied to predict the mechanical properties of concrete [12–23]. Ly et al. [24] employed an optimal deep neural network model on a database of 223 experimental data to predict the 28 days compressive strength of rubber concrete and achieved a high prediction accuracy of $R = 0.9874$. Han et al. [25] utilized an optimized random forest approach on 1030 data samples collected from published literature to predict the compressive strength of high-performance concrete. Furqan et al. [26] used the ANN, SVM, and gene expression programming (GEP) on 300 datasets to predict the compressive strength of self-compacting concrete. Zhang et al. [27] employed nine machine learning models to predict the compressive strength of concrete at the age of 7 days and found that the nonlinear models had better predictive performance than the linear models. Khoa et al. [28] employed deep neural networks (DNNs) and ResNet models for compressive strength prediction of green fly ash-based geopolymer concrete. The results showed that ResNet is superior and indicated that these two machine learning methods can be useful for the mixed design of geopolymer concrete. From the published studies, it can be found that these machine learning algorithms outperform traditional empirical formulations by enabling the capture and mapping of multidimensional nonlinear relationships. It is possible to extract unknown relationships and data information between input and output variables [29].

However, these models also have limitations, and many models require parameter tuning to get better performance. For support vector regression (SVR), the selection of hyperparameters has a great impact on the accuracy of the prediction results. In other words, the prediction accuracy of a single SVR model is limited. To better understand and apply the SVR method, further exploration is still needed in this area using different datasets and optimization algorithms. For this reason, this study aims to propose a hybrid machine learning that combines the SVR model and grid search (GS), namely, the GS-SVR model, to achieve an accurate prediction of the compressive strength of fly ash concrete. Based on the model, the effect of random variation of individual variables on compressive strength is investigated as a reference and guide for concrete mix design and strength prediction.

2. Methodology

2.1. Support Vector Regression. The objective of the SVR is to find a linear regression equation that fits all sample points and minimizes the total variance of the sample points from this regression hyperplane. There is a sample training set $E = \{(x_i, y_i) | i = 1, 2, \ldots n\}$, $x_i \in R^n$, $y_i \in R$. A function $f(x_i)$ is probed on R^n, such that $y_i = f(x_i)$, and there is always a corresponding y-value for any input x. Such a function $f(x_i)$ is called a regression function, and $f(x_i)$ can be described as follows.

$$f(x_i) = \omega \cdot \phi(x_i) + b, \tag{1}$$

where $\omega \in R^n$ is the weight vector, $\phi(x_i)$ is a nonlinear mapping which serves to map the data from the space R^n to the higher feature space, and b is the bias. Equation (1) can be fitted to all sample points at precision ε.

$$\left| y_i - [\omega \cdot \phi(x_i) + b] \right| \le \varepsilon, \quad i = 1, 2, \ldots, n. \tag{2}$$

Since there is a certain fitting error, the slack variables (ξ_i, ξ_i^*) and the penalty parameter C are introduced. The regression fitting problem is changed to an optimization problem.

$$\begin{aligned} &\min\left(R(\omega, \xi_i, \xi_i^*)\right) = \frac{1}{2}\omega \cdot \omega + C\sum_{i=1}^{n}(\xi_i + \xi_i^*), \\ &\text{s.t.} \begin{cases} y_i - [\omega \cdot \phi(x_i) + b] \le \varepsilon + \xi_i, \\ \omega \cdot \phi(x_i) + b - y_i \le \varepsilon + \xi_i^*, \\ \xi_i, \xi_i^* \ge 0. \end{cases} \end{aligned} \tag{3}$$

Using Lagrange multipliers for equation (3), the Lagrange function is introduced to obtain its dual form.

$$\max\left(W(\alpha,\alpha^*) = -\frac{1}{2}\sum_{i,j=1}^{n}(\alpha_i-\alpha_i^*)\left(\alpha_j-\alpha_j^*\right)\left[\phi(x_i)\cdot\phi\left(x_j\right)\right] - \sum_{i=1}^{n}(\alpha_i+\alpha_i^*)\varepsilon + \sum_{i=1}^{n}(\alpha_i-\alpha_i^*)y_i, \right.$$

$$\text{s.t.} \begin{cases} \sum_{i=1}^{n}(\alpha_i-\alpha_i^*) = 0, \\ 0 \le \alpha_i, \alpha_i^* \le C, i = 1,2,\ldots,n, \end{cases} \tag{4}$$

$$\omega = \sum_{i=1}^{n}(\alpha_i-\alpha_i^*)\phi(x_i).$$

The core of optimization at this point is to first determine the feature space and find the flattest function in that space that satisfies the conditions and then use that function to solve the nonlinear problem. For this reason, the kernel function $K(x_i, x_j)$, $K(x_i, x_j) = \phi(x_i)\cdot\phi(x_j)$ is introduced. The regression fitting function at this point is

$$f(x_i) = \sum_{i,j=1}^{n}(\alpha_i-\alpha_i^*)K\left(x_i,x_j\right) + b. \tag{5}$$

There are many choices of kernel functions, and the commonly used RBF function (Figure 1) is chosen in this study [30].

2.2. Grid Search Method. It is well known that the identification results depend heavily on the selection of hyperparameters of the SVR model. Since the parameters are highly nonlinear, a large number of experiments are often required to determine the combination of parameters, such as the penalty parameter C and the kernel parameter g. Although Lin et al. [31, 32] have done much extensive research to simplify the application of SVM, such as proposing LIBSVM, the selection of parameters C and g still depends on experience. Therefore, there is an urgent need to implement automatic tuning of parameters to obtain the optimal value once the parameters are entered. The grid search (GS) method can solve these problems. The GS method is to computationally evaluate the impact of each parameter combination on the model performance by iterating through all the candidate parameter choices in a loop to obtain the optimal combination of hyperparameters [33]. The flowchart of parameter selection is shown in Figure 2.

3. Dataset Description

3.1. Input and Output Variables. In this study, 98 sets of data were retrieved from the literature. Each dataset consisted of six constituents (cement, fly ash, water, super, plasticizer, coarse aggregate, and fine aggregate) and age as input variables and the compressive strength as output variable. The distribution of the input and output variables is shown in Figure 3, and the statistical characteristics of these variables are given in Table 1. It can be seen that the compressive strength varies greatly for different combinations of input variables. Additionally, Pearson correlation coefficients between input and output variables were plotted, as shown in Figure 4. Within the current dataset, linear correlation between any of the input and output variables is weak, which indicates a complex nonlinear relationship between compressive strength and these input parameters. Therefore, the relationship between compressive strength and these parameters is difficult to reflect by an explicit equation.

3.2. Performance Criteria. To describe and compare the performance of the models, five evaluation metrics, linear correlation coefficient (R), mean squared error (MSE), mean root error (RMSE), mean absolute percentage error (MAPE), and mean absolute error (MAPE), were introduced [34]. These metrics are defined as follows.

$$R = \frac{n\sum_{i=1}^{n}\left(y_e y_p\right) - \sum_{i=1}^{n} y_e \sum_{i=1}^{n} y_p}{\sqrt{\left[n\left(\sum_{i=1}^{n} y_e^2\right) - \left(\sum_{i=1}^{n} y_e\right)^2\right]\left[n\left(\sum_{i=1}^{n} y_p^2\right) - \left(\sum_{i=1}^{n} y_p\right)^2\right]}},$$

$$\text{MAE} = \frac{1}{n}\sum_{i=1}^{n}\left|y_e - y_p\right|,$$

$$\text{MSE} = \frac{1}{n}\sum_{i=1}^{n}\left(y_e - y_p\right)^2,$$

$$\text{RMSE} = \sqrt{\frac{1}{n}\sum_{i=1}^{n}\left(y_e - y_p\right)^2},$$

$$\text{MAPE} = \frac{1}{n}\sum_{i=1}^{n}\left|\frac{y_e - y_p}{y_e}\right| \times 100\%, \tag{6}$$

where n is the number of samples, y_e is the experimental value of compressive strength, and y_p is the predicted value. When R is closer to 1 or the other four error indicators are closer to 0, the prediction performance of the model is better.

4. Model Performance

Initially, GS is used for the selection of hyperparameters in the SVR. For the GS-SVR model, C and g are searched in an exponential grid of $[2^{-8}, 2^{8}]$ with step $2^{0.1}$. The evolution of the parameters is shown in Figure 5. The model is trained using 10-fold cross-validation.

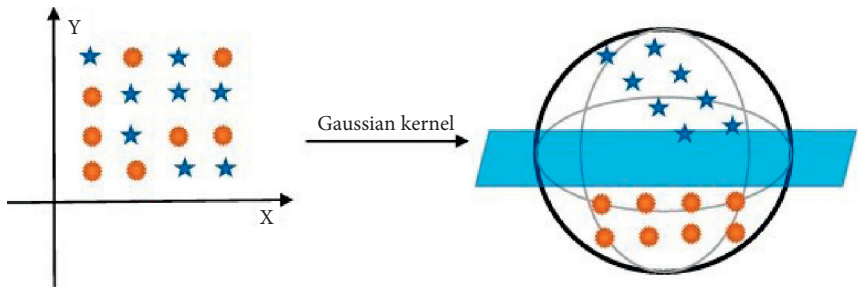

Figure 1: Schematic diagram of support vector machine and Gaussian kernel.

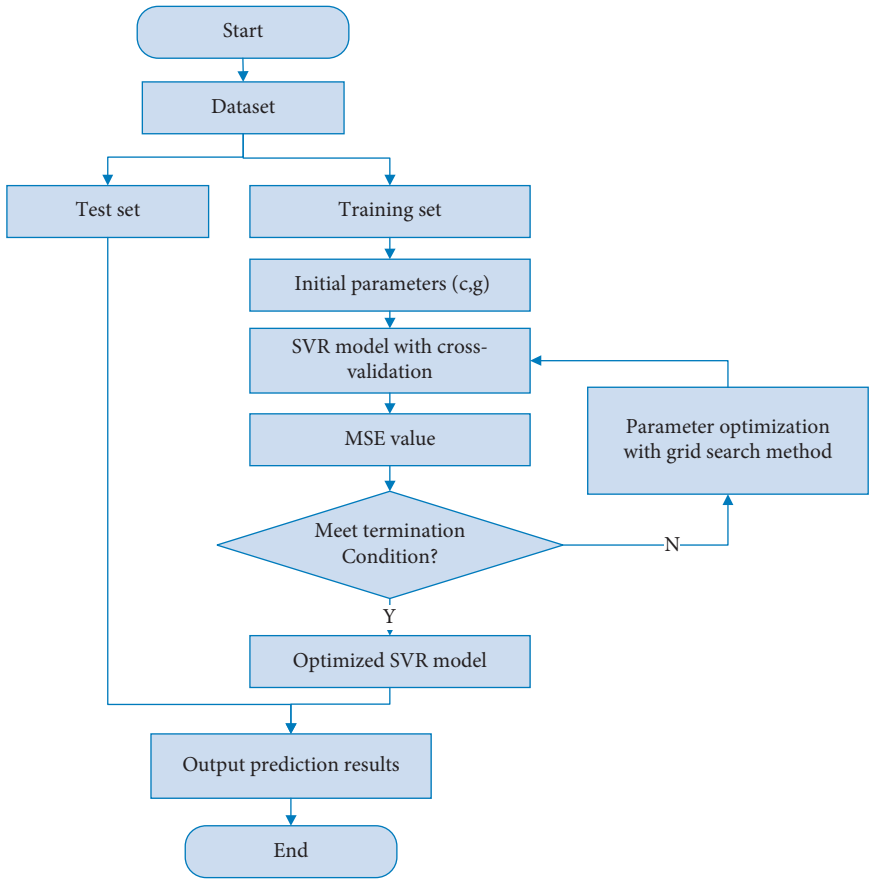

Figure 2: Flowchart of the SVR model using the GS method and cross-validation.

To highlight the superiority of the proposed method in this study, the original SVR model and GS-SVR model were performed on the same training and test set. The model results are shown in Figure 6. It can be clearly observed that compared with the SVR model, the GS-SVR model results have a closer distribution of data points along the diagonal, indicating that the predicted values match better with the experimental values, and the correlation coefficient R exceeds 0.98 for both the training and test sets.

For comparison and evaluation purposes, Figure 7 shows the predicted and experimental values for the training and test sets in more detail. At each sample point, the predicted values agree well with the experimental values, demonstrating the accuracy and effectiveness of the GS-SVR model in capturing the complex nonlinear relationships between the seven input variables and the compressive strength. The error metrics for model training and test are shown in Figure 8. It can be clearly observed from both sets that the four error indicators of the GS-SVR model are smaller, further validating the accuracy and generalization capability of the proposed GS-SVR model.

5. Sensitivity Analysis

The model results in Section 4 show that the compressive strength depends on the input vector consisting of six ingredients and age. However, these variables have almost no deterministic values in a stochastic

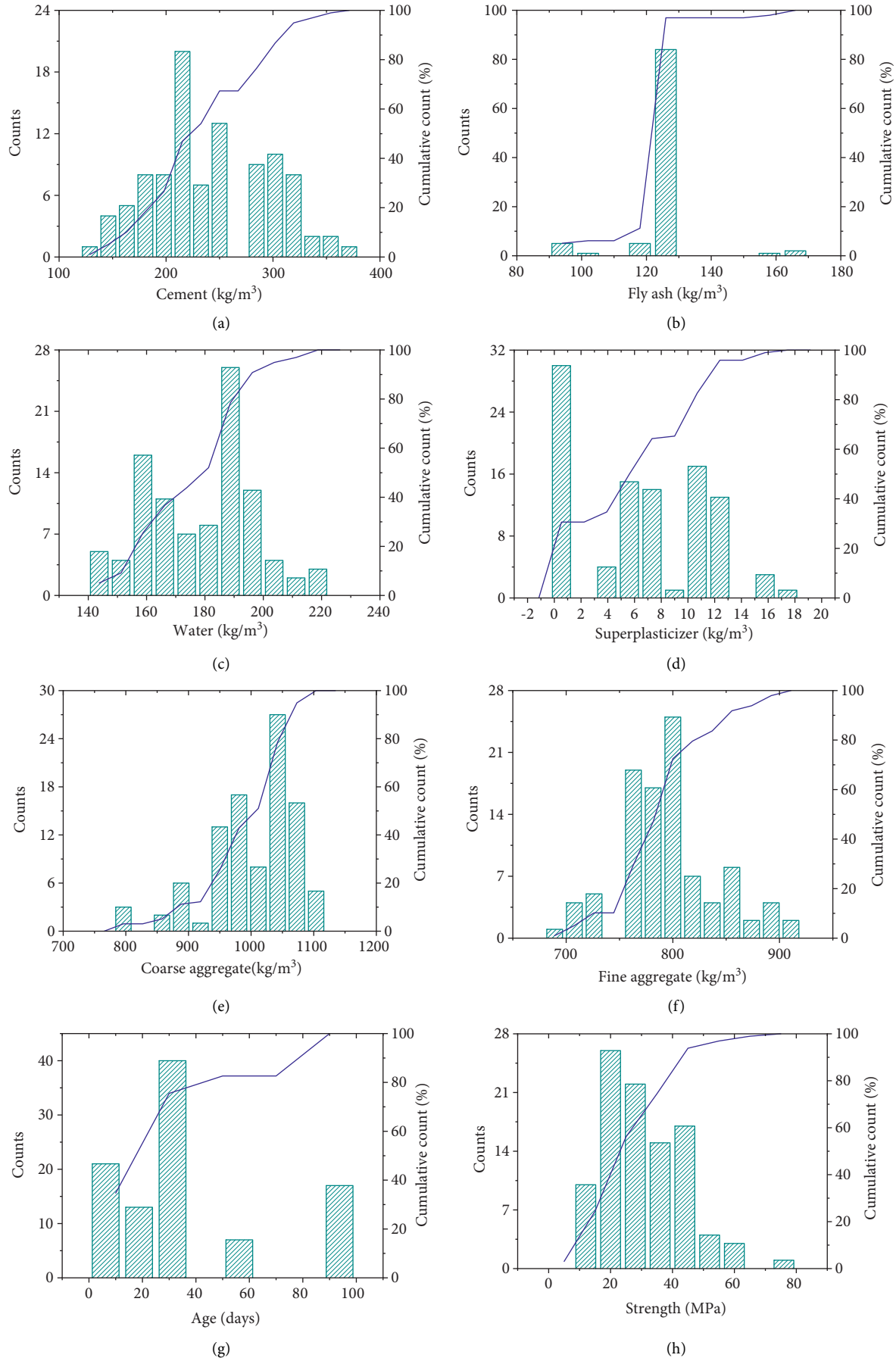

Figure 3: Distribution of input and output variables.

Table 1: Statistical characteristics of variables.

		Cement	Fly ash	Water	Super plasticizer	Coarse aggregate	Fine aggregate	Age	Compressive strength
Training set	Unit	kg/m^3	kg/m^3	kg/m^3	kg/m^3	kg/m^3	kg/m^3	d	MPa
	Count	78	78	78	78	78	78	78	78
	Maximum	376	163.3	216.7	18	1118	905.4	90	72.11
	Minimum	136.1	92.1	141.1	0	801	700	3	9.49
	Standard deviation	54.22	9.68	18.12	4.65	67.60	44.70	29.72	13.37
	Mean	243.95	123.54	177.77	6.46	1010.62	800.34	34.06	31.85
	Skewness	0.25	−0.05	−0.18	−0.07	−0.97	0.63	0.97	0.63
	Kurtosis	−0.75	9.44	−0.81	−0.88	0.79	0.23	−0.40	0.02
Test set	Count	20	20	20	20	20	20	20	20
	Maximum	349	168.3	220.5	16.1	1111.6	856.5	90	41.64
	Minimum	144	95.7	158.2	0	801.1	687	3	9.55
	Standard deviation	59.46	11.81	17.50	5.79	75.95	43.85	25.71	9.53
	Mean	231.28	125.19	182.27	5.77	969.55	771.99	32.70	25.49
	Skewness	0.46	1.78	0.51	0.34	−0.29	−0.17	1.52	0.21
	Kurtosis	−0.80	10.57	−0.11	−1.47	−0.05	−0.73	1.65	−1.20

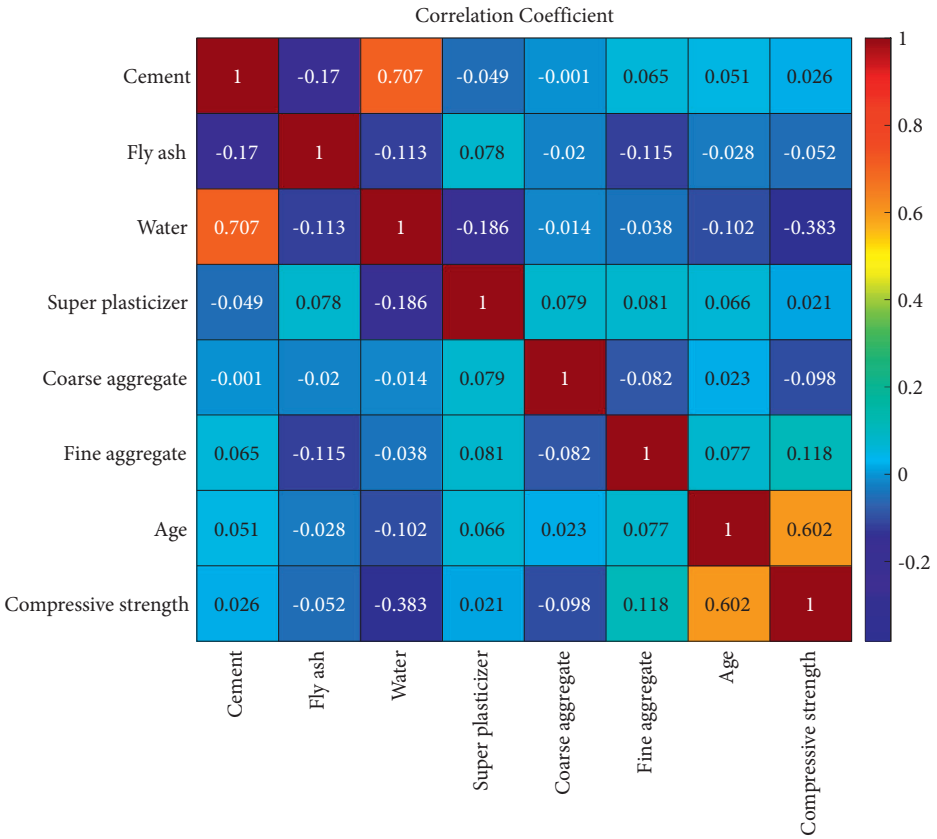

Figure 4: Correlation coefficient of the dataset.

environment. This uncertainty may cause the deviation of the predicted and actual values of the concrete compressive strength. Therefore, this section focuses on the effect of the random variation degree of each input variable on the compressive strength. According to the statistical characteristics of the dataset given in Table 1, a set of input vectors with deterministic configurations is given in Table 2. The input variables are assumed to be at three different values of degree of stochasticity $S_0 = (0.05, 0.1, 0.15)$. In each stochastic setting, 10^4 samples were generated using MATLAB. To quantify and compare the degree of influence on the output variable, the sensitivity of the random input to the compressive strength is defined as follows [35, 36].

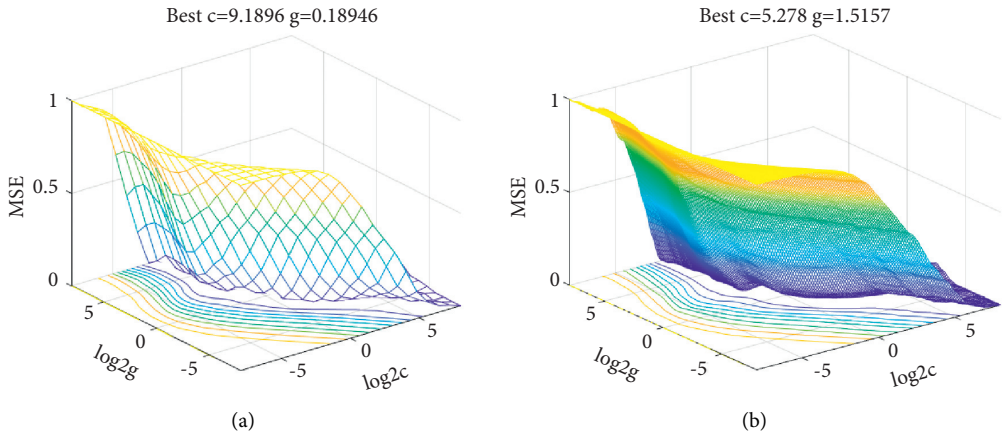

Figure 5: Hyperparameter selection results of the SVR model.

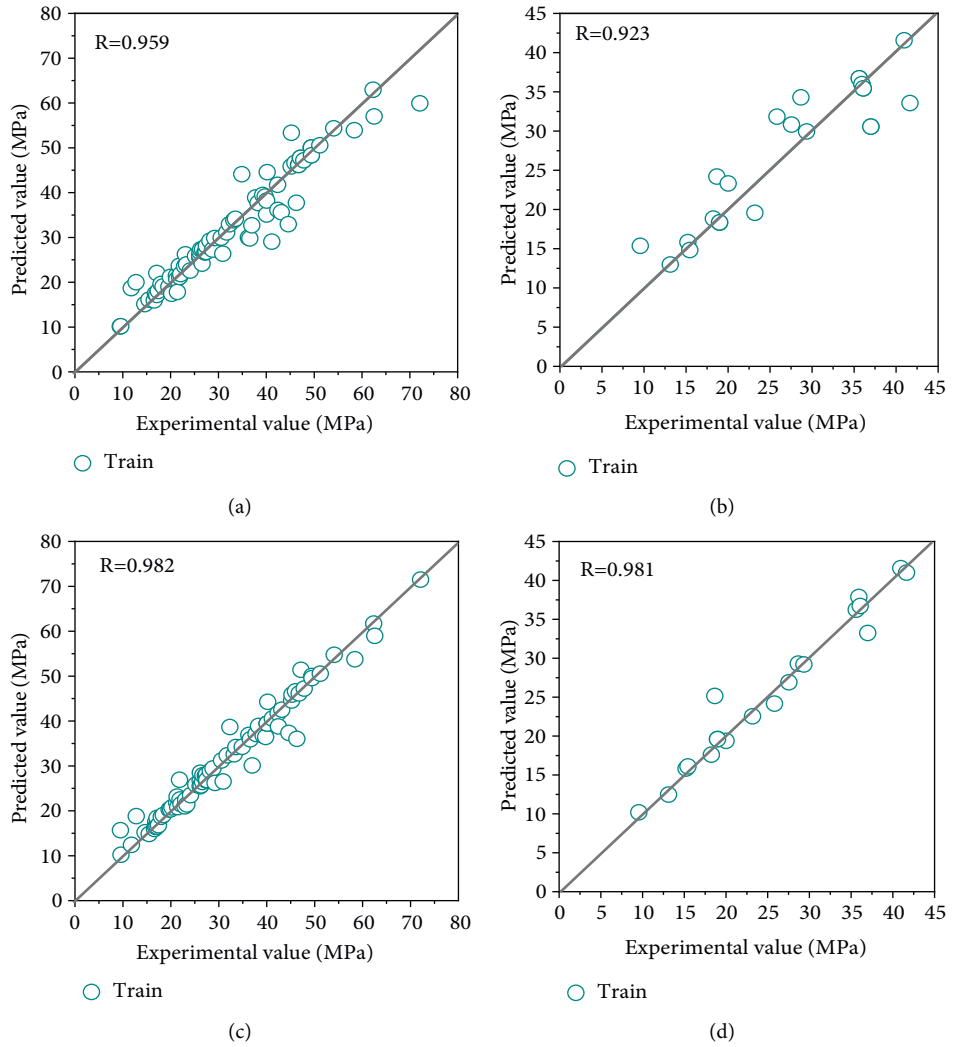

Figure 6: Correlation between predicted and experimental values of two models. (a) SVR model. (b) GS-SVR model.

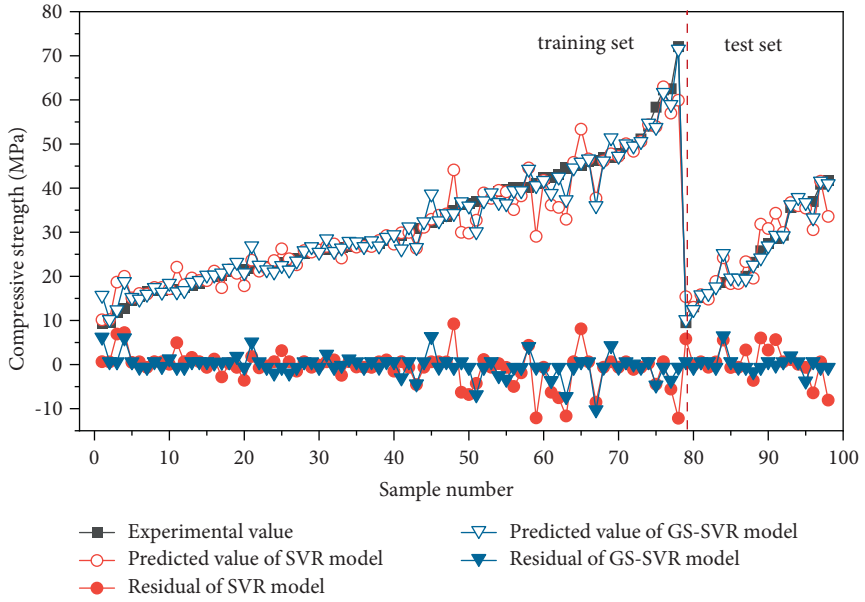

Figure 7: Comparison of predicted and actual values for two models.

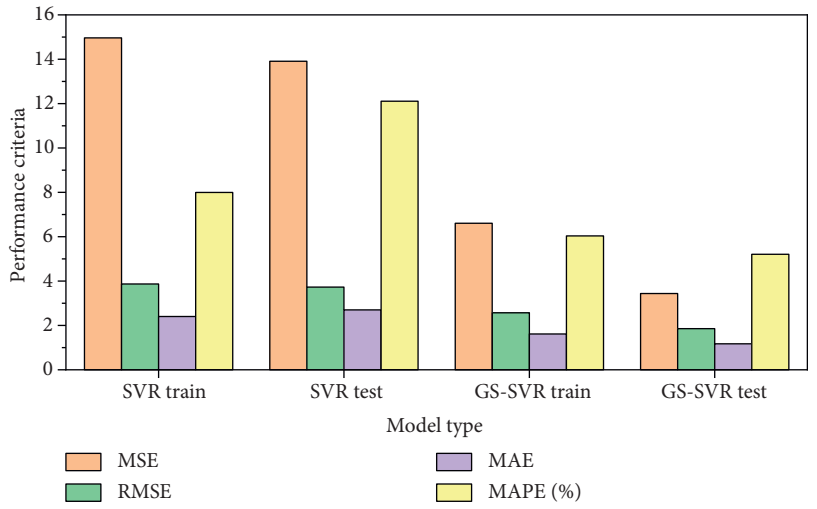

Figure 8: Performance criteria of the models.

Table 2: Deterministic values of configuration parameters.

Variable	Unit	Value
Cement	kg/m^3	230
Fly ash	kg/m^3	125
Water	kg/m^3	180
Superplasticizer	kg/m^3	6
Coarse aggregate	kg/m^3	1000
Fine aggregate	kg/m^3	800
Age	d	28

$$CV = \frac{\sigma}{\mu}, \tag{7}$$

where σ and μ are the standard deviation and mean values of the compressive strength, respectively. The distribution of compressive strength for the three randomness settings is shown in Figure 9.

As the randomness S_0 increases, the sensitivity of compressive strength for the three cases is higher. Additionally, among the seven variables, fly ash and coarse

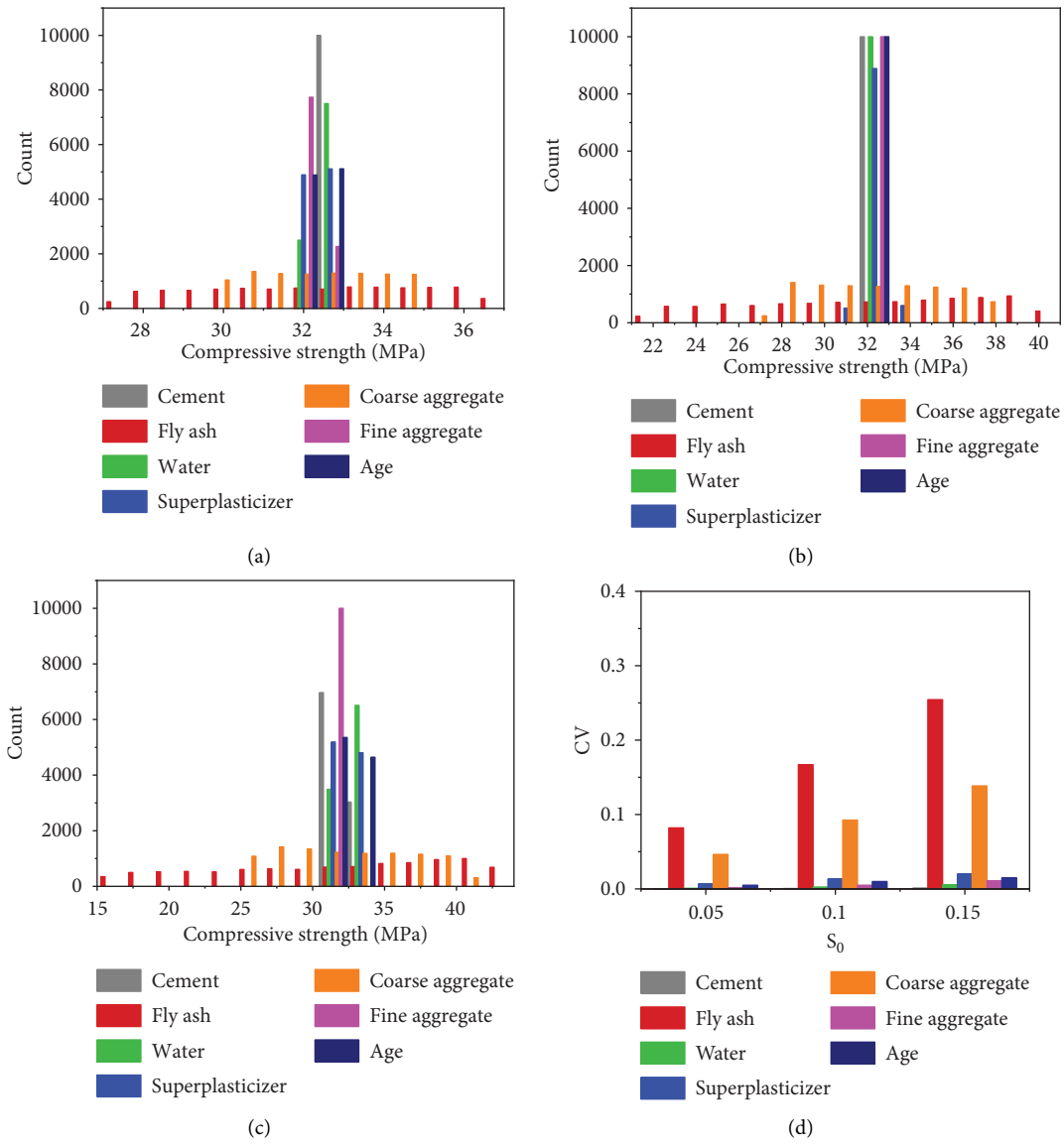

Figure 9: Distribution of the predicted values of compressive strength at different random degrees. (a) $S_0 = 0.05$. (b) $S_0 = 0.1$. (c) $S_0 = 0.15$. (d) Sensitivity.

aggregate resulted in a more discrete distribution of predicted compressive strength values, where fly ash has the greatest influence on the predicted uncertainty of compressive strength values. This insight might also be observed in Figure 9(d). Designers should take more attention to the design of mix design and compressive strength prediction of concrete with fly ash admixture in stochastic environments.

6. GS-SVR Model-Based Interactive Graphical User Interface

Nowadays, structural designers and engineers prefer to develop more robust and user-friendly software to gain wider applicability. In fact, to ensure that the model developed in this study is useful and practical and for ease of use, a graphical user interface (GUI) was compiled using MATLAB as shown in Figure 10. The whole interface is divided into two main parts: the optimization of hyperparameters and the prediction of output results with known input parameters. The operation of the GUI can be obtained by clicking on the Help menu, and the whole process consists of four main steps.

Step 1. Click the Initialize setting button to get the default values of the parameters; these values can also be modified manually.

Step 2. Click the Optimization button to obtain the optimal values of parameters C and g

Step 3. Manually enter each input parameter

Step 4. Click the Predict button to get the final output value

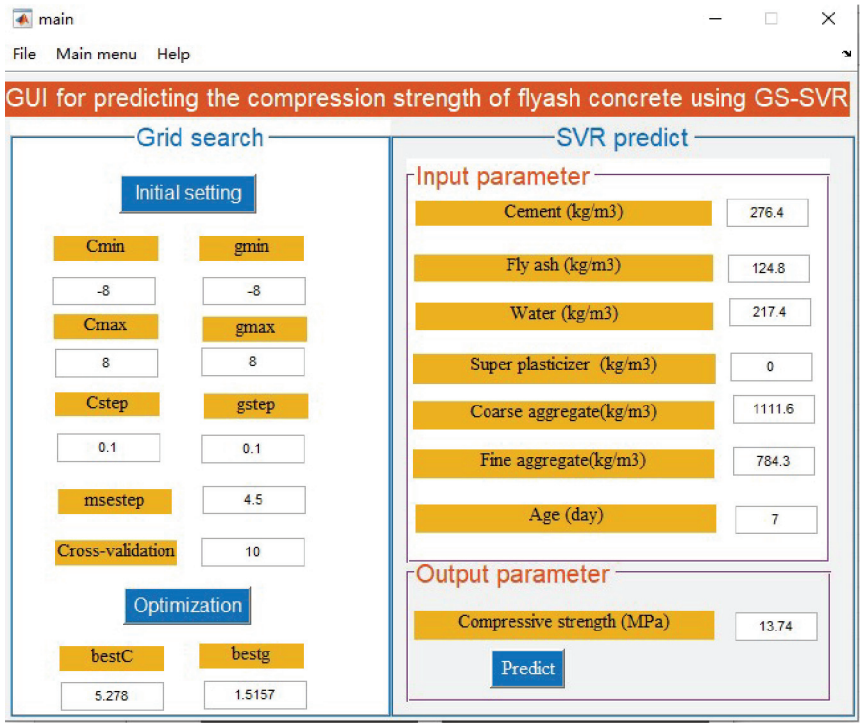

Figure 10: GS-SVR model-based interactive graphical user interface.

Finally, the compressive strength of fly ash concrete is displayed directly by clicking the Predict button. This GUI was developed mainly for the dataset used in this study, and future optimization of the user interface such as adding new datasets and other influencing parameters can be considered to make the model predictions more accurate.

7. Conclusions

In this work, a hybrid machine learning model GS-SVR was employed to predict the compressive strength of concrete with fly ash admixture and quantity the sensitivity of the compressive strength in the stochastic environment. The main findings are as follows.

(1) The proposed GS-SVR model can accurately capture the complex nonlinear relationship between the seven input parameters and the compressive strength of concrete with an accuracy R of over 98% in both the training and test phases

(2) From the performance criteria, the prediction performance of the proposed model is better than that of the original SVR model, which is a promising candidate for evaluating the compressive strength of fly ash concrete

(3) In the stochastic environment, for the dataset used in this study, the compressive strength of concrete with fly ash admixture is most sensitive to fly ash, followed by the coarse aggregate, and the sensitivity to the other five input variables is weak.

(4) As the randomness of variables increases, the distribution range of compressive strength becomes wider and the dispersion becomes larger, and designers and engineers should pay more attention to the effect of random variation of fly ash and coarse aggregate on strength uncertainty.

(5) This study provides a new GUI that can be easily used to predict the compressive strength of fly ash concrete. This tool has been proven to be very successful, exhibiting very reliable predictions. Otherwise, it is idealistic to have some initial estimates of the outcomes before performing any extensive laboratory work or fieldwork.

This work also exhibits several limitations that need to be investigated in the future. First, the dataset used in this study is not large enough, and the effects of aggregate size and water reducing agent type on model prediction accuracy are not studied due to the lack of the dataset. Second, other machine learning algorithms or hybrid models can also be developed appropriately if higher prediction accuracy can be obtained. Finally, the current GUI is relatively simple and rough. As new datasets are added, the model needs to be retrained, and the GUI needs to be further updated and improved.

Data Availability

The dataset used to support the findings of this study and the GUI are available from the corresponding author upon request.

Conflicts of Interest

The authors declare that they have no conflicts of interest.

Acknowledgments

The authors are grateful for the financial support from the Key Scientific and Technological Research Projects of Henan Province (222102210306).

References

[1] S. Barbhuiya, "Effects of fly ash and dolomite powder on the properties of self-compacting concrete," *Construction and Building Materials*, vol. 25, no. 8, pp. 3301–3305, 2011.

[2] A. Fuzail Hashmi, M. Shariq, and A. Baqi, "Flexural performance of high volume fly ash reinforced concrete beams and slabs," *Structures*, vol. 25, pp. 868–880, 2020.

[3] W. Ahmad, A. Ahmad, K. A. Ostrowski, F. Aslam, and P. Joyklad, "A scientometric review of waste material utilization in concrete for sustainable construction," *Case Studies in Construction Materials*, vol. 15, 2021.

[4] W. Ahmad, A. Ahmad, K. A. Ostrowski, F. Aslam, P. Joyklad, and P. Zajdel, "Sustainable approach of using sugarcane bagasse ash in cement-based composites: a systematic review," *Case Studies in Construction Materials*, vol. 15, 2021.

[5] Y. Hefni, Y. A. E. Zaher, and M. A. Wahab, "Influence of activation of fly ash on the mechanical properties of concrete," *Construction and Building Materials*, vol. 172, pp. 728–734, 2018.

[6] R. Hay and C. P. Ostertag, "New insights into the role of fly ash in mitigating alkali-silica reaction (ASR) in concrete," *Cement and Concrete Research*, vol. 144, 2021.

[7] S. Kang, Z. Lloyd, T. Kim, and M. T. Ley, "Predicting the compressive strength of fly ash concrete with the Particle model," *Cement and Concrete Research*, vol. 137, 2020.

[8] M. Sahmaran and V. C. Li, "Durability properties of micro-cracked ECC containing high volumes fly ash," *Cement and Concrete Research*, vol. 39, no. 11, pp. 1033–1043, 2009.

[9] P. Chopra, R. K. Sharma, M. Kumar, and T. Chopra, "Comparison of machine learning techniques for the prediction of compressive strength of concrete," *Advances in Civil Engineering*, vol. 2018, Article ID 5481705, 9 pages, 2018.

[10] J.-S. Chou and A.-D. Pham, "Enhanced artificial intelligence for ensemble approach to predicting high performance concrete compressive strength," *Construction and Building Materials*, vol. 49, pp. 554–563, 2013.

[11] F. Farooq, A. Akbar, R. A. Khushnood, W. L. B. Muhammad, S. K. U. Rehman, and M. F. Javed, "Experimental investigation of hybrid carbon nanotubes and graphite nanoplatelets on rheology, shrinkage, mechanical, and microstructure of SCCM," *Materials*, vol. 13, no. 1, 2020.

[12] A. F. Deifalla, A. G. Zapris, and C. E. Chalioris, "Multivariable regression strength model for steel fiber-reinforced concrete beams under torsion," *Materials*, vol. 14, no. 14, 2021.

[13] O. Sucharda, M. Pajak, T. Ponikiewski, and P. Konecny, "Identification of mechanical and fracture properties of self-compacting concrete beams with different types of steel fibres using inverse analysis," *Construction and Building Materials*, vol. 138, pp. 263–275, 2017.

[14] M. Azimi-Pour, H. Eskandari-Naddaf, and A. Pakzad, "Linear and non-linear SVM prediction for fresh properties and compressive strength of high volume fly ash self-compacting concrete," *Construction and Building Materials*, vol. 230, 2020.

[15] J. Zhang, G. Ma, Y. Huang, J. Sun, F. Aslani, and B. Nener, "Modelling uniaxial compressive strength of lightweight self-compacting concrete using random forest regression," *Construction and Building Materials*, vol. 210, pp. 713–719, 2019.

[16] E. M. Golafshani and A. Ashour, "Prediction of self-compacting concrete elastic modulus using two symbolic regression techniques," *Automation in Construction*, vol. 64, pp. 7–19, 2016.

[17] P. Saha, P. Debnath, and P. Thomas, "Prediction of fresh and hardened properties of self-compacting concrete using support vector regression approach," *Neural Computing & Applications*, vol. 32, no. 12, pp. 7995–8010, 2020.

[18] P. Neira, L. Bennun, M. Pradena, and J. Gomez, "Prediction of concrete compressive strength through artificial neural networks," *Građevinar*, vol. 72, no. 7, pp. 585–592, 2020.

[19] S. Kostic and D. Vasovic, "Prediction model for compressive strength of basic concrete mixture using artificial neural networks," *Neural Computing & Applications*, vol. 26, no. 5, pp. 1005–1024, 2015.

[20] Z. H. Duan, S. C. Kou, and C. S. Poon, "Prediction of compressive strength of recycled aggregate concrete using artificial neural networks," *Construction and Building Materials*, vol. 40, pp. 1200–1206, 2013.

[21] P. Parthiban and J. Karthikeyan, "Artificial neural network to predict the compressive strength of semilightweight concrete containing ultrafine GGBS," *Journal of Testing and Evaluation*, vol. 48, no. 2, pp. 795–810, 2019.

[22] J. Zhang, J. Xu, C. Liu, and J. Zheng, "Prediction of rubber fiber concrete strength using extreme learning machine," *Frontiers in Materials*, vol. 7, no. 465, 2021.

[23] Y. R. Wang, Y. L. Lu, and D. L. Chiang, "Adapting artificial intelligence to improve in situ concrete compressive strength estimations in rebound hammer tests," *Frontiers in Materials*, vol. 7, no. 365, 2020.

[24] H. B. Ly, T. A. Nguyen, H. V. T. Mai, and V. Q. Tran, "Development of deep neural network model to predict the compressive strength of rubber concrete," *Construction and Building Materials*, vol. 301, 2021.

[25] Q. Han, C. Gui, J. Xu, and G. Lacidogna, "A generalized method to predict the compressive strength of high-performance concrete by improved random forest algorithm," *Construction and Building Materials*, vol. 226, pp. 734–742, 2019.

[26] F. Farooq, S. Czarnecki, P. Niewiadomski et al., "A comparative study for the prediction of the compressive strength of self-compacting concrete modified with fly ash," *Materials*, vol. 14, no. 17, 2021.

[27] X. Zhang, M. Z. Akber, and W. Zheng, "Prediction of seven-day compressive strength of field concrete," *Construction and Building Materials*, vol. 305, Article ID 124604, 2021.

[28] K. T. Nguyen, Q. D. Nguyen, T. A. Le, J. Shin, and K. Lee, "Analyzing the compressive strength of green fly ash based geopolymer concrete using experiment and machine learning approaches," *Construction and Building Materials*, vol. 247, Article ID 118581, 2020.

[29] A. K. Al-Shamiri, J. H. Kim, T.-F. Yuan, and Y. S. Yoon, "Modeling the compressive strength of high-strength concrete: an extreme learning approach," *Construction and Building Materials*, vol. 208, pp. 204–219, 2019.

[30] W. Jiang, Y. J. Xie, W. X. Li, J. X. Wu, and G. C. Long, "Prediction of the splitting tensile strength of the bonding interface by combining the support vector machine with the particle swarm optimization algorithm," *Engineering Structures*, vol. 230, 2021.

[31] C.-C. Chang and C.-J. Lin, "Training v-support vector regression: theory and algorithms," *Neural Computation*, vol. 14, no. 8, pp. 1959–1977, 2002.

[32] C.-C. Chang and C.-J. Lin, "LIBSVM: a library for support vector machines," *ACM Transactions on Intelligent Systems and Technology*, vol. 2, no. 3, Article ID 27, 2011.

[33] Y. R. Liu, L. Wang, and K. X. Gu, "A support vector regression (SVR)-based method for dynamic load identification using heterogeneous responses under interval uncertainties," *Applied Soft Computing*, vol. 110, 2021.

[34] M. Hadzima-Nyarko, E. K. Nyarko, N. Ademovic, I. Milicevic, and T. K. Sipos, "Modelling the influence of waste rubber on compressive strength of concrete by artificial neural networks," *Materials*, vol. 12, no. 4, 2019.

[35] M. S. T. Nguyen, M. C. Trinh, and S. E. Kim, "Uncertainty quantification of ultimate compressive strength of CCFST columns using hybrid machine learning model," *Engineering with Computers*, 2021.

[36] M. S. T. Nguyen and S. E. Kim, "A hybrid machine learning approach in prediction and uncertainty quantification of ultimate compressive strength of RCFST columns," *Construction and Building Materials*, vol. 302, 2021.